Dynamical circulation regimes in planetary (and exo-planetary) atmospheres

Fachreddin Tabataba-Vakili
Trinity College

A Thesis submitted for the degree of Doctor of Philosophy

Atmospheric, Oceanic, and Planetary Physics
Department of Physics
University of Oxford

February 2017

Acknowledgements

I would like to extent my gratitude to my supervisor Professor Peter Read. I have learned a lot from him these last three and a half years. His guidance and support was invaluable.

Further thanks go out to Roland Young, Yixiong Wang, Alexandru Valeanu and Luca Montabone for insightful discussions and helpful remarks. Pierre Augier for helping me with rewriting his spectral energy budget code. Moritz Elle for some last minute proofreading.

Finally, I would like to thank my friends and family. My parents, Jutta and Nureddin, for always supporting and believing in me.

And most of all, thank you Alice. For everything.

Abstract

In this thesis, we study the effect of diurnally- and seasonally-varying forcing on the global circulation of planetary atmospheres explored within a large parameter space. This work focusses on studying the spacial and spectral energy budgets across a large range of planetary parameters as well as the momentum transfer as a response to diurnal and seasonal effects.

We simulate planetary atmospheres using PUMA-GT, a simple GCM co-developed for this work, that is forced by a semi-grey two-band radiative-convective scheme, dissipated by Rayleigh friction and allows for temporally varying insolation. Our parameter regime includes the variation of the planetary rotation rate, frictional timescale in the boundary layer, the thermal inertia of the surface and the atmosphere, as well as the short-wave optical thickness.

We calculate the energy transfer in Martian atmosphere to have a reference case of an atmosphere that is subject to very strong seasonal and diurnal variation. For this we present the first Lorenz energy budget calculated from reanalysis data of a non-Earth planet. A comparison between Martian and Earth atmosphere reveals a fundamentally different behaviour of the barotropic conversion term in the global mean. A significant impact of the thermal tide can be discerned in the generation of eddy kinetic energy, especially during global dust storms.

Our study of seasonal variation reaffirms previous work that the equatorial super-rotating jet in the slow-rotating regime is arrested for strong seasonal variation. We find a novel explanation as to why the Titan atmosphere is able to maintain super-rotation despite strong surface seasonality; for non-zero short-wave absorption in the atmosphere the mechanism that hinders equatorial super-rotation is weakened.

Diurnally-varying forcing can significantly enhance the equatorial super-rotation in cases with non-zero short-wave absorption. In our simulations this enhancement is maintained by a convergence of vertical momentum flux at the equator. Efforts to identify the atmospheric waves involved in this enhancement point towards thermally-excited gravity waves.

Contents

List of Symbols

α	surface seasonality parameter
α_r	solar right ascension angle
α_ρ	specific volume, $\alpha = 1/\rho$
α_{atm}	atmospheric seasonality parameter
β	Coriolis parameter in β-plane approximation
$\boldsymbol{u} = (u, v)$	horizontal velocity vector field
$\boldsymbol{u}$	horizontal velocity vector field
$\boldsymbol{u}_c = (u_c, v_c)$	horizontal velocity vector field $(\cdot \cos\phi)$
$\boldsymbol{u}_{th}$	thermal wind vector, $\boldsymbol{u}_{th} = u_{th}e_x + v_{th}e_y$
$\boldsymbol{v} = (\boldsymbol{u}, \omega)$	velocity vector field
χ	horizontal velocity potential
χ	optical depth
χ^*	scaled optical depth, $\chi^* = D_\chi \chi$
χ_{lw}	long-wave optical depth
χ_{sw}	short-wave optical depth
ΔT_H	equator-to-pole potential temperature difference
δ	solar declination
δ_n	diurnal mean declination
δ_s	skin-depth of the surface
$\dot{\sigma}$	vertical velocity in σ coordinates
ϵ	obliquity
ϵ_r	fraction of radiation that is absorbed by the atmosphere
$\gamma = R/[\Lambda p \partial_p \theta_R]$	
Γ	dry adiabatic lapse rate
$\hat{\theta}_s$	surface potential temperature of the reference temperature
$\hat{Z}$	atmospheric height of the reference atmosphere
κ	$\kappa = R/c_p$
κ	adiabatic coefficient
$\Lambda = (p_0/p)^\kappa$	
λ	longitude
λ_{gw}	vertical wavelength of inertial gravity wave
$\langle\theta\rangle$	horizontal mean temperature

$\mathcal{A}$	Thermal relaxation number of the atmosphere
$\mathcal{C}$	cumulative sum of spectral conversion between APE and KE
$\mathcal{G}$	Greenhouse parameter
$\mathcal{P}$	absorbed power
$\mathcal{R}o$	thermal Rossby number
$\mathcal{T}_f$	frictional Taylor number
μ	cosine of solar zenith angle θ_z
μ_n	diurnal mean cosine of solar zenith angle
∇_h	horizontal gradient operator, $\nabla_h = (\partial_x, \partial_y)$
Ω	planetary rotation rate
ω	vertical velocity in pressure coordinates, $\omega = dp/dt$
Ω^*	planetary rotation rate relative to Earth value, $\Omega^* = \Omega/\Omega_E$
ω_{orb}	angular frequency of planetary orbit
$\overline{r}$	mean planet-to-star distance
Φ	geopotential
Φ	geopotential
ϕ	latitude
Φ_m	meridional mass streamfunction
Π	vertically integrated spectral flux
π	pressure of the reference state
ψ	horizontal streamfunction
ρ	density
ρ	density
σ	vertical coordinate, $\sigma = p/p_s$
σ_B	Stefan-Boltzmann constant
τ_f	frictional time scale
τ_r	radiative (thermal) time scale of the atmosphere
τ_r	radiative timescale
τ_{atm}	atmospheric radiative equilibrium time scale, see Eqn. 1.10
$\tau_{conv.adj.}$	convective adjustment timescale
τ_{ft}	frictional spin-down time scale
τ_{surf}	surface thermal inertia timescale
τ_{surf}	thermal inertia time scale of the planetary surface
Θ	Heaviside function
θ	potential temperature
$\theta' = \theta - \langle\theta\rangle$	potential temperature fluctuation
θ_A	departure from horizontal mean of potential temperature
θ_R	horizontal mean of potential temperature
θ_s	surface potential temperature
θ_z	solar zenith angle
ζ	relative vorticity

ζ	vorticity
A	available potential energy
a	planetary radius
A_E	eddy available potential energy
A_Z	zonal available potential energy
C	conversion between APE and KE
C	heat capacity per unit area
c	phase speed of the thermal forcing
C_A	conversion term between AZ and AE
C_E	conversion term between AE and KE
C_K	conversion term between KZ and KE
c_p	heat capacity of air for constant pressure
C_Z	conversion term between AZ and KZ
d	horizontal divergence
d	vertical thickness of frictional layer
$d\sigma$	surface element in isobaric coordinates
$D_\theta(\theta)$	diffusion term
D_A	diffusion of APE
D_K	diffusion of KE
D_m	divergence
$D_{\boldsymbol{u}}(\boldsymbol{u})$	diffusion term
D_χ	diffusivity factor
dm	mass element in isobaric coordinates
E	total energy
e	orbital eccentricity
e_x, e_y, e_z	carthesian unit vectors
E_{tot}	total atmospheric energy
Ek	Ekman number
f	Corilis parameter
f	Coriolis parameter $f = 2\Omega$
$F^\downarrow$	
$F^\uparrow$	
F_s^{net}	net short-wave radiation flux
F_E	dissipation of K_E by friction
F_i	incident flux
F_L	long-wave radiation flux
f_n^m	spectral coefficient (total wavenumber n and zonal wavenumber m)
F_s	short-wave radiation flux
F_t	transmitted flux
F_Z	dissipation of K_Z by friction
$F_{A\uparrow}$	upward flux of APE

$F_{K\uparrow}$	upward flux of KE
G	generation term of APE
G	horizontal angular momentum flux convergence from generated wave activity
g	gravitational acceleration
g_a	mean anomaly
G_E	generation of A_E by diabatic heating
G_Z	generation of A_Z by diabatic heating
H	atmospheric scale height
h	hour angle
H_ζ, H_D, H_T	hyperdiffusion coefficients
H_d	half day length
H_p	total potential energy
h_{th}	height of thermally excited region
I	internal energy
K	kinetic energy
k	total wavenumber
k_a	absorption coefficient
K_E	eddy kinetic energy
k_e	total extinction coefficient
k_e^*	density-adjusted extinction coefficient
k_s	scattering coefficient
K_Z	zonal kinetic energy
k_{th}	thermal conductivity of the surface material
L	horizontal length scale
L	mean solar longitude
L_R	Rhines scale
L_s	solar longitude
L_{ts}	true solar longitude
M	relative specific angular momentum
m	absolute specific angular momentum
M_0	integrated angular momentum of the atmosphere in solid body rotation with the planet
M_d	momentum flux divergence of baroclinic eddies in the tropics
N	buoyancy frequency (Brunt-Väisälä frequency)
N_J	number of jets
$n_{\bar{\mu}}$	switch between diurnally-averaged solar zenith angle ($n_{\bar{\mu}} = 1$), and diurnally-varying solar zenith angle ($n_{\bar{\mu}} = 0$)
N_{eff}	efficiency factor
P	potential energy
p	pressure

p_0	reference pressure at planetary surface
P_ζ	parametrisation term in the vorticity equation
P_D	parametrisation term in the divergence equation
P_n^m	associated Legendre polynomial (total wavenumber n and zonal wavenumber m)
p_s	surface pressure
P_T	parametrisation term in the temperature equation
P_{orb}	planetary orbital period
Q	total heating rate
Q_θ	source term
R	gas constant of dry air, 287 $\mathrm{J}kg^{-1}\mathrm{K}^{-1}$
r	planet-to-star distance
S	global superrotation index
s	local superrotation index
S_0	solar irradiance
S_r	propensity for superrotation
$S_{up,eq}$	upper equatorial superrotation index
T	temperature
t	time
T'	deviation from reference temperature
T_0	reference temperature
T_a	mean temperature of the atmosphere
t_d	time in days
t_n	time in days
T_R	restoration temperature
$u = \tan^2(\epsilon/2)$	
U	unavailable potential energy
u	zonal component of $\boldsymbol{u}$
u_{th}	thermal wind velocity, zonal component
v	meridional component of $\boldsymbol{u}$
v_{th}	thermal wind velocity, meridional component
Y_n^m	spherical harmonic function with total wavenumber n and zonal wavenumber m
Y_{km}	spherical eigenfunctions
Z	atmospheric height
Z_s	terrain height
π_{sZ}	zonal mean of pressure in the reference state

Chapter 1

Introduction

Given not only the set of Solar System planets that host substantial atmospheres, but also the over 3500 extrasolar planets detected up to now[1], we now know of many planetary bodies that are likely to be surrounded by atmospheres that span a very large range of possible parameters. The study of the diversity of atmospheric circulation regimes within this parameter space should not only help in understanding the mechanisms controlling the style and intensity of their general circulation, but may also provide initial information on the global climate of exoplanet worlds.

Given that the possible parameter space is very large, however, the utilised model needs to be sufficiently simple so that it remains applicable to a large subset of the possible space while only having to change a manageable number of controlled parameters. We therefore limit ourselves to terrestrial planets, thereby excluding the free parameter of energy emitted by an internal heat source that is distinctive to jovian and other giant planets. Further approximations include the assumption of a flat surface with evenly distributed thermal properties as well as uniformly mixed absorbing gases in the atmosphere. In addition, most atmospheric parametrisations are too specific to the Earth system to be useful in this broad parameter study. Hence, we use a simplified global circulation model (GCM) and assume a dry atmosphere.

With this comprehensive parameter study of simplified atmospheres, we focus on the zero'th order dynamical properties of a circulating atmosphere. While this approach does not result in a good representation of the intricacies of the Earth's atmo-

[1] www.exoplanet.eu, Jan 27, 2016 (3572 planets)

sphere, it can be shown (e.g. Wang, 2014, Mitchell et al., 2014) that for example, the atmospheric structure of Mars, Venus and Titan can be replicated quite well. Kaspi and Showman (2015) examine the effects of varying planetary parameters of atmospheres with a simplified hydrological cycle. They find that latent heat can provide a significant contribution to the meridional heat flux, however, their resulting circulations compare well with equivalent dry simulations (c.f. e.g. Wang, 2014, or the present work).

In the present work, we choose to focus on seasonal and diurnal effects. These are very important on planets such as Mars, Venus and Titan, but for different reasons. On Saturn's moon Titan, seasonality is important due to Saturn's obliquity ($\epsilon = 27°$) and long year (11000 days). While Titan's mostly rocky surface is very susceptible to seasonal changes, its cold atmosphere ($T \approx 100$ K) responds on longer timescales of up to 20 years. This means that diurnal effects should be negligible on Titan. Venus, on the other hand, has almost no axial tilt, so that seasonal changes do not occur. However, the diurnally-varying slowly-moving solar forcing, focused on the equator, produces a strong and measurable response at the level of the main cloud decks (see e.g. Rossow et al., 1990, Sánchez-Lavega et al., 2008) and has been theorised (Fels and Lindzen, 1974, Plumb, 1975) to be partially responsible for the strong prograde jet in the equatorial region. Both Titan and Venus feature this equatorial superrotation. While both planetary bodies fall into the regime of slowly-rotating planets, the method by which superrotation is formed or maintained may differ.

The general circulation of Mars is more Earth-like than that of Venus or Titan. Both Earth and Mars lie in the rapidly rotating (quasi-geostrophic) regime. They feature extratropical baroclinic jets and multiple meridional circulation cells. Mars, however, is strongly susceptible to both seasonal and diurnal solar forcing, most likely due to its rocky surface (small heat capacity), thin atmosphere (surface pressure $p_0 = 610$ Pa) and comparatively large eccentricity. This causes seasonal and diurnal extremes of e.g. surface temperature of over 100 K. The thermal tide is a set of thermally-forced planetary scale waves that emerge as a response to the diurnal cycle of heating and cooling by the incident solar irradiation. It can provide a significant contribution to the wider circulation by interacting with other components of the circulation, such

as zonal flows and other waves. The thermal tide plays a very important role in the circulation of the Martian atmosphere, especially during dusty seasons (see e.g. Leovy and Zurek, 1979, Wilson and Hamilton, 1996, Banfield et al., 2000).

Studying planetary circulation regimes in terms of nondimensional combinations of key control parameters improves the general applicability of the parameter study so long as the principle of dynamical similarity is still valid. When the most important nondimensional parameters to a sufficiently simplified problem are identified, planets located at the same point in nondimensional parameter space are expected to show similar circulatory behaviour (Read, 2011). If this principle of similarity can be established (see e.g. Dias Pinto and Mitchell, 2014), it would allow first-order approximations of the circulation pattern of exoplanet atmospheres to be obtained from a relatively small ensemble of climate model simulations, if their place in this parameter space is known.

Current observational methods have so far allowed for detailed characterisation only of gas-giant exoplanets. Apart from the orbital period and radius for transiting exoplanets, measurements of e.g. the planetary rotation speed (Snellen et al., 2014), atmospheric clouds (Kreidberg et al., 2014), vertical profiles of temperatures, chemical species (e.g. Madhusudhan et al., 2011), and thermal structure (Stevenson et al., 2014) are possible. With the construction of improved ground-based and Earth-orbiting observatories such as the James Webb Space Telescope (JWST), the Extremely Large Telescope (E-ELT) and the Characterising Exoplanets Satellite (CHEOPS), methods currently used for large exoplanets may become applicable for Super-Earths and Earth-sized exoplanets (see e.g. Seager et al., 2009, Belu et al., 2011, Rauer et al., 2011, Hedelt et al., 2013, Broeg et al., 2013, Tessenyi et al., 2013). In addition, further methods are proposed to measure, for example an exoplanet's obliquity (Carter and Winn, 2010), magnetic field (Driscoll and Olson, 2011), and planetary rotation rate(e.g. Seager and Hui, 2002, Spiegel et al., 2007, Pallé et al., 2008). A parameter study that focuses on the atmospheric characteristics as a function of these parameters is therefore particularly timely.

1.1 Non-dimensional parameters

In the present work, we build a large systematic parameter space of atmospheric simulations. In this parameter space, we focus on terrestrial planets with Earth-like and slower-rotation rates. In addition, we concurrently vary the greenhouse effect, the boundary layer friction and the thermal inertia of both surface and atmosphere. We present important non-dimensional parameters that control the atmospheric circulation below. In Chapter 5 we present our parameter study and show the extent by which these parameters are varied (see Section 5.2).

1.1.1 Thermal Rossby number

The Rossby number is defined as the ratio between the inertial force and the Coriolis force of a rotating fluid. For a planetary atmosphere

$$\mathcal{R}o = \frac{U}{fL} = \frac{U}{2\Omega a}, \tag{1.1}$$

we assume a constant Coriolis parameter $f = 2\Omega$ under the f-plane approximation and the horizontal length scale L is usually approximated by the planetary radius a. Ω is the planetary rotation rate.

The thermal Rossby number $\mathcal{R}o$ is the Rossby number with regard to the thermal wind $U = u_{th}$. The thermal wind can be derived from the geostrophic balance (Vallis, 2006)

$$\boldsymbol{f} \times \boldsymbol{u_{th}} = -\nabla_h \Phi, \tag{1.2}$$

where $\boldsymbol{f} = f(\boldsymbol{e}_x + \boldsymbol{e}_y)$, $\boldsymbol{u_{th}} = u_{th}\boldsymbol{e}_x + v_{th}\boldsymbol{e}_y$, and $\boldsymbol{e}_x$ and $\boldsymbol{e}_y$ are cartesian unit vectors and u_{th} and v_{th} are scalar fields of the zonal and meridional wind respectively. The operator $\nabla_h = (\partial_x, \partial_y)$ is the horizontal gradient (at $p = \text{const.}$) and Φ is the geopotential.

u_{th} can be approximated by

$$u_{th} \approx \frac{R}{2\Omega a}\Delta T_H, \tag{1.3}$$

where ΔT_H is the equator-to-pole potential temperature difference and R is the specific

gas constant of dry air. Substituting Eqn. (1.3) into Eqn. (1.1) results in the thermal Rossby number

$$\mathcal{R}o = \frac{R\Delta T_H}{(2\Omega a)^2}. \tag{1.4}$$

Being the ratio between inertial and Coriolis accelerations, $\mathcal{R}o$ is one of the defining parameters for the influence of rotation. For $\mathcal{R}o < 1$, the Coriolis forces dominate the planetary circulation while for $\mathcal{R}o > 1$ inertial and centrifugal forces gain the upper hand.

1.1.2 Ekman number

The Ekman number indicates the importance of friction in a fluid's boundary layer. It can be defined in different ways. Since the PUMA model works with a rather simplified Rayleigh friction scheme, we define the Ekman number Ek via a characteristic time scale. For this, we use the Rayleigh friction time scale τ_f (see e.g. Mitchell and Vallis, 2010) and compare it to the planetary rotation rate Ω. this results in the Ekman number

$$Ek = (2\Omega\tau_f)^{-1}. \tag{1.5}$$

Larger values of Ek signify an increased importance of friction in the planetary atmosphere. For $Ek \ll 1$, centrifugal and inertial forces dominate (except in a shallow boundary layer adjacent to the surface).

A different approach was used by Wang (2014). He used the frictional Taylor number (see Section 1.3.1)

$$\mathcal{T}_f = (2\Omega\tau_{ft})^4, \tag{1.6}$$

which is again a non-dimensionalised form of representing friction in terms of a characteristic timescale. In Eqn. (1.6) τ_{ft} is the frictional spin-down timescale and represents the characteristic time that the atmosphere takes to lose a significant amount of energy

when thermal forcing is turned off and only frictional damping is active. He finds that

$$\tau_{ft} = \tau_f \frac{H}{d}, \tag{1.7}$$

where H is the atmospheric scale height and d is the vertical thickness of the layer in which friction occurs.

1.1.3 Surface seasonality parameter

Mitchell et al. (2014) introduced the seasonality parameter

$$\alpha = (\omega_{orb}\tau_{surf})^{-1} \tag{1.8}$$

to measure the importance of seasonal variability to a planetary atmosphere. In Eqn. (1.8), ω_{orb} is the angular frequency of the planet's orbit and τ_{surf} is the thermal inertia time scale of the planetary surface. For the derivation of τ_{surf}, see Section 3.4.3 (Eqns. 3.51 - 3.56).

Our parameter study of seasonality (Chapter 5, Section 6.3) is limited to obliquities similar to terrestrial solar system planets (see Table 1.1). As a reference value for this study, we use the Earth-equivalent value of $\epsilon = 23.45$. For the non-seasonally varying, Venus-like simulations in Section 6.2 the obliquity is set to zero.

1.1.4 Thermal relaxation number

The atmospheric thermal relaxation number $\mathcal{A}$ is the ratio between the radiative relaxation timescale to the diurnal period. It measures the importance of radiative forcing in the atmosphere.

We define $\mathcal{A}$ according to a characteristic timescale:

$$\mathcal{A} = 2\Omega\tau_{atm}. \tag{1.9}$$

where τ_{atm} is the atmospheric radiative equilibrium time scale. One can approximate

τ_{atm} from a simple one-layer radiative approach (see e.g. James, 1995, Eqn. 3.11):

$$\tau_{atm} = \frac{p_s c_p}{4(2-\epsilon_r)\sigma_B T_a^3 g}, \tag{1.10}$$

where p_s is the surface pressure, c_p is the heat capacity of air at constant pressure, ϵ_r is the fraction of surface emitted radiation that is absorbed by the atmosphere, σ_B is the Stefan-Boltzmann constant, T_a is the mean temperature of the atmosphere, and g is the planet's gravitational acceleration.

Using the radiative equilibrium time scale τ_{atm}, the thermal relaxation number $\mathcal{A}$ compares the intrinsic radiative response timescale to the length of the day. If $\mathcal{A}$ is small, diurnal variation in the solar irradiance has a significant impact on the thermal profile and radiative balance of the atmosphere. For $\mathcal{A} >> 1$ the atmosphere will react very slowly to temporally-varying forcing on e.g. diurnal or seasonal timescales.

Similar to α (Eqn. 1.8), one can also introduce an atmospheric seasonality parameter α_{atm}, which is the ratio between ω_{orb} and τ_{atm}:

$$\alpha_{atm} = (\omega_{orb}\tau_{atm})^{-1}. \tag{1.11}$$

1.1.5 Greenhouse parameter

The greenhouse parameter $\mathcal{G}$ is the normalised difference between the short-wave χ_{sw} and long-wave optical depth χ_{lw} of the atmosphere:

$$\mathcal{G} = \frac{\chi_{lw} - \chi_{sw}}{\chi_{lw} + \chi_{sw}}. \tag{1.12}$$

$\mathcal{G}$ can be used to ascertain the importance of a simplified greenhouse effect on the planetary circulation (Wang, 2014). With the definition given in Eqn.1.12, $\mathcal{G} > 0$ describes a positive greenhouse effect, with $\chi_{lw} > \chi_{sw}$. The regime of $\mathcal{G} < 0$ describes an anti-greenhouse effect, i.e., short-wave radiation is absorbed in the higher altitudes of the atmosphere and thereby reaches the ground less effectively. $\mathcal{G} = 1$ describes the maximum greenhouse effect for a given opacity and $\mathcal{G} = -1$ the maximum anti-greenhouse effect, i.e. an atmosphere absorbing only long-wave radiation or only short-

wave radiation, respectively.

Wang (2014) defined this parameter as $\mathcal{G}_W = \frac{\chi_{sw}}{\chi_{lw}}$. However, this definition makes $\mathcal{G}$ into an anti-greenhouse parameter, since it is zero at maximum greenhouse and large in the anti-greenhouse case. Real atmospheres will typically lie somewhere in between these extremes.

1.1.6 Diurnally-varying solar zenith angle

The effect of the diurnal cycle on the atmospheric dynamics is one of the main points of interest for the current work. As described in sections 3.4.1 and 3.4.2, the radiative convective scheme of PUMA-GT is able to represent an annually and diurnally varying as well as a diurnally-averaged solar zenith angle. We vary between these two modes by $n_{\bar{\mu}} \in \{0, 1\}$ as an input switch. When turned on, i.e. $n_{\bar{\mu}} = 1$, the radiative scheme uses a diurnal mean value of the solar zenith angle in each model time step. In this mode seasonal variations remain in effect.

1.2 Solar system planets

Planets in the solar system provide an interesting range of different characteristics that can be studied on the basis of their planetary parameters. In Table 1.1, we summarise the terrestrial planets in our solar system in terms of their non-dimensional parameters (in bold) and other associated parameters. We calculate the optical depths χ_{sw} and χ_{lw} using incident fluxes F_i and transmitted fluxes F_t. For χ_{sw}, we considered the effects of short-wave scattering by reducing the incident flux by the amount of the scattered flux. All values for τ_f are obtained from model assumptions for a Rayleigh friction scheme (see Eqn. 3.15).

Using the Rossby number, the listed planets can be grouped into two classes. Slowly-rotating planets with $\mathcal{R}o > 1$ are dominated by a cyclostrophic balance, i.e. rotational forces are weak, so there is a balance between inertial and pressure forces. On these planets, one can observe strong prograde winds at the equator. Venus and Titan both belong to this slowly-rotating class. The atmospheres of fast-rotating planets with $\mathcal{R}o < 1$ are subject to geostrophic balance, i.e. a balance between Coriolis

Planet	Earth	Venus	Mars	Titan	Sources
$a(km)$	6371	6052	3390	2576	
P_{rot} (days)	1	243	1.025	16	
Ω (rad s^{-1})	7.27E-5	3.0E-7	7.1E-5	4.5E-6	
T_a (K)	288	731	214	94	SL11
ΔT_H (K)	60	20	65	4	E:M10; V:Z07; M:R04; T:M14
$\boldsymbol{\mathcal{R}o}$	0.02	300	0.1	10	E,T:M14; V:L12; M:L01
τ_f	1 d	>3 d	2 d	3 d	E:W14; V:R12; M:R04; T: Y16
$\boldsymbol{Ek}$	0.08	$\leq$6.4	0.04	0.4	Eqn. 4.33
p_s (bar)	1	92	0.007	1.5	SL11
T_{rad} (K)	263	238	222	94	SL11
τ_{rad}	32 d	10 y	1 d	20 y	W11, Eqn. 1.10
$\boldsymbol{\mathcal{A}}$	400	190	12	5500	Eqn. 1.9
$\boldsymbol{\alpha}_{atm}$	1.8	0.001	100	0.24	Eqn. 1.11
τ_{rad} ($p \approx 0.1$bar)	16 d	10 d	–	10 y	SL11
$\boldsymbol{\mathcal{A}}(p \approx 0.1\text{bar})$	200	0.5		2800	Eqn. 1.9
obliquity ϵ	23.45°	177.4°	25.19°	26.73°	
$\boldsymbol{\alpha}$	0.04	0	20	> 10	M14
χ_{sw}	0.35	2.2	0.1	2.2	R15 using $\chi = \ln \frac{F_i}{F_t}$
χ_{lw}	3	10	0.31	0.8	R15 using $\chi = \ln \frac{F_i}{F_t}$
$\boldsymbol{\mathcal{G}}$	0.8	0.64	0.51	-0.47	Eqn. 1.12

Table 1.1: Estimated non-dimensional numbers and associated parameters for terrestrial solar system planets. Sources: L01: Leovy (2001), R04: Read and Lewis (2004), Z07: Zasova et al. (2007), M10: Mitchell and Vallis (2010), SL11: Sanchez-Lavega (2011), W11: Wells (2011), L12: Lewis et al. (2012), R12: Russell (2012), M14: Mitchell et al. (2014), W14: Wang (2014), R15: Read et al. (2015), Y16: Yamamoto and Takahashi (2016)

and inertial forces (see Section 1.1.1) In this regime, one observes baroclinic jets (see e.g. Fig. 1.1). Earth and Mars belong to this fast rotating class.

Regarding the surface seasonality parameter α, one can arrange planets into strongly seasonal and weakly seasonal groups. Strongly seasonal planets (Mars, Titan) have low thermal inertias of the surface and, in case of Mars, large values of orbital eccentricity and obliquity. Earth and Venus are both weakly seasonal planets, albeit for different reasons; Earth's oceans provide a large enough thermal inertia to forego extreme seasonal variation, whereas Venus has a fairly small obliquity and thereby receives a nearly unmodulated solar flux over its year.

Using the Ekman number, Ek, we can classify the relative effects of friction. With regard to their frictional time scale, the terrestrial bodies shown in Table 1.1 can be grouped into (a) planets with friction-dominated boundary layers, i.e. Venus and Titan, and (b) planets in which the boundary layer has only weak friction, i.e. Earth and Mars. In our idealised model study, we assume a similar ratio of the between boundary layer thickness d and height scale H for each planet, in which case Ek provides information about the relative impact of friction towards the dynamical circulation. For the solar system planets this comparison is more difficult, as for instance Titan has strong friction with $Ek = 0.4$, but only a small $d/H << 1$, so that overall frictional effects may be less important.

The thermal relaxation number $\mathcal{A}$ is particularly interesting because it leads to a different grouping of the listed planets than for the previously discussed non-dimensional parameters. The radiative equilibrium timescale is large for the slowly rotating planets Venus and Titan and relatively small for Earth and Mars. However, the extremely slow rotation rate of Venus leads to a low value of $\mathcal{A}$ that lies between the thermal relaxation numbers of Earth and Mars. We do not find a similarly reduced $\mathcal{A}$ for Titan because it rotates faster than Venus, and has very long radiative timescales due to its extremely cold atmosphere ($T = 94$ K). As a consequence of this simplified comparison, the atmospheres of both Mars and Venus should be influenced by diurnal effects. Note, however, that the data presented in Table 1.1 focusses only on a representative altitude in the respective atmospheres. In general, the radiative timescale becomes shorter with increasing altitude. Hence, radiative processes will dominate once moving high enough

in any atmosphere.

The values for the atmospheric seasonality parameter show that both Earth and Titan are moderately affected by seasonal variation. For Venus, seasonal forcing is negligible, whereas the Martian atmosphere reacts very strongly to seasonal change.

In terms of the greenhouse parameter $\mathcal{G}$, Earth, Mars and Venus all have significant greenhouse effects (with $\mathcal{G} > 0$), whereas Titan possesses a significant anti-greenhouse effect due to high altitude hazes that absorb 90 % of incoming short-wave radiation (McKay et al., 1991). Venus, despite having a small $\mathcal{G}$, also has a significant short-wave absorption (with $\chi_{sw} = 2.2$). Here, the atmosphere absorbs a large fraction of short-wave radiation flux before it can reach the ground.

1.3 Recent planetary parameter studies

Some recent parameter studies have focus strongly on quantifying the habitability on extrasolar planets (see e.g. Spiegel et al., 2009, Dressing et al., 2010, Rauscher and Menou, 2012, Linsenmeier et al., 2014) in terms of surface temperatures by varying rotation rate, eccentricity and obliquity. Koll and Abbot (2016) have made a detailed parameter study of the day-to-night-side circulation of synchronously rotating exoplanets.

Other recent studies focus on identifying the character of waves that facilitate the transition into the superrotating regime (see Mitchell and Vallis, 2010, Potter et al., 2014, Dias Pinto and Mitchell, 2014), using a idealised simple GCM, forced by Newtonian relaxation. Mitchell et al. (2014) analyses the effect of seasonal variations in solar forcing on the superrotation regime, also using Newtonian relaxation. In addition, Wang (2014) and Kaspi and Showman (2015) have studied a large parameter space of atmospheres, Kaspi and Showman, focussing on meridional heat transport, and Wang focussing on both heat transport and turbulence.

In this section, we summarise the latter half of these works, focussing on the parameter dependence on the atmospheric circulation of idealised terrestrial planets.

1.3.1 Wang et al.

In recent work, Wang (2014) used a hierarchy of Earth-like simple GCMs (SGCM) to create comprehensive circulation regime diagrams of terrestrial planet atmospheres plotted against the thermal Rossby number $\mathcal{R}o$ and the frictional Taylor number $\mathcal{T}_f$. He considered the two simple GCMs PUMA-S, an SGCM forced by Newtonian cooling (see Section 3.2), and PUMA-G, an SGCM forced by a semi-grey two-band radiative scheme with yearly-averaged incoming solar radiation (see Section 3.3). For the latter model, he investigates the effect of varying the planetary parameters, $\mathcal{R}o$, the obliquity ϵ, and $\mathcal{G}$. We use data obtained from PUMA-S in Chapter 4, and briefly review a dataset from PUMA-G in the introduction of Chapter 5. This work is being prepared for publication in Wang et al. (in prep.a) and Wang et al. (in prep.b).

PUMA-S

Fig. 1.1 displays a phenomenological regime diagram, detailing the regions of different flow regimes plotted against the non-dimensional numbers $\mathcal{R}o$ and $\mathcal{T}_f$, which indicate the importance of rotation and friction to the atmospheric dynamics, respectively. (see Sections 1.1.1, 1.1.2). From Section 1.1, we know that $\mathcal{R}o \propto \Omega^{-2}$ and $\mathcal{T}_f \propto \Omega^2$. Thus varying $\Omega^* = \Omega/\Omega_E$ corresponds to moving down diagonal lines in the $\mathcal{R}o$-$\mathcal{T}_f$ plane. The top left of the plane in Fig. 1.1 corresponds to slowly-rotating planets and the bottom right to fast-rotating planets. Variations solely in τ_f correspond to movement along horizontal lines in the depicted $\mathcal{R}o$-$\mathcal{T}_f$ plane. Fig. 1.1 shows that the phenomenological behaviour of the simulated atmospheres shows a well defined transition, upon which frictional timescales τ_f become so short (i.e. friction becomes stronger) that virtually all wave activity is blocked and only axisymmetric circulation is observed. For longer τ_f, one observes no further transition. One can identify four distinct regimes corresponding to the different planetary rotation rates: at small Rossby numbers ($\mathcal{R}o < 10^{-2}$) multiple zonal jets are produced, while slow rotators (with $\mathcal{R}o > 1$) achieve atmospheric superrotation at the equator. At intermediate values of $\mathcal{R}o$, regular or irregular baroclinic wave activity dominates. In this regime, the atmosphere becomes baroclinically unstable, which is characterised by the conversion of available potential energy into eddy kinetic energy.

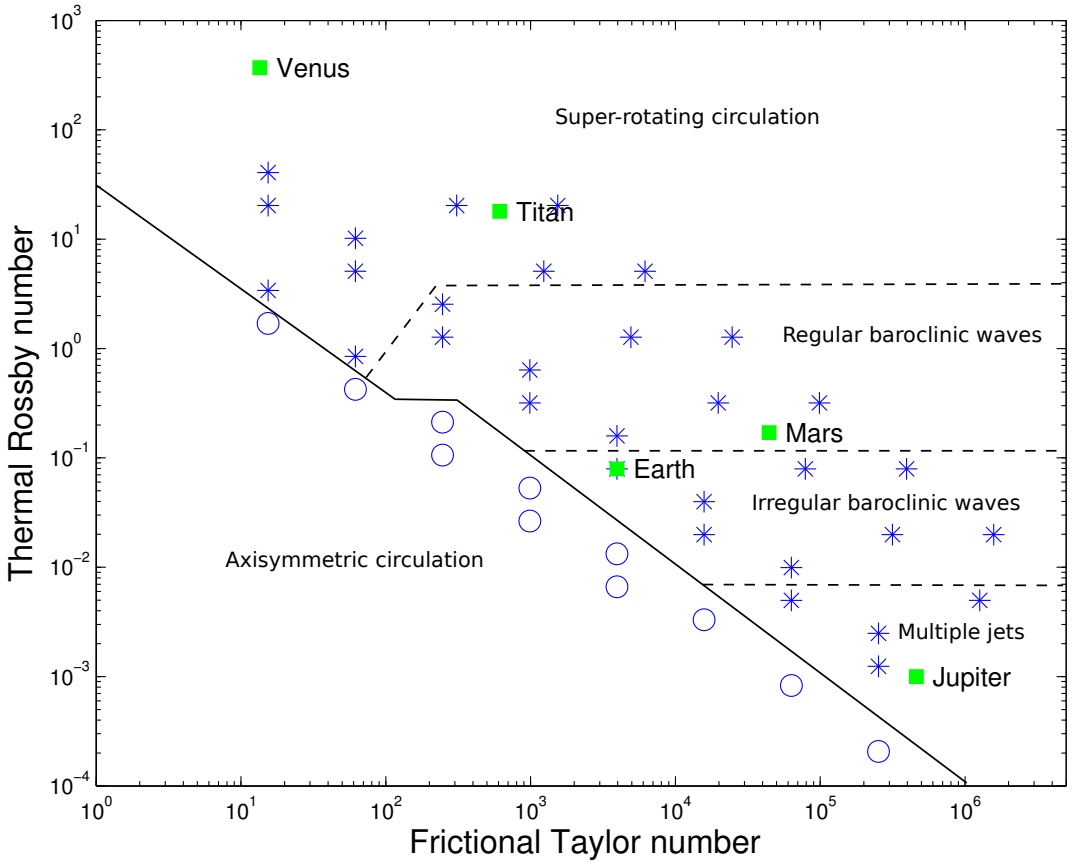

Figure 1.1: Regime diagram of a parameter study performed with PUMA-S under variation rotational and frictional parameters. Reproduced with permission from Wang (2014), their Fig. 3.2.

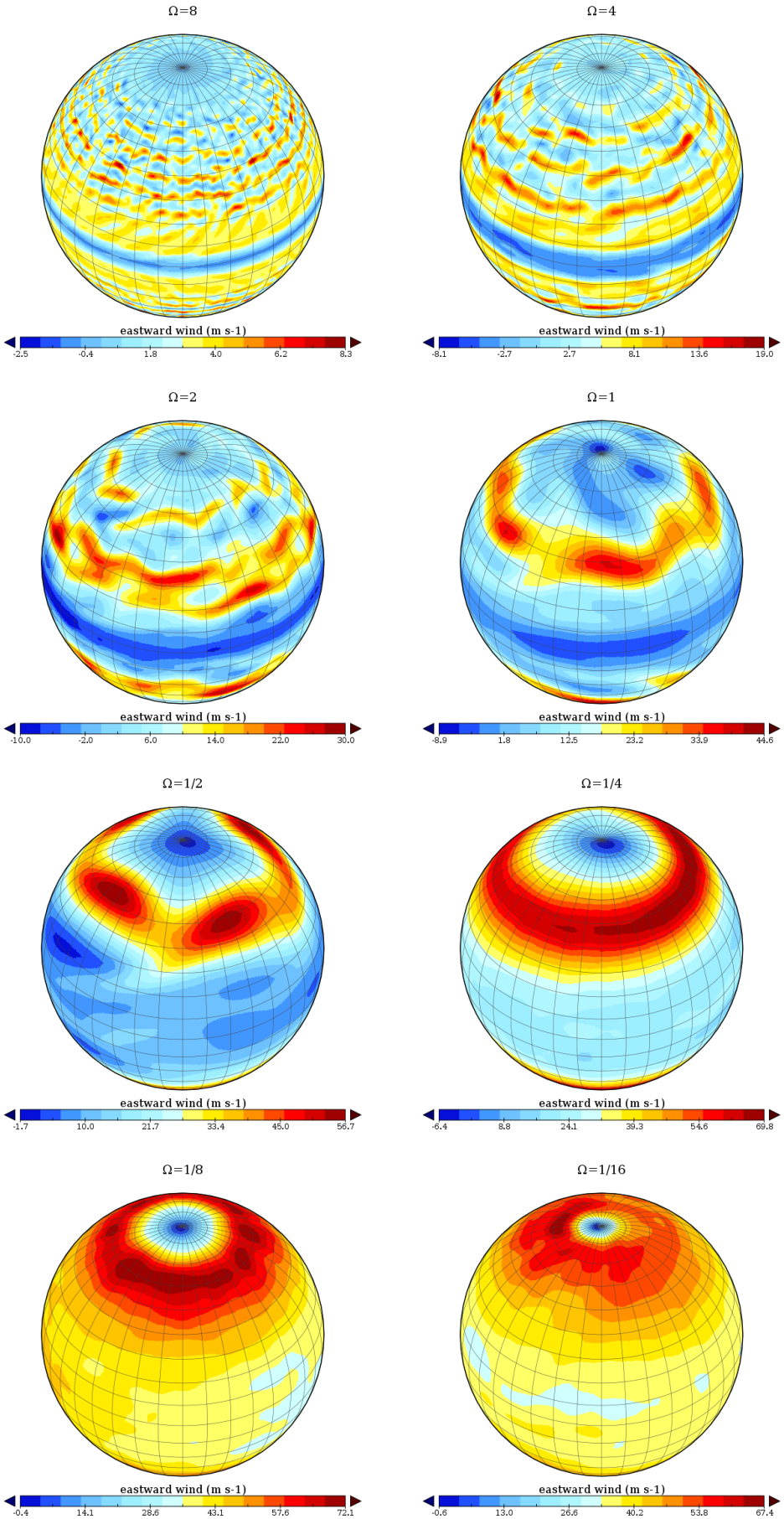

Figure 1.2: Snapshots of eastward wind at 200 hPa for PUMA-S runs with varying rotation rate ($\Omega^* = 8 - \frac{1}{16}$).

In Fig. 1.2, we show snapshots of the eastward wind at $p = 200$ hPa for runs with $\Omega^* = 8 - \frac{1}{16}$. Beginning from the Earth-like simulation at $\Omega^* = 1$, we find an irregular baroclinic jet stream in the extratropics. When moving to higher values of Ω^*, one observes the formation of multiple jets. Wang (2014) confirms that one can approximate the number of jets N_J in a planetary atmosphere via

$$N_J = \frac{a}{L_R}, \tag{1.13}$$

where L_R is the Rhines scale (Rhines, 1975).

$$L_R = \pi \left(\frac{U}{\beta} \right)^{0.5} \tag{1.14}$$

Using the thermal wind u_{th} (Eqn. 1.3) and the β-effect $\beta = 2\Omega \cos\phi$, one can approximate the Rhines scale by (Read, 2011)

$$L_R \approx \pi \left(\frac{R \Delta T_h}{4\Omega^2} \right)^{0.5}. \tag{1.15}$$

Wang (2014) also investigated the turbulence mechanisms of the multiple-jet regime in spectral space (see next subsection).

For rotation speeds ($\Omega^* = \frac{1}{2}, \frac{1}{4}$) that are slightly slower than Earth's rotation speed (see Fig. 1.1, third row), the perturbations to the extratropical baroclinic jets become regularly symmetric, with a stable wavenumber 4 mode for $\Omega^* = \frac{1}{2}$ and a combination of wavenumber 1 and 2 modes for $\Omega^* = \frac{1}{4}$. In this region, the meridional eddy heat flux has a maximum at $\Omega^* = \frac{1}{2}$ and decreases for higher and lower Ω (see discussion of Fig. 1.5 for details). Wang (2014) identified this point as the simulation with maximum baroclinic wave activity (c.f. Lorenz energy budget in Fig. 4.2).

To further understand the regular baroclinic regime, Wang (2014) varied frictional τ_f and radiative (or thermal) time scales τ_r (see Fig. 1.3). For small τ_f and τ_r (strong friction and radiative forcing), one can observe only weak waves. When weakening either the thermal or frictional damping, one observes waves with one dominant wavenumber. At very weak thermal damping (large τ_r), there is a region, in which waves with a combination of two or three different wavenumbers dominate. This points

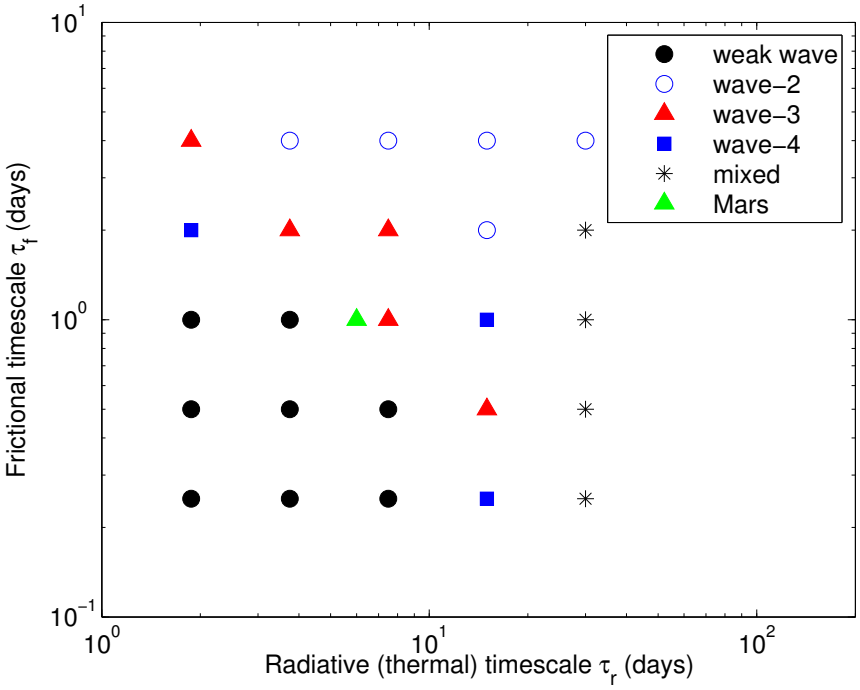

Figure 1.3: Regime diagram of frictional and radiative time scales at $\Omega = \frac{1}{2}$. Reproduced with permission from Wang (2014), their Fig. 3.32.

towards an increase in irregular wave activity. The centre of the graph in Fig. 1.3 shows a data point for Mars, which has a dominant wavenumber 2-3 waves in the northern hemisphere during spring and autumn (e.g. Lewis et al., 2015). Since the regime diagram corresponds with the position of Mars, it is likely that the radiative damping is responsible for the regularity of the Martian baroclinic waves (Wang, 2014).

For even slower rotation rates ($\Omega^* \leq \frac{1}{4}$), strong prograde winds emerge at the equator. This behaviour is termed superrotation when the angular momentum of the atmosphere is larger than the angular momentum of the atmosphere in solid-body rotation with the planet's surface. Wang (2014) identified equator-ward convergence of angular momentum in his simulations, but did not indicate the method by which this momentum is transported. He discounted Rossby waves due to their tendency to transport momentum towards their perturbation source, the extratropics. Instead he discussed the possibility of Kelvin waves (see Section 1.4.1) and the importance of the thermal tide on planets like Venus, which he could not reproduce due to a lack of diurnally-varying forcing in PUMA-S and PUMA-G. In Chapter 6 we aim to explore the potential importance of the diurnal tide on superrotation formation and

maintenance by performing a large parameter study with PUMA-GT and comparing simulations with and without diurnally-varying heating.

Spectral fluxes and turbulence

Wang (2014) analysed the spectral kinetic energy transfer of PUMA-S simulations with Earth-like and faster rotation rates ($\Omega^* = 1, 4, 8$) in order to better understand the formation and maintenance of baroclinic jets in terms of turbulence interactions. For this, he focussed on the applicability of geostrophic (Charney, 1971) and zonostrophic (Galperin et al., 2008, Srinivasan and Young, 2012) turbulence theory. Geostrophic turbulence theory predicts that an upscale energy cascade occurs between the energy containing wavelength and the Rhines wavenumber due to eddy-eddy interactions. The energy containing wavelength is defined by the scale in spectral space with the highest kinetic energy. The Rhines wavenumber is the scale at which turbulent energy is channelled into zonal flows and Rossby waves (see Eqn. 1.15). In addition, there is another scale at which upscale transfers become anisotropic (Vallis and Maltrud, 1993).

Wang (2014) identified that for his simulations in this regime, the energy containing wavelength is roughly equal to the Rhines wavenumber. According to Schneider and Walker (2006), this equality only allows for very small upscale eddy-eddy fluxes. In support of this, Wang (2014) calculated spectral fluxes of rotation kinetic energy and found that the eddy-zonal mean flow interaction component strongly outweighs the eddy-eddy component.

Zonostrophic turbulence describes a special case of geostrophic turbulence under conditions where the Rossby deformation radius is significantly smaller than the planetary scale and a strong planetary rotation is present, for which the large-scale flow is affected by the β-effect and systems of alternating zonal jets emerge (Galperin et al., 2008). Due to this strong "zonation" of mean flow under these circumstances, the zonal component has significantly more energy than the eddy component. This anisotropy between the upscale energy cascades of the zonal (a slope of k^{-5}) and eddy (a slope of $k^{-5/3}$) compentents of the spectral energy is one of the defining features of zonostrophic turbulence (Galperin et al., 2008). Wang's analysis of the kinetic energy spectra of his

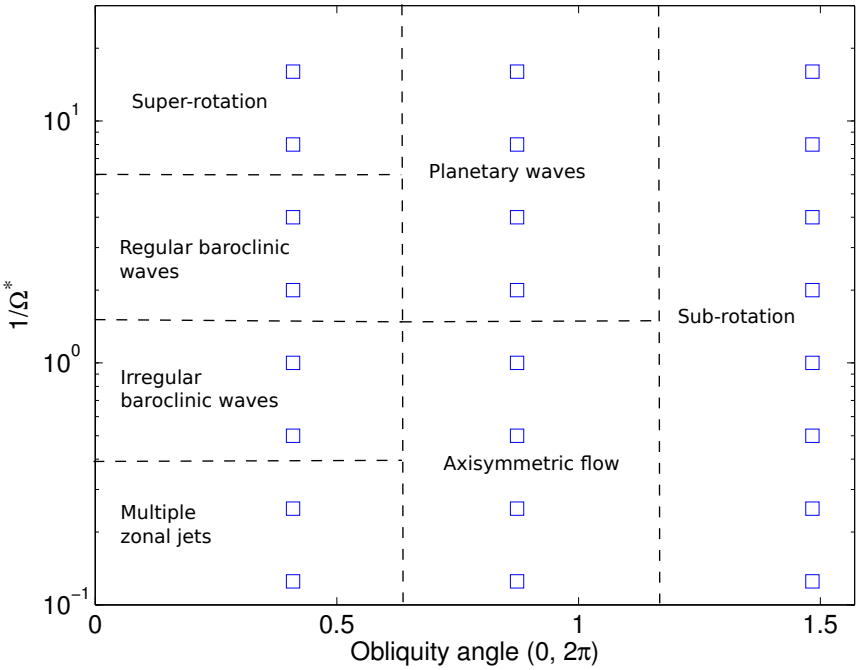

Figure 1.4: Phenomenological regime diagram under variation of rotation rate Ω and the planetary obliquity with PUMA-G for $\mathcal{G} = 0$. Reproduced with permission from Wang (2014), their Fig. 7.1.

simulations revealed an anisotropy between zonal and eddy components. For simulation with weak friction, Wang (2014) also identified slopes in the energy spectra that agree with zonostrophic turbulence theory, making this the first work that unambiguously identified zonostrophic turbulence in 3D atmospheric models, as opposed to 2d simulations and laboratory equivalents.

PUMA-G

For his parameter study with PUMA-G, Wang (2014) studied the effect of varying the Rossby number $\mathcal{R}o$, the planet's obliquity ϵ, and the greenhouse parameter $\mathcal{G}$. Figure 1.4 shows the phenomenological regime diagram for varied Ω and ϵ and constant $\mathcal{G} = 0$. At Earth-like ϵ, one finds the same division into four distinct regimes of planetary rotation rates as for PUMA-S (see Fig. 1.1). In Section 5.1, we present zonal mean diagnostics for this case of varying Ω (see Fig. 5.1).

For $\epsilon = 50°$ (Fig. 1.4, center row), two regimes exist. At fast rotation rates, the simulated atmospheres show barotropically stable axisymmetric flow, while slow rotators can have two separate baroclinic zones per hemisphere (Wang, 2014). The

temperature profile for $\epsilon = 85°$ (Fig. 1.4, right) is meridionally inverted. This produces large thermally direct cells, transporting heat from the poles to the equator. The resulting jets can merge at the equator, producing a strong equatorial subrotation (Wang, 2014). Although these simulations have a significant similarity to Uranus (with $\epsilon = 98°$), the simulations only recreate the retrograde equatorial jet of Uranus, but do not feature Uranus' prograde extratropical jets (Hammel et al., 2005). Wang (2014) assumes that the seasonal forcing, which is missing in his PUMA-G simulations, may be a possible reason for this discrepancy.

1.3.2 Kaspi and Showman

Kaspi and Showman (2015) have recently produced a parameter study that focuses on Earth-like exoplanets. They modelled planets with "wet" atmospheres, i.e. containing a hydrological cycle and a slab ocean. Their gray two-stream radiation scheme features a constant, annually-averaged insolation and a prescribed distribution of optical thickness to reproduce the Earth's temperature distribution in the tropopause. Kaspi and Showman (2015) vary the planetary rotation rate, stellar flux, atmospheric mass, the planetary density, the long-wave optical thickness, and the planetary radius separately and study the responses to the zonal mean circulation. They focus on the equator-to-pole temperature difference and the moist static energy flux. While they do not model these feedbacks directly, their work is motivated by the atmospheric circulation's influence on global climate feedbacks such as global glaciation or a run-away greenhouse effect, which influence the planet's habitability.

In this section, we present some of their results to explain the general reaction of the planetary temperature field to the variation of specific parameters. The consequences of varying the rotation rate Ω are discussed in Sections 1.3.1 and 4.1.1.

Figure 1.5 shows the equator-to-pole temperature difference (top), the mean heat transport (bottom, blue) and the poleward eddy heat transport (bottom, red) as a function of planetary rotation rate for an Earth-sized planet. One can observe that the equator-to-pole temperature difference decreases with decreasing rotation rate. This occurs because the expanded Hadley cell (see Fig. 5.1) induces an enhanced meridional heat flux. The monotonically increasing mean heat transport curve in

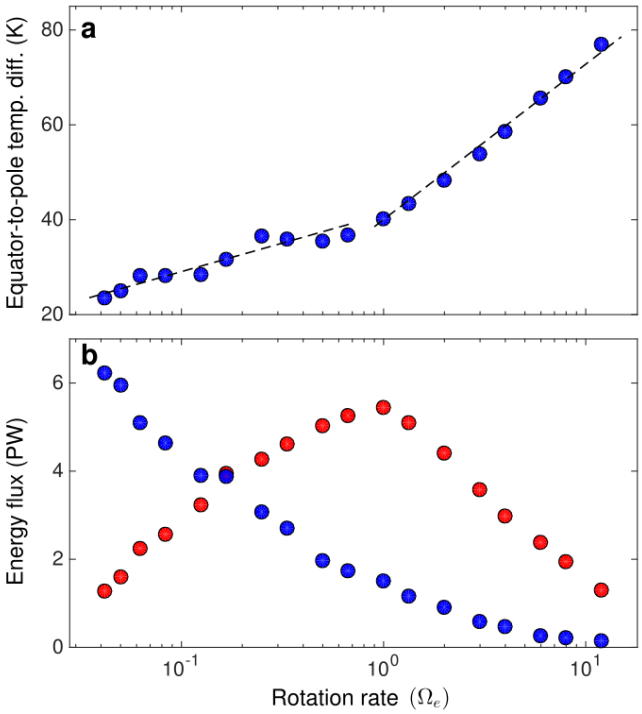

Figure 1.5: Equator-to-pole temperature difference (top), mean heat flux (bottom, blue) and eddy heat flux (bottom, red) depending on the planetary rotation rate. ©AAS. Reproduced with permission from Kaspi and Showman (2015), their Fig. 8.

Fig.1.5b (blue) indicates this enhancement of meridional heat flux. The eddy heat flux in red, on the other hand, has a maximum at the Earth's rotation rate. This result is similar to that of Wang (2014), where a maximum baroclinic eddy activity and eddy heat flux is seen at rotation rates around $\Omega = 0.5\Omega_E$. Kaspi and Showman (2015) identify Ω_E as the transition point between a slowly-rotating ($\Omega < \Omega_E$) and a fast-rotating regime ($\Omega > \Omega_E$). In the slowly-rotating regime, the eddy heat flux increases with increasing Ω, while the mean heat flux decreases with increasing Ω. In the fast-rotating regime, both eddy and mean heat flux decrease with increasing Ω. Due to this difference in slope of the eddy heat flux, planetary rotation has a larger effect on the heat distribution of the fast-rotating regime than on the slowly-rotating regime. Accordingly, one observes the two different slopes of the equator-to-pole temperature difference as a function of Ω in the slowly-rotating and fast-rotating regime (see Fig. 1.5a)

Increasing the solar irradiance S_0 of a planet moves it closer to its parent star and considerably increases planetary temperatures. Kaspi and Showman (2015) found that

an increased solar irradiance reduces the equator-to-pole temperature difference. The Hadley circulation is not responsible for this reduction of equator-to-pole temperature difference because the mass streamfunction of the Hadley cell decreases in strength which results in less heat redistribution. Instead, the reduction of the temperature difference occurs due to an increase in atmospheric water vapour, which significantly increases the meridional eddy latent heat flux. The increased meridional eddy latent heat flux leads to a more effective meridional heat redistribution with increasing solar flux.

Increasing the surface pressure p_s leads to an increase in the total mass of the atmosphere. Kaspi and Showman (2015) found, that with increasing surface pressure p_s, the meridional mass stream function (which is integrated over pressure, see Eqn. 4.1) increases, but the actual velocities of the corresponding jets decrease. They link the decrease of jet velocity to a decline in equator-to-pole temperature difference, which arises due to an increase in meridional eddy heat flux. In addition, the surface temperature also increases with increasing p_s. This occurs via a reduction of the vertical heat flux in those atmospheres at higher pressures.

1.4 Super-rotation on slowly rotating planets

According to Hide (1969), superrotation cannot be maintained by axisymmetric processes if a diffusion mechanism for angular momentum is present. Hence superrotation must be caused by eddy fluxes via an anisotropic, non-diffusive upscale momentum transfer, which enhances the zonal flow (Hide, 1969, Mitchell and Vallis, 2010).

The Gierasch-Rossow-Williams (GRW)"mechanism" proposes that angular momentum generated at the surface via friction is transported first equatorward and then upward via large scale Hadley circulations. At upper levels, the poleward branch of the Hadley cell transports this momentum towards an extratropical jet stream. Once this extratropical jet stream is sufficiently intensified, the meridional shear between equator and extratropical jet will trigger instabilities. The resulting eddies can transport angular momentum equatorwards where it subsequently converges, which causes an equatorial jet to appear (Gierasch, 1975, Rossow and Williams, 1979, Read, 2013).

However, GRW does not sufficiently explain how or by what specific mechanism eddy momentum is transported towards the equator. Both Gierasch (1975) and Rossow and Williams (1979) invoke instabilities in their models to show a conceptual scenario in which convergence of eddy momentum flux can strengthen equatorial zonal flow. Gierasch (1975) uses an eddy viscosity and heat diffusivity to constrain the size of these diffusivities to obtain a strong super-rotation, while Rossow and Williams (1979) use Rossby waves that arise due to horizontal shear in their baroclinic model. These studies are an important proof of concept to showcase how slow-rotating planets may attain equatorial super-rotating jets via eddy momentum convergence, but they do not address the actual mechanism by which this conversion occurs.

Recent simplified GCM studies have shown that increasing the Rossby number $\mathcal{R}o = \frac{RT_0\Delta_H}{(2\Omega a)^2}$ by either deceasing the planetary radius a (e.g. Mitchell and Vallis, 2010) or decreasing the planetary rotation rate Ω (e.g. Williams, 1988a,b, Del Genio et al., 1993, Williams, 2003, 2006, Wang, 2014) can form superrotation without artificial forcing.

While these studies agree that momentum is transported equatorwards by eddy-activity, the kind of wave-generating instability responsible for this momentum flux is contested. Possible sources of superrotation via an equatorial convergence of momentum flux are barotropic-instabilities (Williams, 2003, 2006), Kelvin-Helmholtz waves (Potter et al., 2014), barotropic Rossby-Kelvin instability (Wang and Mitchell, 2014), or Rossby waves generated by tropical convection (Laraia and Schneider, 2015). Mitchell et al. (2014) studied the impact of seasonal changes to superrotation in a simple GCM, finding that a strong seasonal signal can suppress atmospheric superrotation. This suppression occurs due to two reasons. Firstly, with strong seasonality, the vertical flux of momentum is no longer solely concentrated at the equator, but moves meridionally according to the seasonal forcing. Secondly, the extratropical jets in each hemisphere can be strongly asymmetrical during seasonal extremes. During this time, it is possible that angular momentum does not converge at the equator, but is instead transported into the hemisphere with the weaker extratropical jet. However, increasing the thermal damping timescale to Titan-like values restored atmospheric superrotation.

More sophisticated models of Titan (Newman et al., 2011, Lebonnois et al., 2012)

have attributed the momentum convergence to the development of barotropically unstable mid-latitude jets. For Venus GCMs, e.g. Yamamoto and Takahashi (2003), Lee et al. (2007) identify the involvement of Rossby, gravity, and mixed-Rossby-gravity waves in the equatorial eddy momentum flux, whereas more recent Venus GCMs have identified a baroclinic forcing due to cloud layer heating (Yamamoto and Takahashi, 2016) and a strong influence of thermally driven diurnal tides to the vertical momentum flux (Yamamoto and Takahashi, 2006, Lebonnois et al., 2010, 2016, Mendonça and Read, 2016).

In addition, non-axisymmetric forcing has been shown to generate equatorial superrotation in simplified dry GCMs with Earth-like parameters in the form of zonally asymmetric heating (e.g. Suarez and Duffy, 1992, Saravanan, 1993, Kraucunas and Hartmann, 2005, Arnold et al., 2012). Other such forcing that induces superrotation includes e.g. radiative heating on tidally-locked exoplanets (e.g. Showman and Polvani, 2011), or thermally excited gravity waves (Fels and Lindzen, 1974).

We review recent parameter studies that focus on the formation and maintenance of superrotation, below.

1.4.1 Mitchell et al.

Mitchell and Vallis (2010) use a simplified GCM with a spectral dynamical core and a Newtonian cooling scheme to study the emergence of superrotation. For large $\mathcal{R}o$ (which they vary via the planetary radius a instead of the rotation rate Ω), they found super-rotating winds with velocities up to 40 ms^{-1}. In their simulations, initially a global baroclinic wave transported eastward zonal momentum towards the equator (leading toward equatorial momentum convergence). Once superrotation emerged, this baroclinic mode vanished. Mitchell and Vallis (2010) found that once the superrotation is established, a global barotropic mode is responsible for the maintenance of the equatorial superrotation. For smaller $\mathcal{R}o$, Mitchell and Vallis (2010) reported the generation of Rossby waves at the mid-latitudes, which break at the equator and thereby discharge retrograde momentum, which hinders an equatorial momentum flux convergence. This in turn arrests the emergence of super-rotating flow.

Potter et al. (2014) continued this work by studying a larger parameter space.

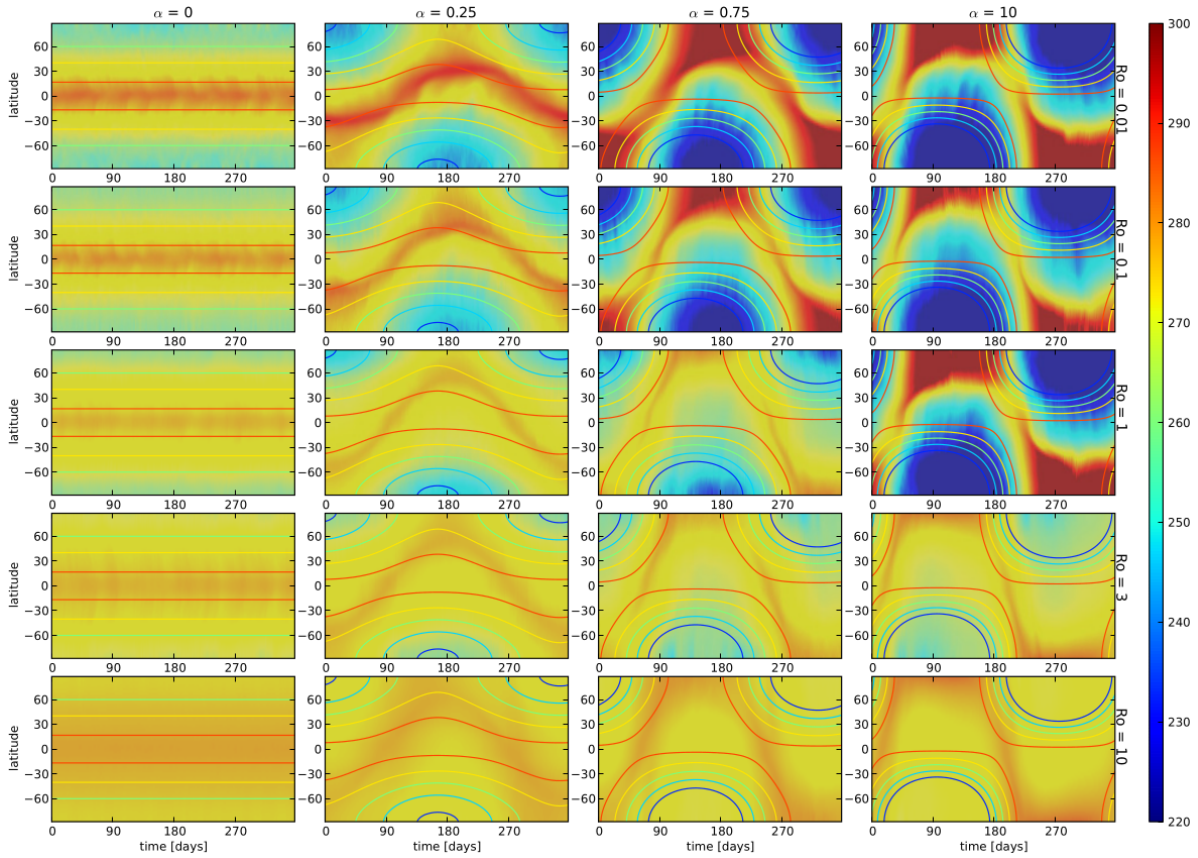

Figure 1.6: Zonal mean surface temperature fields plotted over latitude and time for varying seasonality $\alpha = 0$ to $\alpha = 10$ (left to right) and thermal Rossby number $\mathcal{R}o = 0.01$ to $\mathcal{R}o = 10$ (top to bottom). ©AAS. Reproduced with permission from Mitchell et al. (2014), their Fig. 1.

They separately varied the Rossby number $\mathcal{R}o$, the model-inherent frictional τ_f, and radiative τ_r timescales. They found that among those parameters, $\mathcal{R}o$ has the most dominant effect on superrotation, and that variation of any of the other parameters alone does not result in significant super-rotating equatorial winds. Moreover, they found that eddy momentum convergence due to superposed Rossby-Kelvin waves is responsible for the transition towards superrotation in their simulations.

In a recent study, Mitchell et al. (2014) have investigated the effect of seasonal cycles on the emergence of superrotation via Newtonian cooling of the surface temperature using a seasonal forcing profile. They mainly varied the seasonality α (see Section 1.1.3) and $\mathcal{R}o$. In their simulations, α controls the seasonal time evolution of the surface temperature. Figure 1.6 shows the zonal mean surface temperatures over latitude and time of year for a range of $0 \leq \alpha \leq 10$ (increasing from left to right) and $0.01 \leq$

$\mathcal{R}o \leq 10$ (increasing from top to bottom). Simulations with increased α exhibit larger seasonal temperature differences, where the summer hemisphere is significantly warmer (even reaching up to the poles for large α) than the winter hemisphere. For large $\mathcal{R}o$, the seasonal temperature differences are less pronounced due to the expanded Hadley cells, which strengthen the meridional redistribution of heat. Strongly seasonal simulations feature cross-equator Hadley cells that expand across the equator during summer months, reaching far into the winter hemisphere (c.f. Fig. 5.3).

Mitchell et al. (2014) found that strong seasonality (large α) prevents the formation of super-rotating equatorial winds, even at large $\mathcal{R}o$ (which tends to weaken seasonal temperature variation). They find that during seasonal extremes (i.e. around solstices) strong cross equatorial Hadley cells will affect both vertical and horizontal momentum fluxes to no longer converge onto the equator. However, when reducing the radiative timescale τ_r, the cross-equatorial behaviour of the Hadley circulation decreases and equatorial superrotation reemerges. This setup allows their simplified model to correctly simulate the equatorial superrotation of a Titan-like planet (small τ_r, large α, $\mathcal{R}o \approx 10$).

1.4.2 Laraia and Schneider

Laraia and Schneider (2015) conducted another parameter study to investigate the emergence of superrotation. Their results suggest that tropical convection is responsible for generating Rossby wave activity, which in turn accelerates the zonal flow.

They used scaling theory to identify a new non-dimensional parameter that describes superrotation. They varied the rotation rate Ω, the equator-to-pole temperature difference ΔT_H of a Newtonian cooling scheme, and the convective lapse rate Γ simultaneously (as opposed to separately). They then quantified their results regarding superrotation formation in their simulations using the equatorial ($\pm 5^\circ$ latitude) horizontal angular momentum flux convergence G from generated wave activity

$$\langle G_e \rangle = \frac{1}{\Delta\phi} \int_{-5^\circ}^{5^\circ} \frac{1}{\Delta\sigma} \int_{\sigma_t+\Delta\sigma}^{\sigma_t} G^+ \cos\phi d\sigma d\phi \tag{1.16}$$

where G^+ are the positive values of

$$G = -\frac{1}{\cos\phi}\mathrm{div}_y\,(\overline{u'v'}\cos\phi)_e, \tag{1.17}$$

and the momentum flux divergence M_d due to dissipation of baroclinic eddies in the tropics,

$$\langle M_d\rangle = \frac{1}{\Delta\phi}\int_{\phi_2}^{\phi_1}\frac{1}{\Delta\sigma}\int_{\sigma_t+\Delta\sigma}^{\sigma_t} M\cos\phi d\sigma d\phi, \tag{1.18}$$

where

$$M = \mathrm{div}_y\,(\overline{u'v'}\cos\phi)_x. \tag{1.19}$$

The e and x subscripts denote equatorial and extratropical regions, respectively (Laraia and Schneider, 2015). div_y is the meridional divergence operator, ϕ is the latitude angle, and $[\sigma_t, \sigma_t + \Delta\sigma]$ is a vertical region of the upper atmosphere with $\sigma = p/p_s$.

Using scaling theory, they identified a non-dimensional number

$$S_r = \frac{\langle G_e\rangle}{\langle M_d\rangle} \propto \frac{N_x^2}{(H_e^3 N_e^3 \beta_e)^{\frac{1}{2}}}\left(\frac{Q}{N_e\Delta\theta}\right)^2 \tag{1.20}$$

that they termed the propensity for superrotation. Here, N_x is the extratropical buoyancy frequency, H_e is the scale height at the equator, N_e is the equatorial buoyancy frequency and $\beta_e = 2\Omega/a$ is the meridional derivative of the Coriolis parameter near the equator (Laraia and Schneider, 2015). Figure 1.7 shows a comparison of the values of equatorial wind for two non-dimensional parameters ($\mathcal{R}o$ and S_r). One can observe that planets with super-rotating equatorial winds are better described by $S_r > 1$ than by $\mathcal{R}o > 1$. While the S_r in Figure 1.7 fits better, there is still a correlation between superrotation on the equator and $\mathcal{R}o$. S_r is positive for large values of $\mathcal{R}o \propto \Omega^{-2}$. This is due to the G_e^+ term, which features a proportionality to $Q^2/\beta_e^{-1/2}$. Laraia and Schneider (2015) identify an empirical $Q \propto \Omega^{-3/4}$ proportionality so that in total:

$$G_E^+ \propto \beta_e^{-1/2} \propto \Omega^{-1/2} \tag{1.21}$$

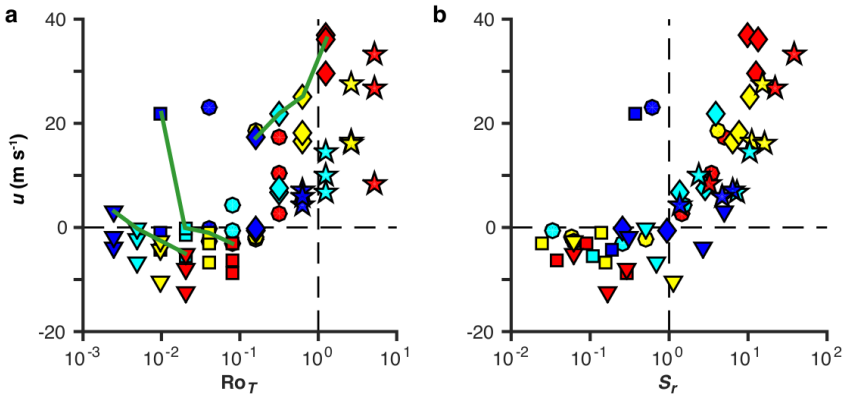

Figure 1.7: Equatorial wind speeds for 60 runs performed by Laraia and Schneider (2015) with varying rotation rate (symbols), equator-to-pole temperature difference (colours), and convective lapse rate as a function of a) the thermal Rossby number $\mathcal{R}o$ and b) the propensity for superrotation S_r. ©American Meteorological Society. Reproduced with permission from Laraia and Schneider (2015), their Fig. 7.

$$G_E^+ \propto Q^2 \propto \Omega^{-3/2} \tag{1.22}$$

and hence $S_r \propto \Omega^{-2}$.

Laraia and Schneider (2015) conclude that, in their model simulations, Rossby waves are responsible for the horizontal momentum flux convergence that leads to superrotation.

1.5 Equatorial Super-rotation

Our parameter study of slowly-rotating planets aims to characterise the effect of rotation rate, friction, radiative properties, and other factors to understand the emergence and maintenance of equatorial superrotation on bodies similar to Venus and Titan. To analyse and compare the dominant contributions to their circulation in the most general way, it is beneficial to study the properties of different circulation regimes with reference to nondimensional parameter spaces (Read, 2011). Of particular interest is the effect of diurnal forcing on the emergence and acceleration of super-rotating flow in planets with $\mathcal{R}o > 1$.

According to Hide (1969), superrotation cannot be maintained by axisymmetric processes if a diffusion mechanism with respect to angular momentum is present. Hence, superrotation must be caused by eddy fluxes via an upgradient momentum

transfer, which enhances the zonal flow (Hide, 1969, Mitchell and Vallis, 2010). Non-axisymmetric forcing has been shown to generate equatorial superrotation in a simplified dry GCM with Earth-like parameters in the form of periodic, zonally asymmetric heating (e.g. Suarez and Duffy, 1992, Saravanan, 1993, Kraucunas and Hartmann, 2005, Arnold et al., 2012). Other such forcing that induces superrotation includes e.g. radiative heating on tidally-locked exoplanets (e.g. Showman and Polvani, 2011), or thermally excited gravity waves (Fels and Lindzen, 1974). Another study using a simplified GCM (Del Genio and Zhou, 1996) prescribes an optically thick cloud layer between 150 and 550 mb, using a constant solar forcing, resulting in strong superrotation even with extremely different initial conditions. In addition Caballero and Huber (2010) find that increasing CO_2 concentrations in an Earth AGCM can also cause superrotation to occur.

Recent simplified GCM studies have shown that increasing the Rossby number $\mathcal{R}o = \frac{R\Delta T_H}{(2\Omega a)^2}$ by either decreasing the planetary radius a (e.g. Mitchell and Vallis, 2010) or decreasing the planetary rotation rate Ω (e.g. Del Genio et al., 1993, Williams, 2003, 2006, Wang, 2014) can form superrotation without artificial forcing. While these studies agree that momentum is transported equatorwards by eddy-activity, the kind of wave-generating instability responsible for this momentum flux is contested. Possible sources of superrotation via an equatorial convergence of momentum flux are barotropic-instabilities (Williams, 2003, 2006), Kelvin-Helmholtz waves (Potter et al., 2014), barotropic Rossby-Kelvin instability (Wang and Mitchell, 2014), or baroclinic waves (Laraia and Schneider, 2015). Mitchell et al. (2014) studied the impact of seasonal changes on superrotation in a simple GCM, finding that a strong seasonal signal can suppress atmospheric superrotation. However, increasing the thermal damping timescale to Titan-like values restored atmospheric superrotation.

More sophisticated models of Titan (Newman et al., 2011, Lebonnois et al., 2012) have attributed equatorial superrotation to the development of barotropically unstable mid-latitude jets. For Venus GCMs, Yamamoto and Takahashi (2003) and Lee et al. (2007) identify the involvement of Rossby, gravity, and mixed-Rossby-gravity waves in the equatorial eddy momentum flux. More recent Venus GCMs have identified a baroclinic forcing due to cloud layer heating (Yamamoto and Takahashi, 2016) and

a strong influence of thermally driven diurnal tides on the vertical momentum flux (Lebonnois et al., 2010, 2016).

When keeping these studies in mind, the need for a parameter study arises that assesses the effect of short-wave and long-wave optical thicknesses quantitatively. In addition, the diurnal variation in temperature forcing is in effect a zonally asymmetric heating term which may well influence the superrotation regime. Studying the interplay of the effects of both seasonally- and diurnally-varying forcing in a systematic way will help in quantifying their ability to strengthen or weaken the super-rotating circulation.

1.6 Science questions

In the current work, we focus on the general effect of dynamical and radiative changes on an idealised atmosphere. Specifically, we focus on the conversion of mechanical energy within the atmosphere, and the influence of diurnally and seasonally varying cycles in solar forcing.

For this thesis we have performed a large set of planetary circulations with seasonally- and diurnally-varying forcing with a large range of parameters. In this set, the thermal Rossby number $\mathcal{R}o$, the thermal inertia of both atmosphere (τ_{rad}) and surface τ_{surf}, the greenhouse parameter $\mathcal{G}$ and the bottom layer friction Ek have been varied simultaneously. With this dataset we can aim to answer important questions regarding the basic behaviour of the general circulation of planetary atmospheres.

In this thesis, we aim to answer the following scientific questions.

How does seasonally-varying and diurnally-varying forcing affect the way energy is propagated through the atmosphere? Mars is an important example case for this question as it is influenced strongly by both diurnal and seasonal variation. We study the seasonal and diurnal variation of the mechanical energy budget of the Martian atmosphere using reanalysis data from satellite observation (see Chapter 2). In Chapter 5, we compute Lorenz conversion terms for a large fraction of our simulations with seasonally-varying forcing (see Section 5.5). In Chapter 6, we then compare these terms to those of simulations with both seasonally- and diurnally-varying forcing (see Section 6.3.5).

How is energy transferred between scales in dependence upon our parameters? In the constant forcing case, we analyse the spectral flux of both available potential energy and kinetic energy for simulations with different rotation rates, identifying the difference in spectral flux between geostrophic and cyclostrophic regimes (see Section 4.3). Section 5.6 deals with the spectral energy budget for varying the surface and atmospheric timescales in both the geostrophic and cyclostrophic regimes under seasonally-varying forcing.

How does diurnally- and seasonally-varying forcing affect the dynamics of super-rotating equatorial jets on slowly-rotating planets? In the Solar System both Venus and Titan are slowly-rotating planetary bodies that both feature significant equatorial superrotation. They differ in that Titan is subject to a strongly seasonal variation, while on Venus the thermal tide has been shown to be involved in the super-rotating flow. We focus on seasonal effects in Chapter 5 and diurnal effects in Chapter 6.

How is momentum transferred when the diurnal tide injects energy into the system? In Chapter 6, we compare horizontal and vertical momentum fluxes for simulations with and without diurnally-varying forcing in cases without seasonally-varying forcing (see Section 6.2) and with seasonally-varying forcing (see Sections 6.3 and 6.4). We find that the diurnal forcing results in significant vertical momentum convergence at the equator. In Section 6.5, we perform an initial comparison of the diurnally-induced difference in super-rotating wind with a theory of momentum redistribution via thermally excited gravity waves.

Chapter 2

Energy cycle of the Martian atmosphere

2.1 Computation of the Lorenz energy cycle

The Lorenz energy cycle (Lorenz, 1955) is a useful tool for assessing and quantifying the pathways by which energy is transferred between different components of kinetic and potential energies, from the generation of potential energy via differential heating to dissipation of kinetic energy via frictional effects. Most previous studies have used calculations of the Lorenz energy cycle to understand the energy in the Earth atmosphere. Local calculations of Lorenz energy cycles have focussed for instance on the eddy formation mechanism and evolution of cyclones (Dias Pinto and da Rocha, 2011) or local rainy seasons (Berry and Thorncroft, 2012). Such localised studies, however, require large additional energy transport terms, as the borders of the studied region are permeable. In addition, the local integrands of the Lorenz cycle can be mapped, for instance in studying the eddy kinetic energy of northern hemisphere winter jets (Jiang et al., 2013). In their global-mean, energy cycles can be used to analyse discrepancies between reanalysis datasets (Oort, 1983, Li et al., 2007) or to validate model simulations with reanalysis data on the basis of their atmospheric energies (Boer and Lambert, 2008, Marques et al., 2011). These studies found that the considered models successfully grasp the general scheme of the expected Lorenz cycle, but most models overestimate the efficiency of the cycle, showing excesses in both the

generation of zonal available potential energy and in the dissipation of eddy kinetic energy. To the author's knowledge, applications of the Lorenz energy cycle to other planets are limited. Del Genio et al. (1993) have calculated a simplified version of the Lorenz cycle for super-rotating GCM simulations with regard to Titan and Venus conditions. Recently, Lee and Richardson (2010) have used the Lorenz cycle scheme to assess the effect of damping and the choice of different numerical cores on the forced superrotation in Venus models.

The energy cycle equations that are used in the current work were derived by Boer (1989). He used the hydrostatic primitive equations without further approximation (such as quasigeostrophic or flat-surface approximations as in e.g. Peixóto and Oort (1974), Lorenz (1955)). Hence, we refer to Boer's equations as "exact". In the following section, we introduce atmospheric energetics, describe a method to numerically determine the reference state of the atmosphere and present the "exact" energy budget equations of Boer (1989). In section 2.2, we compute the Lorenz energy cycle of Mars from reanalysis data. The "exact" approach is required because Mars exhibits large topographical variations.

2.1.1 Lower boundary condition and isobaric coordinates

We define the mass element in isobaric coordinates

$$dm = g^{-1} a^2 \cos\phi dp d\phi d\lambda \tag{2.1}$$

and the corresponding surface area element

$$d\sigma = a^2 \cos\phi d\phi d\lambda \,, \tag{2.2}$$

where ϕ is the latitude, λ is the longitude, p is the pressure, a is the planetary radius, and g is the gravitational acceleration. Accordingly, the global integration over the atmospheric mass M of an arbitrary field $X(t, p, \phi, \lambda)$ is given by

$$\int_M X dm = \int_0^{2\pi} \int_{-\pi/2}^{\pi/2} \int_0^{p_s} X g^{-1} a^2 \cos\phi dp d\phi d\lambda \tag{2.3}$$

and the integration over the planetary surface S is defined as

$$\int_S X d\sigma = \int_0^{2\pi} \int_{-\pi/2}^{\pi/2} X a^2 \cos\phi d\phi d\lambda \,, \tag{2.4}$$

where p_s is the surface pressure.

One can decompose an arbitrary field $X(t, p, \phi, \lambda)$ into a mean component and a deviation from that mean component. Most common for this kind of study is the zonal decomposition into the zonal mean [ ] and its corresponding deviation. We refer to this deviation as the "eddy component". When taking into account topography, Boer (1982) defined the zonal mean of X

$$[X]_R = \begin{cases} [\Theta X]/[\Theta], & [\Theta] \neq 0 \\ [X], & [\Theta] = 0 \end{cases} \,, \tag{2.5}$$

with a Heaviside function

$$\Theta(p - p_s) = \Theta(\lambda, \phi, p, t) = \begin{cases} 1, & p < p_s \\ 0, & p > p_s \end{cases} \,, \tag{2.6}$$

which transitions from 1 to 0 where isobaric levels intersect the planetary surface. By introducing $\Theta(p - p_s)$, one can account for surface elevation. Equation (2.6) performs zonal average only over the parts of the atmosphere that lie above the surface of the topography, and adjusts the weighting accordingly. One can define the corresponding deviation from the zonal mean

$$X^* = X - [X]_R \,. \tag{2.7}$$

as the eddy component.

2.1.2 Atmospheric energy

One can separate the energy E of an atmosphere into kinetic energy K, potential energy P, and internal energy I.

$$E = K + P + I \tag{2.8}$$

$$= K + H_p \,, \tag{2.9}$$

where $H_p = P + I$ is termed the total potential energy. Since not all of H_p is freely available for conversion into kinetic energy (Margules, 1905), a further separation can be made into unavailable potential energy U and available potential energy (APE) A:

$$H = U + A \,. \tag{2.10}$$

The APE is the amount of potential energy that can be converted into kinetic energy. The unavailable potential energy U is the total potential energy of a specific reference state. This reference state is reached by minimizing the total potential energy of a given atmospheric state via adiabatic redistribution of its mass (Boer, 1989, Koehler, 1986, see Section 2.1.3).

Available potential energy

One can calculate the total potential energy in isobaric coordinates (Boer, 1989) via

$$H = \int_M c_p \Theta T dm + \int_S p_s \Phi_s d\sigma / g \tag{2.11}$$

where the first term corresponds to the internal energy I and the second term corresponds to the potential energy P at the surface. Here, c_p is the heat capacity of the ambient atmosphere at constant pressure, T is the temperature, and Φ_s is the surface geopotential. When pressures π and temperatures $\hat{T}$ of the reference atmosphere (with energy U) are known, one can compute the APE via

$$A = H - U \tag{2.12}$$

$$= \int_M c_p \Theta (T - \hat{T}) dm + \int_S (p_s - \pi_s) \Phi_s d\sigma / g \, . \tag{2.13}$$

2.1.3 Determination of the reference atmosphere

The reference atmosphere is in a state of minimum total potential energy. Such a state has a horizontal, statically stable density stratification (Dutton and Johnson, 1967), so that defining parameters such as pressure p and potential temperature θ are functions only of the atmospheric height Z (Koehler, 1986).

One can obtain the reference atmosphere by following a numerical terrain-dependent method (Koehler, 1986). This method requires knowing the terrain height Z_s, the surface pressures p_s, surface potential temperatures θ_s, and pressure p values for each isentropic layer (i.e. surfaces of constant potential temperature θ) in the atmosphere. The latter requires a change from isobaric to isentropic coordinates. For this we interpolate the point function $\theta(p)$ to obtain the values of $p(\theta)$ on isentropic surfaces. Apart from the reference pressure variable π, the resulting variables describing the reference state will be denoted by the symbol $\hat{}$ (i.e. $\hat{Z}_k$, $\hat{\theta}_s$).

In this method the atmosphere will be adiabatically redistributed until it reaches a stably stratified state (Koehler, 1986). The adiabatic redistribution must conserve the mass of the atmosphere between two isentropic levels. Under hydrostatic conditions, the mass above a certain isentropic level is proportional to the average pressure on that level, hence mass is conserved when

$$\overline{\pi}_k = \overline{p}_k \tag{2.14}$$

where the operator $\bar{}$ denotes a global average over the k-th isentropic surface. It is defined as

$$\overline{p}_k = \sum_{\phi,\lambda}^{S} \begin{cases} p_k(\phi,\lambda), & Z_k > Z_s(\phi,\lambda) \\ p_s(\phi,\lambda), & Z_k < Z_s(\phi,\lambda) \end{cases} \, , \tag{2.15}$$

where Z_k denotes the altitude of the k-th isentropic level of the given atmosphere. For cases where terrain can be assumed as flat, the pressure $\pi_k(\theta)$ of the reference state in an isentropic level k is given by the areal average of the atmospheric pressure p in

that level:

$$\pi_k(\theta) = \overline{p}_k \,. \tag{2.16}$$

However, when terrain is uneven and the k-th isentropic level intersects the surface, π_k is no longer that easily obtainable. In this case, the following iterative computation is required (Koehler, 1986).

1. An initial reference pressure profile π_k is estimated, where the easiest such estimate is simply $\pi_k = \overline{p}_k$.

2. The height of the isentropic levels in the reference atmosphere is computed using a hypsometric formula, obtained by employing the hydrostatic approximation and assuming an adiabatic expansion:

$$\hat{Z}_{k+1} = \hat{Z}_k + \frac{c_p}{2gp_0^\kappa}(\pi_k - \pi_{k+1})^\kappa \cdot (\theta_k + \theta_{k+1}) \,, \tag{2.17}$$

   where $\hat{Z}_1$ is the lowest elevation on the planetary surface, $\kappa = R/c_p$, R is the specific gas constant of the atmospheric gas, c_p is the specific heat capacity at constant pressure, and p_0 is the standard surface pressure (e.g. $p_0(\text{Earth}) = 100000\,\text{Pa}$, $p_0(\text{Mars}) = 610\,\text{Pa}$).

3. The reference potential temperature $\hat{\theta}_s$ and the reference pressure π_s at surface elevation Z_s are computed for each grid point (Koehler, 1986):

$$\hat{\theta}_s = \left\{ \frac{2gp_0^\kappa}{c_p(\pi_k - \pi_{k+1})^\kappa} \left[\theta_{k+1}(Z_s - \hat{Z}_k) + \theta_k(\hat{Z}_{k+1} - Z_s) \right] - \theta_k\theta_{k+1} \right\}^{1/2} \tag{2.18}$$

$$\pi_s = \left[\pi_{k+1}^\kappa + \frac{2gp_0^\kappa(\hat{Z}_{k+1} - Z_s)}{c_p(\theta_{k+1} + \hat{\theta}_s)} \right]^{1/\kappa} \tag{2.19}$$

   where $\hat{Z}_k \leq Z_s \leq \hat{Z}_{k+1}$.

4. Then $\overline{\pi}_k$ values are computed using equation (2.15) and the newly obtained π_s values.

5. In the last step, the π_k of the n-th iteration are readjusted to conserve mass via

$$\pi_k^{n+1} = \pi_{k+1}^{n+1} + \frac{(\overline{p}_k - \overline{p}_{k+1})}{(\overline{\pi}_k^n - \overline{\pi}_{k+1}^n)}(\pi_k^n - \pi_{k+1}^n) \tag{2.20}$$

starting at the level $k = K^*$ that intersects the highest mountains of the surface and continuing down towards the bottom level.

Steps 2 through 5 are repeated until

$$\sum_{\phi,\lambda}^{S} |\pi_s^{n+1} - \pi_s^n| < 1\,\mathrm{Pa}\,. \tag{2.21}$$

The whole process (steps 1 through 5) is then repeated for the subsequent time steps, where the reference pressure profile of the previous time step is used as an initial profile in step 1.

2.1.4 Decomposed energy budget and conversion terms

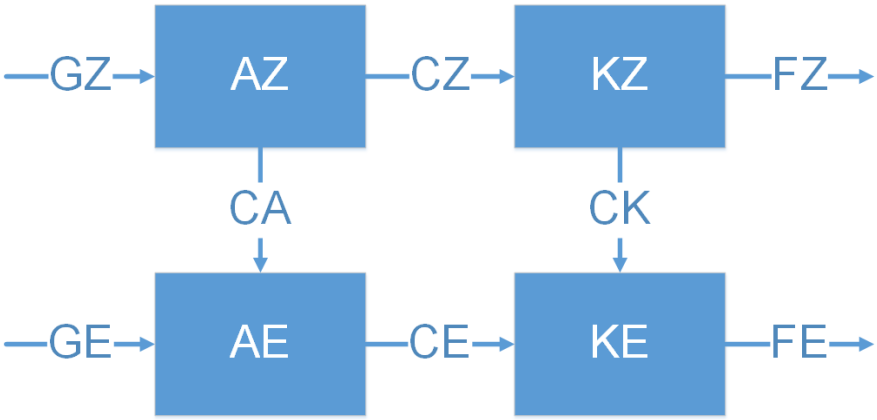

Figure 2.1: Box diagram of Lorenz energy budget. The depicted energies are the zonal available potential (AZ), eddy available potential (AE), zonal kinetic (KZ), and eddy kinetic (KE) energy, respectively. The conversion terms CA, CE, CK, and CZ are directed as depicted. GE and GZ denote generation of APE by diabatic heating and FE and FZ loss of kinetic energy by friction.

Boer (1989) presented exact equations for the energy cycle in the atmosphere:

$$\frac{\partial K}{\partial t} = C - F\,, \tag{2.22}$$

$$\frac{\partial A}{\partial t} = -C + G\,, \tag{2.23}$$

where C is the conversion rate between available potential energy A and kinetic energy K, F is the dissipation rate of K by friction, and G is the generation rate of A by diabatic heating. Boer (1989) decomposed these equations into their zonal and eddy components using equations (2.5) and (2.7) and methods presented in Boer (1982). This results in

$$\frac{\partial K_Z}{\partial t} = C_Z - C_K - F_Z \tag{2.24}$$

$$\frac{\partial K_E}{\partial t} = C_E + C_K - F_E \tag{2.25}$$

$$\frac{\partial A_Z}{\partial t} = G_Z - C_Z - C_A \tag{2.26}$$

$$\frac{\partial A_E}{\partial t} = G_E - C_E + C_A\,, \tag{2.27}$$

where the subscripts denote zonal (Z) and eddy (E) components. C_A, C_E, C_K, C_Z signify the conversion terms between the four energy terms as depicted in Fig. 2.1. Note that the box notation of the Lorenz energy cycle usually elevates subscript letters, hence both notations of term symbols (e.g. A_E and AE) are used interchangeably. The individual terms of equations (2.24) through (2.27) are:

$$K_Z = \int_M \frac{1}{2}[\Theta][\boldsymbol{u}]_R \cdot [\boldsymbol{u}]_R dm \tag{2.28}$$

$$K_E = \int_M \frac{1}{2}[\Theta \boldsymbol{u}^* \cdot \boldsymbol{u}^*] dm \tag{2.29}$$

$$\begin{aligned} A_Z &= A_{Z1} + A_{Z2} \\ &= \int_M C_p \Theta N_{eff,Z} [T]_R dm + \int_S (p_s - \pi_{sZ}) \Phi_s d\sigma / g \end{aligned} \tag{2.30}$$

$$\begin{aligned} A_E &= A_{E1} + A_{E2} \\ &= \int_M C_p \Theta (N_{eff} - N_{eff,Z}) T dm + \int_S (\pi_{sZ} - \pi_s) \Phi_s d\sigma / g \end{aligned} \tag{2.31}$$

$$\begin{aligned} C_K &= C_{K1} + C_{K2} \\ &= -\int_M a\cos\phi \left\{ \left([\Theta u^* \boldsymbol{u}^*] \cdot \nabla + [\Theta u^* \omega^*] \frac{\partial}{\partial p} \right) \left(\frac{[u]_R}{a\cos\phi} \right) \right. \\ &\quad \left. + \left([\Theta v^* \boldsymbol{u}^*] \cdot \nabla + [\Theta v^* \omega^*] \frac{\partial}{\partial p} - \frac{\tan\phi}{a} [\Theta \boldsymbol{u}^* \cdot \boldsymbol{u}^*] \right) \left(\frac{[v]_R}{a\cos\phi} \right) \right\} dm \\ &\quad + \int_M \left\{ \left[\Theta \frac{\partial \Phi^*}{\partial t} \right] + [\boldsymbol{u}]_R \cdot [\Theta \nabla \Phi^*] + [\omega]_R \left[\Theta \frac{\partial \Phi^*}{\partial p} \right] \right\} dm \end{aligned} \tag{2.32}$$

$$C_Z = C_{Z1} + C_{Z2}$$

$$= -\int_M [\Theta][\omega]_R[\alpha_\rho]_R dm - \int_S \left[\frac{\partial p_s}{\partial t}\Phi_s\right] d\sigma/g \tag{2.33}$$

$$C_E = -\int_M [\Theta\omega^*\alpha^*_{rho}]dm \tag{2.34}$$

$$C_A = -\int_M C_p\left(\frac{\theta}{T}\right)\left([\Theta T^*\boldsymbol{u}^*]\cdot\nabla + [\Theta T^*\omega^*]\frac{\partial}{\partial p}\right)\left(\frac{T}{\theta}N_{eff,Z}\right)dm \tag{2.35}$$

$$G_Z = \int_M \Theta N_{eff,Z}[Q]_R dm \tag{2.36}$$

$$G_E = \int_M \Theta(N_{eff} - N_{eff,Z})Q dm \tag{2.37}$$

$$F_Z = \int_M [\Theta][\boldsymbol{u}]_R \cdot [F]dm \tag{2.38}$$

$$F_E = \int + - \int_M [\Theta\boldsymbol{u}^* \cdot \boldsymbol{F}^*]dm \tag{2.39}$$

with

$$N_{eff}(\pi) = 1 - (\pi/p)^\kappa \tag{2.40}$$

$$N_{eff,Z} = N_{eff}(\pi_Z) \tag{2.41}$$

$$\pi_Z = \pi([\theta]_R, t) \tag{2.42}$$

$$[\theta]_R = [T]_R\left(\frac{p_0}{p}\right)^\kappa \tag{2.43}$$

$$\nabla = \begin{pmatrix}\partial_x \\ \partial_y\end{pmatrix} = \begin{pmatrix}\frac{1}{a\cos\phi}\partial_\lambda \\ \frac{1}{a}\partial_\phi\end{pmatrix} \tag{2.44}$$

and

A_E: eddy available potential energy

A_Z: zonal available potential energy

C_A: conversion term between AZ and AE

C_E: conversion term between AE and KE

C_K: conversion term between KZ and KE

C_Z: conversion term between AZ and KZ

F_E: dissipation of K_E by friction

F_Z: dissipation of K_Z by friction

G_E: generation of A_E by diabatic heating

G_Z: generation of A_Z by diabatic heating

K_E: eddy kinetic energy

K_Z: zonal kinetic energy

N_{eff}: efficiency factor

$\boldsymbol{u}$: horizontal velocity vector field

u: zonal component of $\boldsymbol{u}$

v: meridional component of $\boldsymbol{u}$

α_ρ: specific volume $(1/\rho)$

$\hat{\theta}_s$: potential at k-th isentropic level of the reference state

κ: R/c_p

π_{sZ}: zonal mean of pressure in the reference state

ρ: density

Φ: geopotential

ω: vertical velocity vector in pressure coordinates

The terms in equations (2.30) to (2.33) labelled with a subscript "2" result from the explicit inclusion of topography and vanish if a flat surface is assumed (Boer, 1989). Another major difference between this scheme and more approximate schemes (e.g. Peixóto and Oort, 1974) is the usage of an efficiency factor $N_{eff}(\pi)$ (Eqn. 2.40) for the APE related calculations (Eqns. 2.30, 2.31, 2.35). This requires the calculation of the reference state of the atmosphere (detailed in Section 2.1.3). Using N_{eff} to determine APE terms can have a significant impact on results when compared to the more conventional approximate APE determination. The efficiency factor N_{eff} can assume negative values (see e.g. Boer, 1975, Lorenz, 1955, Siegmund, 1994), which leads to local regions of negative APE (c.f. Fig. 2.11).

Figure 2.2 depicts common interpretations of the Lorenz energy cycle (James, 1995). In general, net diabatic forcing produced by imbalances between solar heating and IR cooling generates APE. If the radiative time constant for the atmosphere is much longer than a day, differential solar heating/cooling is more or less axisymmetric

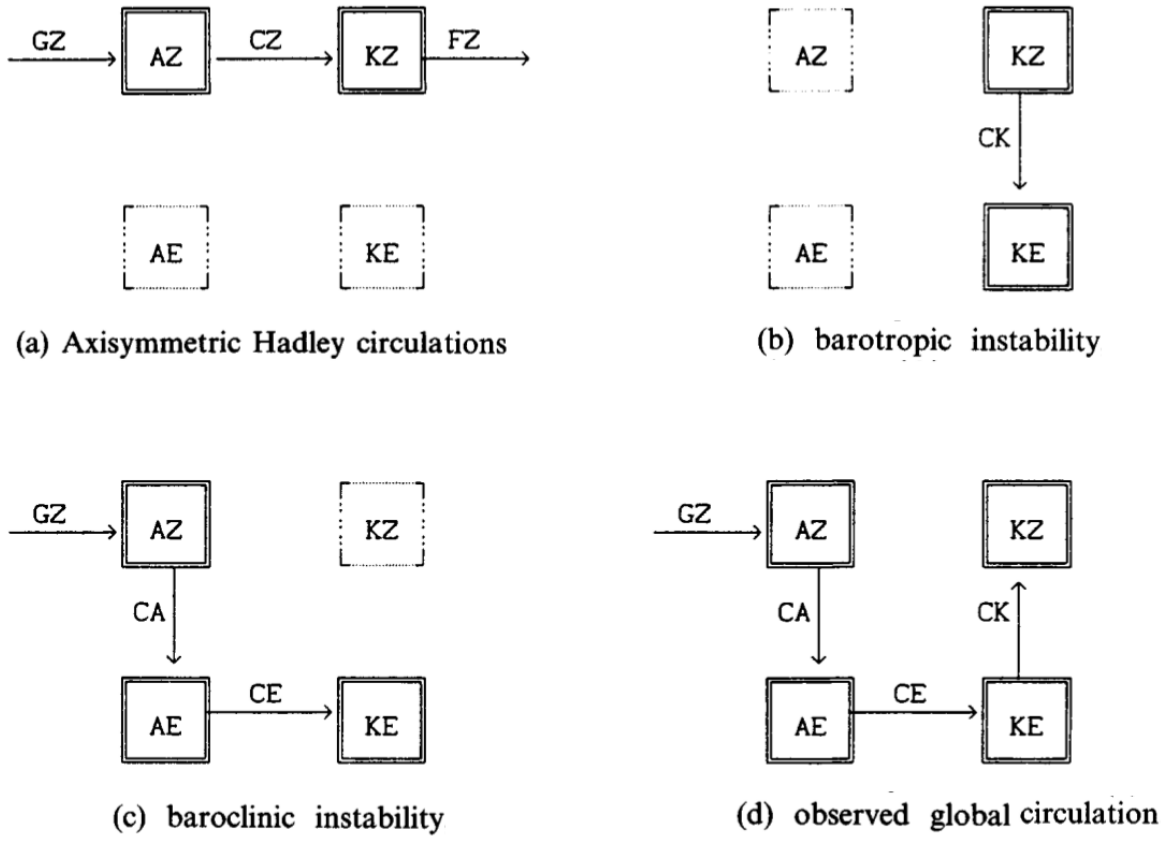

Figure 2.2: Interpretations of the Lorenz energy cycle. © Cambridge University Press 1994. Reproduced with permission from James (1995).

(contibuting mainly towards A_Z). Otherwise it is non-axisymmetric and contributes directly to A_E. For the Earth atmosphere the following paradigms can be identified.

1. Positive C_Z is interpreted as axisymmetric circulation via direct heating such as the Hadley circulation (see Fig. 2.2a).

2. A conversion from A_Z to K_E via A_E so that both C_A and C_E are positive is associated with baroclinic instabilities (Fig. 2.2c), as eddies are generated from potential energies.

3. A conversion from K_Z to K_E (negative C_K) can be related to barotropic instabilities (Fig. 2.2b). A conversion from K_E to K_Z (positive C_K) is connected to the generation of zonal flows via mechanical eddy forcing.

Fig. 2.2d shows the observed global circulation on Earth, revealing a strong baroclinic behaviour as well as eddy driven zonal flow.

2.2 Lorenz energy cycle of Mars

The following work has been published in Geophysical Research Letters in October of 2015 (Tabataba-Vakili et al., 2015).

In this section, we apply the Lorenz energy cycle equations to the Martian atmosphere. Since Mars has an extreme topography, with a range of elevation of over 16 km (Smith et al., 2001), we use the Lorenz energy cycle equations derived by Boer (1989), which explicitly include surface elevation (see Section 2.1). The study of energy conversion on Mars has many points of interest. Firstly, the Lorenz energy cycle has been up to this point only calculated for Earth (Li et al., 2007, Oort, 1983, Boer and Lambert, 2008) from reanalysis datasets and for a model of the Venus atmosphere Lee et al. (2007). Thereby, Tabataba-Vakili et al. (2015) is the first work to apply Lorenz cycle diagnostics to a non-Earth atmosphere using reanalysis data. This provides one of the first points of comparison of the atmospheric energy conversion between Earth and another terrestrial planet. Note that only recently Battalio et al. (2016) have studied the generation of the eddy kinetic energy K_E with a version of the MACDA dataset where diurnal and semi-diurnal tides were filtered out. In addition, the com-

puted values of this study can help in validating free-running models of the Martian atmosphere. Finally, the features of Mars make a global analysis of the atmospheric energy interesting in itself. Apart from its non-trivial topography, Mars features large diurnal and seasonal variability due to its thin atmosphere, a lack of surface oceans, and larger orbital eccentricity ($e = 0.0934$) and obliquity $\epsilon = 25.19°$ compared to Earth. Mars is also host to repeating global dust storm events (GDSE) that can cover large parts of the planet with a haze of dust. Calculating the energy cycle of Mars reveals how this diagnostic method responds to the Martian characteristics above.

The atmosphere of Mars varies seasonally in mass due to the deposition of carbon dioxide ice at the poles in winter. This effect is not explicitly included in our Lorenz energy cycle analysis. However, the MACDA dataset incorporates surface carbon ice. Hence our analysis should include the indirect effects of carbon dioxide deposition with regard to changes in atmospheric temperature and mass.

In addition to these reasons, diagnosing atmospheres with strong seasonal and diurnal effects provides valuable preparation for the parameter study on the effects of seasonal and diurnal variations to dynamical regimes (see Sections 4.1.2, 5.5).

2.2.1 Data sources

For this analysis of the Lorenz energy cycle, we use data from the Mars reanalysis dataset MACDA (Mars Analysis Correction Data Assimilation Montabone et al., 2014a), which calculates reanalysis of the Martian atmosphere using the UK version of the LMD-UK Mars GCM (Forget et al., 1999) and measurements from the Thermal Emission Spectrometer (TES) on NASA's Mars Global Surveyor (MGS). The MACDA reanalysis dataset covers almost three Martian years of data from solar longitude $L_s = 141°$ in MY 24 to $L_s = 82°$ in MY 27 with a time step of two hours. The solar longitude L_s is a measure describing the current orbital position of a planet as an angle between the planet's northern hemisphere (NH) spring equinox ($L_s = 0°$) and the sun. Accordingly defined are the summer solstice ($L_s = 90°$), autumn equinox ($L_s = 180°$), and winter solstice ($L_s = 270°$), respectively for the northern hemisphere.

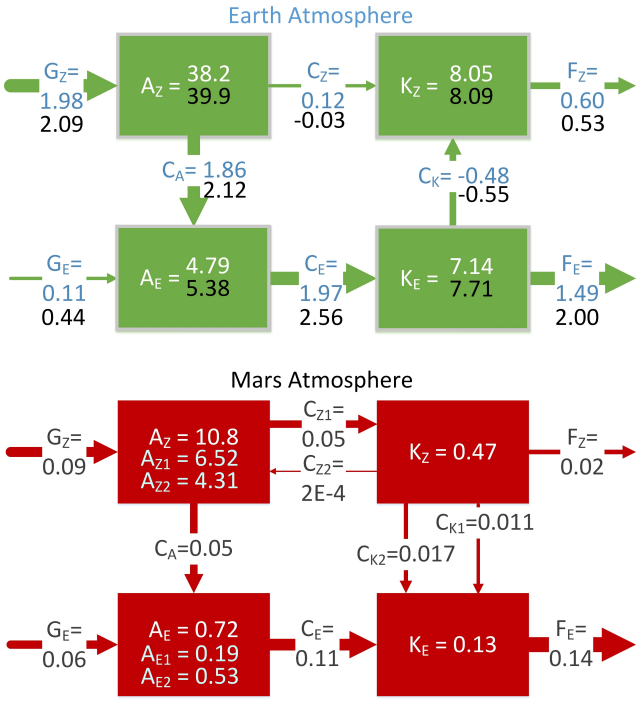

Figure 2.3: Mean values of energy and conversion terms **per unit area** of Earth (top, Boer and Lambert (2008)) from NCEP (white/blue) and ERA (black) reanalysis data over 17 years (1979-1995); of Mars over almost 3 Martian years (bottom, Tabataba-Vakili et al. (2015)). All Energies (A_Z, A_E, K_Z, K_E) are given in $10^5\,\mathrm{Jm}^{-2}$ and all conversion terms in Wm^{-2}.

2.2.2 Annual-mean energy cycle

In Figure 2.3, we show schematic global and annual mean Lorenz energy budgets for both Earth and Mars. The Earth data were taken from a previous energy cycle analysis computed from NCEP reanalysis data over 17 years (1979-1995) by Boer and Lambert (2008, see their table 4). Their analysis used the approximated Lorenz energy scheme of Peixóto and Oort (1974). It would be ideal to compare our Mars results to Earth values computed with the same scheme, but such data were not available. However, the scheme used for the Earth data (Boer and Lambert, 2008) has terms that are in general comparable to the terms used in the current work when excluding terms labelled with the subscript "2". These terms vanish in the flat surface approximation (Boer, 1989), which suggests that they are less important for the comparatively flat topography of Earth.

The energy and conversion term values per unit area for Mars (Fig. 2.3, bottom) are significantly smaller than for Earth. When considering the generation rates G_Z, G_E of APE via diabatic heating, one expects lower values per unit area for Mars for two reasons. Firstly, Mars receives less solar irradiance compared to Earth due to its larger orbital distance. Secondly, Mars' atmosphere is less dense and consequently has a smaller column-integrated mass. The direct generation of eddy APE (G_E) gains in importance on Mars, because the ratio $G_E/G_Z(\text{Mars}) = 0.5$ is larger than the corresponding value for Earth.

The atmospheric energy reservoirs per unit area (A_Z, A_E, K_Z, and K_E) are also lower than the corresponding energy reservoirs for Earth. The additional surface-related energy terms, A_{Z2} and A_{E2}, provide a significant contribution to the total energy reservoir. In the case of A_E, A_{E2} even outweighs A_{E1} by a factor of five. This shows that the Martian surface is uneven enough to require the inclusion of surface terms to the energy equations.

The conversion terms per unit area (C_A, C_E, C_K, C_Z) on Mars are again small compared to Earth, but both budgets favour baroclinic conversion from A_Z to A_E to K_E. The direction of C_K, however, is in the opposite sense for Earth and Mars (see Fig. 2.3). The negative value of C_K (conversion from K_E to K_Z) for Earth indicates that eddies strengthen the zonal flow, whereas on Mars the positive values of C_K can

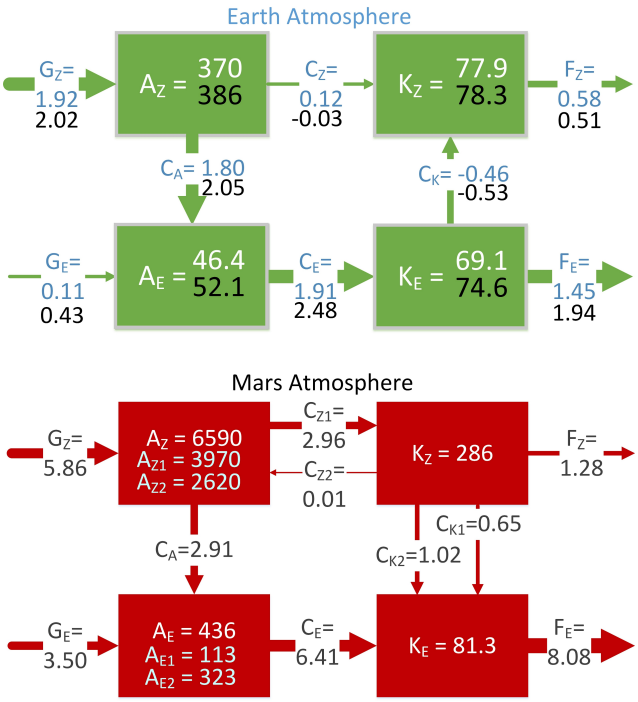

Figure 2.4: Mean values of energy and conversion terms **per unit mass** of Earth (top, Boer and Lambert (2008)) from NCEP (white/blue) and ERA(black) reanalysis data over 17 years (1979-1995); of Mars over almost 3 martian years (bottom, Tabataba-Vakili et al. (2015)). All Energies (A_Z, A_E, K_Z, K_E) are given in J/kg and all conversion terms in 10^{-4}W/kg.

be associated with a weakening of the zonal flow. Note that C_{K2} contributes roughly 60% to the total C_K. This indicates that the effect of surface topography plays an important role for the kinetic energy budget of the Martian atmosphere.

When comparing C_Z to the dominant conversion terms (C_A and C_K) of each respective planet, Martian C_Z has a larger relative impact on the total budget than its terrestrial counterpart (see Section 2.2.3). Overall, this means that on Mars two significant pathways of energy conversion can be observed in the global mean:

1. a strong baroclinic conversion from A_Z to A_E to K_E, which is also the dominant pathway for Earth,

2. a weaker conversion pathway from A_Z to K_Z to K_E.

The frictional dissipation terms on Mars and Earth favour dissipation mainly in the eddy component.

We compute the energy and conversion terms in units per kilogram by dividing by p_0/g, where p_0 is the reference surface pressure of the respective planet and g is

the respective planetary gravitational acceleration. Then, the energy and conversion terms for Mars become larger than those of Earth (see Fig. 2.4). This difference can be explained via the generation of energy due to solar input. The atmospheric density of Mars is 75 times less than that of Earth while the solar irradiation is 2.3 times less. This makes the Mars atmosphere roughly 33 times more susceptible to solar forcing (Tyler and Barnes, 2013). However, instead of this factor we only see an increase by a factor of around 4 to 5 when comparing $G = G_Z + G_E$ of Mars and Earth. This difference between expected and observed increase of G from Earth to Mars is likely due to differences in the absorption of energy by the atmospheric constituents, which are higher for Earth compared to the mostly transparent CO_2 on Mars. Nonetheless, the overall increase of energy and conversion terms from Earth to Mars indicates that the decreased density of the Mars atmosphere seems to outweigh other factors, producing larger energy and conversion terms per unit mass.

We present further decompositions in time and space below to further understand seasonal and diurnal effects on the Martian Lorenz energy cycle.

2.2.3 Hemispheric and seasonal decomposition

The energy cycle of an open domain such as a hemisphere is not in equilibrium unless additional surface and boundary terms are taken into account. While ignoring such additional terms disregards local equilibrium, one can still learn about the transfer of energy between these open domains. In particular, the partition into northern and southern hemispheres (NH and SH) can be helpful in understanding the atmospheric energy cycle during different seasons (see e.g. Li et al., 2007) as well as the role of the cross-equator Hadley circulation of Mars. From here on, we do not calculate generation and dissipation terms from the residuals because integration times may be too short to let us assume atmospheric equilibrium.

In Figure 2.5, we show data for all energies and conversion terms of the Lorenz energy cycle for the NH, SH, and the whole globe in annual and seasonal mean for the four main cardinal seasons. The seasons depicted are centred about the solstices and equinoxes (for values bounded by solstices/equinoxes see Table 2.1). The energy reservoirs exhibit different responses to the changing seasons. Overall, the zonal energies

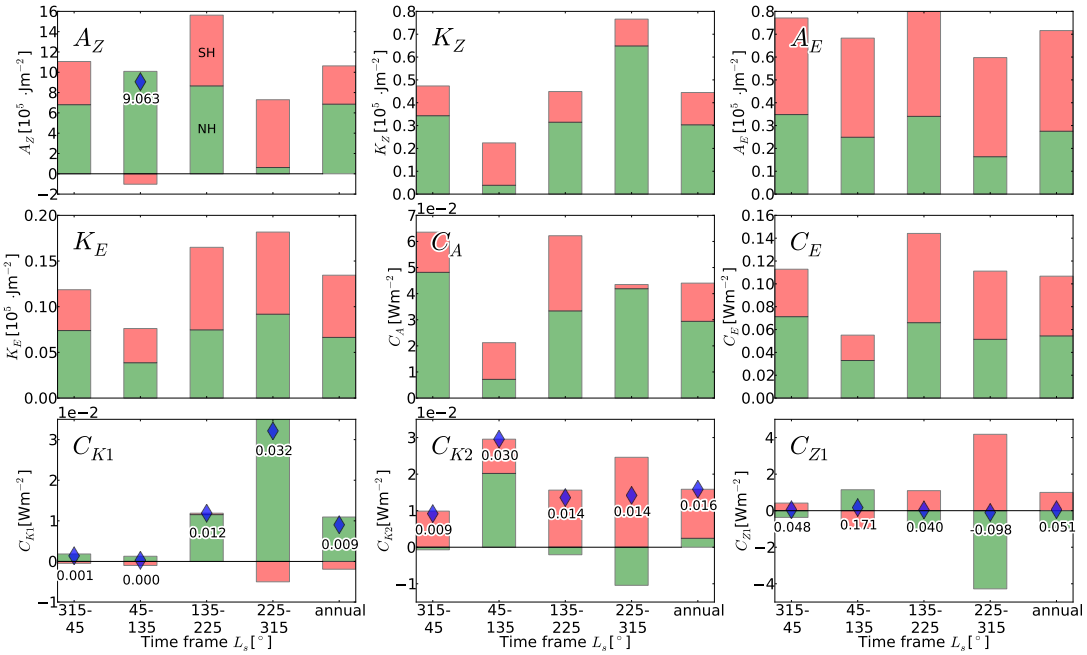

Figure 2.5: Lorenz energy budget of Mars in seasonal and hemispheric decomposition. Global values are given by the sum of northern (green) and southern (red) hemisphere contribution (or by blue diamonds when one of the hemispheric contributions is negative). Seasons are given in solar longitudes, where $L_s = 0°$ is the northern hemisphere spring equinox. Annual values were averaged over two full years (MY 25 and MY 26). Seasonal values are the mean of either two (L_s =45-135°) or three (L_s =135-225°, 225-315°, 315-45°) years of data.

	$L_s[^\circ]$	A_Z [10^5 J/m^2]	A_E	K_Z [10^5 J/m^2]	K_E	C_A [W/m^2]	C_E	C_K [W/m^2]	C_Z	C_{K1} [W/m^2]	C_{K2}	C_{Z1} [W/m^2]	C_{Z2}
	0-90	10.8	0.74	0.29	0.08	0.04	0.07	0.02	0.16	-0.003	0.020	0.16	-0.002
	90-180	10.3	0.76	0.24	0.08	0.02	0.07	0.01	0.10	-0.004	0.019	0.09	0.009
global	180-270	14.2	0.68	0.71	0.23	0.07	0.17	0.04	-0.07	0.033	0.012	-0.06	-0.014
	270-360	7.6	0.66	0.66	0.15	0.06	0.11	0.04	-0.03	0.021	0.017	-0.03	0.008
	annual	10.6	0.72	0.44	0.13	0.04	0.11	0.02	0.05	0.009	0.016	0.05	5E-4
	0-90	20.0	0.58	0.21	0.09	0.04	0.09	0.02	1.77	-0.004	0.022	1.78	-0.002
	90-180	18.5	0.62	0.12	0.08	0.01	0.07	0.02	1.10	0.001	0.018	1.08	0.02
NH	180-270	9.91	0.53	1.22	0.20	0.10	0.16	0.04	-7.36	0.064	-0.022	-7.33	-0.04
	270-360	3.71	0.48	1.15	0.19	0.11	0.14	0.04	-4.64	0.041	-0.006	-4.66	0.02
	annual	13.7	0.55	0.61	0.13	0.06	0.11	0.03	-1.90	0.022	0.005	-1.90	2E-4
	0-90	1.16	0.90	0.38	0.08	0.03	0.05	0.02	-1.45	-0.003	0.019	-1.45	-0.002
	90-180	2.17	0.93	0.36	0.08	0.03	0.07	0.01	-0.90	-0.008	0.019	-0.90	0.002
SH	180-270	18.5	0.82	0.20	0.25	0.03	0.18	0.05	7.21	0.001	0.045	7.20	0.01
	270-360	11.5	0.83	0.17	0.11	0.01	0.09	0.03	4.59	0.001	0.034	4.59	-0.004
	annual	7.54	0.88	0.28	0.14	0.03	0.10	0.02	2.00	-0.003	0.027	2.00	0.001

Table 2.1: Lorenz energy budget of Mars in seasonal and hemispheric decomposition. Seasons are given in solar longitudes, where $L_s = 0^\circ$ is northern hemisphere spring equinox. Hence e.g. $L_s = 0 - 90^\circ$ is spring on the northern hemisphere, followed by summer, autumn and winter. Annual values were averaged over two full years (MY 25 and MY 26). Seasonal values are the mean of either two ($L_s = 0 - 180^\circ$) or three ($L_s = 180 - 360^\circ$) full seasons.

are stronger in the NH. Zonal energy terms show a direct dependence on the season, so that the summer and winter hemisphere have a dominating contribution to A_Z and K_Z, respectively. Hence, the SH contribution to A_Z and K_Z dominates over the NH contribution in SH summer and winter, respectively. This difference between the hemispheric contributions to the zonal energy reservoir is likely related to the surface dichotomy (Marinova et al., 2008) between the hemispheres.

The eddy APE A_E remains mostly constant over the year, but decreases in the NH during solstices. The eddy kinetic energy K_E receives roughly equal contributions from NH and SH throughout the year, however, the total of K_E shows a strong seasonal variation. Total K_E is minimal during the NH summer solstice and maximal during the NH winter solstice. We observe the same seasonal variation of total values of kinetic energy in K_Z. This yearly modulation of kinetic energies is related to the difference of energy throughput over the aphelion-perihelion cycle.

We observe large values with opposing signs in the hemispheric decomposition of C_{Z1}. Positive C_{Z1} values are indicative of a thermally direct circulation, negative

values are associated with thermally indirect circulation (Lorenz, 1967). Thus, we find that the circulation in summer hemispheres is thermally direct, and that the circulation of the winter hemispheres is thermally indirect. The overall hemispheric strength of this conversion is four times stronger in SH summer than in NH summer. This result is in agreement with Richardson and Wilson (2002), who concluded that asymmetries in the topography of Mars favour a predominating southern hemisphere summer circulation. We observe that the hemispheric values of C_{Z1} nearly cancel each other out. The thermally indirect contribution arises from a strong Ferrel-like circulation in the winter hemispheres as well as from heating induced by compression in the downward branch of the cross-equatorial Hadley-circulation (see e.g. Haberle et al., 1993).

On global scales both C_A and C_E are highest during equinoxes. During solstices, and especially during the northern winter solstice (L_s =45-135°), this baroclinic conversion decreases (see Section 2.2.4).

Regarding the conversions with additional terms (C_{K2}, C_{Z2}), we find that C_Z is dominated by C_{Z1} and that C_{Z2} is negligible (see Table 2.1). For C_K, however, both terms have significant contributions. During NH winter, C_K is dominated by C_{K1}, converting K_Z to K_E, whereas C_{K2} is stronger during the summer of each hemisphere.

During northern hemisphere summer ($L_s = 45 - 135°$), the baroclinic conversion terms (C_A, C_E) are small despite a large reservoir of A_Z. It seems that A_Z is mainly converted into K_Z via C_Z during this time-frame. In Figure 2.9, it is apparent that an increase in C_Z correlates with a yearly low in C_A and C_E. It is interesting to note that the K_Z value in the NH during this time is very small. As a consequence there must be a significant loss of K_Z in the NH due to either friction F_Z or transport into the southern hemisphere via cross-equatorial transport.

2.2.4 Diurnal and synoptic frequency components

In this section, we compute time-resolved values of the Lorenz energy cycle terms to investigate variations in atmospheric energy conversions for instance during the global-scale dust storm of MY 25. In addition, we filter out the diurnal component of each term to assess the importance of the diurnal tides to the energy conversion within the

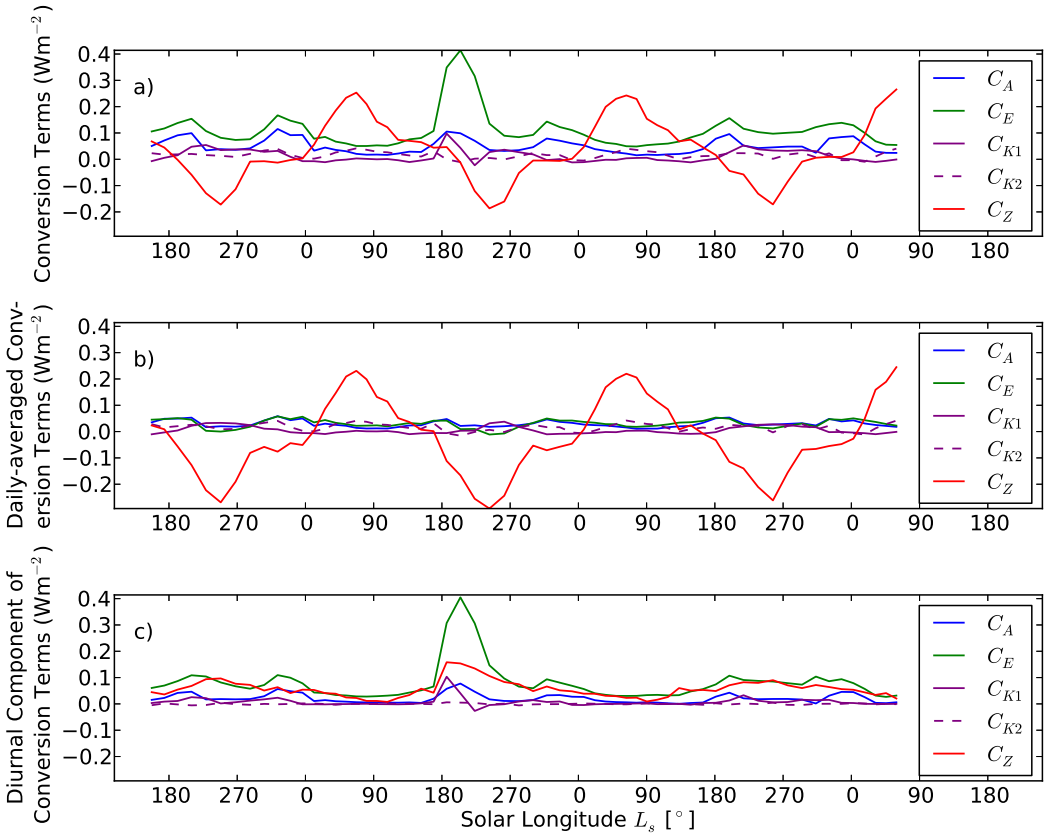

Figure 2.6: Total X (a), daily averaged $\overline{X}$ (b) and diurnal X_{diurnal} (c) component of the **conversion terms** of the Lorenz energy budget of the Mars atmosphere given in 30-sol mean values from $L_s = 141°$ MY 24 to $L_s = 82°$ MY 27.

Martian atmosphere relative to other components of the circulation. The filtering was performed by taking the daily running mean (i.e. averaging over the length of one day) of all input variables and then computing the daily-averaged Lorenz energy cycle terms $\overline{X}$ for each term X of the Lorenz energy cycle. Then, we determine the diurnal component X_{diurnal}, representing the contribution from periods equal to or shorter than the diurnal period to each term, from

$$X = \overline{X} + X_{\text{diurnal}}\,. \tag{2.45}$$

Figure 2.6 depicts (a) total X, (b) daily-mean $\overline{X}$, and (c) the diurnal values X_{diurnal} of the conversion terms with each data point representing a time-frame of 30 sols. The zonal conversion rate C_Z shows a strong yearly repetition, being positive in NH spring and summer and negative in NH autumn and winter. This behaviour indicates a

change between thermally indirect and direct circulations. We separate C_{K1} and C_{K2} in this instance to further study the contribution to C_K in seasonal decomposition. In the global mean, C_{K1} assumes positive values from L_s =180° to L_s =360° , while C_{K2} assumes values between 0.01 and 0.02 Wm^{-2} over the whole year. This indicates a barotropic contribution to the generation of eddies.

At L_s = 180° of MY 25, there is first a positive peak in C_{K1} (i.e. conversion from K_Z to K_E), followed closely by a small negative peak (originating from the SH, see Fig. S7). Even more striking is a large spike in C_E at around L_s =180-270° L_s of MY 25. The K_E reservoir also increased during that time (see Fig. 2.7). This behaviour coincides in time with the global dust storm event (GDSE) that occurred during L_s =180-240° of MY 25 (c.f. Lewis and Barker, 2005, their Fig. 5).

The daily averaged (Fig. 2.6b) and diurnal (Fig. 2.6c) components show which conversions take place on time scales longer and shorter than one sol, respectively. We find that most zonal conversion (C_Z) occurs on longer time scales, apart from a small offset that is generated at the equatorial surface region (see Fig. 2.12). A small amount of baroclinic conversion (C_A, C_E) also occurs on longer time scales. Apart from C_{K2} all conversion terms exhibit non-negligible diurnal components (Fig. 2.6c). While the offset between total and daily averaged C_Z provides comparable values to the other diurnal conversions, it represents only a small fraction of zonal conversion compared with the hemispheric C_Z values discussed above. A latitude pressure plot of the diurnal component of the integrands of C_Z (see Fig. 2.12) reveals that diurnal C_Z occurs near the equatorial surface. This can be either associated with the diurnally modulated up- and down-slope winds or with the generation of zonal flows by tidal interactions (Lewis and Read, 2003).

Most diurnal conversion terms assume their maximum values during the GDSE. This behaviour shows that dust storms on Mars are strongly correlated with diurnal effects, such as thermal tides, and coincide with both baroclinic and barotropic conversions, which noticeably increase K_E production. This correlation between dust storms and thermal tides has been shown by Leovy and Zurek (1979) using observations of pressure oscillations measured by the Viking I and II landers. In addition, Lewis and Barker (2005) investigated variations of thermal tides in an assimilated reanalysis of

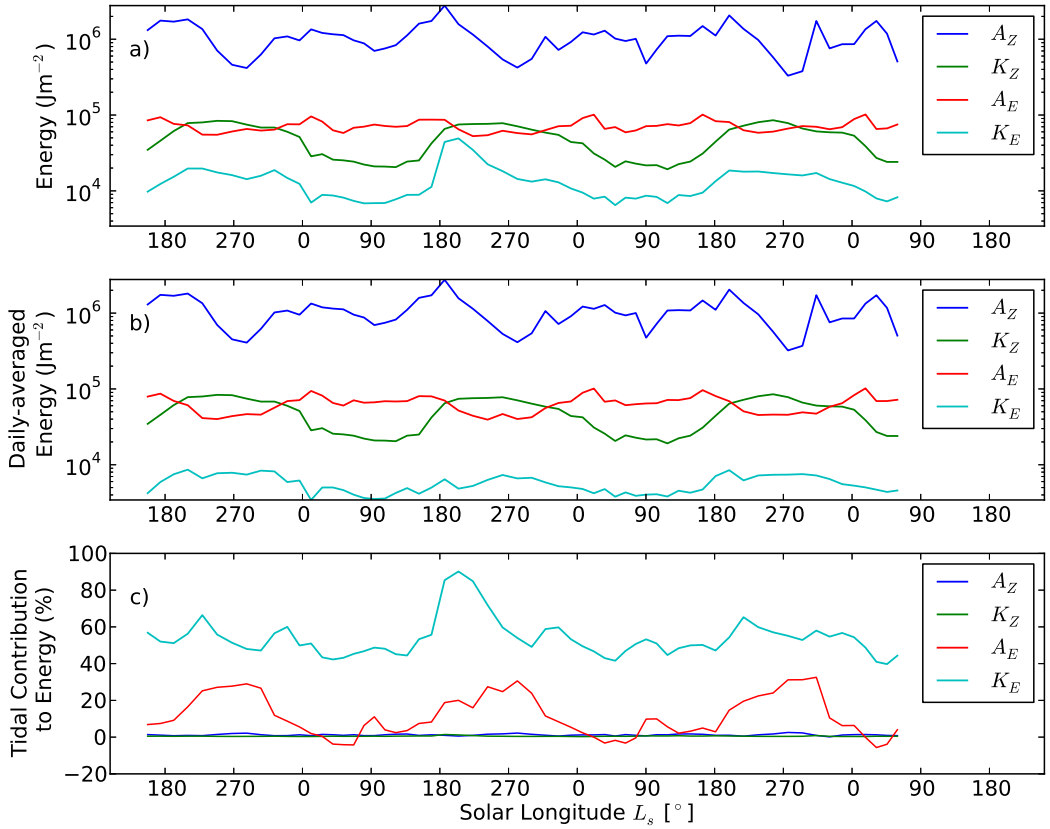

Figure 2.7: Total X (a), daily averaged $\overline{X}$ (b) and diurnal X_{diurnal} (c) component of the **energy terms** of the Lorenz energy budget of the Mars atmosphere given in 30-sol mean values from $L_s = 141°$ MY 24 to $L_s = 82°$ MY 27. The diurnal component (c) shows the contribution ($X_{\text{diurnal}}/X \cdot 100\%$) of the diurnal component to the total energies in percent.

the same period as discussed here and found mainly semi-diurnal signatures during the global-scale dust storm in MY 25.

Regarding the energy reservoirs (see Fig. 2.7b), the daily-averaged energy components show clear seasonal oscillations, with kinetic energy reservoirs rising in NH summer and falling in NH winter and with APE reservoirs acting inversly. While diurnal contributions to zonal energies are negligible (see Fig. 2.7c) eddy energy terms have substantial amplitudes in their diurnally varying components. A_E shows seasonally recurring contributions of up to 25% during L_s =180-360° (Northern spring/summer, dust season) and negligibly small amounts during the other half of the year. Moreover, the diurnal component of K_E contibutes over 50% of its total value. This contribution rises to 90% during the global-scale dust storm event of MY 25.

Figure 2.8 (bottom) summarises the importance of the diurnal components, by

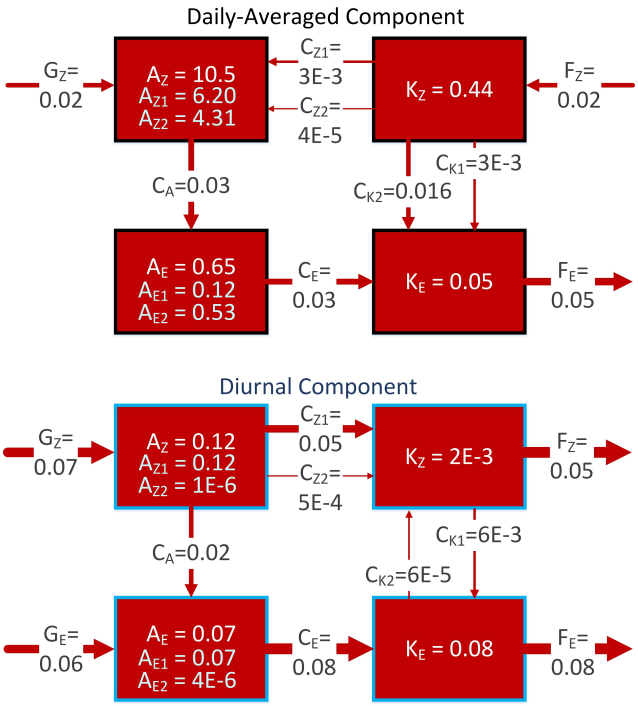

Figure 2.8: Global and annual mean values of daily-averaged (top) and diurnal (bottom) components of energy and conversion terms per unit area of Mars over 2 full Mars years. All Energies (A_Z,A_E,K_Z,K_E) are given in 10^5 Jm^{-2} and all conversion terms in Wm^{-2}.

showing their global and annual mean values per unit area. When compared with the daily averaged values from Fig. 2.8 (top), we see that overall the conversion terms C_E, C_{K1}, and C_A are controlled on diurnal and shorter timescales, favouring the production of K_E. In addition, in the annual-mean 10% of the A_E and 60% of the K_E reservoir resides on such timescales. The direct generation of eddy and zonal APE (G_Z,G_E) seems to be strong in the diurnal components but weak in the more slowly varying components. Note also the reversal of C_Z between Fig. 2.8 upper and lower, suggesting that the global and annual circulation behaves in a thermally direct sense in the diurnal component and slightly indirect on longer timescales.

2.2.5 Hemispheric and diurnal decomposition

Further hemispheric decompositions of Fig. 2.6 (see Figs. 2.9 and 2.10) show the diurnally-varying and diurnally-averaged components by hemisphere. As in Section 2.2.3, we find that an overwhelming zonal conversion with up to 10 Wm^{-2} occurs on longer than daily time scales, but these larger values are largely balanced in the global mean

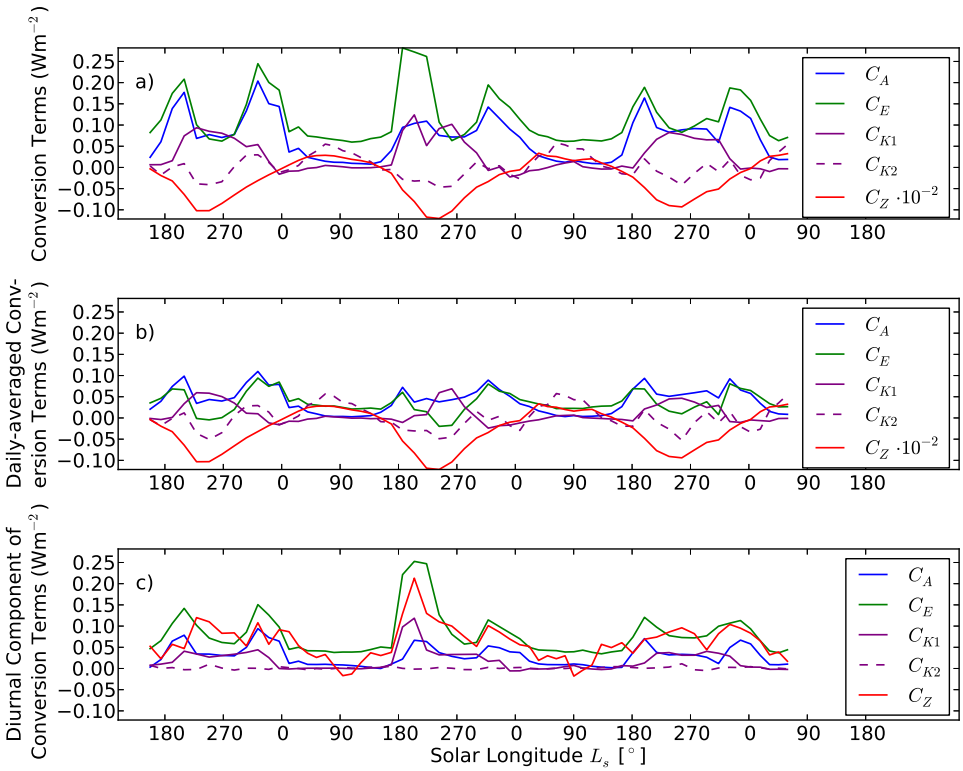

Figure 2.9: Total (a), daily averaged (b) and diurnal (c) component of the conversion terms of the Lorenz energy budget of the **northern hemisphere** of the Mars atmosphere given in 30-sol mean values from $L_s = 141°$ MY 24 to $L_s = 82°$ MY 27.

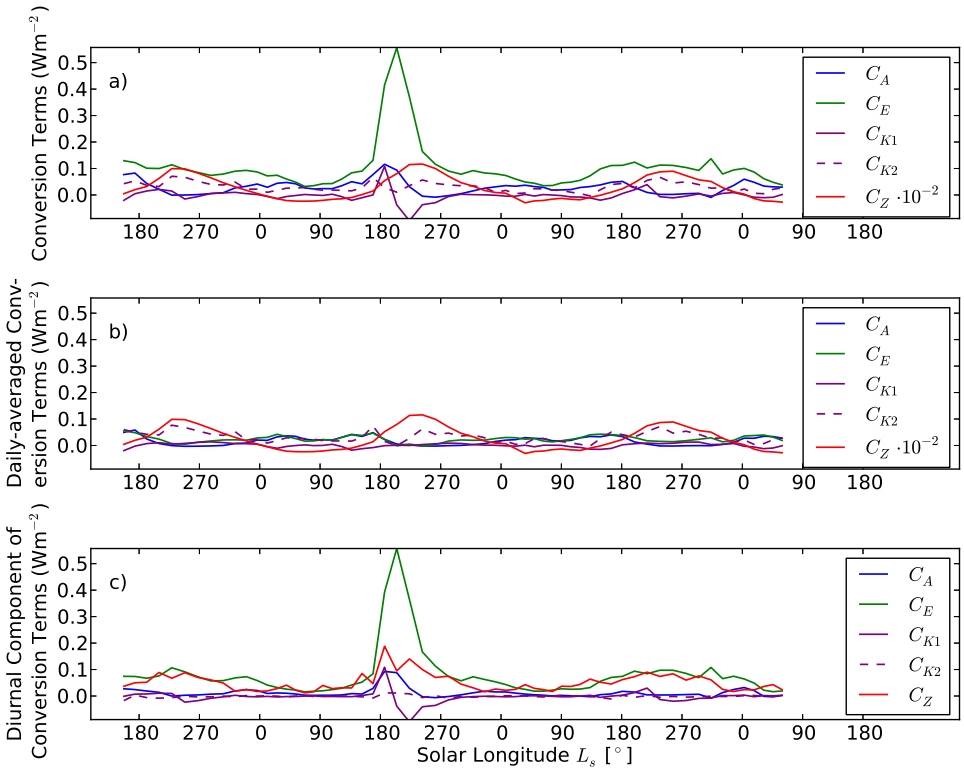

Figure 2.10: Same as Fig. 2.9, but for the **southern hemisphere**

(Fig. 2.6). Both southern and northern hemisphere feature increased C_K, C_Z, and C_{K1} during the GDSE, as descibed in the previous section.

During the northern winter solstice (around $L_s = 270°$, see Fig. 2.6a,b, Fig. 2.9) we see a decrease in baroclinic activity (C_A, C_E), which coincides with an increase in barotropic conversion. This behavior coincides with the "solsticial pause", where transient eddy activity is strong before and after the winter solstice, but decreases during this time span (Read et al., 2011, Wang et al., 2013, Kavulich et al., 2013, Lewis et al., 2015, Mulholland et al., 2015). Fig. 2.9 shows that this behaviour occurs both in the daily-averaged as well as the diurnal components in the northern hemisphere. In the southern hemisphere (Fig. 2.10) the solsticial pause also occurs, but is significantly less pronounced.

In Figures 2.11 and 2.12 we show the integrands of the annually- and zonally-averaged energy and conversion terms of the Lorenz budget plotted against pressure and latitude. The data was averaged over two full Martian years, to filter out seasonal bias. Figure 2.11 displays the total integrand values, while Fig. 2.12 displays only

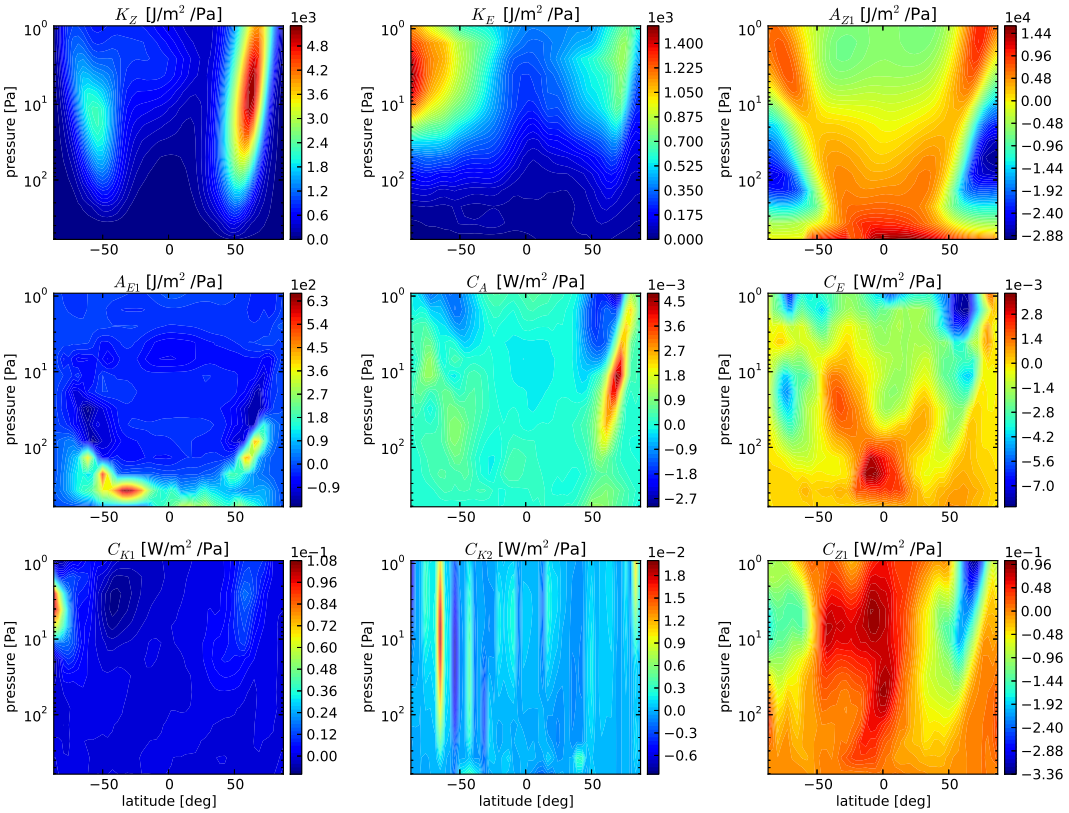

Figure 2.11: Integrands of energy and conversion terms resolved over latitude and pressure coordinates. Displayed data is a mean over two full martian years.

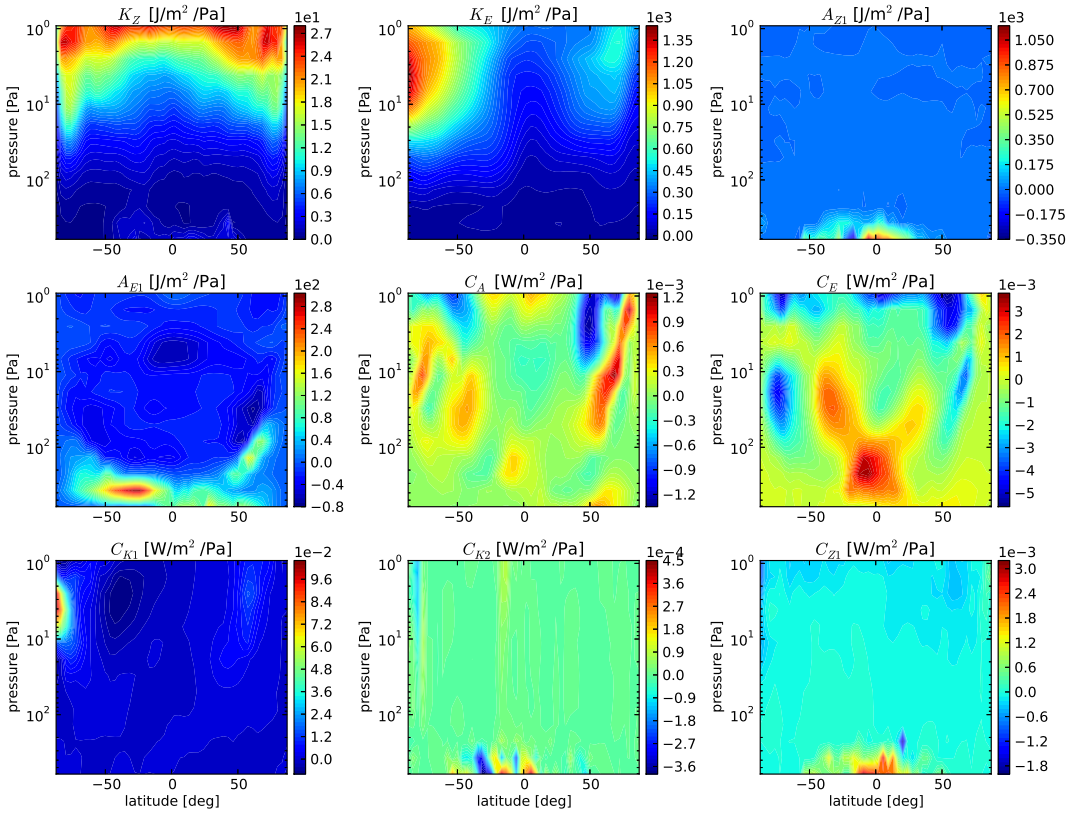

Figure 2.12: Diurnal components of the integrands of energy and conversion terms resolved over latitude and pressure coordinates. Displayed data is a mean over two full martian years.

the diurnally filtered component. A comparison of both figures shows that the diurnal components of C_A, C_E, and C_{K1} provide the dominant contribution to the total values.

2.2.6 Conclusion

We have computed both global and temporal mean as well as seasonal, diurnal and hemispheric components of the Lorenz energy cycle of the Martian atmosphere during Mars years 24 to 27. In global and temporal means the Martian atmosphere shares many of the overall characteristics of Earth's Lorenz energy cycle. Important differences can be observed when decomposing the integrands, however, most notably the opposing signs in the conversion between kinetic energy reservoirs, which reveals a barotropically unstable contribution to eddy generation in the Martian atmosphere. This difference implies that on Mars there isn't the same tendency for upscale energy transfer as observed on Earth with regard to the eddy-zonal flow interaction. This occurs because baroclinic instability occurs at the planetary scale on Mars, which leaves little room for an upscale cascade. When including the surface topography in the derivation of the Lorenz energy equations for Mars, essential contributions to A_E, A_Z and C_K can be observed from the additionally arising terms in the "exact" budget equations (see Boer, 1989).

Hemispheric decomposition of C_Z reveals a large seasonal variation between thermally direct and indirect heating mechanisms. We have also found that zonal energy terms are dependent on the season of their hemisphere, whereas eddy kinetic energy changes globally and has its maximum during southern hemisphere summer apparently following the aphelion/perihelion cycle.

Filtering out diurnal and smaller timescales shows that thermal tides provide an important contribution to the conversion of energy in the Martian atmosphere. The generation of kinetic eddy energy K_E via C_E and C_K occurs predominantly on such timescales. During global-scale dust storm events, K_E increases considerably, of which 90% can be attributed to processes that operate on diurnal and smaller timescales such as thermal tides.

Further comparison of seasonal and diurnal effects of the Lorenz energy cycle with regard to our comprehensive parameter study can be found in Sections 5.5 and 6.3.5.

Chapter 3

Model description

In this study, we use a hierarchy of simple GCMs with increasing temporal resolution in thermal forcing (i.e. annually averaged, seasonal cycle, seasonal and diurnal cycle) using a simple, 2-band semi-gray radiation scheme for a dry, terrestrial-style planetary atmosphere with well-mixed radiative constituents.

We use the Portable University Model of the Atmosphere (PUMA, see e.g. Fraedrich et al., 1998, 2005). The model's dynamical core is based upon the semi-implicit method used in the SGCM (Simple Global Circulation Model) from Hoskins and Simmons (1975) (see Section 3.1). PUMA incorporates a select few physical processes - namely surface friction and diabatic heating - to derive atmospheric wind, temperature and pressure patterns. It ignores more complex processes such as clouds, humidity, chemistry, and the non-gray details of molecular absorption spectra. While this may be downside for the detailed modelling of Solar System planets, simplified models can produce planetary circulation regimes that compare reasonably well to existing planets and can provide a first order approximation to the circulation of exoplanets (e.g. Mitchell and Vallis, 2010, Kaspi and Showman, 2015). Furthermore, the relationship between cause and effect of the atmospheric response to changes in parameters is more easily identifiable, because these simplified models neglect nonlinear interdependencies with other processes. The original version of PUMA (referred to as PUMA-S), uses a Newtonian relaxation scheme for its diabatic heating source and Rayleigh friction at the surface. This relaxation scheme forces the atmosphere towards a prescribed temperature profile within a specified timescale.

Wang (2014) has developed PUMA-G, an updated version of PUMA, that introduces a 2-band semi-gray radiative heating scheme (see Section 3.3.1). True radiative relaxation is both height and scale dependent. Thus a 2-band gray radiation allows for a more physically complete and self-consistent representation of radiative forcing than Newtonian relaxation. One can therefore use PUMA-G for a first-order investigation of the impact of the greenhouse effect. Using this simplified model, we can keep the considered parameter space minimal by avoiding going through multiple configurations of various radiatively-active atmospheric gases.

In the present work, we use results from PUMA-S and PUMA-G performed by Wang (2014) as a starting point to review the general, annually averaged circulation over a range of parameters (Chapter 4). Furthermore, we developed PUMA-GT, an updated version of PUMA-G, featuring time-dependent seasonal and/or diurnally-varying incident solar radiation and a variable thermal inertia of the surface. We use PUMA-GT to perform a comprehensive parameter study to analyse the effect of the diurnal and seasonal cycle on the atmospheric circulation (Chapters 5 and 6). This will help us understand the way seasonal and diurnally-varying forcing affects the way energy is propagated through the atmosphere. In the Solar System both seasonal (Mars, Titan) and diurnal (Mars, Venus) effects provide important contributions in the atmospheres of planetary bodies. We carried out most simulations with T42 horizontal resolution (equivalent to a grid resolution of 64×128 in latitude $\times$ longitude) and 10 vertical layers for at least 20 model years with each year having a total of 360 solar days (unless specified otherwise). The planetary orbit is equivalent to that of Earth with obliquity $\epsilon = 23.44°$, but an orbital eccentricity of $e = 0$.

While a vertical resolution of 10 layers may seem low, it is enough to simulate the first order dynamical response of the circulation regime in our simplified atmospheric model. Test simulations with higher vertical resolution result in very similar circulation regimes. Studies on state-of-the-art full-physics GCMs (e.g. Roeckner et al., 2006) show that simulations with spectral resolution higher that T42 profit from having more vertical levels. As our simulations are in T42 and only focus on dynamics in the troposphere, this does not seem to be a strong limiting factor.

Section 3.1 describes the dynamical core. In Section 3.2, we briefly describe the

Newtonian relaxation parameterisation used in PUMA-S. The semi-grey two-band radiative-convective is described in Section 3.3.1. In Section 3.4, we describe model improvements made for the PUMA-GT model in the current work.For this we added a time-varying solar forcing and a thermal inertia of the surface to the model.

3.1 Dynamical core

The dynamical core solves the following primitive equations in dimensionless form (see Fraedrich et al., 1998, Hoskins and Simmons, 1975):

$$\frac{\partial(\zeta+f)}{\partial t} = \frac{1}{1-\mu^2}\frac{\partial F_v}{\partial \lambda} - \frac{\partial F_u}{\partial \mu} + P_\zeta, \tag{3.1}$$

$$\frac{\partial D_m}{\partial t} = \frac{1}{1-\mu^2}\frac{\partial F_u}{\partial \lambda} + \frac{\partial F_v}{\partial \mu} - \nabla^2\left(\frac{u_c^2+v_c^2}{2(1-\mu^2)} + \Phi + T_0 \ln p_s\right) + P_D, \tag{3.2}$$

$$\frac{\partial \Phi}{\partial \ln \sigma} = -T, \tag{3.3}$$

$$\frac{\partial \ln p_s}{\partial t} = -\int_0^1 A_m d\sigma, \tag{3.4}$$

$$\frac{\partial T'}{\partial t} = -\frac{1}{(1-\mu^2)}\frac{\partial u_c T'}{\partial \lambda}\frac{\partial v_c T'}{\partial \mu} + D_m T' - \dot{\sigma}\frac{\partial T}{\partial \sigma} + \kappa\frac{T}{p}\omega + P_T. \tag{3.5}$$

Equations (3.1) - (3.5) are the vorticity equation, divergence equation, hydrostatic approximation, continuity equation, and the thermal energy equation, respectively. In eqns. (3.1) and (3.2), F_u and F_v are horizontal forces

$$F_u = v_c(\zeta+f) - \dot{\sigma}\frac{\partial u_c}{\partial \sigma} - T'\frac{\partial \ln p_s}{\partial \lambda} \tag{3.6}$$

$$F_v = -u_c(\zeta+f) - \dot{\sigma}\frac{\partial v_c}{\partial \sigma} - T'(1-\mu^2)\frac{\partial \ln p_s}{\partial \mu}. \tag{3.7}$$

In Eqn. (3.4) A_m denotes

$$A_m = D_m + \boldsymbol{u}_c \cdot \nabla \ln p_s \tag{3.8}$$

and the variables u_c, v_c, and μ are determined by the latitude ϕ and the horizontal velocity $\boldsymbol{u} = (u, v)$

$$u_c = u \cos \phi \tag{3.9}$$

$$v_c = v \cos \phi \tag{3.10}$$

$$\mu = \sin \phi \tag{3.11}$$

A full list of the physical quantities that appear in equations (3.1) - (3.11), see below:

T:	temperature	scaled by $a^2\Omega^2/R$
T_0:	reference temperature	scaled by $a^2\Omega^2/R$
T':	deviation from T_0	scaled by $a^2\Omega^2/R$
ζ:	relative vorticity	scaled by Ω
D_m:	divergence	scaled by Ω
p_s:	surface pressure	scaled by p_0
p:	pressure	scaled by p_0
Φ:	geopotential	scaled by $a^2\Omega^2/g$
t:	time	scaled by Ω^{-1}
λ, ϕ:	longitude,latitude	
$\sigma = p/p_s$:	sigma vertical coordinate	
$\dot{\sigma} = d\sigma/dt$:	vertical velocity in σ-system	
$\omega = dp/dt$:	vertical velocity in p-system	
$\boldsymbol{u} = (u, v)$:	horizontal velocity	
$\boldsymbol{u}_c = (u_c, v_c)$:	horizontal velocity $(\cdot \cos \phi)$	
f:	Coriolis parameter	
c_p:	specific heat at constant pressure	
κ:	adiabatic coefficient	
Ω:	planetary rotation rate	
a:	planetary radius	
R:	gas constant of dry air	
p_0:	standard surface pressure	

The variables of equations (3.1)-(3.5) are nondimensionalised by scaling according to the table above. The derivation and nondimensionalisation of these equations is described by Liakka (2006).

To solve the primitive equations, PUMA uses a pseudo-spectral approach with dynamical time-stepping (see Hoskins and Simmons, 1975). The dynamical core uses a finite difference method for the vertical σ-levels and spherical harmonic transformation in the horizontal direction. One can represent an arbitrary horizontal variable Q as a linear combination of the spherical harmonic function $Y_n^m(\lambda, \phi)$ at latitude ϕ and longitude λ:

$$Q(\lambda, \phi) = \sum_{n=0}^{\infty} \sum_{m=-n}^{n} f_n^m Y_n^m(\lambda, \phi), \tag{3.12}$$

$$Y_n^m(\lambda, \phi) = e^{im\lambda} P_n^m(\sin \phi), \tag{3.13}$$

where $P_n^m(\sin \phi)$ is the associated Legendre polynomial and f_n^m is the spectral coefficient at total wavenumber n, and zonal wavenumber m. The model supports a truncation of this expansion at total wavenumbers $n_T = 21, 31, 42, 85, 127, 170$, which corresponds to triangular truncation resolutions T21, T31, ..., T170, respectively.

3.1.1 Parametrisations

Friction

In all versions of PUMA, frictional dissipation is linearly parametrised as Rayleigh friction. The parametrisation terms, P_ζ and P_D, are used in the vorticity equation (Eqn. 3.1) and the divergence equation (Eqn. 3.2) to dampen the relative vorticity and the divergence towards a state of rest,

$$P_\zeta = \frac{\zeta}{\tau_f} + H_\zeta, \tag{3.14}$$

$$P_D = \frac{D_m}{\tau_f} + H_D, \tag{3.15}$$

where τ_f is the frictional damping timescale and H_ζ and H_D are hyperdiffusion coefficients (see below). The default value for the frictional damping timescale is roughly

τ_f =1 day near the surface ($\sigma > 0.8$). At $\sigma \leq 0.8$ the frictional timescale is set to ∞, so that no friction arises.

Hyperdiffusion

The spectral range where energy dissipates is not resolved at low truncation wavenumbers. Hence, the hyperdiffusion terms H_ζ, H_D, and H_T are used to parametrise the dissipation of energy and horizontal mixing in unresolved scales. The hyperdiffusion for one spectral mode γ is defined as (Holton and Hakim, 2013, Fraedrich et al., 1998)

$$H_\gamma = -(-1)^h K \nabla^{2h} Q_\gamma(t) Y_\gamma(\lambda, \mu) \tag{3.16}$$

$$= -K \left(\frac{n(n+1)}{a^2} \right)^h. \tag{3.17}$$

The spectral mode at the truncation wavenumber n_T is damped with a hyperdiffusion timescale τ_H

$$H_\gamma = -\frac{1}{\tau_H} Q_\gamma(t) Y_\gamma(\lambda, \mu) \tag{3.18}$$

$$\Rightarrow K = \frac{1}{\tau_H} \left(\frac{a^2}{n_T(n_T+1)} \right)^h \tag{3.19}$$

Inserting Eqn. (3.19) into Eqn. (3.17) results in

$$H_\gamma = -\frac{1}{\tau_H} \left(\frac{n(n+1)}{n_T(n_T+1)} \right)^h Q_\gamma(t) Y_\gamma(\lambda, \mu). \tag{3.20}$$

where $h = 4$ and where Q is either ζ, D_m or T. The shortest wave at $n = n_T$ is damped by $\tau_H = 1/4$ Earth days.

3.2 PUMA-S

3.2.1 Diabatic heating

The diabatic heating process in PUMA-S is described by Wang (2014). It follows a Newtonian cooling scheme, which is a linear parametrisation where the temperature relaxes towards a restoration temperature T_R within the timescale τ_r. One can calculate

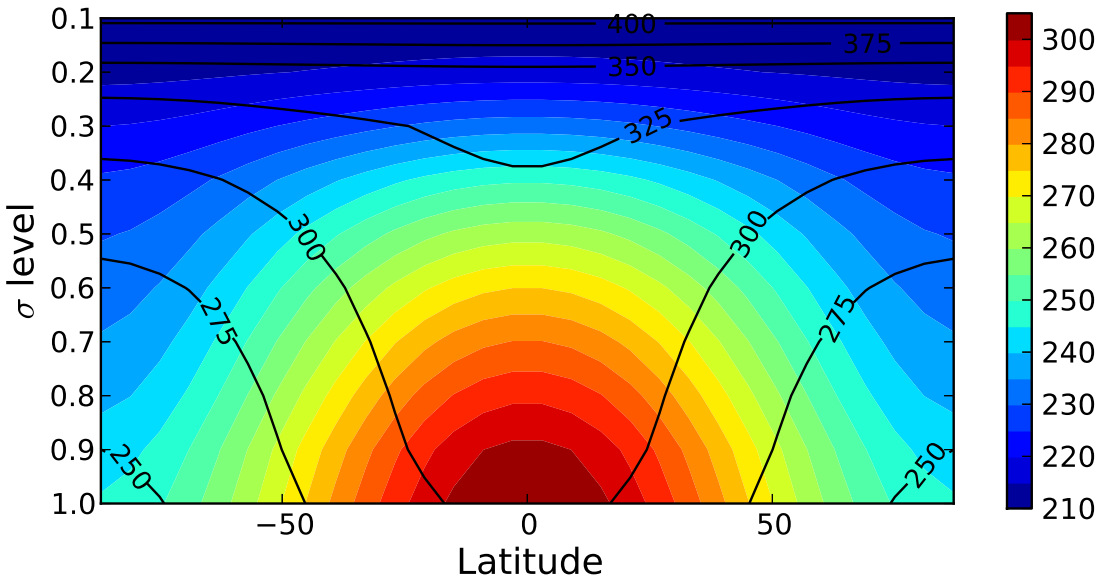

Figure 3.1: Newtonian cooling temperature profile for PUMA-S with $\Delta T = 60$ K. Reproduced with permission from Wang (2014), Fig. 2.2.

the parametrisation term P_T via

$$P_T = \frac{T_R - T}{\tau_r} + H_T \tag{3.21}$$

where

$$T_R(\phi, \sigma) = T_{Rv}(\sigma) + f(\sigma) T_{Rm}(\phi)$$

with parametrisations for the vertical temperature profile $T_{Rv}(\sigma)$, and the meridional temperature component $T_{Rm}(\phi)$. The height-dependent factor $f(\sigma)$ vanishes above the tropopause to parametrise a constant adabatic lapse rate (see Wang (2014), Fraedrich et al. (1998)). H_T is a hyperdiffusion coefficient.

3.3 PUMA-G

3.3.1 2-band radiative-convective scheme

The 2-band semi-grey radiative-convective scheme of PUMA-G is described in detail by Wang (2014). Having only two bands, one in the long-wavelength region (1.7-250 μm) and one in the short-wavelength region (0.1 - 5.0 μm), it provides a simple and computationally favourable radiative transfer scheme for a broad parameter study. We approximate each of the separate bands as grey, with their own constant extinction

coefficient. Due to a rather larger size of the bands, wavelength-dependent scattering effects are only partially covered with this approach. To keep our generalised parameter study simple, we largely disregard clouds. Their effect on the climate is only present in the overall planetary albedo and the ratio between long and short-wave extinction coefficients. For simplicity, we assume all radiatively-active constituents to be well-mixed (Wang, 2014). This approach assumes no local accumulation of radiative gases (e.g. the ozone layer on Earth) because this would firstly add too many variable parameters to our study, and secondly make the studied planetary atmosphere too Earth-like to be generalised to wider classes of planets.

The radiative-convective scheme operates one-dimensionally. It assumes the modelled atmosphere to be plane-parallel and considers only the radiative transfer in the vertical direction. The model calculates the radiative transfer separately for each vertical column of grid-boxes.

We compute the propagation of the incoming solar short-wave radiation flux $F_s^{\downarrow}$ is computed using the Beer-Lambert law,

$$F_s^{\downarrow}(i,\mu) = F_s^{\downarrow}(i-1,\mu)e^{-\chi_i(\mu)}, \tag{3.22}$$

while receiving the stellar irradiance S_0 at TOA,

$$F_s^{\downarrow}(1,\mu) = S_0\mu. \tag{3.23}$$

When the short-wave radiation flux reaches the surface level, parts of it are absorbed using the Earth-equivalent planetary bond albedo of 0.3 and the remaining long-wave flux is reflected upwards where it is subject to further extinction according to Eqn. 3.22 (Wang, 2014).

The model discretises the atmosphere into N layers (from TOA, top of atmosphere, to the surface) and N+1 levels, which correspond to the edges of the layers. The optical thickness χ_i of a given layer i (counted from the top so that $i = 1$ is at TOA) is calculated via

$$\chi_i(\mu) = \frac{k_e^* \Delta p_i}{\mu g}, \tag{3.24}$$

Here, Δp_i is the pressure difference between the top and bottom boundaries of the ith layer, g is the planetary gravitational acceleration, and $\mu = \cos\theta_z$ depends on the solar zenith angle θ_z. The density-adjusted extinction coefficient $k_e^* = k_e\rho_e/\rho_a$ depends on the mass density ρ_e of gas that absorbs the radiation and the mass density ρ_a of the atmosphere, and the total extinction coefficient $k_e = k_a + k_s$, where k_a and k_s denote the absorption coefficient and the scattering coefficient, respectively (Wang, 2014).

In the long-wave, our radiative-convective scheme solves the radiative transfer equation in local thermal equilibrium under the diffusivity approximation (see Andrews, 2010):

$$-\frac{dF^{\uparrow}}{d\chi^*} + F^{\uparrow} = \pi B(T), \tag{3.25}$$

$$\frac{dF^{\downarrow}}{d\chi^*} + F^{\downarrow} = \pi B(T), \tag{3.26}$$

with

$$\chi^* = D_\chi \cdot \chi, \tag{3.27}$$

where χ^* is a scaled optical depth. The diffusivity factor D_χ is calculated using the parametrisation of Ramanathan et al. (1985),

$$D_\chi = 1.5 + 0.5/(1 + 4\chi + 10\chi^2). \tag{3.28}$$

The long-wave thermal radiation fluxes $F_L^{\downarrow}$ and $F_L^{\uparrow}$ are calculated similarly using e.g.

$$F_L^{\downarrow}(i) = E^{\downarrow}(i) + F_L^{\downarrow}(i-1)e^{-\chi_i/D_R} \tag{3.29}$$

where $D_R = 1/D_\chi$ and $E^{\downarrow}(i)$ is the downward thermal emission of layer i. To calculate $E^{\downarrow}(i)$, the model uses the relation (see Lacis and Oinas (1991)),

$$E^{\downarrow}(i) = (B(T_b) - B(T_t)e^{-\chi_i/D_R})\frac{\chi_i}{\chi_i - D_R ln[B(T_t)/B(T_b)]}, \tag{3.30}$$

where B is the Planck blackbody radiation flux and T_b and T_t are the atmospheric temperatures at the bottom and top of layer i, respectively. The upward propagation of long-wave radiation is treated similarly.

The long-wave surface radiation flux,

$$F_s^{net}(N+1) + F_L^{\downarrow}(N+1) = \sigma_B T_s^4, \tag{3.31}$$

is assumed as a black body in radiative equilibrium, where F_s^{net} is the net short-wave radiation flux, $F_L^{\downarrow}$ is the downward long-wave radiation at the surface level $N+1$, and T_s is the ground temperature.

Using the above fluxes a net radiative flux F_n can be computed for each level. One can then obtain the total heating rate Q in layer i via

$$Q(i) = \frac{g}{c_p} \frac{F_n(i+1) - F_n(i)}{p(i+1) - p(i)}. \tag{3.32}$$

The heating rate induces a change in temperature in layer i via

$$T(i) = T_0(i) + Q(i)\Delta t, \tag{3.33}$$

where T_0 is the temperature during the previous time step and Δt is the duration of a time step. (Wang, 2014)

We also apply a convective adjustment scheme (Manabe and Strickler, 1964, Manabe and Wetherald, 1967) to the temperature profile in cases in which the lapse rate between adjacent layers exceed the dry adiabatic lapse rate $\Gamma = g/c_p$. The convective adjustment scheme adjusts the temperature so that total enthalpy is conserved and the resulting atmosphere is statically stable with a local lapse rate of Γ (see Wang, 2014, Manabe and Wetherald, 1967). However, this scheme assumes very low thermal inertia of the surface when coupled with the improved time-resolved solar-zenith code (see Section 3.4.2). A solution to this issue is presented in Section 3.4.4.

3.4 PUMA-GT

In the previous sections we have described PUMA-S and PUMA-G, the models used by Wang (2014) for his parameter study of planetary circulation regimes. What follows now describes the development of PUMA-GT. We developed it to analyse the effects of diurnally and seasonally-varying forcing in a large range of possible circulation regimes. PUMA-GT builds upon the semi-gray two-band radiative-convective scheme from PUMA-G and adds a diurnally- and/or seasonally-varying stellar zenith angle and a variable thermal inertia of the surface.

In this section, we describe the calculations necessary to compute a time-dependent stellar zenith angle for the radiative transfer scheme and the required changes to the surface energy balance.

3.4.1 Diurnal mean solar flux

The incoming solar radiation $F_s^{\downarrow}$ at TOA is given by

$$F_s^{\downarrow} = S_0 \mu \left(\frac{\overline{r}}{r(t)} \right)^2, \tag{3.34}$$

where $\overline{r}$ is the mean planetary distance from its host star, $r(t)$ is the time-dependent distance, and S_0 is the stellar irradiance at $\overline{r}$ ($S_0 = 1366\mathrm{W/m}^2$ for an Earth-like case). In the present section, we focus on the method of calculating μ in diurnal mean after Vardavas and Taylor (2011). Calculation of a fully time-dependent, diurnally varying μ can be found in Section 3.4.2.

To calculate the diurnal mean insolation during slow seasonal variation of $r(t)$, the Eqn. (3.34) becomes

$$(F_s^{\downarrow})_n = S_0 \mu_n \left(\frac{\overline{r_n}}{r(t)} \right)^2 \frac{H_d}{\pi}, \tag{3.35}$$

where the subscript $\cdot_n$ specifies the mean value on day n. H_d is the half day length in radians with

$$H_d = \arccos(-\tan\phi \tan\delta_n), \tag{3.36}$$

where ϕ is the latitude and δ is the solar declination. We can obtain the mean value μ_n between sunrise and sunset via

$$\mu_n = A_n + \frac{B_n \sin H_d}{H_d}, \tag{3.37}$$

where

$$A_n = \sin\phi \sin\delta_n, \tag{3.38}$$

$$B_n = \cos\phi \cos\delta_n. \tag{3.39}$$

Given the planet's obliquity ϵ and the time t_n (in days), one can calculate the host star's diurnal-mean declination δ_n via

$$\delta_n = -\epsilon \cos(2\pi \frac{t_n}{360}). \tag{3.40}$$

3.4.2 Time-dependent stellar zenith angle

In the current work, we improve upon the radiative scheme of PUMA-G by adding time-dependency to the calculation of the stellar zenith angle (see Vardavas and Taylor, 2011). This allows full modelling of diurnal incoming stellar radiation (ISR) or of daily mean ISR with changing seasonality. We call this version of the model PUMA-GT (G for "gray" and T for "time-dependent").

The incoming solar radiation at TOA is given by

$$F_s^{\downarrow} = S_0 \mu \left(\frac{\overline{r}}{r(t)} \right)^2 \tag{3.41}$$

where $\overline{r}$ is the mean planetary distance from its host star and $r(t)$ is the time-dependent distance. The cosine of the solar zenith angle μ can be obtained from

$$\mu(t) = \mathcal{A} + \mathcal{B} \cos h(t), \tag{3.42}$$

where

$$\mathcal{A} = \sin\phi \sin\delta, \tag{3.43}$$

$$\mathcal{B} = \cos\phi \cos\delta, \tag{3.44}$$

where ϕ is the latitude and δ and h are the host star's declination and hour angle, respectively (Vardavas and Taylor, 2011).

One can compute the solar declination via

$$\delta = \arcsin(\sin\epsilon \sin L_{ts}) \tag{3.45}$$

where ϵ is the planetary obliquity and L_{ts} is the true solar longitude:

$$L_{ts} = L + 2e \sin g_a + (5e^2/4) \sin 2g_a. \tag{3.46}$$

in equation 3.46, L denotes the mean solar longitude, e denotes the orbital eccentricity and g_a the mean anomaly. One can obtain the mean solar longitude and the mean anomaly from

$$L(t) = L_o + \frac{2\pi t_d}{P_{orb}}, \tag{3.47}$$

$$g_a = g_0 + \frac{2\pi t_d}{P_{orb}}, \tag{3.48}$$

where t_d is the time in days ($t_d = 0$ at 1st January), $L_o = 1.5581\pi$ is the mean solar longitude at $t_d = 0$, $g_o = 1.986\pi$ is the mean anomaly at $t_d = 0$, and P_{orb} is the planetary orbital period in days. One can then obtain the time-dependent hour angle via

$$h(t) = (t_d - 12 + \lambda/15 + E/15)\pi/12, \tag{3.49}$$

where t_d is the time in hours, λ is the longitude and $E = L - \alpha_r$ (with L and α_r both in degrees), and lastly α_r is the solar right ascension angle, which we compute via

$$\alpha_r = L_{ts} - u \sin 2L_{ts} + (u^2/2) \sin 4L_{ts} \tag{3.50}$$

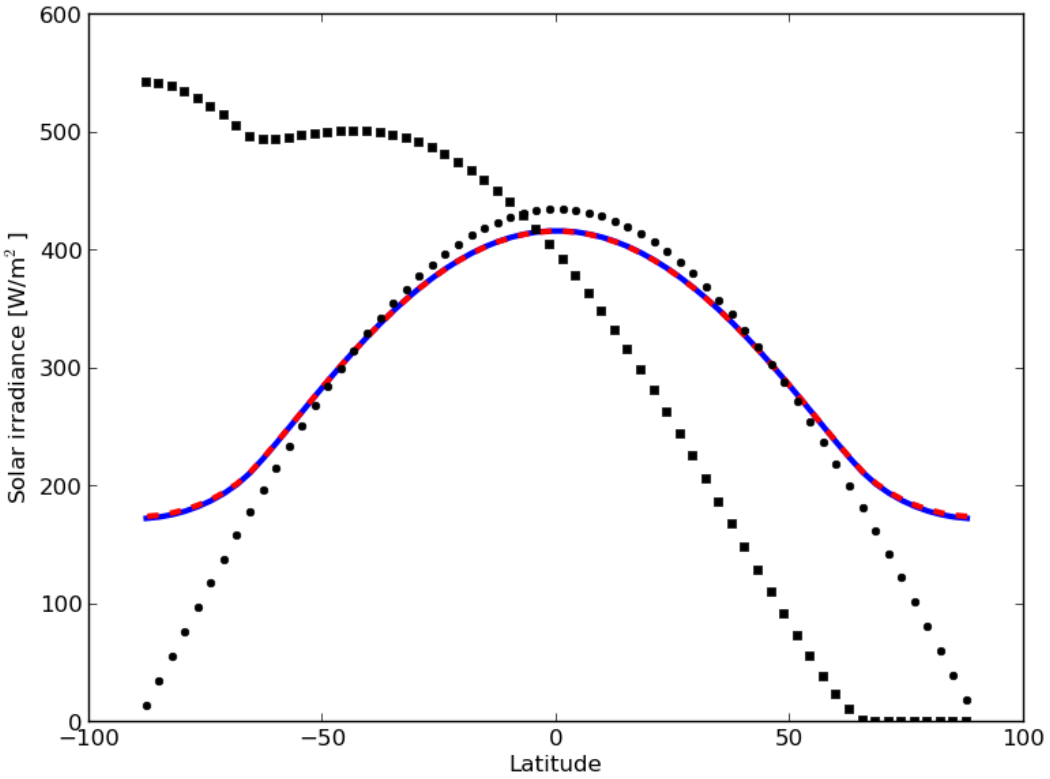

Figure 3.2: Annual mean, zonal mean solar irradiance at top of atmosphere with Earth equivalent obliquity for both diurnally-varying forcing (blue solid curve) and diurnally-averaged forcing (red dashed curve). Black symbols show zonal mean solar irradiance at spring equinox (circles) and northern winter solstice (squares).

with $u = \tan^2(\epsilon/2)$ (Vardavas and Taylor, 2011).

We show a comparison between solar forcing in the diurnal mean and a full representation of diurnally-varying forcing in Fig. 3.2, where we plotted the annual and zonal mean solar irradiance for both cases (blue and red curves). It is apparent that both cases receive the same total irradiance. The black symbols in Fig. 3.2 show the zonal mean solar irradiance of the diurnally-varying forcing during spring equinox (dots) and northern winter solstice (squares). At $\phi = 60°$S there is a small dip in the solar irradiance, which occurs due to the transition from the day-night cycle in the extratropics to the permanent day at the summer pole.

3.4.3 Surface thermal inertia

In Wang (2014), the surface temperature in PUMA-G was assumed to change instantly with the solar forcing, effectively resulting in a surface with no thermal inertia. This

assumption was reasonable for the previous investigation using PUMA-G (Wang, 2014) because it operated with a constant solar forcing using an annually averaged pattern of solar zenith angles. In PUMA-GT, this setup causes large interhemispheric Hadley circulations to appear during the solstices. While such a phenomenon can be observed on Mars, this issue prevents the modelling of an Earth-like circulation regime (due to the large thermal inertia of the oceans). In the following sections, we present multiple approaches to improving the surface and atmospheric response, with the goal of simulating an Earth-like circulation, as a reference case.

We use an approach that allows for changes in the surface temperature according to a heat capacity C per unit area:

$$C\frac{dT_s}{dt} = (F_s^{net} + F_l^{\downarrow} - \sigma_B T_s^4), \tag{3.51}$$

where F_s^{net} is the net surface shortwave flux, $F_l^{\downarrow}$ is the downwards longwave flux at the surface, and σ_B is the Stefan-Boltzmann constant. The specific heat capacity can be obtained from

$$C = c_p \rho \delta_s \tag{3.52}$$

with the specific heat capacity at constant pressure c_p, the density ρ, and the thickness or skin depth of the surface δ_s. For instance a 1 m deep slab ocean of pure water would have a C-value of

$$C = 4.2 \cdot 10^3 \frac{\mathrm{J}}{\mathrm{kg\ K}} \cdot 10^3 \frac{\mathrm{kg}}{\mathrm{m}^3} \cdot 1\mathrm{m} \tag{3.53}$$

$$C = 4.2 \cdot 10^6 \frac{\mathrm{J}}{\mathrm{m}^2\ \mathrm{K}} \tag{3.54}$$

For solid surfaces we obtain the skin depth δ_s from

$$\delta_s = \sqrt{\frac{k_{th}}{\omega_{orb} \rho c_p}}, \tag{3.55}$$

where ω is the annual frequency (based on 360 days) and k_{th} is the thermal conductivity of the surface material. The thermal conductivity depends strongly on the material

Surface material	c_p $[\frac{\text{J}}{\text{kg K}}]$	ρ $[\frac{\text{kg}}{\text{m}^3}]$	k $[\frac{\text{W}}{\text{m K}}]$	δ_s [m]	C $[\frac{\text{J}}{\text{m}^2 \text{K}}]$	τ_{surf}
dry sand	800	1300	0.2	0.98	$1 \cdot 10^6$	2.2 days
pure olivine	800	3300	6	3.4	$9 \cdot 10^6$	20 days
1 m ocean	4200	1000	-	1	$4.2 \cdot 10^6$	9 days
100 m ocean	4200	1000	-	100	$4.2 \cdot 10^8$	2.6 years
4000 m ocean	4200	1000	-	4000	$1.7 \cdot 10^{10}$	104 years

Table 3.1: Heat capacity and thermal inertia timescales for different surface materials. For water oceans an ocean depth is used in place of the skin depth, because we assume a convective heat flux.

and temperature and varies from roughly 1 to 10 $\frac{\text{W}}{\text{m K}}$ for common Earth minerals (and 0.2 $\frac{\text{W}}{\text{m K}}$ for dry sand). The heat capacity and density also depend very strongly on the material. When limiting to rocks or soil, specific heat capacities can vary between roughly 500 to 1500 $\frac{\text{J}}{\text{kg K}}$ (whereas pure metals have lower and organic materials, e.g. wood, have higher c_p), with densities of rocks between roughly 2000 and 3000 $\frac{\text{kg}}{\text{m}^3}$ (and 1300 $\frac{\text{kg}}{\text{m}^3}$ for dry sand).

The relationship between C and τ_{surf} is given by (Mitchell et al., 2014) as

$$\tau_{surf} = \frac{C}{4\sigma_B \bar{T}_s^3}, \tag{3.56}$$

where $\bar{T}_s$ is the mean surface temperature.

In this case, we chose $C = 1 \cdot 10^8 \frac{\text{J}}{\text{m}^2\text{K}}$, which corresponds to $\tau_{surf} \approx 220$ days according to Eqn. 3.56. Fig. 3.3 shows that both the diurnally-varying (left) and the diurnally-averaged (right) forcing cases result in the same annually averaged temperature profile. This means that this approach (Eqn. 3.51) to modelling the surface temperature correctly simulates the balance day-night cycle of incident and outgoing energy of the surface due to diurnally-varying solar forcing.

3.4.4 Convective adjustment relaxation

The convective adjustment scheme originally used in PUMA-G (see Wang, 2014, Manabe and Wetherald, 1967) acts nearly instantly (i.e. after a single timestep). According to the convective scheme presented in Manabe and Wetherald (1967), the temperature difference between levels is compared to the dry adiabatic lapse rate Γ starting from the bottom (level N). Manabe and Wetherald (1967) first adjust temperature of the

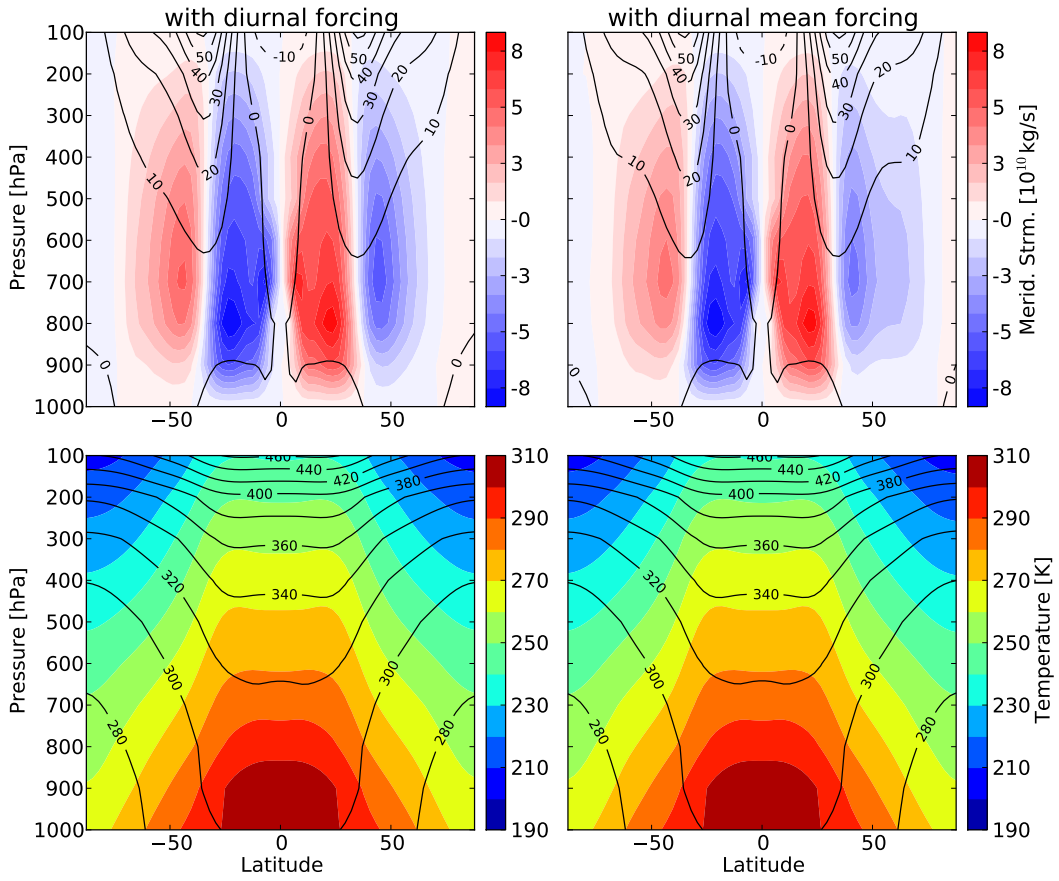

Figure 3.3: Zonal-mean, annual-mean diagnostics. Top: zonal wind (contour) and meridional mass stream function (colour); Bottom: temperature (colour) and potential temperature fields (contour) for two runs with diurnally-varying (left) and diurnally-averaged (right) solar forcing using the surface thermal inertia approach (Eqn. 3.51).

bottom layer according to

$$\frac{c_p}{g}\Delta p_N[T_N^{(1)} - T_N^{(0)}] = \sigma\Delta t\{[T_g^{(0)}]^4 - [T_g^{(1)}]^4\} \tag{3.57}$$

$$T_N^{(1)} = T_g^{(1)} - LRC_N \tag{3.58}$$

where Δp_N is the pressure difference between layer N and the ground, T_N is the temperature in layer N, T_g is temperature at the ground, $T^(0) = T_{rad}$ is the temperature before convective adjustment (i.e. in radiative equilibrium), and $T^{(1)} = T_\Gamma$ is the temperature after convective adjustment, and LRC is the critical temperature difference between layers. Upper layers i that are unstable, i.e. where $\frac{dT}{dz} < -\Gamma$, are adjusted via

$$\{\frac{c_p}{g}\Delta p_i[T_i^{(1)} - T_i^{(0)}] + \Delta p_{i-1}[T_{i-1}^{(0)} - T_{i-1}^{(1)}]\} = 0 \tag{3.59}$$

$$T_i^{(1)} - T_{i-1}^{(1)} = LRC_i \tag{3.60}$$

This process is repeated until the atmosphere is no longer unstable.

The change in temperature from the convective adjustment is converted into a temperature tendency via

$$\frac{dT}{dt} = \frac{T^{(1)} - T^{(0)}}{2\Delta t}, \tag{3.61}$$

which is then added to the advection scheme. Here $T^{(0)}$ is the temperature before convective adjustment and $T^{(1)}$ is temperature after convective adjustment. PUMA-G used a timescale of $2\Delta t$, so that the convective adjustment occurs nearly instantaneous.

In PUMA-GT the above convection scheme would often crash. With diurnally-varying solar forcing, PUMA-GT may require timesteps of order one minute and smaller. For short Δt, an instantaneous adjustment may cause problems, such as the artificial excitement of artificial gravity waves. Additionally, on Earth, convective overturning timescales can be of the order of tens of minutes. Hence, an instantly occurring convective adjustment may be unphysical at such short timesteps. We have

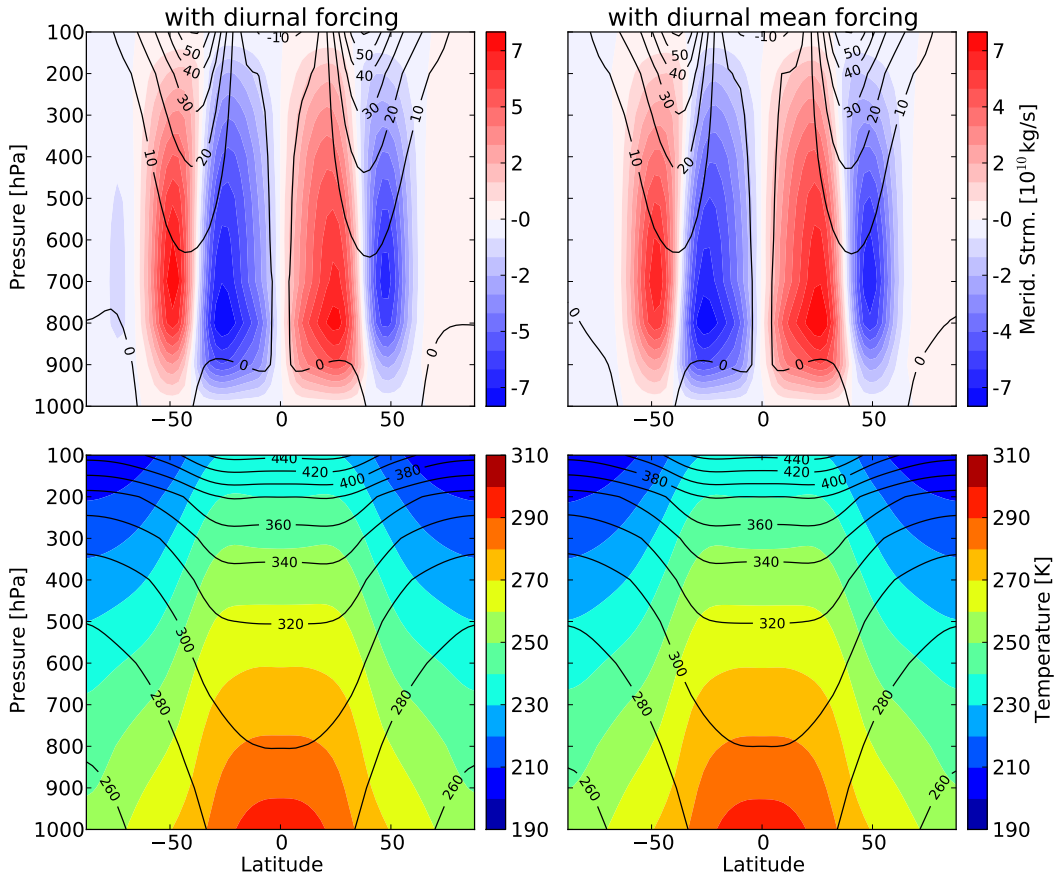

Figure 3.4: Same as Fig. 3.3, but also using the convective adjustment relaxation (Eqn. 3.62)

therefore added a convective adjustment timescale $\tau_{conv.adj.}$, so that

$$\frac{dT}{dt} = \frac{T^1 - T^{(0)}}{\tau_{conv.adj.}}, \tag{3.62}$$

to stabilize the operation of the radiative-convective model (Betts, 1986). We adopt a standard value of $\tau_{conv.adj.} = 2$ hours according to Betts (1986). While this value may be specific to Earth, using this convective adjustment relaxation allows for PUMA-GT to run without crashing. The physical motivation behind this approach is to simulate the lag of the convective response due to a change in the large-scale field (Betts, 1986).

The resulting modelled atmospheres (with $\tau_{surf} \approx 220$ days) have zonal mean fields that are again the same for the case with diurnally-varying forcing and with diurnally-averaged forcing. Compared to the first two approaches, the values in temperature are now in better agreement with the reference case of PUMA-G (shown in Fig. 3.4),

which was set up by Wang (2014) to have an Earth-like temperature distribution at the surface. We use this model version for the studies presented in this thesis (see Chapters 5 and 6).

Chapter 4

Analysis of studies with constant forcing (PUMA-S)

In this chapter we first briefly review some basic behaviours of idealised atmospheres with constant forcing (in Section 4.1). Afterwards, in Section 4.2 we analyse the spectral energy budget of these simulations using a recent spectral energy budget formulation (Augier and Lindborg, 2013).

4.1 Brief review of varying the planetary rotation rate

Here we briefly review some results from Wang (2014) and Wang et al. (in prep.a) to understand the basic behaviour of the modelled idealised atmospheres with PUMA-S. This will serve as a point of reference for our analysis of the spectral energy budget under Earth-like conditions but with varying rotation rate (see Section 4.2). In addition, this review can be used as a point of comparison with the seasonal and diurnal effects presented in subsequent chapters.

4.1.1 Zonal mean diagnostics

In this section, we show the effect of varying the rotation rate in the range of $\Omega = [\frac{1}{16}\Omega_E - 8\Omega_E]$. The data for this section was produced by Wang (2014) using PUMA-S. This serves as a baseline for the changes we add due to seasonal and other variations, which are discussed in Chapters 5 and 6.

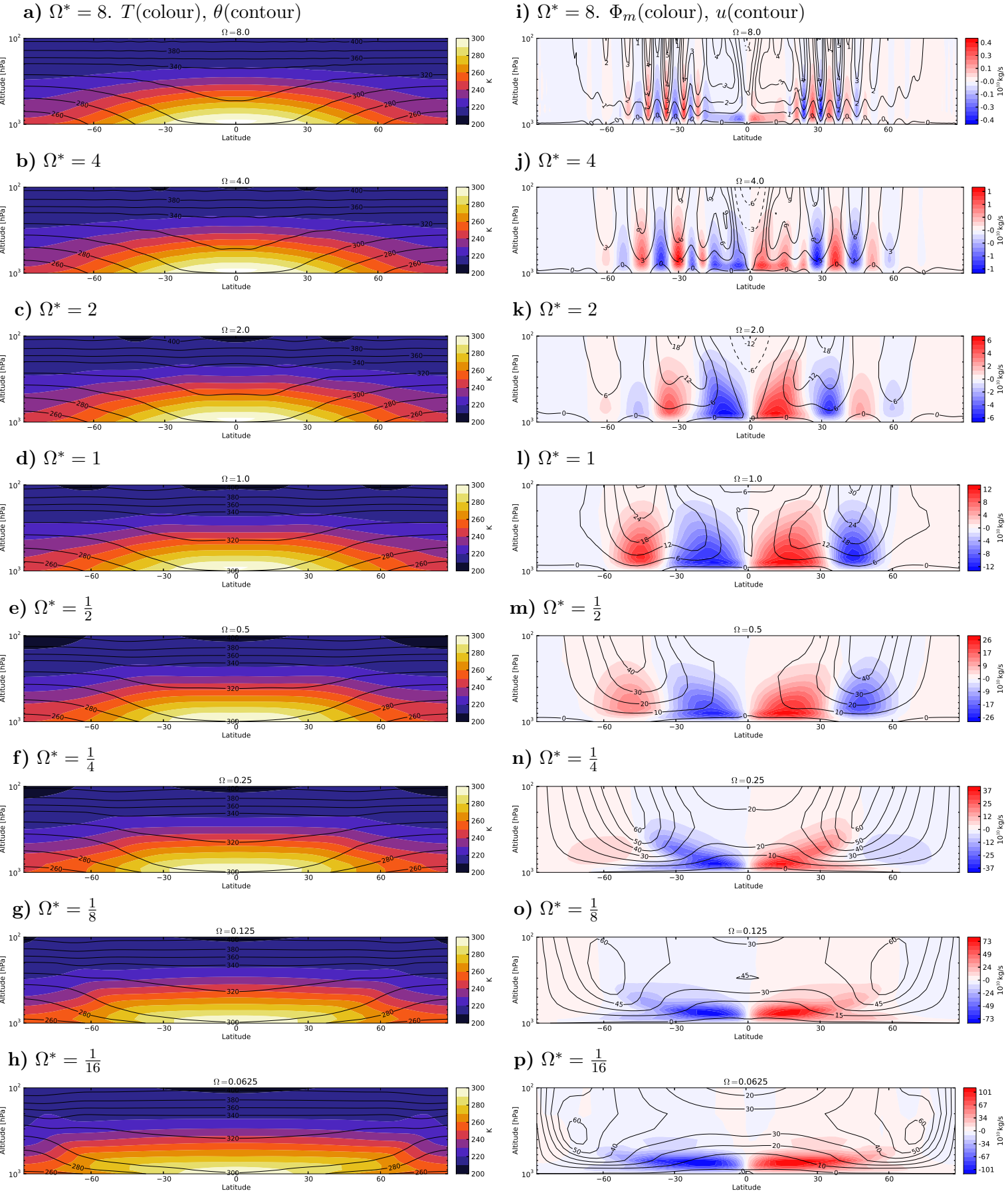

Figure 4.1: Zonal mean fields of temperature T (colour), and potential temperature θ (contour) [(a) - (h)] and meridional streamfunction and zonal wind (contour) (colour) [(i) - (p)] for different values of $\Omega^* = \Omega/\Omega_E$.

In Figure 4.1, we show zonal-mean maps in latitude and height of annual-mean zonal-mean diagnostics for different planetary rotation rates Ω. The atmospheres were simulated using PUMA-S with varying $\Omega^* = [8 - \frac{1}{16}]$, where $\Omega^* = \Omega/\Omega_E$ is the relative rotation rate and Ω_E is the Earth rotation rate. Plots on the left side of the figure show the atmospheric temperature T in colour and the potential temperature θ in contours. On the right side of Fig. 4.1 the zonal wind is depicted in contours and the meridional mass streamfunction Φ_m with

$$\Phi_m = 2\pi a \cos\phi \int v \frac{dp}{g}. \tag{4.1}$$

is shown in colour.

The atmospheres of fast-rotating planets (with $\mathcal{R}o \ll 1$, e.g. in this case rotation rates of $\Omega^* \approx 1/2$ and higher) are in geostrophic balance (in the extratropics). This means that Coriolis and pressure-gradient forces dominate over other forces. When the planetary rotation rate is increased the number of zonal jets increases. These jets occur due to two different mechanisms, as either thermally-driven or eddy-driven jets.

The subtropical jets (the ones on each hemisphere nearest the equator) form due to thermally-direct Hadley circulation. Air ascends at the equator, moves poleward and descends at the downward branch of the Hadley cell (see e.g. Fig. 4.1l between 0° and $\pm 30^\circ$ latitude). Due to Coriolis acceleration, an eastward jet forms at the Hadley cells downward branch. In this region there is a steep temperature gradient. Under geostrophic conditions, the thermal wind balance (Eqn. 1.2) applies, so that the temperature gradient is balanced by a strong, vertically sheared zonal flow.

Further jets are located farther poleward and are eddy-driven by virtue of the mechanical and thermal stresses exerted in a zonal mean sense on the background flow. In the Earth-like simulation case, Fig. 4.1l, the subtropical and the eddy-driven polar jet are somewhat fused together, but at higher rotation speeds the jets can be easily discerned. Eddy-driven jets are likely a result of an upscale kinetic energy transfer due to geostrophic turbulence (see Section 4.2) with the assumption of a latitudinally-varying Coriolis parameter $f = \beta(\phi)$ (Charney, 1971, Rhines, 1975).

As the rotation rate increases the meridional width of the Hadley cell decreases and

multiple zonal jets appear. The alternating pattern of zonal winds hinders efficient meridional heat transports and the equator-to-pole temperature gradient increases (Wang, 2014, Kaspi and Showman, 2015).

When decreasing the rotation rate, the Hadley cells expand. This expansion leads to a more pronounced meridional redistribution of heat, and thus causes a decrease of the temperature gradient. At low rotation rates $\mathcal{R}o$ is in the order of one and larger. In this regime, rotational effects are weak, so that geostrophic balance no longer holds. Instead, pressure-gradient forces are balanced with centrifugal forces, which is called cyclostrophic balance. In this regime, momentum is transported to the equatorial upper troposphere and one can observe equatorial superrotation (e.g. Mitchell and Vallis, 2010, Potter et al., 2014, Wang, 2014, Laraia and Schneider, 2015).

4.1.2 Lorenz energy cycle of idealised planets

Previous work by Wang (2014) performed Lorenz energy cycle calculations of simulations with varying planetary rotation rate using a model with a Newtonian cooling scheme (PUMA-S). In this section we compare the energy cycle of these simulations with those of Earth and Mars presented in Section 2.2.

Method

The energy cycle in this section was computed by Wang (2014) using a more widely used, quasi-geostrophic approach presented by Peixóto and Oort (1974). This approach differs from the method presented in Section 2.1 by neglecting both surface effects and the determination of the reference atmosphere.

Energies were computed after James (1995) via

$$A_Z = \int_M \gamma \overline{[\theta_A]^2} dm \tag{4.2}$$

$$A_E = \int_M \gamma \overline{[\theta^{*2}]} dm \tag{4.3}$$

$$K_Z = \int_M \frac{1}{2} \overline{[u]^2} dm \tag{4.4}$$

$$K_E = \int_M \frac{\overline{[u^{*2} + v^{*2}]}}{2} dm \tag{4.5}$$

where $\gamma = R/[\Lambda p \partial_p \theta_R]$, $\Lambda = (p_o/p)^\kappa$, and θ_R is the horizontal mean of the potential temperature θ and θ_A its departure from horizontal mean: $\theta_A = \theta - \theta_R$.

Conversion terms were computed after Peixóto and Oort (1974):

$$C_A = -\int_M \gamma \frac{\partial \overline{[\theta]}}{a\partial\phi} \overline{[v^*\theta^*]} + \frac{\partial}{\partial p}\left(\overline{\gamma[\theta]}\right) \overline{[\omega^*\theta^*]} dm \tag{4.6}$$

$$C_E = -g\int_M \left(\overline{\frac{u'}{a\cos\phi}\frac{\partial\Phi'}{\partial\lambda}} + \overline{\frac{v'}{a}\frac{\partial\Phi'}{\partial\phi}} + \frac{\overline{u}^*}{a\cos\phi}\frac{\partial\overline{\Phi}^*}{\partial\lambda} + \frac{\overline{v}^*}{a}\frac{\partial\overline{\Phi}^*}{\partial\phi} \right) dm \tag{4.7}$$

$$C_K = -\int_M \left\{ \overline{[u^*v^*]}\frac{\partial\overline{[u]}}{a\partial\phi} + [\overline{v'^2} + \overline{v}^{*2}]\frac{\partial\overline{[v]}}{a\partial\phi} + \overline{[\omega^*u^*]}\frac{\partial\overline{[u]}}{\partial p} \right. \tag{4.8}$$

$$\left. + \overline{[\omega^*v^*]}\frac{\partial\overline{[v]}}{\partial p} - \overline{[v]}[\overline{u'^2} + \overline{u}^{*2}]\frac{\tan\phi}{a} \right\} dm \tag{4.9}$$

$$C_Z = \int_M \overline{[v]} g \frac{\partial\overline{[\Phi]}}{a\partial\phi} dm \tag{4.10}$$

where X^* is the deviation from the zonal mean $[X]$ and X' is the deviation of the time mean $\overline{X}$ of an arbitrary variable X and Φ is the geopotential height (Peixóto and Oort, 1974). The generation and dissipation rates are calculated from the residuals as before.

Comparing the Lorenz cycle of idealised atmospheres with Earth and Mars

Figure 4.2 depicts the Lorenz energy cycle of simulations performed by Wang (2014) with PUMA-S. Each of these varies the planetary rotation rate by a range of factors from 1/16 to 8 times the Earth's rotation rate (i.e. the same simulations as presented in Fig. 4.1). These simulation were performed for at least 20 model years until equilibrium was reached.

The following effects occur with varying rotation rate. A change in direction of C_K between $\Omega^* = 1/2$ and $\Omega^* = 1/4$ occurs, which signifies an increase in the contribution of barotropic instability towards eddy generation (Wang, 2014). With decreasing rotation rate, this barotropic component becomes stronger until it dominates over the baroclinic component at $\Omega^* = 1/16$. In addition, there is a maximum in baroclinic conversion (C_A, C_E) occuring between $\Omega^* = 1$ and $\Omega^* = 1/2$. Both Wang (2014) and Kaspi and Showman (2015) find a peak in meridional eddy heat flux for this Ω range. Another conversion term that changes directions at around $\Omega^* = 1/4$ is C_Z, which

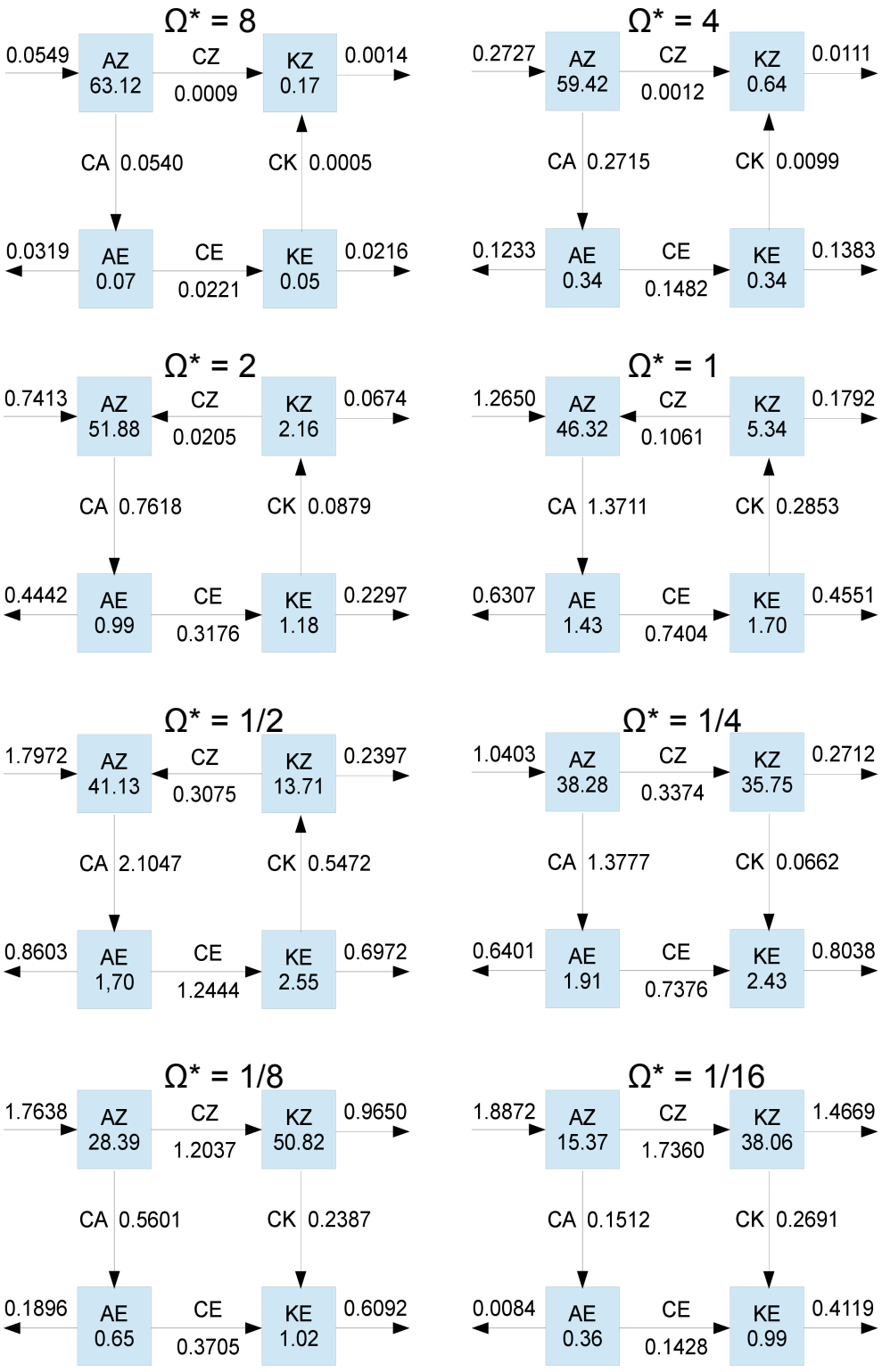

Figure 4.2: Lorenz energy cycle for PUMA-S simulations with varying planetary rotation rate Ω^*. Reproduced with permission from Wang (2014), their Fig. 4.6.

becomes positive for $\Omega^* \leq 1/4$. With decreasing rotation rate, C_Z increases signifying a stronger thermally direct circulation via the increasing meridional extent of the Hadley circulation. With increasing rotation rate, the conversion directions remain similar to the Earth case, but weaker in magnitude. This decrease can be attributed to the decrease in wind speeds observed in these cases (see Fig. 4.1i-k). Kaspi and Showman (2015) argue that with increasing Ω^* zones with baroclinic activity become narrower and eddy length scales become smaller which reduces the strength of the meridional eddy momentum flux. In addition, the meridional extent of the Hadley circulation decreases with rotation rate, which decreases the effectivity of the zonal mean meridional heat (see Fig. 1.5) and energy exchange. Due to both of these reasons, less energy is transported from the equator to the extratropics, which reduces both global wind speeds and the magnitude of the energy conversion terms in the Lorenz cycle.

When comparing Fig. 4.2 with reanalysis data from Earth and Mars (see Fig. 2.3) we find that G_E (generation of A_E) is negative for all PUMA-S simulations. This is likely due to thermal dissipation in middle latitudes and may be countered by latent heat release in case of Earth (Lorenz, 1955) and non-axisymmetric thermal forcing (e.g. thermal tides) in case of Mars (c.f. Fig. 2.8, bottom, $G_E > 0$). Apart from this, the Earth data and the simulation at $\Omega^* = 1$ feature another difference with the direction of C_Z. The model results at $\Omega^* = 1$ seem to feature slightly more indirect heating (negative C_Z) than the Earth reanalysis data. However, the Earth data in Fig. 2.3 (top) features two datasets, of which one (black text) also results in slightly negative C_Z. All in all though, the models and the reanalysis data are qualitatively consistent. Further comparison of the values themselves would go into too much detail, given the simplicity of the models used.

With regard to thermal Rossby number, Mars (with $\mathcal{R}o \approx 0.11$) lies between the cases for $\Omega^* = 1/2$ (with $\mathcal{R}o = 0.08$) and $\Omega^* = 1/4$ (with $\mathcal{R}o = 0.32$), which is the region where both C_K and C_Z flip directions in the PUMA-S simulations (Figs. 4.2). The Lorenz energy diagram from reanalysis data of Mars (Fig. 2.3) compares very well with the simulations with $\Omega^* = 1/4$; both show thermally direct circulation (positive C_Z) and an overall barotropic contribution to the generation of eddies (positive C_K). Compared to the baroclinic contribution to eddy generation, the barotropic component

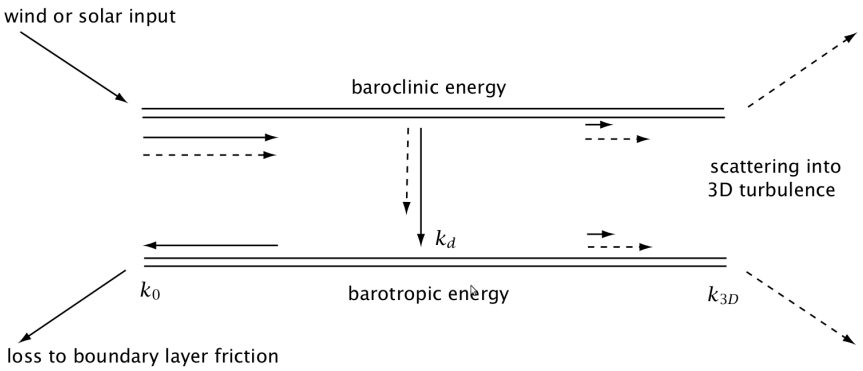

Figure 4.3: Idealised scheme of geostrophic turbulence. Reproduced with permission from Vallis (2006), their Fig. 9.6. Adapted from Salmon (1980).

is weaker in both the simulations and the Mars reanalysis data. The difference in the total values of both conversion rates and energies is due to Mars having a thinner atmosphere compared to the Earth-like configuration in the simulations.

In Chapters 5 and 6, we will further detail the seasonal and diurnal behaviour of the Lorenz energy cycle for time-varying forcing simulations performed with PUMA-GT.

4.2 Spectral energy budget

4.2.1 Introduction

Under quasigeostrophic conditions the turbulent large-scale dynamics (or macroturbulence) of a baroclinic atmosphere is expected to share certain features in common with two-dimensional turbulence theory (Charney, 1971). This phenomenon is termed geostrophic turbulence and it postulates that potential energy is converted into kinetic energy at intermediate lengthscales (the Rossby deformation radius k_d) and is then anticipated to be transported in both upscale and downscale directions (see Fig. 4.3). Energy is transported upscale via an inverse energy cascade (with a $k^{-5/3}$ slope) which is inhibited at the Rhines scale, at which point Rossby waves emerge (Rhines, 1975, Salmon, 1980, Sukoriansky et al., 2007). The downscale transport is predicted to occur via a forward cascade that is dominated by enstrophy[2] flux and has a slope of k^{-3}. This cascade continues until a point is reached where viscous forces dissipate the turbulent flow (see Fig. 4.4). The theory proposes that the wavenumber ranges

[2] $Enst = \frac{1}{2}\int_V \zeta^2 dV$ where ζ is the relative vorticity

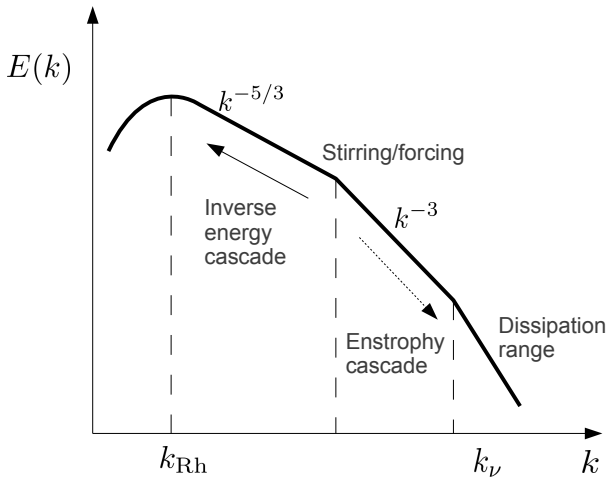

Figure 4.4: Energy over total wavenumber k plot detailing the idealised schematic of geostrophic turbulence. Reproduced with permission from Wang (2014), their Fig. 5.5

where both of these cascades occur are inertial ranges, i.e. ranges in wavenumber space where energy is transported from one end of the range to the other without viscous dissipation occuring (i.e. a constant energy flux through the scales).

However, the geostrophic turbulence theory meets its limits even for the Earth atmosphere. Here the injection scale at the Rossby radius and the Rhines scale are located very close to one another, so that there is not enough room for an upscale inertial range to develop. This inhibition of upscale energy transfer is associated with a stabilisation of the thermal stratification due to baroclinic eddies (Schneider and Walker, 2006).

Other points of criticism of the geostrophic turbulence paradigm are that the barotropic inverse cascade may not be a cascade (in the sense that energy is transported from one wavenumber to the an adjacent one), but that this transport occurs via direct interaction between eddies and zonal flows. This "waterfall"-like process directly intensifies zonal jet flow even when truncating the intermediate scales between the Rossby deformation scale and the jet scale (Kaspi and Flierl, 2007). Another issue is that this upscale energy transport may not be singularly energised by the purely 2D barotropic mode but also by baroclinic modes (see e.g. Scott and Arbic, 2007, Thompson and Young, 2007).

At even smaller lengthscales (termed mesoscales), measurements of the Earth's atmosphere show another inertial range in the form of a $k^{-5/3}$ slope (Nastrom and

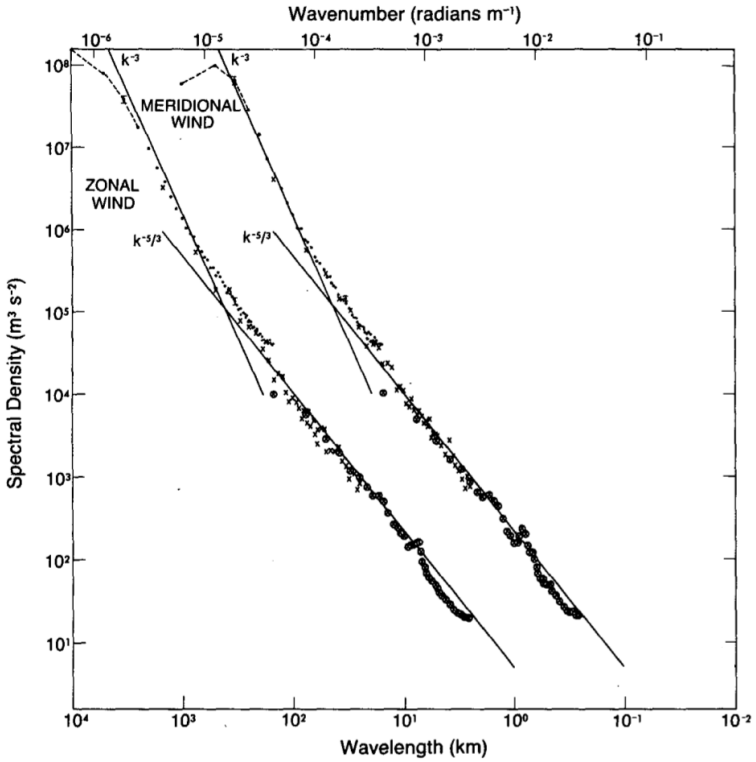

Figure 4.5: Mesoscale kinetic energy spectra of the Earth atmosphere from aircraft data, measured by. Adapted from Nastrom and Gage (1985), their Fig. 3

Gage, 1985). Fig. 4.5 shows measurements of the zonal and meridional spectral kinetic energy density. While the k^{-3}-slope at larger wavelengths[3] is generally accepted as representing the forward enstrophy cascade of geostrophic turbulence, the source and even the direction of energy transfer of the $k^{-5/3}$-slope in the spectral energy density at mesoscales is largely contested. While some propose an upscale energy cascade (e.g. Lilly, 1983), many others propose downscale cascades (e.g. Dewan, 1997, Tung and Orlando, 2003, Lindborg, 2006, Tulloch and Smith, 2009, Vallgren et al., 2011). The latter of which has some observational support from structure function calculations (Cho and Lindborg, 2001, Lindborg, 2015).

For planets other than Earth, atmospheric turbulence is less well understood, due to less available observations and less modelling efforts. Some studies (e.g. Schneider and Walker, 2006, Wang, 2014) investigate the turbulent behaviour of planets with Earth-like and faster rotation rates with simplified GCMs. Others simulate specific planets with more detailed models, to study energy spectra of e.g. Jupiter (Showman,

[3]With a planetary circumference of roughly $4 \cdot 10^5$ km the left edge of the plot at $\lambda = 1 \cdot 10^4$ km lies at a spherical total wavenumber of 40

2007, Schneider and Liu, 2008).

Other studies have used satellite-based cloud-top wind measurements (e.g. for Jupiter Choi and Showman, 2011, Galperin et al., 2014, Young and Read, submitted), lander measurements (for Mars (e.g. Lovejoy et al., 2014)), or reanalysis data (e.g. for Mars, Valeanu et al., 2017) to identify and interpret turbulence spectra in Solar system planets. Many questions regarding the turbulence in general planetary atmospheres are still unanswered. Are there inertial ranges on other planets? Is there downscale or upscale energy transport? Does this transport occur as a continuous flux between adjacent scales (cascade) or directly and non-locally between two separate scales (waterfall)? How is energy transported between scales when there is no inertial range present?

We first introduce the spectral energy budget formulation of Augier and Lindborg (2013) in Section 4.2.2. Then Section 4.3 aims to answer some of the above questions for a subset of PUMA-S simulations by Wang (2014), where the rotation rate is varied by factors between $\frac{1}{16}$ and 8 by characterising their spectral KE and APE fluxes. The spectral flux results of the PUMA-GT parameter study for slowly-rotating planets are presented and discussed in Section 5.6 for comparison.

4.2.2 Calculation of spectral flux budget

Augier and Lindborg (2013) have recently developed a scheme to calculate the full spectral energy budget of an atmosphere, including consideration of both available potential energy (APE) and kinetic energy (KE), vertical fluxes, the separate contributions of horizonally rotational and divergent flow, as well as surface topography. They show that high resolution reanalysis data for Earth has problems in recreating the measured spectral behaviour in the mesoscales. Below, the spectral energy budget scheme of Augier and Lindborg (2013) is detailed. We show formulae in the flat-surface approximation as our simplified simulations do not feature elevated terrain.

Energy budget

The dynamical equations of the atmosphere in pressure coordinates p can be written as (Augier and Lindborg, 2013):

$$\partial_t \boldsymbol{u} = -\boldsymbol{v} \cdot \boldsymbol{\Delta u} - f(\phi) e_z \wedge \boldsymbol{u} - \boldsymbol{\nabla}_h \Phi D_{\boldsymbol{u}}(\boldsymbol{u}) \tag{4.11}$$

$$\partial_t \theta' = -\boldsymbol{v} \cdot \boldsymbol{\theta'} - \omega \partial_p \langle\theta\rangle + Q_\theta - \partial_t \langle\theta\rangle + D_\theta(\theta) \tag{4.12}$$

where all variables are functions of t, λ, ϕ, p (time, longitude, latitude, and pressure, respectively) unless stated otherwise. Here $\boldsymbol{v} = (\boldsymbol{u}, \omega)$ is the velocity, where $\boldsymbol{u}$ is the horizontal velocity and ω the vertical velocity (with bold symbols denoting vectors). $\theta' = \theta - \langle\theta\rangle$ is the potential temperature fluctuation where $\theta = \Lambda(p)T$ is the potential temperature with $\Lambda(p) = (p_0/p)^\kappa$, $p_0 = 1$ bar, $\kappa = R/c_p \approx 2/7$ (R is the specific gas constant and c_p is the heat capacity at constant pressure). The operator $\langle\cdot\rangle$ is the horizontal mean (over one pressure level). In addition $f(\phi)$ is the Coriolis parameter, Φ is the geopotential, e_z is the unit vector in radial direction (upward), $D_{\boldsymbol{u}}(\boldsymbol{u})$ and $D_\theta(\theta)$ are diffusion terms, and Q_θ is a source term. The conservation of mass in p coordinates is $\boldsymbol{\Delta} \cdot \boldsymbol{v} = 0$ and the hydrostatic equation is given by $\partial_p \Phi = -\alpha_\rho = -RT/p$, where $\alpha_\rho = 1/\rho$ is the specific density and ρ is the density.

The kinetic energy E_K (KE) and available potential energy E_A (APE) of the atmosphere can be computed from

$$E_K(p) = \langle|\boldsymbol{u}|^2\rangle/2 \tag{4.13}$$

$$E_A(p) = \gamma(p)\langle\theta'^2\rangle/2 \tag{4.14}$$

$$\gamma(p) = R/[\Lambda(p) p \partial_p \langle\theta\rangle] \tag{4.15}$$

The energy budget of atmospheric KE and APE can be derived from combining Eqns. (4.13) and (4.14) with Eqns. (4.11) and (4.12)

$$\partial_t E_K(p) = C(p) + \partial_p F_{K\uparrow}(p) - D_K(p) + S(p) \tag{4.16}$$

$$\partial_t E_A(p) = G(p) - C(p) + \partial_p F_{A\uparrow}(p) - D_A(p) + J(p) \tag{4.17}$$

Here $G(p)$ is an APE generation term due to e.g. differential heating, $C(p)$ is the conversion from APE to KE, $F_{K\uparrow}(p)$ and $F_{A\uparrow}(p)$ are vertical fluxes of KE and APE, respectively, and $D_K(p)$, $D_A(p)$ are diffusion terms with:

$$G(p) = \gamma\langle\theta' Q'_\theta\rangle \tag{4.18}$$

$$C(p) = -\langle\omega\alpha_\rho\rangle \tag{4.19}$$

$$F_{A\uparrow}(p) = -\gamma(p)\langle\omega\theta'^2\rangle/2 \tag{4.20}$$

$$F_{K\uparrow}(p) = -\langle\omega|\boldsymbol{u}|^2\rangle/2 - \langle\omega\Phi\rangle \tag{4.21}$$

$$S(p) = -\langle\delta_{ps}\partial_t(p_s\Phi_s)\rangle \tag{4.22}$$

$$J(p) = -(\partial_p\gamma)\langle\omega\theta'^2\rangle/2 - \langle\omega\rangle\langle\alpha_\rho\rangle \tag{4.23}$$

where p_s and Φ_s are surface pressure and surface geopotential, respectively, and δ_{ps} is one when $p = p_s$ and zero otherwise. The $S(p)$ and $J(p)$ terms are adiabatic processes, which do not conserve total available energy $E_K + E_A$. However, these terms have been shown to be negligible in the global mean (Siegmund, 1994, Augier and Lindborg, 2013), and will not be considered in further equations.

‘

Spherical harmonic transformation

A scalar function (e.g. θ') on a sphere can be transformed into spherical harmonic spectral space via

$$\theta'(\boldsymbol{x}_h, p) = \sum_{k\geq 0}\sum_{-k\leq m\leq k}\theta'_{km}(p)Y_{km}(\boldsymbol{x}_h) \tag{4.24}$$

where k is the total and m is the zonal wavenumber. Y_{km} are spherical eigenfunctions (see Eqn. 3.13) with $\nabla_h^2 Y_{km} = -\frac{k(k+1)}{a^2}Y_{km}$. The horizontal mean of the product of two scalar variables is then

$$\langle\omega\Phi\rangle = \sum_{k\geq 0}\sum_{-k\leq m\leq k}(\omega,\Phi)_{km} \tag{4.25}$$

where

$$(\omega, \Phi)_{km} = \mathrm{Re}\{\omega^*_{km}\Phi_{km}\} \tag{4.26}$$

where $\mathrm{Re}\{X\}$ is the real part and X^* is the complex conjugate of a complex number X (Augier and Lindborg, 2013).

For vector fields (e.g. the horizontal velocity field $\boldsymbol{u}$) a decomposition into divergent and rotational (non-divergent) components can be performed via the Helmholtz decomposition

$$\boldsymbol{u} = \boldsymbol{\nabla}_h \wedge (\psi e_z) + \boldsymbol{\nabla}_h \chi \tag{4.27}$$

with the horizontal streamfunction $\psi(\boldsymbol{x}_h, p)$ and the horizontal velocity potential $\chi(\boldsymbol{x}_h, p)$. Using this decomposition we can obtain the vorticity ζ and the horizontal divergence d:

$$\zeta = \mathrm{rot}_h\,(\boldsymbol{u}) = e_z \cdot (\boldsymbol{\nabla} \wedge \boldsymbol{u}) = \boldsymbol{\nabla}_h^2 \psi \tag{4.28}$$

$$d = \mathrm{div}_h\,(\boldsymbol{u}) = \boldsymbol{\nabla}_h \cdot \boldsymbol{u} = \boldsymbol{\nabla}_h^2 \chi. \tag{4.29}$$

This decomposition is then used to calculate the horizontal mean of a scalar product between two horizontal vector fields $\boldsymbol{a}$ and $\boldsymbol{b}$

$$\langle \boldsymbol{a} \cdot \boldsymbol{b} \rangle = \sum_{k \geq 0} \sum_{-k \leq m \leq k} (\boldsymbol{a}, \boldsymbol{b})_{km} \tag{4.30}$$

with

$$(\boldsymbol{a}, \boldsymbol{b})_{km} = \frac{a^2}{k(k+1)} \mathrm{Re}\{\mathrm{rot}_h\,(\boldsymbol{a})^*_{km} \mathrm{rot}_h\,(\boldsymbol{b})_{km} + \mathrm{div}_h\,(\boldsymbol{a})^*_{km} \mathrm{div}_h\,(\boldsymbol{b})_{km}\}. \tag{4.31}$$

Using Eqn. 4.25 for scalars and Eqn. 4.30 for vector fields, the spectral versions of APE and KE can be obtained:

$$E_A^{km} = \gamma(p) \frac{(\theta', \theta')_{km}}{2} = \gamma(p) \frac{|\theta'_{km}(p)|^2}{2} \tag{4.32}$$

$$E_K^{km} = \frac{(\boldsymbol{u}, \boldsymbol{u})_{km}}{2} = \frac{a^2(|\zeta_{km}|^2 + |d_{km}|^2)}{2k(k+1)} \tag{4.33}$$

Spectral energy budget

Inserting Eqn. 4.32 and Eqn. 4.33 into Eqns. 4.16 and 4.17 results in (Augier and Lindborg, 2013):

$$\partial_t E_K^{km}(p) = C^{km}(p) + T_K^{km}(p) + L^{km}(p) + \partial_p F_{K\uparrow}^{km}(p) - D_K^{km}(p) \tag{4.34}$$

$$\partial_t E_A^{km}(p) = G^{km}(p) - C^{km}(p) + T_A^{km}(p) + \partial_p F_{A\uparrow}^{km}(p) - D_A^{km}(p). \tag{4.35}$$

where G^{km} is the spectral APE generation term, C^{km} is the spectral conversion term, T_K^{km} and T_A^{km} are the spectral transfer terms (of KE and APE, respectively) due to non-linear interactions. L^{km} is a spectral transfer term due to Coriolis forces and $F_{K\uparrow}^{km}$ and $F_{A\uparrow}^{km}$ are vertical fluxes. D_K^{km} and D_A^{km} are diffusion terms. These terms are computed via

$$C^{km}(p) = -(\omega, \alpha_\rho)_{km} \tag{4.36}$$

$$T_K^{km}(p) = -(\boldsymbol{u}, \boldsymbol{v} \cdot \boldsymbol{\nabla} \boldsymbol{u})_k m + \partial_p(\boldsymbol{u}, \omega \boldsymbol{u})_{km}/2 \tag{4.37}$$

$$T_A^{km}(p) = -\gamma(\theta', \boldsymbol{v} \cdot \nabla\theta')_{km} + \gamma\partial_p(\theta', \omega\theta')_{km}/2 \tag{4.38}$$

$$L^{km}(p) = -(\boldsymbol{u}, f[\phi] e_z \wedge \boldsymbol{u})_{km} \tag{4.39}$$

$$F_{A\uparrow}^{km}(p) = -\gamma(\theta', \omega\theta')_{km}/2 \tag{4.40}$$

$$F_{K\uparrow}^{km}(p) = -(\omega, \Phi)_{km} - \partial_p(\boldsymbol{u}, \omega\boldsymbol{u})_{km}/2 \tag{4.41}$$

$$G^{km}(p) = \gamma(\theta', Q'_\theta)_{km} \tag{4.42}$$

$$D_A^{km}(p) = -\gamma(\theta', D_\theta[\theta])_{km}. \tag{4.43}$$

Wavenumber summation and vertical integration

The spectral energy and tendency terms obtained in the previous sections are functions of time, zonal wavenumber m, total wavenumber k, and pressure p. To obtain a one dimensional spectrum or spectral flux from these terms, a dependence upon k alone would be ideal. The time dependency is removed by averaging the resulting spectral

quantities over multiple time steps. Following a summation over zonal wavenumbers and a vertical integration over a pressure range from p_b to p_t, the vertically integrated KE spectrum is obtained via

$$E_K[k]_{p_t}^{p_b} = \int_{p_t}^{p_b} \frac{dp}{g} \sum_{-k \leq m \leq k} E_K^{km}(p) \tag{4.44}$$

and the vertically integrated KE spectral flux via

$$\Pi_K[k]_{p_t}^{p_b} = \sum_{n \geq k} \int_{p_t}^{p_b} \frac{dp}{g} \sum_{-n \leq m \leq n} T_K^{nm}(p) \tag{4.45}$$

where $\sum_{n \geq k} \sum_{-n \leq m \leq n}$ denotes a cumulative sum (from large to small wavenumbers). Other spectral quantities can be similarly vertically integrated and summed so that in total Eqns. 4.16 and 4.17 become

$$\partial_t \mathcal{E}_A[k]_{p_t}^{p_b} = \mathcal{C}[k]_{p_t}^{p_b} + \Pi_K[k]_{p_t}^{p_b} + \mathcal{L}[k]_{p_t}^{p_b} + \mathcal{F}_{K\uparrow}[k](p_b) - \mathcal{F}_{K\uparrow}[k](p_l) - \mathcal{D}_K[k]_{p_t}^{p_b} \tag{4.46}$$

$$\partial_t \mathcal{E}_K[k]_{p_t}^{p_b} = \mathcal{G}[k]_{p_t}^{p_b} - \mathcal{C}[k]_{p_t}^{p_b} + \Pi_A[k]_{p_t}^{p_b} + \mathcal{F}_{A\uparrow}[k](p_b) - \mathcal{F}_{A\uparrow}[k](p_t) - \mathcal{D}_A[k]_{p_t}^{p_b} \tag{4.47}$$

where $\mathcal{F}_\uparrow[k](p) = \sum_{n \geq k} F_\uparrow[n]$ are termed cumulative vertical fluxes and the other terms are integrated cumulative fluxes of the terms detailed in the previous section (e.g. cumulative kinetic energy $\mathcal{E}_K[k]_{p_t}^{p_b} = \sum_{n \geq k} E_K[n]_{p_t}^{p_b}$ and cumulative conversion $\mathcal{C}[k]_{p_t}^{p_b} = \sum_{n \geq k} C[n]_{p_t}^{p_b}$). Note that the cumulative summation is performed from large wavenumbers to small wavenumbers and that all spectral fluxes (barring conversion and vertical fluxes) are conserved, meaning the cumulative sum adds up to zero.

4.3 Spectral energy budget for varying rotation rates

In this section, we present energy spectra and spectral fluxes of PUMA-S simulations performed by Wang (2014). He focussed on understanding the jet formation mechanism for runs with $\Omega = 1, 4, 8\Omega_E$, using kinetic energy spectra and spectral fluxes of eddy kinetic energy and enstrophy. He identified behaviour consistent with zonostrophic turbulence in simulations with $\Omega = 1 - 8\Omega_E$ and 200 times weaker friction (not shown).

The current work does not aim to repeat this study, but instead provide a more de-

Variable	Formula	Description
$E_K^{km}(p)$	Eqn. 4.34	spectral kinetic energy (KE)
$E_A^{km}(p)$	Eqn. 4.35	spectral available potential energy (APE)
$C^{km}(p)$	Eqn. 4.36	spectral conversion rate from APE to KE
$T_K^{km}(p)$	Eqn. 4.37	spectral transfer rate of KE due to non-linear interactions
$T_A^{km}(p)$	Eqn. 4.38	spectral transfer rate of APE due to non-linear interactions
$L^{km}(p)$	Eqn. 4.39	spectral transfer rate due to Coriolis forces
$F_{A\uparrow}^{km}(p)$	Eqn. 4.40	spectral vertical transport rate of KE
$F_{K\uparrow}^{km}(p)$	Eqn. 4.41	spectral vertical transport rate of APE
$G^{km}(p)$	Eqn. 4.42	spectral generation rate of APE
$D^{km}(p)$	Eqn. 4.43	spectral diffusion rate of APE/KE
$E_K[k]_{p_t}^{p_b}$	$= \int_{p_t}^{p_b} \frac{dp}{g} \sum_{-k\leq m\leq k} E_K^{km}(p)$	vertically integrated KE spectrum
$E_A[k]_{p_t}^{p_b}$	$= \int_{p_t}^{p_b} \frac{dp}{g} \sum_{-k\leq m\leq k} E_A^{km}(p)$	vertically integrated APE spectrum
$C[k]_{p_t}^{p_b}$	$= \int_{p_t}^{p_b} \frac{dp}{g} \sum_{-k\leq m\leq k} C^{km}(p)$	vertically integrated conversion rate tendency
$T_K[k]_{p_t}^{p_b}$	$= \int_{p_t}^{p_b} \frac{dp}{g} \sum_{-k\leq m\leq k} T_K^{km}(p)$	vertically integrated non-linear KE spectral tendency
$T_A[k]_{p_t}^{p_b}$	$= \int_{p_t}^{p_b} \frac{dp}{g} \sum_{-k\leq m\leq k} T_A^{km}(p)$	vertically integrated non-linear APE spectral tendency
$L[k]_{p_t}^{p_b}$	$= \int_{p_t}^{p_b} \frac{dp}{g} \sum_{-k\leq m\leq k} L^{km}(p)$	vertically integrated Coriolis KE spectral tendency
$F_{A\uparrow}[k](p)$	$= \sum_{-k\leq m\leq k} F_{A\uparrow}^{km}(p)$	spectral tendency of vertical APE transport
$F_{K\uparrow}[k](p)$	$= \sum_{-k\leq m\leq k} F_{K\uparrow}^{km}(p)$	spectral tendency of vertical KE transport
$G[k]_{p_t}^{p_b}$	$= \int_{p_t}^{p_b} \frac{dp}{g} \sum_{-k\leq m\leq k} G^{km}(p)$	vertically integrated APE generation spectral tendency
$D[k]_{p_t}^{p_b}$	$= \int_{p_t}^{p_b} \frac{dp}{g} \sum_{-k\leq m\leq k} D^{km}(p)$	vertically integrated KE/APE diffusion spectral tendency
$\mathcal{E}_K[k]_{p_t}^{p_b}$	$= \sum_{n\geq k} E_K[n]_{p_t}^{p_b}$	vertically integrated cumulative KE spectrum
$\mathcal{E}_A[k]_{p_t}^{p_b}$	$= \sum_{n\geq k} E_A[n]_{p_t}^{p_b}$	vertically integrated cumulative APE spectrum
$\mathcal{C}[k]_{p_t}^{p_b}$	$= \sum_{n\geq k} C[n]_{p_t}^{p_b}$	vertically integrated cumulative conversion rate
$\Pi_K[k]_{p_t}^{p_b}$	$= \sum_{n\geq k} T_K[n]_{p_t}^{p_b}$	vertically integrated non-linear KE spectral flux
$\Pi_A[k]_{p_t}^{p_b}$	$= \sum_{n\geq k} T_A[n]_{p_t}^{p_b}$	vertically integrated non-linear APE spectral flux
$\mathcal{L}[k]_{p_t}^{p_b}$	$= \sum_{n\geq k} L[n]_{p_t}^{p_b}$	vertically integrated Coriolis KE spectral flux
$\mathcal{F}_{A\uparrow}[k](p)$	$= \sum_{n\geq k} F_{A\uparrow}[n](p)$	cumulative vertical spectral flux of KE
$\mathcal{F}_{K\uparrow}[k](p)$	$= \sum_{n\geq k} F_{K\uparrow}[n](p)$	cumulative vertical spectral flux of KE
$\mathcal{G}[k]_{p_t}^{p_b}$	$= \sum_{n\geq k} G[n]_{p_t}^{p_b}$	vertically integrated cumulative generation rate of APE
$\mathcal{D}[k]_{p_t}^{p_b}$	$= \sum_{n\geq k} D[n]_{p_t}^{p_b}$	vertically integrated cumulative diffusion rate of KE/APE

Table 4.1: Comprehesive table of spectral variables. Top: variables in spherical harmonics (total wavenumber k and zonal wavenumber m), middle: variables as a function of total wavenumber k (summation over zonal wavenumber m), bottom: variables as a cumulative sum over total wavenumber k (summation from large to small values of k).

tailed view of the general spectral transfer pathways within our simulated atmospheric circulations across a range of parameter space, using the spectral energy budget formulation of Augier and Lindborg (2013).

Using the spectral energy budget, we can answer the question of how the energy of macroturbulent fluid motion is transported between scales and converted between APE and KE. More specifically, we are interested at which scale kinetic energy is inserted into the system and where this energy ends up. Two modes of transfer between scales are possible, which are termed cascades and waterfalls. Cascading flux is spectrally local, meaning it transfers energy from one to an adjacent scale. In contrast, waterfalls directly transfers energy from one scale to another across large wavenumber intervals (i.e. the spectral flux is non-local). This can occur, for instance between an arbitrary wavenumber and the zonal flow.

To identify this interaction between eddies and the zonal flow we perform a zonal-mean eddy decomposition. This decomposition is achieved by using the eddy component (via $X_{eddy} = X - [X]$, where $[\cdot]$ denotes the zonal mean) of each input variable (i.e. u, v, ω, Φ, T) to recalculate the eddy component of the spectral fluxes. The zonal component is then obtained as the residual between the eddy component and the total flux. For spectral fluxes, the "eddy" component encompasses eddy-eddy interactions, while the "zonal" component consists of residual interactions with the zonal mean flow (i.e. eddy-zonal and zonal-zonal interactions). In the text below the terms wavenumber, total wavnumber and k are used synonymously.

4.3.1 Energy spectra of PUMA-S runs

Figure 4.6 shows the KE and APE spectra of simulations with $1\Omega_E \leq \Omega \leq 8\Omega_E$. These simulation were performed at T170 resolution (except for the $\Omega^* = 1$ simulation at T127). The Earth-like run at Ω_E (Figure 4.6a) possesses a k^{-3} slope between wavenumbers 20 and 90 as well as a fairly consistent k^{-5} slope in the zonal component. It is interesting to note that both KE and APE behave fairly similarly in this region. At smaller wavenumbers the zonal component dominates while at larger wavenumbers the eddy component is largers. With rising rotation rate (see Figs. 4.6b-d) the maximum of the eddy component moves to higher wavenumbers and the k^{-3} slope that could

a) $\Omega^* = 1$, T127 Resolution

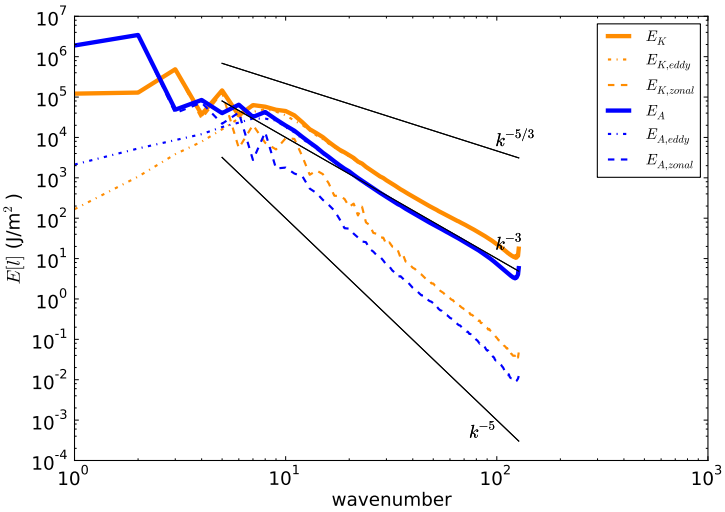

b) $\Omega^* = 2$, T170 Resolution

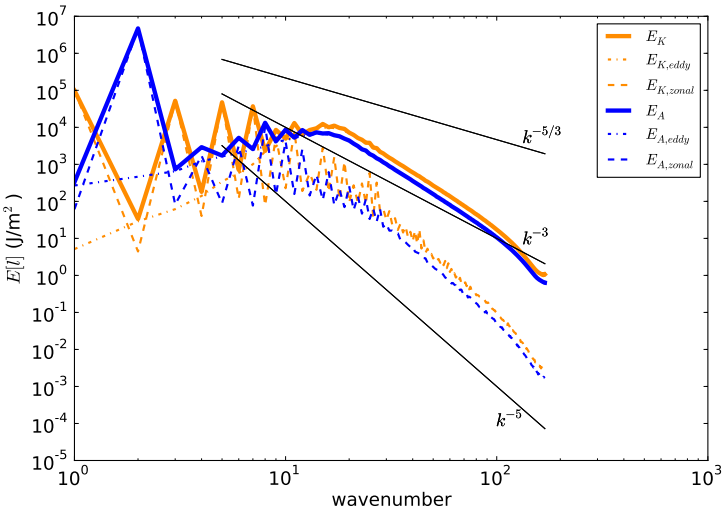

c) $\Omega^* = 4$, T170 Resolution

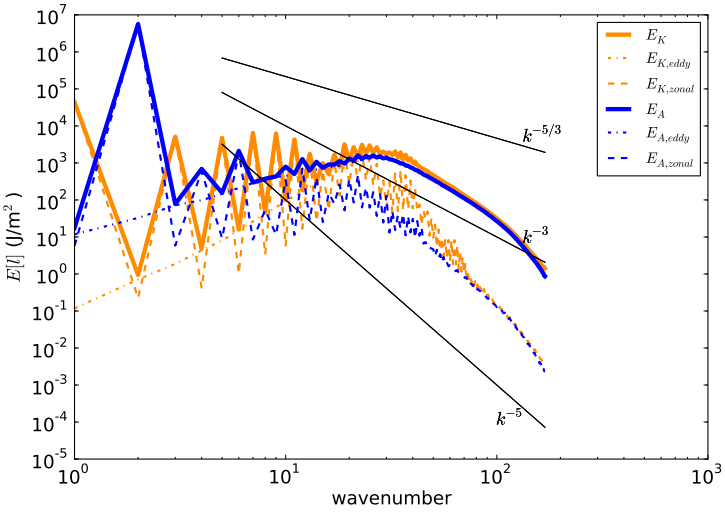

d) $\Omega^* = 8$, T170 Resolution

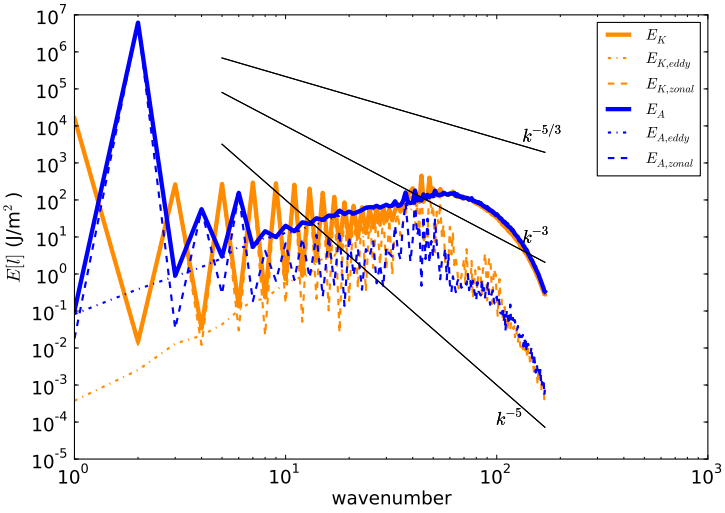

Figure 4.6: KE (orange) and APE (blue) spectra (each decomposed into zonal and eddy components) for PUMA-S runs with $\Omega = 1, 2, 4, 8\Omega_E$ at resolutions T127, T170.

be so well identified at $\Omega^* = 1$ becomes slanted towards a more steeper slope at higher wavenumbers, likely due to the effect of the model-inherent hyperdiffusion (see Sect. 3.1.1). Consequently, the region in which a k^{-3} slope can be discerned becomes smaller and smaller. Wang (2014) calculated the spectral enstrophy flux (see Burgess et al., 2013) for the Ω_E simulations to show that the k^{-3} slope is indeed consistent with a downscale eddy enstrophy flux and an inertial range.

The same hyperdiffusion effect can be identified for the k^{-5} slope of the zonal component. The k^{-5} slope is discussed by Wang (2014), who mention that Rhines (1975) prediced an k^{-5} energy slope near the Rhines scale. However, in our (and Wang's) cases the k^{-5} slope extends down to the smallest modeled scales. When including the β-effect, the Rayleigh-Kuo criterion, one of the necessary criteria for baroclinic instability, is expanded from $\frac{\partial^2}{\partial y^2}u = 0$ to $\beta - \frac{\partial^2}{\partial y^2}u = 0$. This enables the atmosphere to remain stable even for inflection points in the zonal wind velocity (i.e. $\frac{\partial^2}{\partial y^2}u = 0$). Wang (2014) argues that this allows more energy to be stored in the zonal energy component at smaller scales (Huang et al., 2001). Overall, however, the slope of zonal kinetic energy spectrum is not well understood. Nevertheless, our work can report that the zonal component of the APE spectrum has the same slope.

There is a sawtooth-like pattern of alternating intensity of the spectral energy in the zonal component for both APE and KE. This was also observed by Wang (2014), who produced this dataset. The sawtooth pattern is an effect of the symmetry of the diagnostic fields about the equator, which cause extinction in every second total wavenumber of spherical harmonic space (Wang et al., in prep.b). To test this, Wang (2014) performed certain simulation with permanent January forcing. One of these is shown in our dataset in the simulation with $\Omega^* = 1$ in T127 resolution (Fig. 4.6a). The energy spectrum of this case does not feature a sawtooth pattern. Performing further simulations of the other rotation rates at permanent January forcing is outside the scope of this work.

The energy spectra for lower rotation rates are shown in Fig. 4.7. Here we show a low resolution simulation at $\Omega^* = 1$ at T42 to provide a better comparison with the other spectra. When comparing Fig. 4.7a with its higher resolution version in Fig. 4.6a, it is apparent that low resolution simulations do not properly convey the slopes iden-

a) $\Omega^* = 1$, T42 Resolution

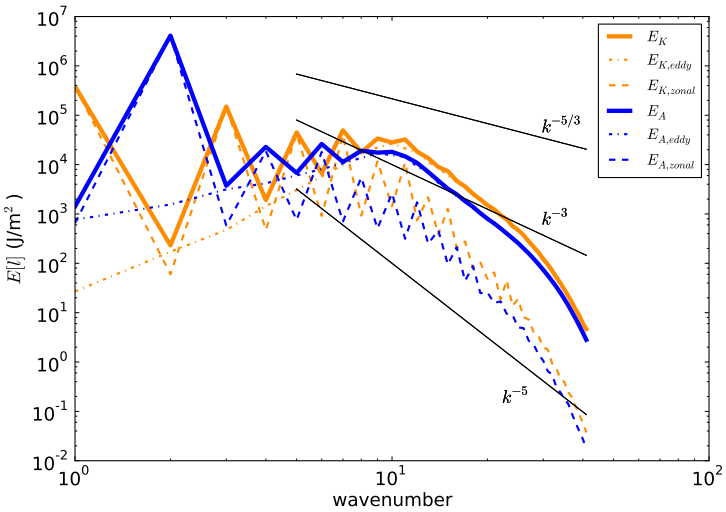

b) $\Omega^* = \frac{1}{2}$, T42 Resolution

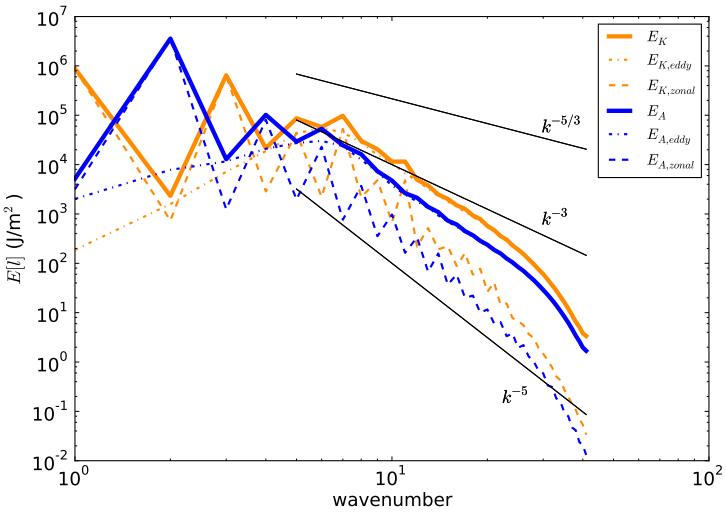

c) $\Omega^* = \frac{1}{4}$, T42 Resolution

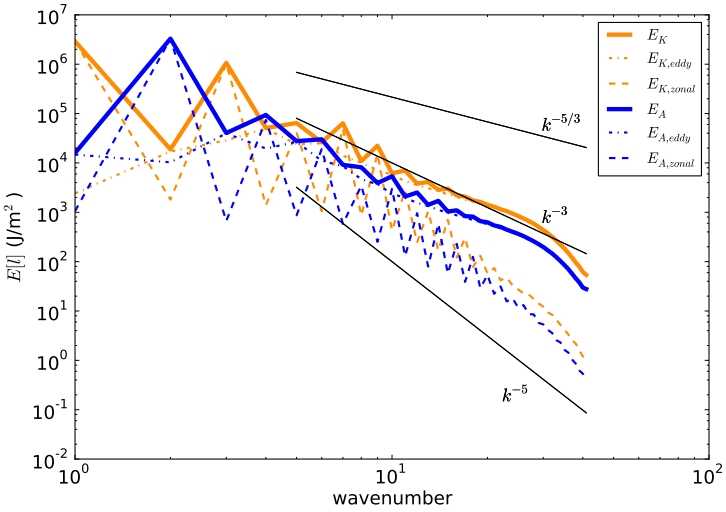

d) $\Omega^* = \frac{1}{8}$, T42 Resolution

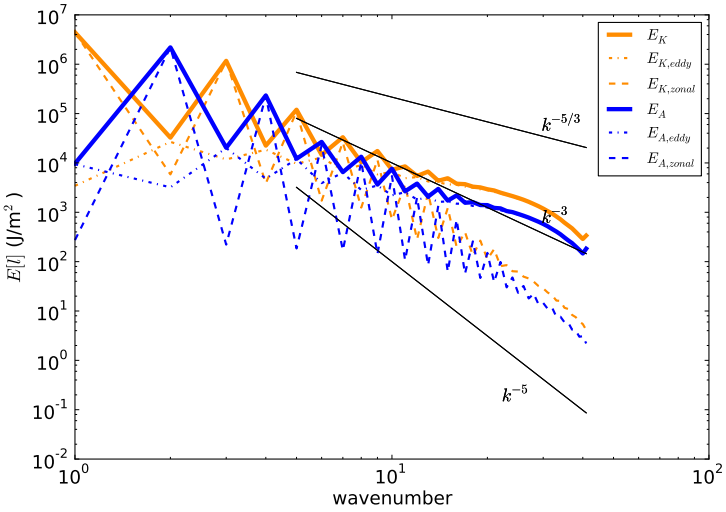

e) $\Omega^* = \frac{1}{16}$, T42 Resolution

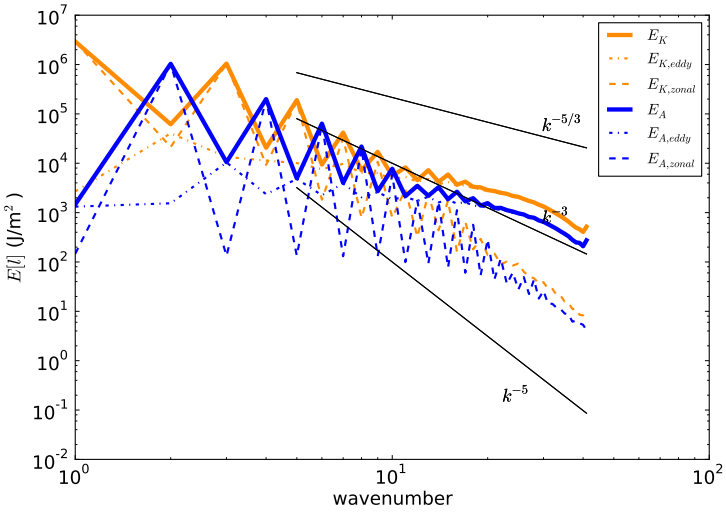

Figure 4.7: KE (orange) and APE (blue) spectra (each decomposed into zonal and eddy components) for PUMA-S runs with $\Omega = 1, \frac{1}{2}, \frac{1}{4}, \frac{1}{8}, \frac{1}{16}\Omega_E$ at T42 resolution.

tified above, due to the hyperdiffusion acting at larger scales (smaller wavenumbers). Nevertheless, as will be shown in the next section, spectral fluxes of both $\Omega^* = 1$ simulations are qualitatively similar. In this respect, the spectral fluxes presented below are more helpful in identifying and characterising turbulent behaviour, as opposed to the slopes in the energy spectra of Figs. 4.6 and 4.7. With that said a quick glance at Figs. 4.7a-e shows that with decreasing rotation rate, the slopes of the energy spectra become flatter and approach a $k^{5/3}$ slope. The change in slope may indicate a different kind of turbulent regime, which we investigate in the following sections using the spectral flux diagnostics. In addition, the zonal components of the energies continue to show a k^{-5} slope for certain ranges in wavenumber space.

4.3.2 Spectral fluxes

Identifying the spectral transfer and inertial ranges of atmospheric energy by the slope of its spectral decomposition is an important tool in characterising the macroturbulent behaviour of an atmosphere. This is done by e.g. identifying scaling laws that point towards a specific theory of macroturbulence. However, this method alone is inaccurate, because the slope alone does not provide information about the direction of the flux. There may exist an external influence (e.g. the dissipative effect in our low resolution simulations) that alters the scaling law of an inertial range into an indiscernable slope, or there may not exist an inertial range at all. In these cases, fluxes between length-scales can still occur and are identifiable by calculating either structure functions or spectral fluxes. In this section, we calculate and discuss spectral fluxes of PUMA-S simulations with varying Ω using the spectral energy budget formulation presented above.

Spectral fluxes of rapidly-rotating planets

Figure 4.8 shows spectral fluxes for KE (Π_K), APE (Π_A), and the total energy $\Pi = \Pi_K + \Pi_K$ as well as the cumulative conversion $\mathcal{C}$ from APE to KE for simulations with $\Omega = 1, 2, 4, 8\Omega_E$. In addition, the fluxes were decomposed into eddy-eddy ("eddy") and residual zonal ("zonal") interaction components. The terms presented here are integrated over the whole pressure range of the simulated atmospheres (see Section 4.2.2).

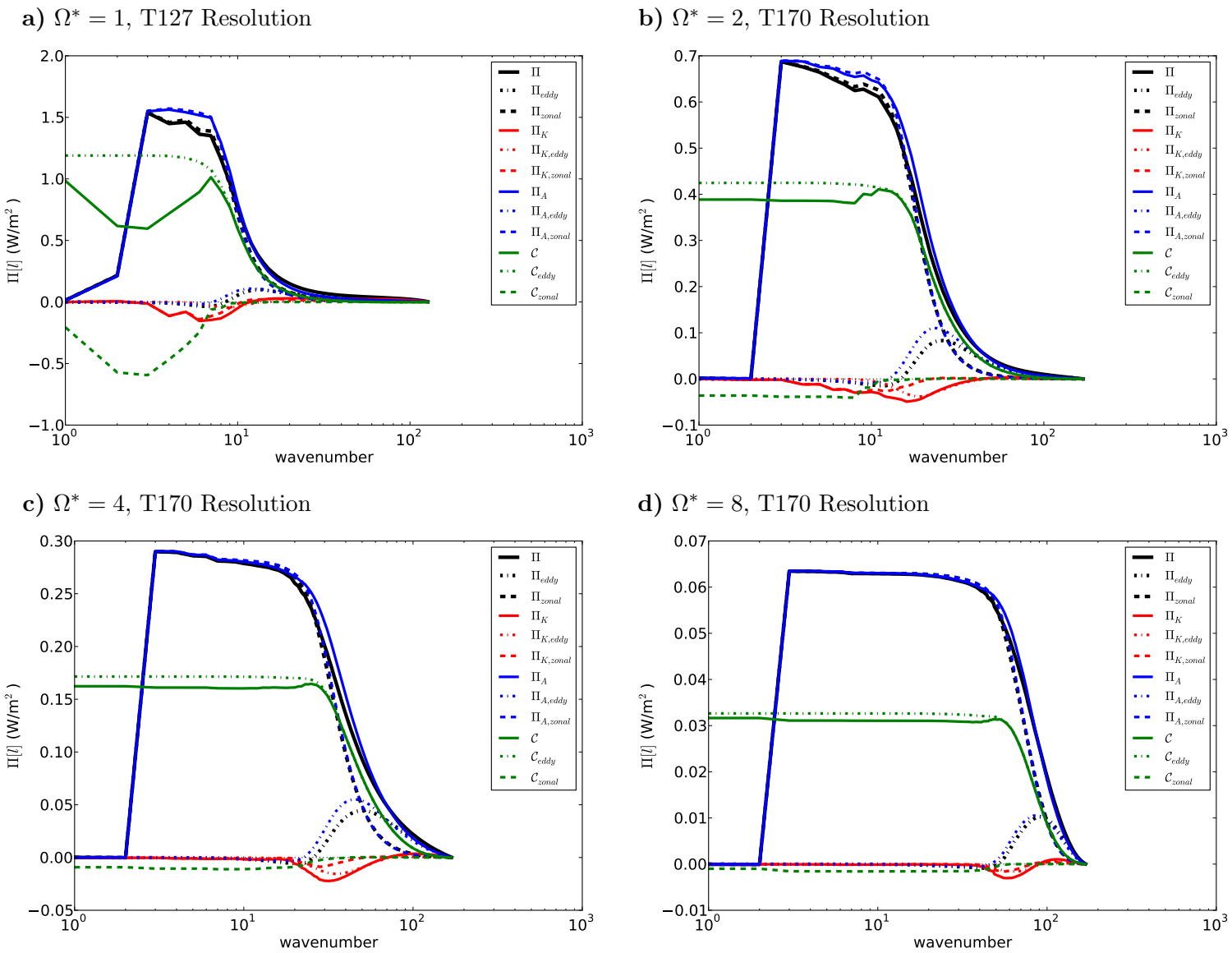

Figure 4.8: Spectral fluxes of KE Π_K, APE Π_A and total energy $\Pi = \Pi_A + \Pi_K$ as well as conversion $\mathcal{C}$ (each decomposed into eddy-eddy and residual zonal interaction components) for PUMA-S runs with $\Omega = 1, 2, 4, 8\Omega_E$ at resolutions T127, T170.

The figure shows that the total energy flux Π is always positive, signifying a downscale transfer (towards higher wavenumbers) of energy. For the Earth equivalent simulation at $\Omega^* = 1$ (Fig. 4.8a) the total flux Π (black solid line) rises sharply at wavenumbers 2 and 3 to a value of 1.6 W/m^2, stays roughly constant until wavenumber 7 and then falls rapidly between wavenumbers 8 and 12 and is then decreasing more slowly towards zero at the highest wavenumbers. Π has two components of which the APE component Π_A dominates over the KE component up to a wavenumber of 50. Because of its larger magnitude, the trend of the APE flux Π_A is similar to that of Π, except that its slope at the "constant" region between wavenumbers 3 and 8 is less steep. This difference between Π and Π_A is the result of an upscale (towards lower wavenumbers) energy transfer of the KE spectral flux Π_K between wavenumbers 3 and 10. At around wavenumber 11 there is an inflection point in the KE spectrum where Π_K changes signs. This implies that kinetic energy is being transported towards smaller scales (i.e. larger wavenumbers) for wavenumbers > 10 and towards larger scales for wavenumbers < 10. In this region, $\mathcal{C}$ has a steep slope. Being the cumulative term (c.f. Eqn. 4.45), a strong slope in $\mathcal{C}$ denotes a conversion of

$$C = \mathcal{C}(k = 15) - \mathcal{C}(k = 7) = 0.9\,\mathrm{Wm}^{-2}, \tag{4.48}$$

APE to KE in this wavenumber range.

Regarding eddy-eddy and residual zonal components, zonal components dominate Π_K and Π_A at smaller wavenumbers (1-20) and eddy-eddy components gain relative importance at the larger wavenumber regime (> 20), where the total fluxes are relatively low. On the other hand, the main component of the conversion term $\mathcal{C}$ occurs in the eddy component. Taking all of these points together the Earth-like case is evidently consistent with the defining behaviour of idealized baroclinic turbulence (see e.g. Vallis, 2006). At the injection wavenumber (around the Rossby deformation radius), APE is converted into KE via the eddy component of C (which is similar to the baroclinic C_E values of the Lorenz energy budget, Fig. 4.2). The resulting KE is transported mostly upscale in the zonal component by inverse barotropic conversion (see C_K in Lorenz budget), with a smaller amount of KE being transported downscale

where the eddy-eddy interaction component dominates (c.f. Fig 4.9a).

At smaller wavenumbers, there is a non-zero zonal component in $\mathcal{C}$. The total sum of $\mathcal{C}_{\ddagger\wr\backslash\dashv\updownarrow}$ (which is shown at wavenumber $k = 1$) is comparable to C_Z in the Lorenz energy budget (Fig. 4.2).[4] This conversion shows that negative C_Z occurs from wavenumbers 4-7 and positive C_Z at the smallest wavenumbers. It is likely that the zonal-zonal components dominate at low wavenumbers and zonal-eddy components at higher wavenumbers.

When considering that spectral regions with constant spectral flux Π_K are defined as inertial ranges, two such regions can be discerned. Firstly, the region between wavenumbers 3 and 8 where Π_A is constant (and Π and Π_K are almost constant) may describe an inertial range characterised by a forward baroclinic APE transport and an inverse barotropic KE transport. The second region lies at about $k = 20 - 80$ (see Fig 4.9a for a close-up of Π_K) with both forward APE and KE cascades. The second wavenumber region can be identified with the region in the energy spectrum where the k^{-3} slope in Fig. 4.6a. Both of these inertial ranges occur in the zonal-eddy component, which means that energy jumps directly between the zonal wind and the significant wavenumbers (more like a "waterfall" than a "cascade"). This means that the identified inertial ranges are not so much scales at which no dissipation occurs while cascading, but rather scales where no interaction between the zonal flow and the respective eddy-scale occurs.

With increasing rotation rate (Figs. 4.8b-d) the Rossby deformation radius decreases so that the wavenumber at which baroclinic conversion occurs increases with it. At $\Omega^* \geq 2$, the KE inertial range at large wavenumbers can no longer be discerned because it closes in on the resolution cut-off at wavenumber 170 and the corresponding hyperdiffusion at intermediate lengthscales. However, the inertial range in the APE flux widens and flattens with increasing rotation rate in a region that corresponds to a positive slope in the energy spectra (Figs. 4.6b-d).

Figure 4.9 shows the spectral kinetic energy flux for simulations with $\Omega^* = 1, 2, 4, 8$ in detail. For $\Omega^* = 1$ (Fig. 4.9a) we can see that the energy injected at the Rossby deformation lengthscale is transported both upscale and downscale (red solid line).

[4]Note that the data for the $\Omega^* = 1$ plot in Fig. 4.2 come from the run with T42 resolution.

a) $\Omega^* = 1$, T127 Resolution

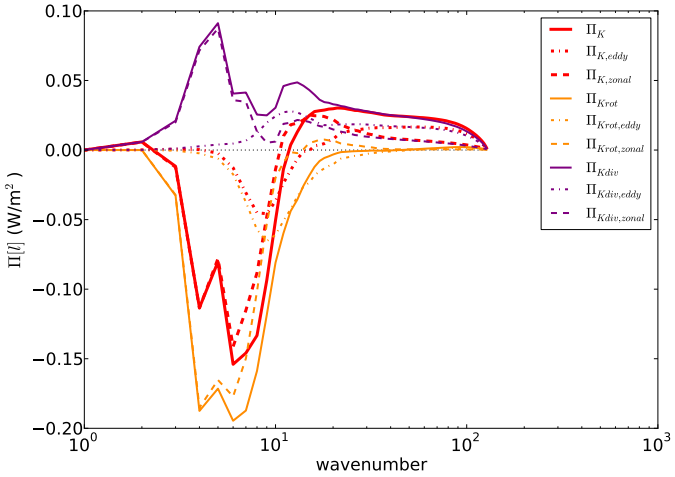

b) $\Omega^* = 2$, T170 Resolution

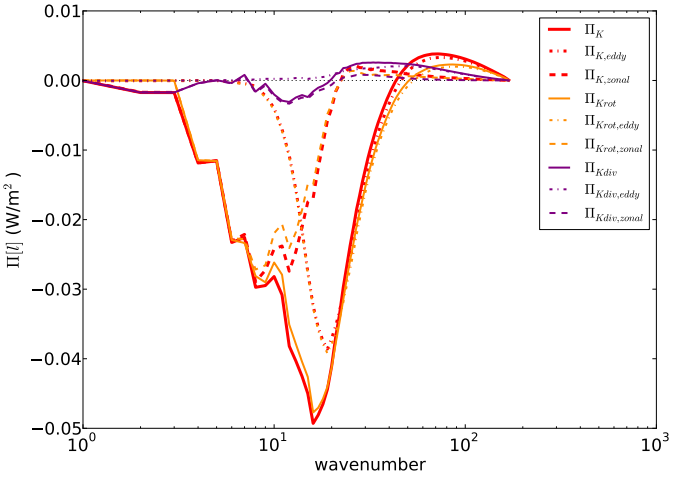

c) $\Omega^* = 4$, T170 Resolution

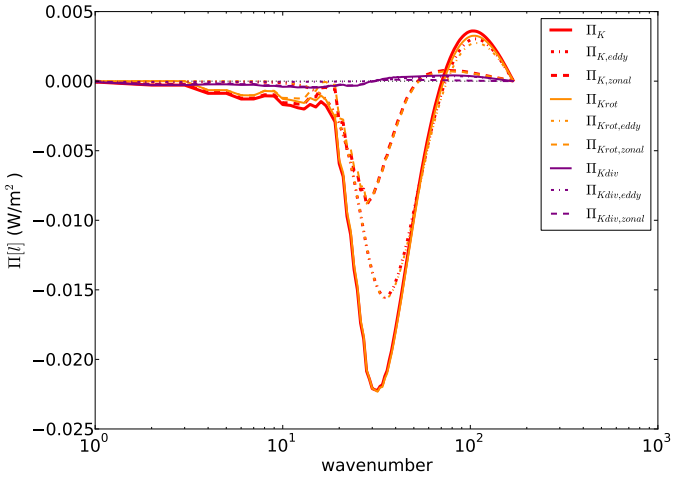

d) $\Omega^* = 8$, T170 Resolution

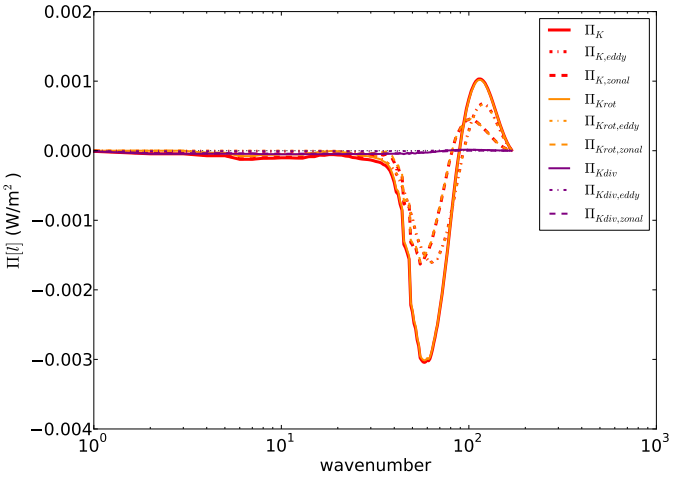

Figure 4.9: Spectral fluxes of KE Π_K, decomposed into divergent and rotational component (each decomposed into eddy-eddy and residual zonal interaction components) for PUMA-S runs with $\Omega = 1, 2, 4, 8\Omega_E$ at resolutions T127, T170.

The upscale component can be identified with an upscale barotropic transfer which is dominated by the zonal interaction component. In this case a further decomposition into a rotational and a divergent component of the KE flux has been performed (c.f. Augier and Lindborg, 2013, their Fig. 1). This separation can give information between the type of wave present in the atmosphere. For example, a pure Rossby wave only has a rotational component and a pure gravity wave would only have a divergent component. We find that the purely rotational component of the flux provides an approximately flat slope at the range of upscale transfer (wavenumbers 3-8), which makes this component an inertial range. However, the total KE flux at this range is offset by a downscale divergent component. In addition, this region is dominated by zonal interactions. For the downscale flux at larger wavenumbers (10-100) the divergent part of the flux becomes negligible and only the rotational part contributes towards the total KE flux. In this range the flux is influenced by both the zonal and eddy-eddy interaction terms. This means that our simulation at $\Omega^* = 1$ has both rotational and divergent waves.

With increasing rotation rate (Figs. 4.9b-d) the divergent mode becomes strongly diminished and only the rotational part of the flux transfers energy. Additionally, the contribution of the eddy-eddy interaction term at larger wavenumber becomes stronger.

4.3.3 Spectral fluxes of slowly-rotating planets

Figure 4.10 shows the spectral fluxes for slowly-rotating simulations ($\Omega^* = 1, \frac{1}{2}, \frac{1}{4}, \frac{1}{8}, \frac{1}{16}$). In this Figure, the Earth-like case (Fig. 4.10a) is given on a lower model resolution of T42. Although the magnitudes are slightly diminished compared to the T127 simulation (Fig. 4.8a), it is remarkable how well the qualitative behaviour of the fluxes match. This qualitative similarity shows that, even though the T42 simulation does not feature a properly identifiable slope in the energy spectra (Fig. 4.6a) due to the model inherent hyperdiffusion, the same spectral fluxes occur nonetheless.

With decreasing rotation rate (Figs. 4.10b-e), the baroclinic region (i.e. downscale Π_A, upscale Π_K, positive slope in $\mathcal{C}$) identified in the previous section moves towards smaller wavenumbers. Between $\frac{1}{4}\Omega_E$ and $\frac{1}{8}\Omega_E$ this baroclinic behaviour is arrested.

a) $\Omega^* = 1$, T42 Resolution

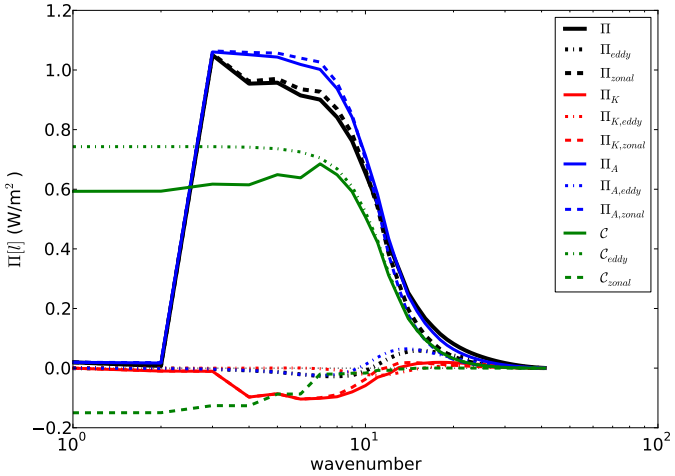

b) $\Omega^* = \frac{1}{2}$, T42 Resolution

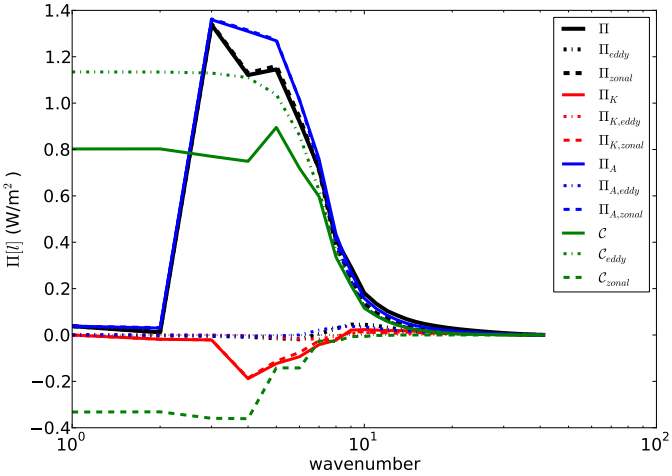

c) $\Omega^* = \frac{1}{4}$, T42 Resolution

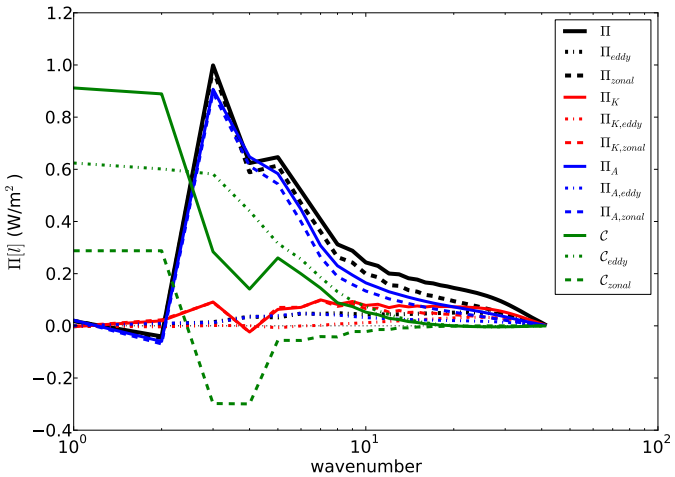

d) $\Omega^* = \frac{1}{8}$, T42 Resolution

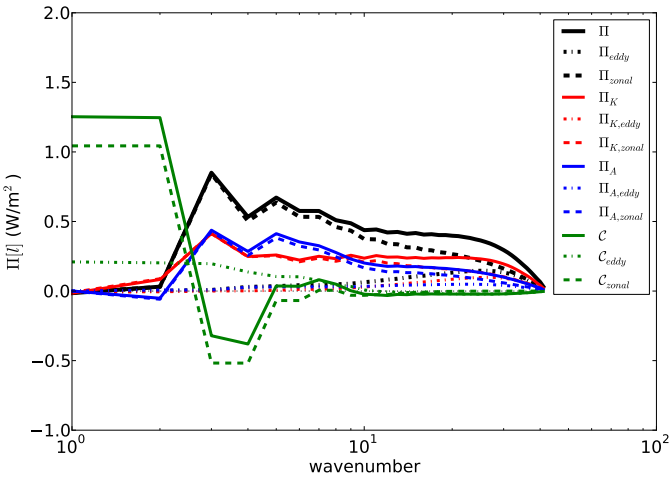

e) $\Omega^* = \frac{1}{16}$, T42 Resolution

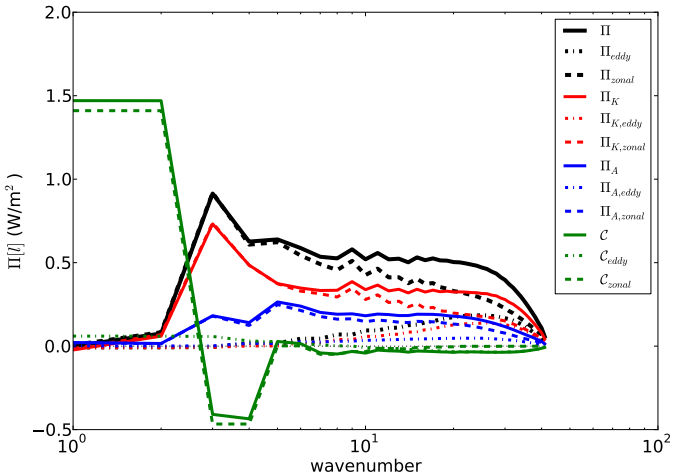

Figure 4.10: Spectral fluxes of KE Π_K, APE Π_A and total energy $\Pi = \Pi_A + \Pi_K$ as well as cumulative conversion $\mathcal{C}$ (each decomposed into eddy-eddy and residual zonal interaction components) for PUMA-S runs with $\Omega^* = 1, \frac{1}{2}, \frac{1}{4}, \frac{1}{8}, \frac{1}{16}$ at T42 resolution.

This result is similar to that of Mitchell and Vallis (2010) who find that their super-rotating atmospheres do not feature baroclinic turbulence shown by a lack of divergence of vertical EP-fluxes (c.f. Mitchell and Vallis, 2010, their Fig. 7). In addition the zonal component of $\mathcal{C}$, which was comparatively small until now, begins to dominate at all lengthscales. This occurs because at smaller rotation rates (larger $\mathcal{R}o$) the Rossby deformation lengthscale exceeds the planetary radius and APE is injected into the KE reservoir directly via interactions with the zonal mean flow. $\mathcal{C}_{zonal}$ is again very similar to C_Z in the Lorenz budget, which points towards a strong influence of zonal-zonal interactions in this conversion term.

At $\frac{1}{8}\Omega_E$ and $\frac{1}{16}\Omega_E$ the qualitative structure of the fluxes is entirely different to faster rotating simulations. Conversion from APE to KE occurs at the smallest wavenumbers via zonal interactions. In addition both Π_K and Π_A now feature an inertial range in the form of a forward transfer with an approximately constant spectral flux between wavenumbers 6 to 30. This is indicative of a forward barotropic waterfall. In both cases the zonal interactions dominate. However, the influence of eddy-eddy interactions still increases at larger wavenumbers.

Figure 4.11 again features the kinetic energy flux in detail. In the case of decreasing Ω, it is the rotational component that diminishes and the divergent component of the flux controls the forward energy cascade. This suggests a greater role for gravity and equatorial inertia-gravity planetary waves as these do not possess a rotational component.

The behaviour identified in this section fits well with other results obtained for the large Rossby number ($\mathcal{R}o > 1$) regime. For $\frac{1}{8}\Omega_E$ and $\frac{1}{16}\Omega_E$ baroclinic conversion becomes weak and barotropic effects become stronger (see e.g. Fig. 5.16). The flow becomes largely zonal and super-rotating flow emerges. Unfortunately, the spectral energy budget method presented in this Section is computed over a global mean and outputs the non-zonal spherical wavenumber spectrum. Hence, it does not help in identifying the mechanism responsible for formation and maintenance of the equatorial superrotation, as this process occurs mostly in the zonal component in a specific region of the globe. What we can learn, however, is that the kinetic energy in the zonal mode of the super-rotating atmosphere dissipates via a downscale cascade that is dominated

a) $\Omega^* = 1$, T42 Resolution

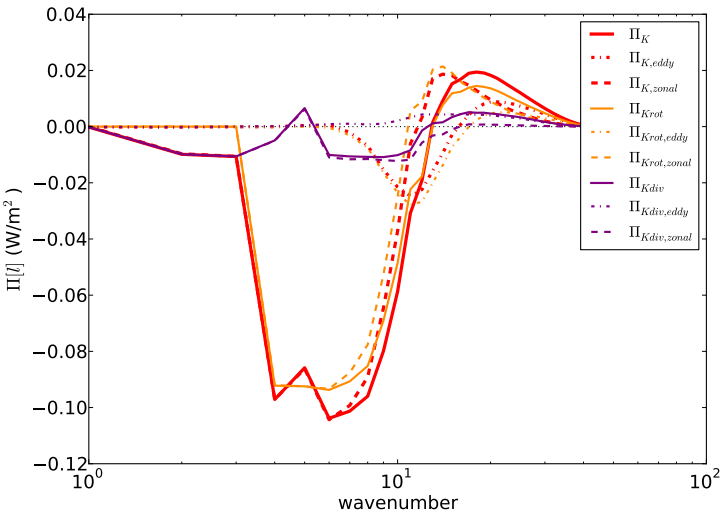

b) $\Omega^* = \frac{1}{2}$, T42 Resolution

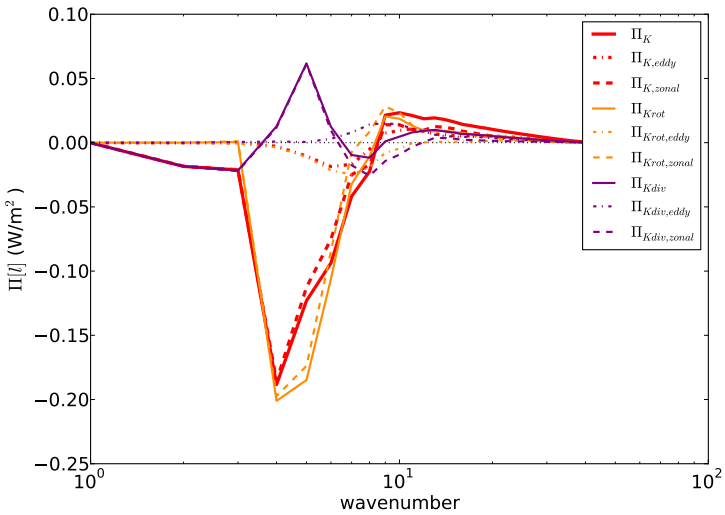

c) $\Omega^* = \frac{1}{4}$, T42 Resolution

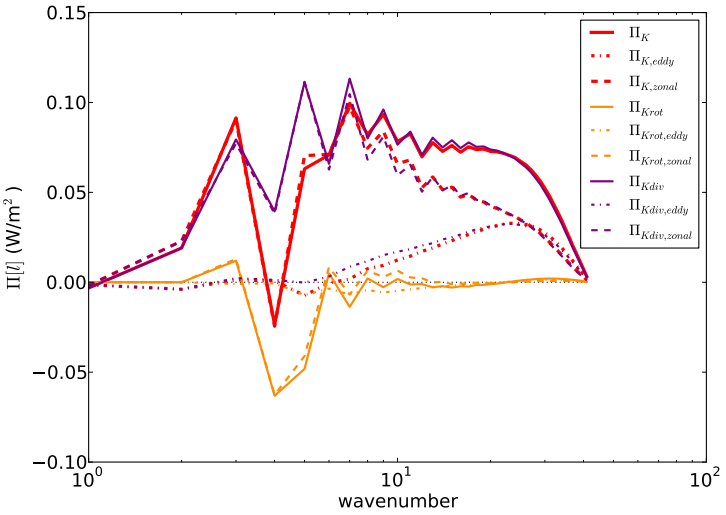

d) $\Omega^* = \frac{1}{8}$, T42 Resolution

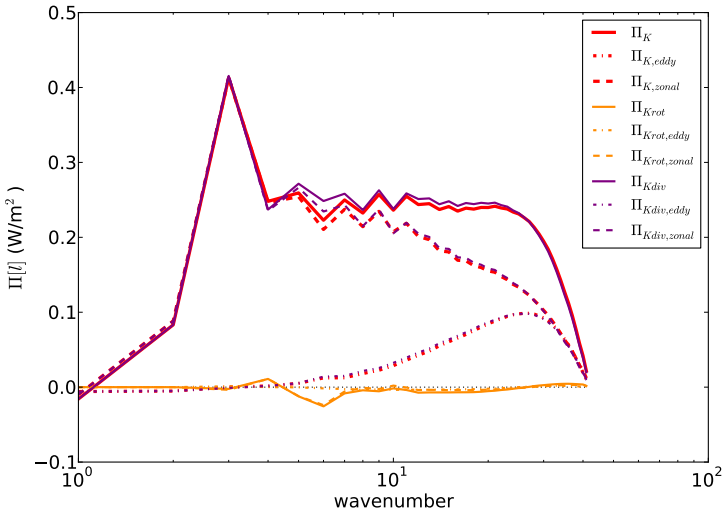

e) $\Omega^* = \frac{1}{16}$, T42 Resolution

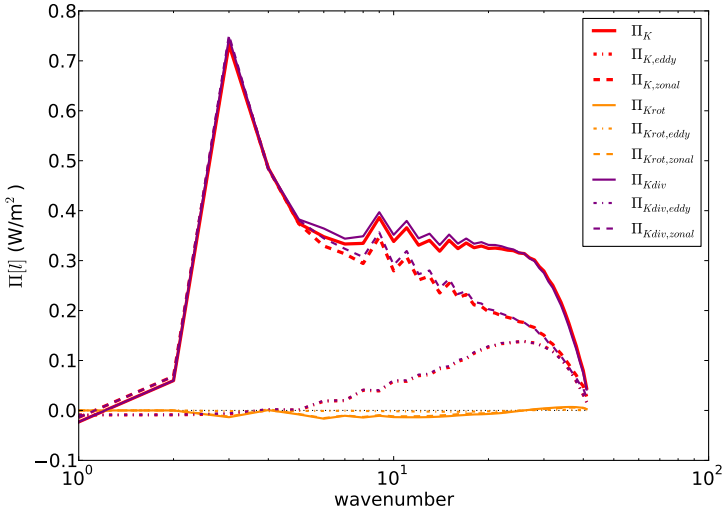

Figure 4.11: Spectral fluxes of KE Π_K, decomposed into divergent and rotational component (each decomposed into eddy-eddy and residual zonal interaction components) for PUMA-S runs with $\Omega = 1, \frac{1}{2}, \frac{1}{4}, \frac{1}{8}, \frac{1}{16}\Omega_E$ at T42 resolution.

by zonal-mean interactions.

4.4 Conclusion

We show that our simulations behave largely like the geostrophic turbulence theory in the fast-rotating regime ($\Omega^* \gtrsim \frac{1}{2}$). However, instead of incrementally cascading flow, we mostly find direct "waterfalls" between the zonal flow and different wavenumbers.

At fast rotation rates the rotational component of the KE spectral flux dominates, while at slow rotation rates the divergent component dominates. The turnover point between these two components occurs between $\Omega^* = \frac{1}{2}$ and $\Omega^* = \frac{1}{4}$. Hence one could argue that a fundamental change in wave activity occurs here, which is likely as this is also roughly the cross-over point between geostrophic and cyclostrophic balance in our simulations. In addition, Mars lies near this point in parameter space, which would be interesting to explore in future work.

Chapter 5

Systematic studies with seasonal forcing (PUMA-GT)

5.1 Introduction

In this chapter, we present simulations we have performed using PUMA-GT with seasonally-varying solar forcing over a large range of parameters. In this parameter space, we vary the planetary rotation rate Ω, the surface thermal inertia timescale τ_{surf}, the atmospheric thermal inertia timescale τ_{atm}, the short-wave optical depth χ_{sw} (at constant long-wave optical depth $\chi_{lw} = 2$), and the frictional timescale τ_f at the boundary layer. Variation of each of these parameters was already performed by the studies reviewed in Section 1.3. However, most of these studies have focussed only on a subset of these parameters (e.g. Wang, 2014, Mitchell et al., 2014, Kaspi and Showman, 2015, Laraia and Schneider, 2015). For instance, Kaspi and Showman (2015) have varied each of these parameters (except χ_{sw}) separately and studied the efficiency of meridional heat transport. In the current study, we vary most parameters in conjunction with each other, which can shed light on non-linear effects of varying multiple parameters. In addition, Mitchell et al. (2014) have studied the response of super-rotating equatorial jets to seasonal forcing, varying both τ_{surf} and Ω. One of the novel aspects of our study is the investigation of concurrently varying τ_{surf}, Ω, and τ_{atm} (and χ_{sw}) on the way seasonality affects superrotation. Also the τ_{surf}, Ω, and τ_{atm} responses can give insights on the seasonally and diurnally responsive atmosphere

of Mars.

Some phenomenological effects of varying the parameters separately have already been demonstrated in sections 1.3 and 4.1.1. In the subsequent sections of this chapter, we focus mainly on the seasonal behaviour of the simulated atmospheres. In the current section, we provide a quick reminder of the general atmospheric dynamics response of varying the rotation rate without seasons in Fig. 5.1. These figures displays annual-mean, zonal-mean fields of the zonal wind, meridional mass stream function (Eqn. 4.1) in their top half and the temperature and potential temperature in their bottom half. The simulations presented in Fig. 5.1 were performed using PUMA-G (Wang, 2014), and thereby vary only in the temporal variation of solar forcing from all subsequently presented results. PUMA-G is constantly forced with an annually averaged solar flux, whereas PUMA-GT can model fully time-resolved solar flux.

The dynamical response to Ω is already detailed in Section 4.1.1. Note that for PUMA-G (and PUMA-GT), no ad hoc tuning of the thermal parametrisation has been performed to artificially re-create the Earth-like, ozone-induced temperature inversion above the tropopause (in contrast, for example, to the Newtonian cooling schemes of Mitchell and Vallis, 2010, Potter et al., 2014, Wang, 2014, Laraia and Schneider, 2015, or the meridionally prescribed short-wave optical-depth of Kaspi and Showman, 2015). Therefore, extra-tropical jets in our simulations are not closed off at the top of the plotted atmosphere. We chose this approach in order to ensure the applicability of the simple GCM to a wide range of different planets, rather than reproducing the specific characteristics of Earth's atmosphere. In addition, the fact that we still produce reasonably realistic tropospheric circulations shows that moisture and ozone do not profoundly impact the lower atmosphere circulation, but merely perturb its quantitative behaviour. This shows that moisture or ozone are not necessary to capture the most important physics in the atmosphere.

In Section 5.2, we briefly describe the range of values of our parameter space. Section 5.3 introduces dynamical phenomena that occur as a response to seasonal forcing. Section 5.3.2 focuses on the response of equatorial superrotation to seasonal forcing. In Section 5.4 we characterise the response of atmospheric waves to the varied parameters. The final sections focus on the atmospheric energy transport in our simulations

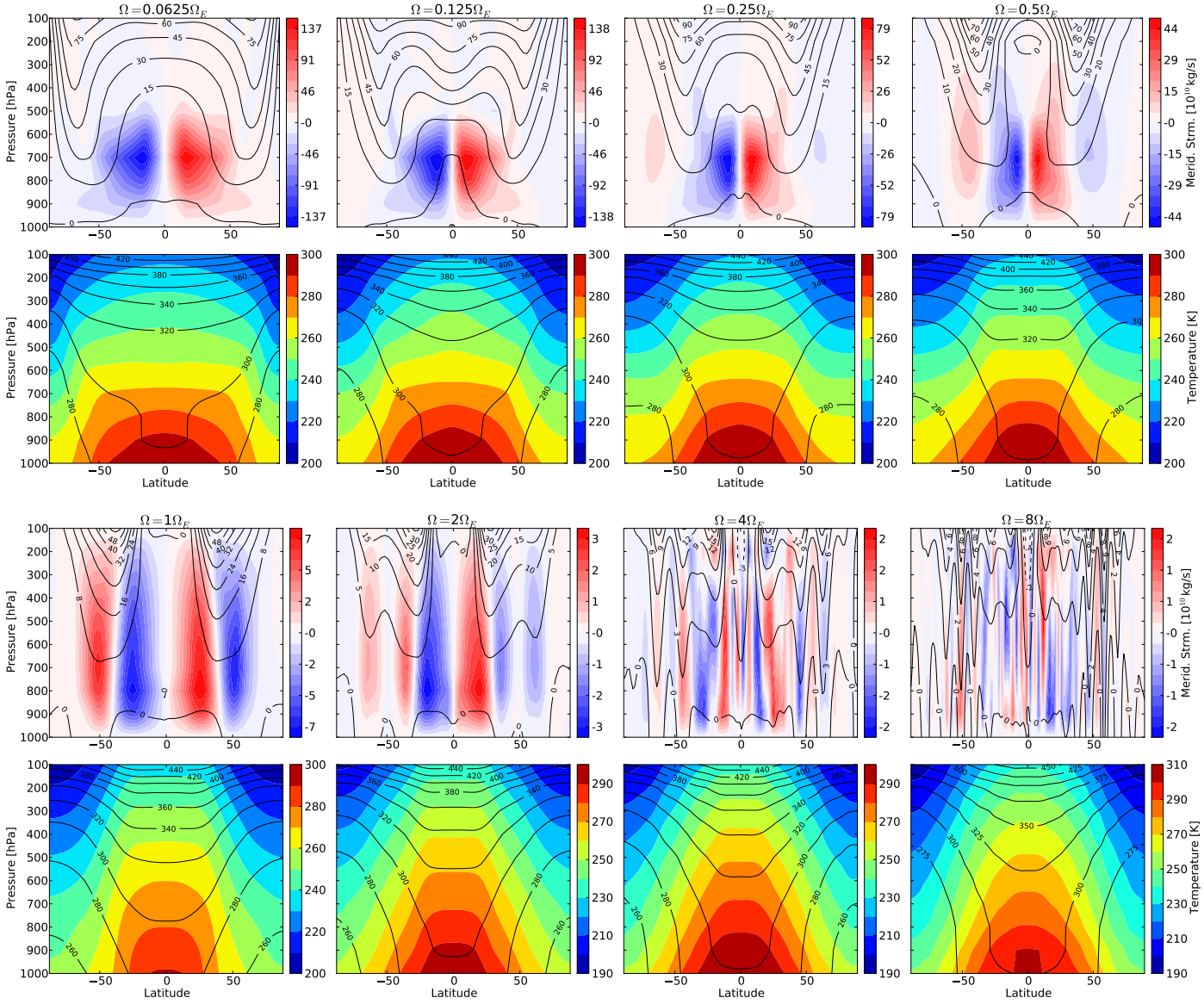

Figure 5.1: Top: zonal mean zonal wind (contour) and meridional mass stream function (colour); bottom: zonal mean temperature (colour) and potential temperature fields (contour) for PUMA-G runs with **rotation rate** Ω from $\frac{1}{8}\Omega_E$ to $\frac{1}{2}\Omega_E$ (top row) and from $\frac{1}{2}\Omega_E$ to $8\Omega_E$ (bottom row). The plotted fields are averaged over one model year. (Constants: $\mathcal{G} = 0$, $\tau_{atm} = 40$ days, $\tau_f = 1$ day)

in both physical space (Lorenz energy cycle, Section 5.5) and spectral space (spectral energy budget, Section 5.6). In both sections, we discuss annual-mean and seasonal responses to the varied parameters.

5.2 Parameter space

As mentioned before, our parameter space is spanned by concurrent variation of the rotation rate Ω, the surface thermal inertia timescale τ_{surf}, the atmospheric thermal inertia timescale $\tau_{atm}(p_0)$, the short-wave optical depth χ_{sw} (at constant long-wave optical depth $\chi_{lw} = 2$), and the frictional timescale τ_f. These can be non-dimensionalised according to the equations presented in Section 1.1. This results in the non-dimensional parameters $\mathcal{R}o$ (via Ω), Ek (via τ_f), α (via τ_{surf}), $\mathcal{G}$ (via χ_{sw}) and $\mathcal{A}$ (via p_0). In addition, we can apply a switch $n_{\bar{\mu}}$ for daily-averaged ($n_{\bar{\mu}} = 1$) or diurnally-varying ($n_{\bar{\mu}} = 0$) insolation to study the effect of diurnal solar forcing directly. In this chapter, however, only seasonal forcing is considered (i.e. $n_{\bar{\mu}} = 1$). The considered sampling of the parameter space amounts to over 800 different parameter combinations, for each of which we performed a separate simulation using the simplified GCM PUMA-GT. The table below lists the ranges of each varied parameter and the corresponding change of affected non-dimensional parameters.

changed parameters	**nondim. parameters**
$\Omega = 2\Omega_E - \frac{1}{16}\Omega_E$	$\mathcal{R}o = 0.005 - 5$
	$Ek = 0.04 - 1.28$
	$\mathcal{A} = 1000 - 31$
$\tau_{surf} = 3.6, 36, 360$ days	$\alpha = 16, 1.6, 0.16$
$\chi_{sw} = 0, 2, 10$	$\mathcal{G} = 1, 0, -0.7$(with $\chi_{lw} = 2$)
$p_{surf} = 0.2, 1, 5$ bar	
$\Rightarrow \tau_{atm} \approx 1.6, 8, 40, 200$ days	$\mathcal{A} = 16, 80, 400, 2000$
	$\alpha_{\mathcal{A}} = 35.8, 7.2, 1.43, 0.29$
$\tau_f = 0.1, 1, 10$ days	$Ek = 0.008, 0.08, 0.8$

diurnal cycle = on/off $n_{\bar{\mu}} = 0, 1$

5.3 Seasonal Phenomena

In this section, we present the phenomenological effects in the atmospheric circulations with our parameter space that occur in response to seasonally-varying forcing.

Figure 5.2 shows the seasonal behaviour of our parameter space with varying $\mathcal{R}o$, $\mathcal{A}$, $\mathcal{G}$ and α and constant $Ek(\tau_f = 1 \text{ day})$ and seasonally-varying solar forcing ($n_{\overline{\mu}} = 1$).

The regime diagram given here requires some explanation. The plot displays multiple coloured dots, each representing a single value result for one model simulation (in this case the single value result is the standard deviation from the annual mean of the total energy $E = A + K$ over the final model year). These results are given by the colour of the dot and in dependence upon 4 variables: the thermal Rossby number $\mathcal{R}o$ on the x-axis and the Atmospheric relaxation number $\mathcal{A}$ on the y-axis; for each combination of $\mathcal{R}o$ and $\mathcal{A}$, 9 dots are displayed in the form of a 3 by 3 cluster. These clusters have the same $\mathcal{R}o$ and $\mathcal{A}$ values, but are artificially offset to display the greenhouse parameter $\mathcal{G} = 1, 0, -0.7$ (from bottom to top) in the y-direction and the seasonality parameter $\alpha = 0.16, 1.6, 16$ (from left to right) in the x-direction. The Earth-like reference simulation with $\Omega = \Omega_E$, $\alpha = 0.16$, $\mathcal{G} = -1$, $\mathcal{A} = 400$, $\tau_f = 1$ day, is located at the point where the $\mathcal{G}$ and α arrows meet.

Figure 5.2 displays the seasonal variability of the total energy in colours (red is weakly seasonal, yellow is moderately seasonal, and white is strongly seasonal). We can see three effects that vary the seasonal responsiveness:

1. Increasing α will increase seasonal variability.

2. Increasing $\mathcal{G}$ will increase seasonal variability.

3. For $\mathcal{R}o \gtrsim 0.1$ (roughly in the cyclostrophic regime), decreasing $\mathcal{A}$ will increase seasonal variability.

When combining these parameters, the above dependencies may change and seasonal variability may not always behave monotonically.

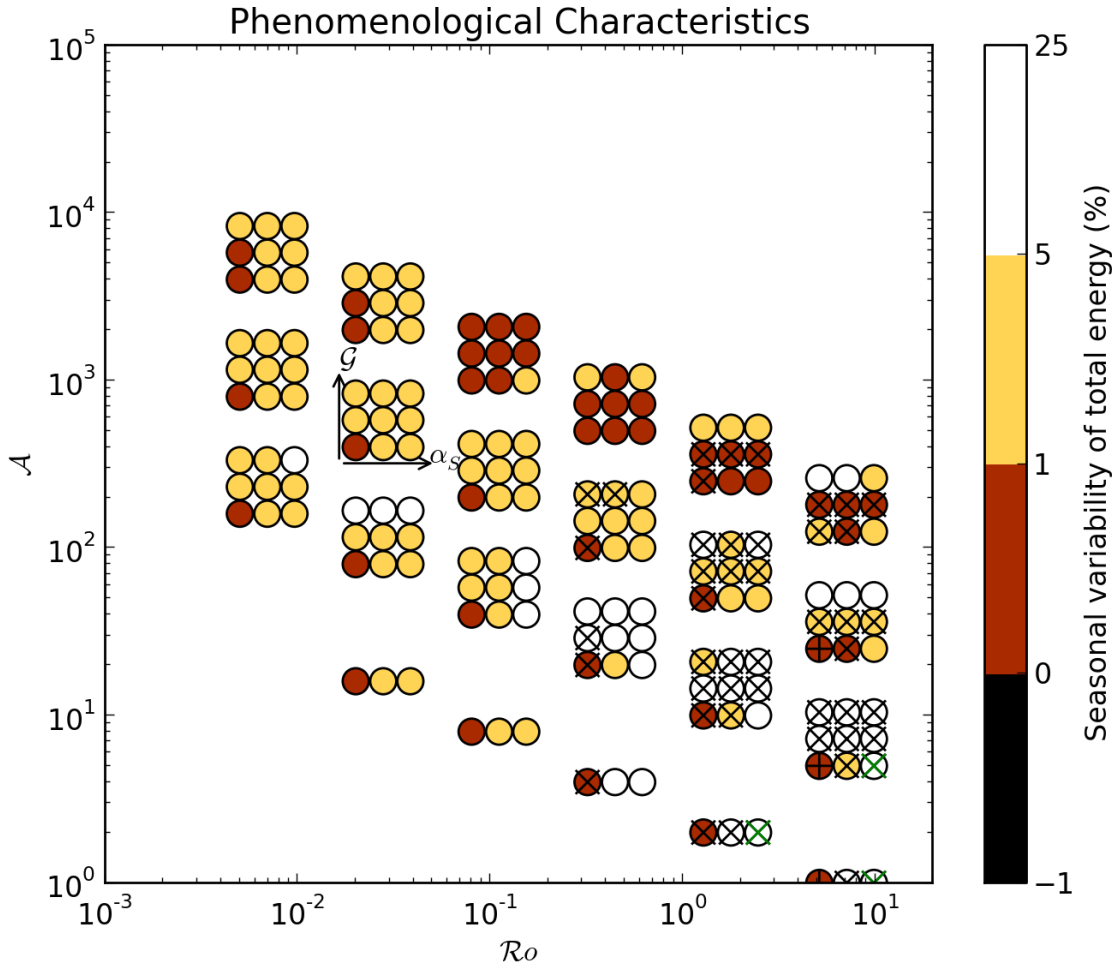

Figure 5.2: Phenomenological regime diagram given in dependence upon $\mathcal{R}o$, $\mathcal{A}$, $\mathcal{G}$ and α. Clusters of points are artificially moved to discern variations in greenhouse parameter $\mathcal{G} = 1, 0, -0.7$ (in y direction) and seasonality parameter $\alpha = 0.16, 1.6, 16$ (in x direction). Colours show how strongly the total energy of the atmosphere reacts to seasons. Crosses(pluses) signify atmospheres with a global superrotation index larger than 0.25(1.0). Green crosses are cases with global superrotation that do not have an equatorial prograde jet. Constants: $\tau_f = 1$ day, $n_\mu = 1$ (diurnally-averaged insolation).

In the cyclostrophic regime, equatorial superrotation can occur. To investigate the effect of seasonal forcing to the super-rotaion in this regime, we calculate the global superrotation index S (Read, 1986). S is given by

$$S = \int\int\int m dV/M_0 - 1, \tag{5.1}$$

where m is the absolute atmospheric specific angular momentum:

$$m = a\cos\phi(\Omega a\cos\phi + u). \tag{5.2}$$

Here, a is the planetary radius, ϕ is the latitude, Ω is the planetary ration rate, u is the zonal wind velocity, dV is the volume element, and M_0 is the integrated total angular momentum of the atmosphere in solid body rotation with the planet. Using this definition, global values of $S > 0$ describe a super-rotating and $S < 0$ a sub-rotating atmosphere. Being a globally-integrated value, this method cannot specifically inform about superrotation at the equator, but instead shows global trends of superrotation behaviour.

In Figure 5.2, simulations with $S > 0.25$ are identified as crosses and $S > 1$ as pluses. In the cyclostrophic regime ($\mathcal{R}o > 0.1$), at $\mathcal{G} = 1$, the surface seasonality parameter α has a significant effect on both the seasonal variability and the superrotation of the atmosphere. In this regime, the atmosphere is only moderately seasonally variable for small α, and atmospheric superrotation can develop. However, with increasing α, our modelled atmospheres become more strongly seasonally variable, and the development of super-rotating circulation is hindered. This dependency of super-rotating jets on α was also identified by Mitchell et al. (2014). They have studied the effect of varying $\mathcal{R}o$ and α on equatorial super-rotating circulation. With regard to the strongly seasonal and super-rotating atmosphere of Titan, Mitchell et al. (2014) have found that significantly increasing the radiative timescale of the atmosphere (represented by $\mathcal{A}(\tau_{atm})$ in the current work) to Titan-like levels, will result in superrotation even at large τ_{surf} (strong surface seasonality α). In the current study, we additionally consider the concurrent variation of $\mathcal{G}$ and $\mathcal{A}$.

At $\mathcal{G} = 0$ and 0.7, varying α has no significant effect on the seasonal variability.

This is because, in these cases, a large fraction of the solar power is absorbed in the atmosphere, which reduces the heating of the surface. Consequently, thermal inertia of the surface and thereby α becomes less important. Instead, in this regime, seasonal variability is strongly dependent on $\mathcal{A}$. Super-rotation is only affected at $\mathcal{G} = -0.7$ once a critical value of $\mathcal{A}$ is reached. In this case, however, seasonal variability and superrotation are not as strongly correlated as in the regime with $\mathcal{G} = 1$ and varying α.

The green crosses in Fig. 5.2 represent simulations where global superrotation index $S > 0.25$, but where this superrotation does not occur at the equator (i.e. where the annual-mean zonal-mean zonal wind at the equator is smaller than 10ms^{-1}). In these cases, strong extratropical jets are produced, but the seasonal variability is too large to allow for the development of equatorial super–rotation.

Below, we show a few examples of the intensity of the atmospheric response to seasonal forcing. In Section 5.3.1, we take a look at the Earth-like, geostrophic regime. In Section 5.3.2, we focus on the effect of seasonality on the equatorial superrotation in the cyclostrophic regime.

5.3.1 Seasonal effects in rapidly-rotating planets

In this section, we describe phenomenological effects of seasonal forcing in the geostrophic regime $\mathcal{R}o < 0.1$.

Surface seasonality parameter

In Figures 5.3A-C) we can see that, when annually averaged, variations of the seasonality parameter at $\Omega^* = 1$ have only a small effect on the atmospheric diagnostics. The only difference one can observe is that with rising seasonality two local maxima of the extratropical temperature develop at latitudes $\lambda = \pm 40°$.

However, a stronger influence of α on the atmospheric diagnostics can be observed during the northern winter solstice (see Figs. 5.3D-F). With increasing α, the solsticial Hadley circulation moves strongly in the meridional direction. This phenomenon is termed cross-equatorial Hadley cell circulation. This circulation is very efficient in transporting heat and momentum into the winter hemisphere. At its edge one can

Annual mean

A) $\Omega^* = 1$, $\alpha = 16$ **B)** $\Omega^* = 1$, $\alpha = 1.6$ **C)** $\Omega^* = 1$, $\alpha = 0.16$

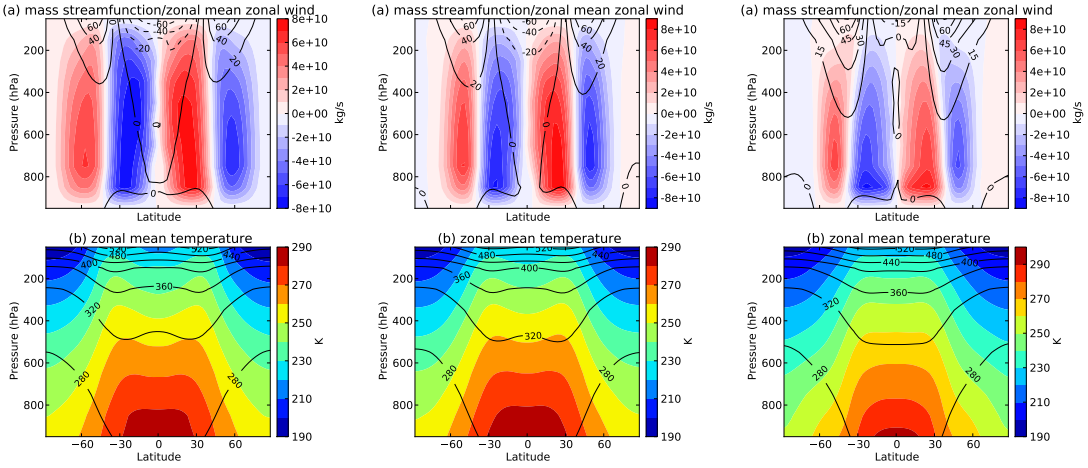

Snapshot at winter solstice

D) $\Omega^* = 1$, $\alpha = 16$ **E)** $\Omega^* = 1$, $\alpha = 1.6$ **F)** $\Omega^* = 1$, $\alpha = 0.16$

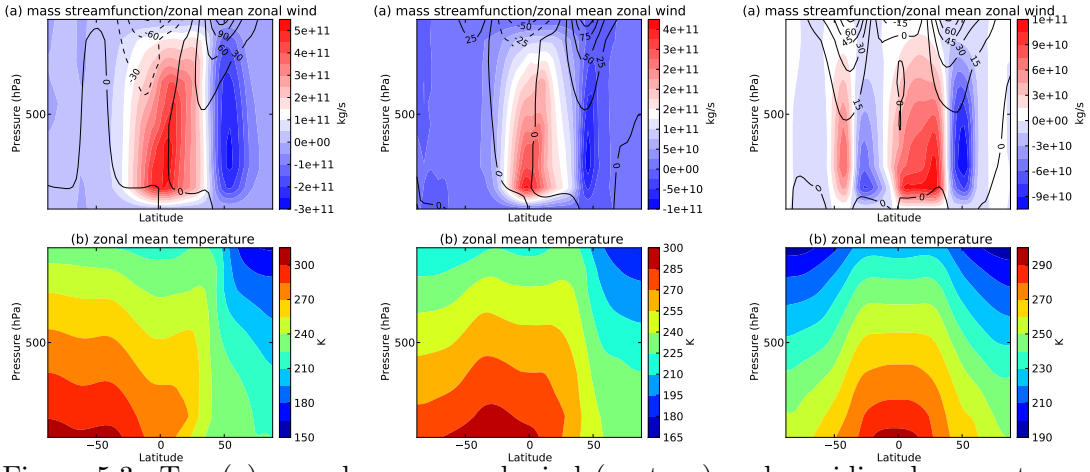

Figure 5.3: Top (a): zonal mean zonal wind (contour) and meridional mass stream function (colour); Bottom (b): zonal mean temperature (colour) for simulations with **seasonality parameter** $\alpha = 16, 1.6, 0.16$, i.e. $\tau_s = 3.6, 36, 360$ days. Plots A, B, C show annual mean fields, while plots D, E, F show a snapshot at northern winter solstice. (Constants: $\Omega^* = 1$, $\mathcal{G} = 1$, $\tau_{atm} = 40$ days, $\tau_f = 1$ day)

observe a sharp increase in the meridional temperature gradient that produces strong baroclinic jets in the extratropics of the winter hemisphere and a subrotating jet near the equator, similar to Mitchell et al. (2014). This rapid drop in temperatures is also responsible for the local maxima seen in annual average.

Greenhouse parameter $\mathcal{G}(\chi_{sw})$

The greenhouse parameter $\mathcal{G}$ strongly controls the thermal structure of the atmosphere (see Fig. 5.4A-C). At positive $\mathcal{G}$ (e.g. $\mathcal{G} = 1$) the atmosphere is being heated from the bottom, at negative $\mathcal{G}$ (e.g. $\mathcal{G} = -0.7$) the atmosphere is heated from the top. At $\mathcal{G} = 0$ there is a neutral greenhouse effect, and the vertical temperature gradient is nearly zero (Wang, 2014). At a rotation rate of Ω_E, this change in temperature has only a minor effect on the corresponding baroclinic jets in the extratropics. This is likely due to the fact that the meridional temperature gradient is not greatly affected by variation in $\mathcal{G}$.

At $\mathcal{G} = 1$ (Fig. 5.4D), the seasonal response is controlled by the surface seasonality parameter α. In Fig. 5.4, $\alpha = 0.16$, so the surface reacts only moderately to seasons. However, at $\mathcal{G} = 0, -0.7$ solar flux is largely absorbed in the atmosphere and the surface receives less heat. As a consequence, the atmospheric relaxation timescale $\mathcal{A}$ becomes important. The simulations presented here are at constant $\mathcal{A} = 400$ ($\tau_{atm} = 40$ days). In terms of the atmospheric seasonality parameter (Eqn. 1.11) this would be equivalent to $\alpha_{atm} = 1.4$. When compared to α, we see that $\alpha_{atm} \approx 1$ will react strongly to seasonal changes. The effect of α_{atm} is apparent in Fig. 5.4E and F. Here, the circulation during the winter solstice becomes strongly assymmetrical. At neutral greenhouse effect ($\mathcal{G} = 0$), this will produce a nearly uniformly heated summer side and a cold winter side. With an antigreenhouse effect $\mathcal{G} = -0.7$, only the stratospheric part of the summer side is effectively heated.

Overall, this shows that the atmospheric timescale (τ_{atm}) has a large influence on the seasonality of simulations with $\mathcal{G} \neq 1$ (i.e. $\chi_{sw} \neq 0$).

Annual mean

A) $\Omega^* = 1$, $\mathcal{G} = 1$ **B)** $\Omega^* = 1$, $\mathcal{G} = 0$ **C)** $\Omega^* = 1$, $\mathcal{G} = -0.7$

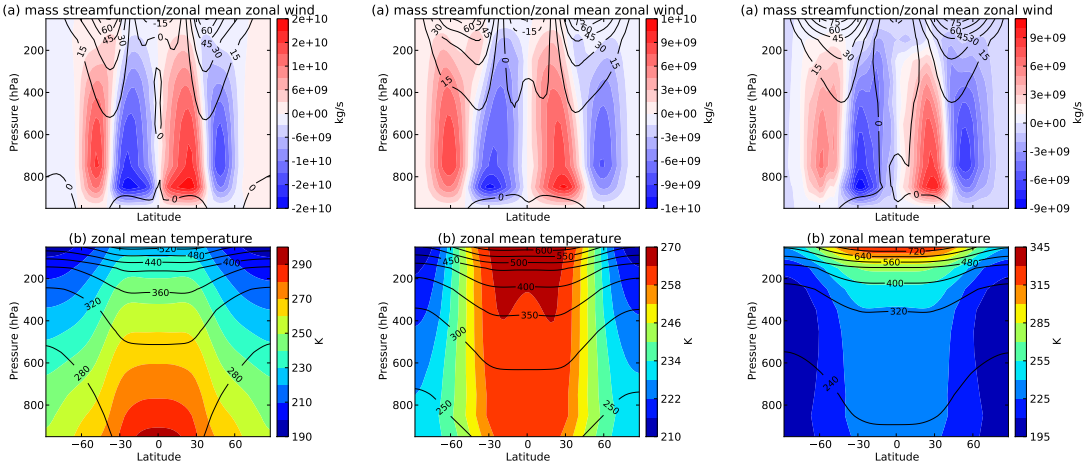

Snapshot at winter solstice

D) $\Omega^* = 1$, $\mathcal{G} = 1$ **E)** $\Omega^* = 1$, $\mathcal{G} = 0$ **F)** $\Omega^* = 1$, $\mathcal{G} = -0.7$

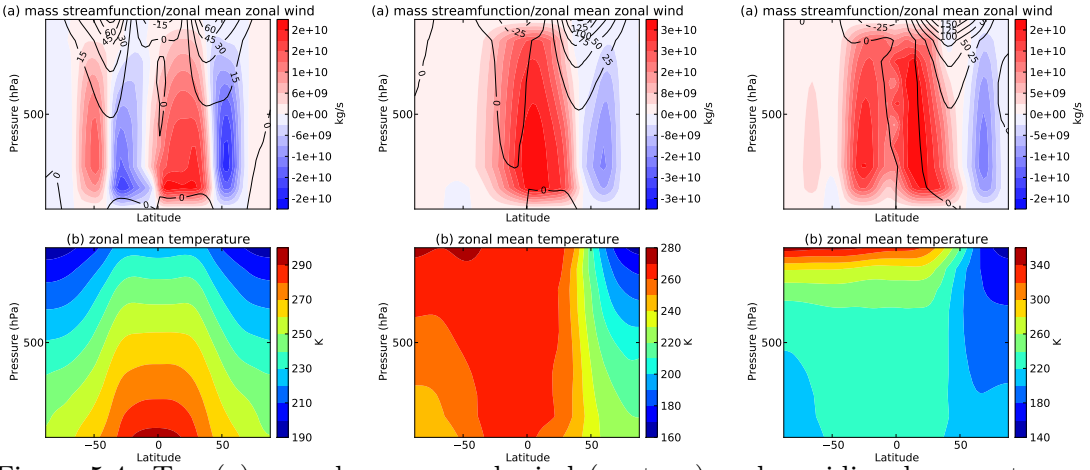

Figure 5.4: Top (a): zonal mean zonal wind (contour) and meridional mass stream function (colour); Bottom (b): zonal mean temperature (colour) for simulations with **greenhouse parameter** $\mathcal{G} = 1, 0, -0.7$, i.e. $\chi_{sw} = 0, 2, 10$ at constant $\chi_{lw} = 2$. Plots A, B, C show annual mean fields, while plots D, E, F show a snapshot at northern winter solstice. (Constants: $\Omega^* = 1$, $\alpha = 0.16$, $\tau_{atm} = 40$ days, $\tau_f = 1$ day)

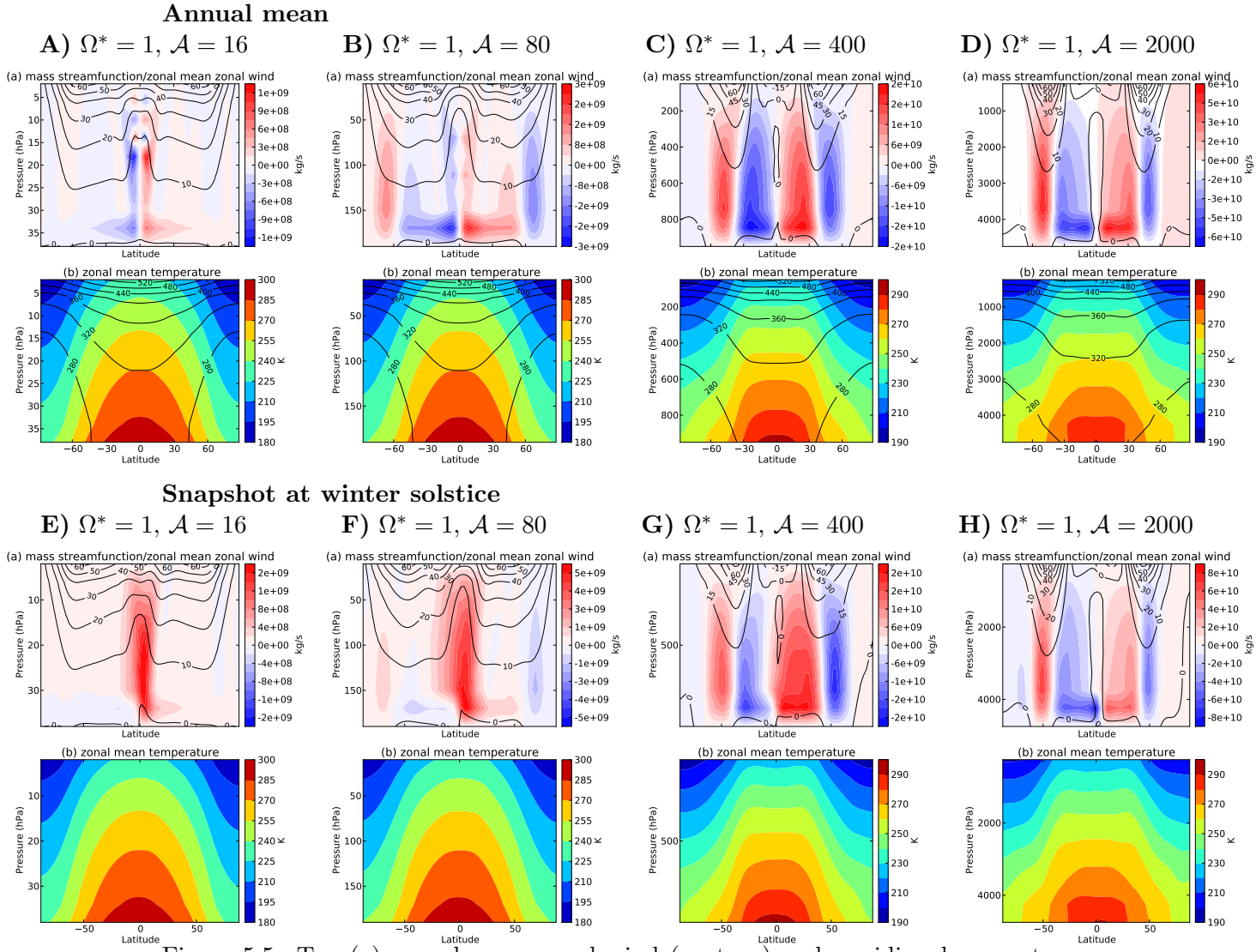

Figure 5.5: Top (a): zonal mean zonal wind (contour) and meridional mass stream function (colour); Bottom (b): zonal mean temperature (colour) for simulations with **atmospheric relaxation parameter** $\mathcal{A} = 16, 80, 400, 2000$, i.e. $p_s = 0.04, 0.2, 1, 5$ bar. Plots A-D show annual mean fields, while plots E-H show a snapshot at northern winter solstice. (Constants: $\Omega^* = 1$, $\mathcal{G} = 1$, $\alpha = 0.16$, $\tau_f = 1$ day)

Atmospheric thermal relaxation number $\mathcal{A}(p_0)$

Variation of the surface pressure p_s, and thereby of the atmospheric mass, varies linearly with the radiative equilibrium timescale of the atmosphere (see Eqn. 1.10), which will again vary linearly with the atmospheric relaxation number $\mathcal{A} \propto \tau_{atm} \propto p_s$. In Fig. 5.5A-D, we show the annual-mean zonal-mean diagnostics for varying $\mathcal{A}(p_s)$ at constant $\Omega^* = 1$, $\mathcal{G} = 1$, and $\alpha = 0.16$. Note the mass streamfunction is obtained via integration over the atmosphere's pressure range (see Eqn. 4.1). Hence, the intensity of the meridional mass stream function scales with the surface pressure.

Kaspi and Showman (2015) vary along the same parameter and find that the meridional streamfunction increases for increasing p_s. However, they say that this increase comes from the integration of larger pressure levels and that, overall, the meridional circulation is weakened at higher p_0. We find, that the general effects of changing p_s in PUMA-GT (Fig. 5.5A-D) are the same as found by Kaspi and Showman (2015) with their model: the meridional temperature gradient decreases with increasing atmospheric mass due to an improved polewards heat transport efficiency. Due to the decreased thermal gradient, we observe weaker zonal jets. With decreasing atmospheric mass, meridional temperature gradients become larger. The resulting stronger baroclinic jets almost meet at the equator and seem to converge enough angular momentum towards the equator to achieve equatorial superrotation.

The seasonal behaviour of this case (varying $\mathcal{A}(p_s)$ at constant $\Omega^* = 1$, $\mathcal{G} = 1$, $\alpha = 0.16$) is indicated by a snapshot during the winter solstice (Fig. 5.5E-H). This this case, surface seasonality is small and no solar flux is absorbed in the atmosphere. Hence we do not see a strong deviation from the annual-mean in the temperature fields during the winter solstice. The dynamic diagnostic fields change more strongly with varying $\mathcal{A}$. At large $\mathcal{A}$, solstice snapshots of wind and streamfunction are nearly symmetrical about the equator. With decreasing $\mathcal{A}(p_0)$, the seasonal extremes become more discernible. Note that for the two lowest $\mathcal{A}$, one large circulation cell is located directly at the equator.

Figure 5.6 also shows the effect of varying $\mathcal{A}$, but this time at $\mathcal{G} = 0$. In this regime, we can clearly see the increase in seasonal variability with decreasing $\mathcal{A}$ (see Fig. 5.6D-F).

Annual mean

A) $\Omega^* = 1$, $\mathcal{G} = 0$, $\mathcal{A} = 80$ **B)** $\Omega^* = 1$, $\mathcal{G} = 0$, $\mathcal{A} = 400$ **C)** $\Omega^* = 1$, $\mathcal{G} = 0$, $\mathcal{A} = 2000$

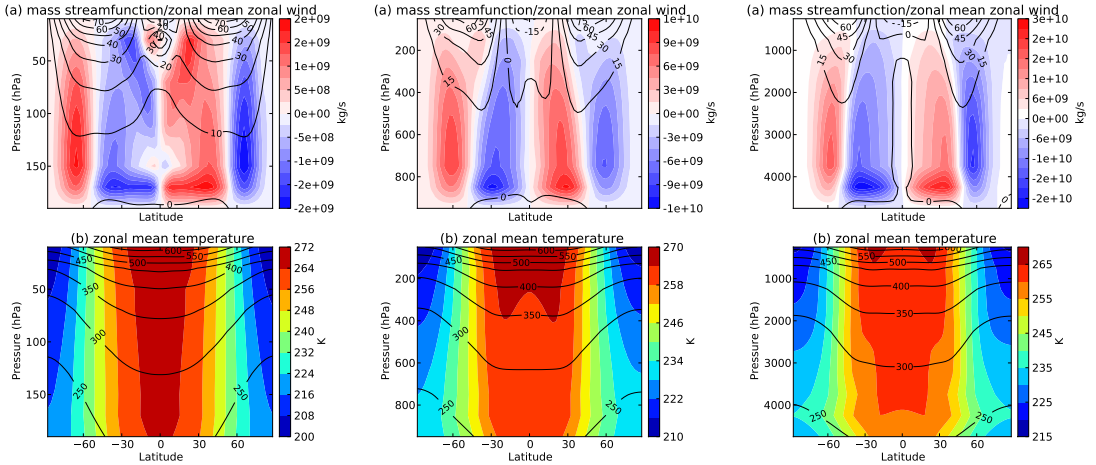

Snapshot at winter solstice

D) $\Omega^* = 1$, $\mathcal{G} = 0$, $\mathcal{A} = 80$ **E)** $\Omega^* = 1$, $\mathcal{G} = 0$, $\mathcal{A} = 400$ **F)** $\Omega^* = 1$, $\mathcal{G} = 0$, $\mathcal{A} = 2000$

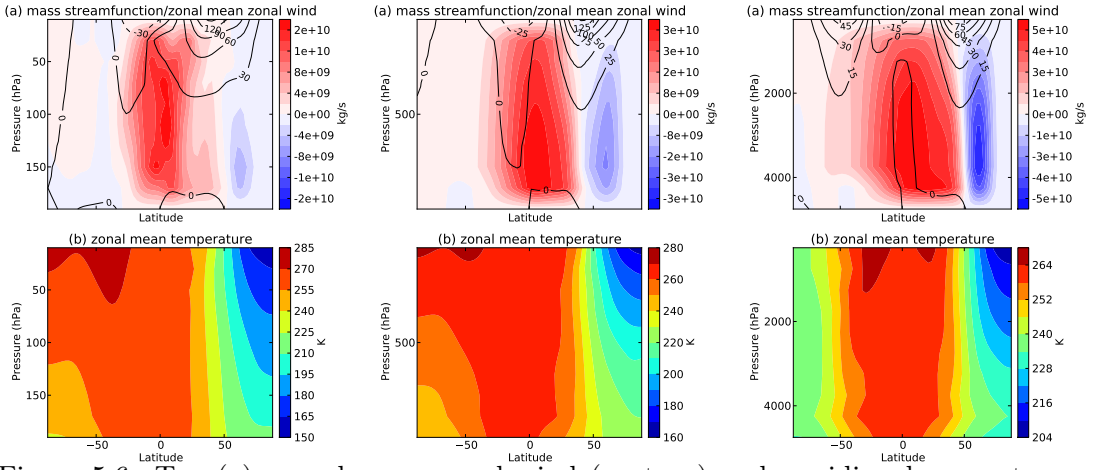

Figure 5.6: Top (a): zonal mean zonal wind (contour) and meridional mass stream function (colour); Bottom (b): zonal mean temperature (colour) for simulations with **atmospheric relaxation parameter** $\mathcal{A} = 80, 400, 2000$, i.e. $p_s = 0.2, 1, 5$ bar. Plots A, B, C show annual mean fields, while plots D, E, F show a snapshot at northern winter solstice. (Constants: $\Omega^* = 1$, $\mathcal{G} = 0$, $\alpha = 0.16$, $\tau_f = 1$ day)

5.3.2 Super-rotation in the slowly-rotating regime

Figure 5.2 reveals that seasonal variability has a strong effect on the superrotation in the cyclostrophic regime. In this section, we describe phenomenological effects of the seasonal forcing on the atmospheric circulation, exemplified by simulations at a rotation rate of $\Omega^* = \frac{1}{8}$.

Surface seasonality parameter

Figure 5.7 shows the zonal-mean diagnostics with varying surface seasonality parameter α for a slowly-rotating planet with $\Omega^* = \frac{1}{8}$.

In the annual mean (Fig. 5.7A-C), the weakly-seasonal case with $\alpha = 0.16$ is very similar to the $\Omega^* = \frac{1}{8}$ case without seasons in Fig. 5.1. The difference between non-seasonal and weakly-seasonal cases lies mainly in the distribution of zonal winds. The non-seasonal case (Fig. 5.1) has a stronger equatorial prograde jet (over 90 ms^{-1} compared to $80\mathrm{ms}^{-1}$), whereas the weakly-seasonal run (Fig. 5.7C) has stronger extratropical jets (with over $120\mathrm{ms}^{-1}$ compared to $90\mathrm{ms}^{-1}$). According to Mitchell et al. (2014), seasonal variation weakens the equatorial convergence of momentum due to the meridional movement of the upward momentum flux at the surface. Hence, in our case, it is likely that the non-seasonal case has a constant vertical and meridional momentum convergence at the equator, whereas in the seasonally varying case in Fig. 5.7C this conversion is slightly perturbed.

When increasing α, the superrotation at the equator vanishes in the annual mean (Fig. 5.7A-B). At the very seasonal case with $\alpha = 16$, there is a sub-rotating jet in its place instead. In addition, the surface temperature gradient in the annual mean becomes weaker with increasing α. This signifies that heat is distributed more equally in the meridional direction. This flattening temperature gradient does not necessarily mean that the meridional heat transport in the atmosphere is improved by increasing α. Much rather, solar energy directly reaches higher latitudes during summer, this is absorbed by the surface, which then gives off energy to the atmosphere.

While the snapshot of the weakly seasonal run with $\alpha = 0.16$ (Fig. 5.7F) only differs slightly from the annual mean, the other two cases show significant differences. When looking at the snapshot plots (Fig. 5.7D,E), we see that the surface is indeed heated far

Annual mean

A) $\Omega^* = \frac{1}{8}$, $\alpha = 16$ **B)** $\Omega^* = \frac{1}{8}$, $\alpha = 1.6$ **C)** $\Omega^* = \frac{1}{8}$, $\alpha = 0.16$

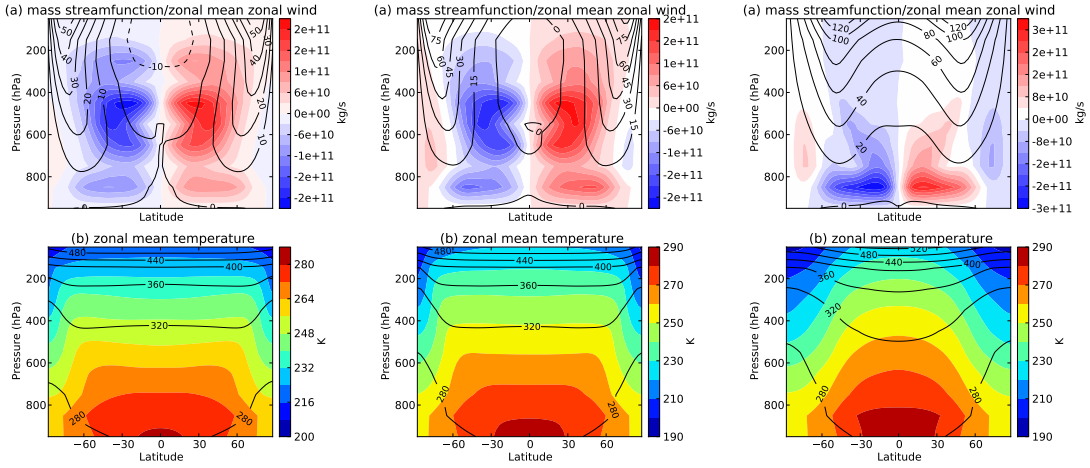

Snapshot at winter solstice

D) $\Omega^* = \frac{1}{8}$, $\alpha = 16$ **E)** $\Omega^* = \frac{1}{8}$, $\alpha = 1.6$ **F)** $\Omega^* = \frac{1}{8}$, $\alpha = 0.16$

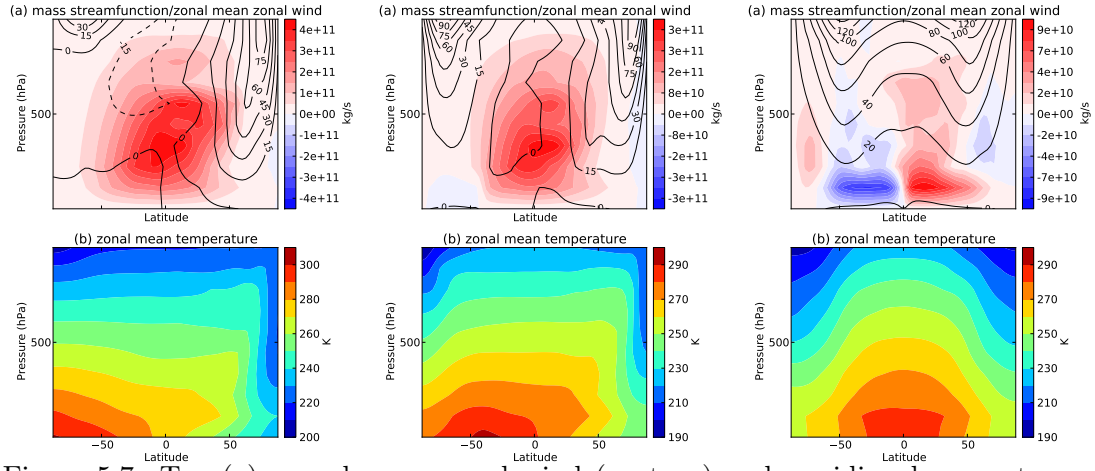

Figure 5.7: Top (a): zonal mean zonal wind (contour) and meridional mass stream function (colour); Bottom (b): zonal mean temperature (colour) for simulations with **seasonality parameter** $\alpha = 16, 1.6, 0.16$, i.e. $\tau_s = 3.6, 36, 360$ days. Plots A, B, C show annual mean fields, while plots D, E, F show a snapshot at northern winter solstice. (Constants: $\Omega^* = \frac{1}{8}$, $\mathcal{G} = 1$, $\tau_{atm} = 40$ days, $\tau_f = 1$ day)

away from the equator (with maxima at $\lambda = -45°$ when $\alpha = 1.6$ and $\lambda = -90°$ when $\alpha = 16$). Consequently, the flattening of the temperature profile in the annual-mean is a consequence of direct heating from the surface, rather than an increased atmospheric heat flux. In addition an extremely large cross-equatorial Hadley cell is present over most of the atmosphere (spanning from $\lambda = -45°$ to $45°$ when $\alpha = 1.6$ and $\lambda = -60°$ to $50°$ when $\alpha = 16$). Both $\alpha = 1.6$ and $\alpha = 16$ cases still show extratropical jets, but the equatorial jet is absent.

In the annual mean, the $\alpha = 16$ case shows a remarkably flat meridional temperature profile. From this alone it may be possible to relate this simulated atmosphere to the weak temperature gradient (WTG) approximation (Sobel et al., 2001), which assumes a flat atmospheric temperature gradient above the frictional boundary layer. However, when looking at the snapshot during the winter solstice in Fig. 5.7D, we see a significant drop in temperature at $\phi = 60°$N which is associated with a strong jet in the winter hemisphere with wind speeds of up to 75 ms^{-1}. This seasonal behaviour may make the WTG approximation unusable here. According to Mills and Abbot (2013), the WTG approximation is valid if the propagation of gravity waves around the globe has a shorter timescale than the radiative timescale. In our simulation the atmospheric radiative timescale is 40 days, however, the radiative timescale of the surface is $\tau_{surf} = 3.6$ days. Assuming an inverse buoyancy frequency $\frac{1}{N}$ of a few minutes and a scale height of $H = 10$ km, the global gravity wave timescale $\tau_{gw} = 2\pi r_{Earth} \cdot HN$ of the order of a day. While $\tau_{gw} < \tau_{surf}$ is still valid, the values may be too close.

A previous study by Mitchell et al. (2014) has identified that strong surface seasonality can arrest equatorial superrotation via two distinct mechanisms. Firstly, seasonality causes a reduction of the average atmospheric angular momentum. Secondly, strong seasonality prevents the convergence of eddy momentum flux. We explain these points using diagnostics from our PUMA-GT simulations.

In Figure 5.8, we show the mass flux of the Hadley circulation, where blue regions signify the upward mass flux of the inter-tropical convergence zone (ITCZ) (Mitchell et al., 2014). Angular momentum is generated in the frictional boundary layer near the surface and is then transported upwards by the ITCZ. At $\alpha = 0.16$ (Fig. 5.8C), the ITCZ has only minor departures from the equator. However, at larger α, larger

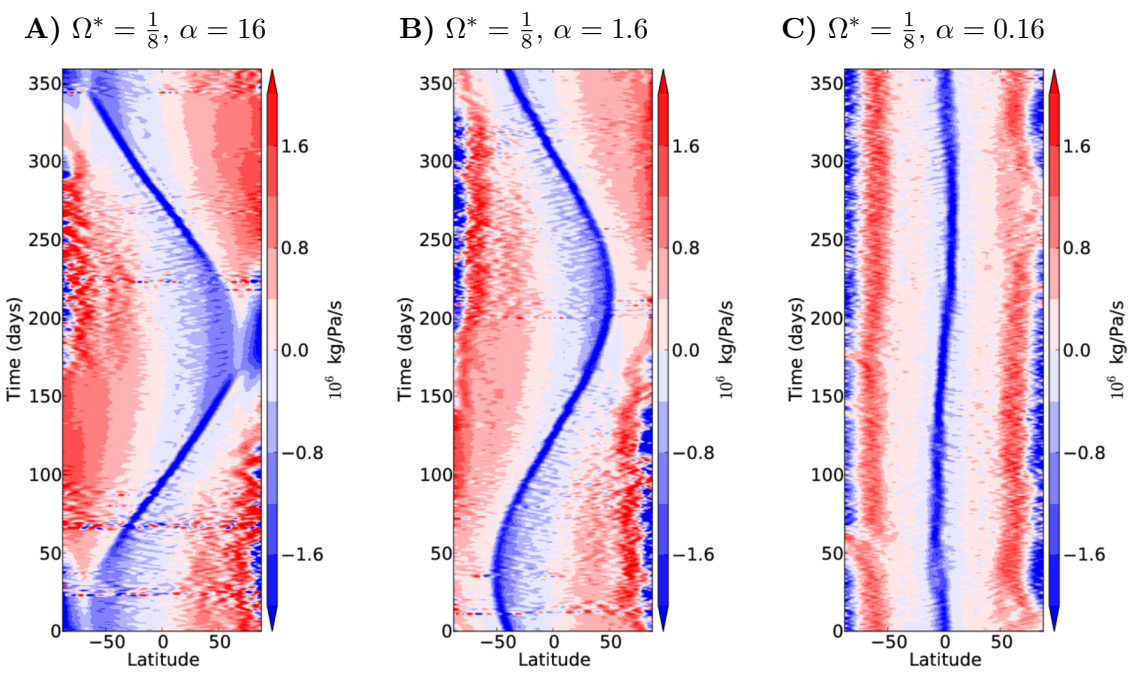

Figure 5.8: Zonal mean Vertical mass flux $[\rho\omega]$ shown over the last model year. (Constants: $\Omega^* = \frac{1}{8}$, $\mathcal{G} = 1$, $\tau_{atm} = 40$ days, $\tau_f = 1$ day)

departures from the equator can be seen during summer and winter. In the $\alpha = 16$ case (Fig. 5.8A), the ITCZ is capable of reaching the poles. As the momentum at the surface is maximal at the equator, Mitchell et al. (2014) argue that significant departures of the ITCZ from the equator will result in less angular momentum being transported up into the atmosphere.

Previous works (see e.g. Mitchell and Vallis, 2010, Potter et al., 2014, Wang, 2014, Laraia and Schneider, 2015) have established that in simulations with constant forcing emerging equatorial superrotation is maintained by convergence of an eddy angular momentum flux. Mitchell et al. (2014) show that with added seasonal variation, this convergence can become arrested. In cases with very with large seasonality, they find that eddy angular momentum flux convergence at the equator only occurs during instances when the zonal mean zonal wind is approximately symmetrical about the equator. At other times, angular momentum flux is asymmetric about the equator. In Fig. 5.9 we visualise this effect by showing the meridional eddy momentum flux $\overline{u'v'\cos\phi}$, where primes denote the deviation from the annual mean, both in annual mean (Fig. 5.9 A-C) and at the winter solstice (Fig. 5.9 D-F). In these plots northward flux is positive (solid) and southward flux is negative (dashed). In the case with weak

Annual mean

A) $\Omega^* = \frac{1}{8}$, $\alpha = 16$ **B)** $\Omega^* = \frac{1}{8}$, $\alpha = 1.6$ **C)** $\Omega^* = \frac{1}{8}$, $\alpha = 0.16$

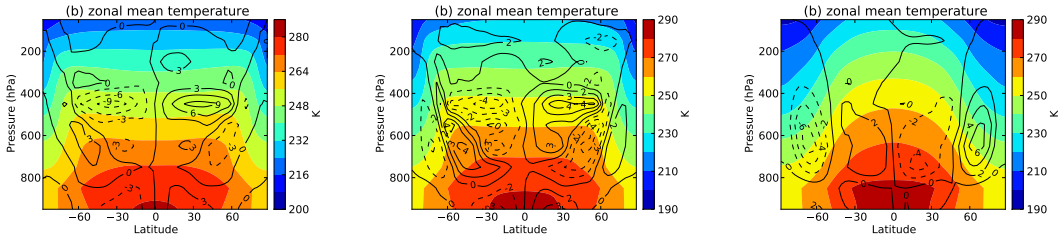

Snapshot at winter solstice

D) $\Omega^* = \frac{1}{8}$, $\alpha = 16$ **E)** $\Omega^* = \frac{1}{8}$, $\alpha = 1.6$ **F)** $\Omega^* = \frac{1}{8}$, $\alpha = 0.16$

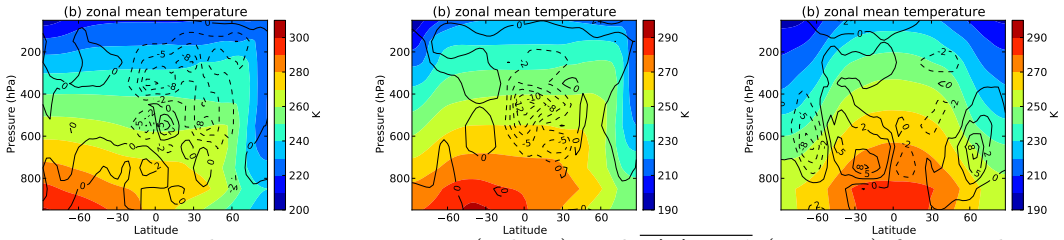

Figure 5.9: Zonal mean temperature (colour) and $\overline{u'v'}\cos\phi$ (contour) for simulations with seasonality parameter $\alpha = 16, 1.6, 0.16$, i.e. $\tau_s = 3.6, 36, 360$ days. Plots A, B, C show annual mean fields, while plots D, E, F show a snapshot at northern winter solstice. (Constants: $\Omega^* = \frac{1}{8}$, $\mathcal{G} = 1$, $\tau_{atm} = 40$ days, $\tau_f = 1$ day)

seasonality ($\alpha = 0.16$, Fig. 5.9 C, F) we see that eddy angular momentum converges at the equator in annual mean. During the winter solstice the eddy angular momentum flux is stronger in the southern hemisphere, nevertheless the flux is still centred about the equator. This cannot be said for the cases with stronger seasonality (Fig. 5.9 D, E). Here the region where eddy angular momentum flux converges is shifted towards the southern hemisphere at 30°S and 15°S, respectively. In addition, the northern hemisphere component is significantly stronger than its southern counterpart. This behaviour persists during most of the year and hence total eddy angular momentum is transported away from the equator so that equatorial superrotation is being arrested.

Greenhouse parameter $\mathcal{G}(\chi_{sw})$

When varying the greenhouse parameter $\mathcal{G}$ at slow rotation rates, the annual mean diagnostic fields (Fig. 5.10A-C) reveal that the vertical temperature gradient reverses with increasing $\mathcal{G}$. At negative $\mathcal{G}$, radiative heating is concentrated in the upper atmosphere, with only little heat reaching the surface. In addition the meridional temperature gradient decreases with decreasing $\mathcal{G}$. This can be attributed to the seasonal behaviour (Fig. 5.10A-C) of runs with $\chi_{sw} \neq 0$ at $\mathcal{A} = 400$ (c.f. Section 5.3.1).

Annual mean

A) $\Omega^* = \frac{1}{8}$, $\mathcal{G} = 1$ **B)** $\Omega^* = \frac{1}{8}$, $\mathcal{G} = 0$ **C)** $\Omega^* = \frac{1}{8}$, $\mathcal{G} = -0.7$

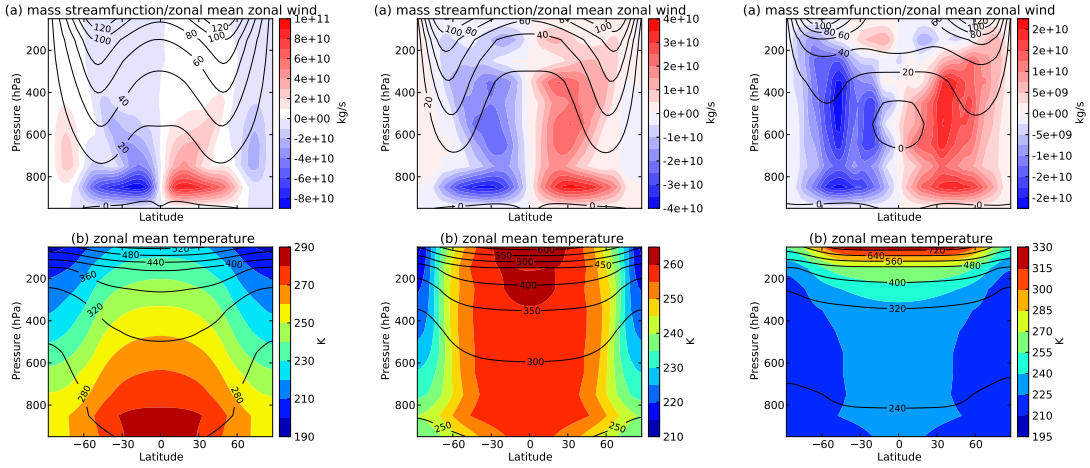

Snapshot at winter solstice

D) $\Omega^* = \frac{1}{8}$, $\mathcal{G} = 1$ **E)** $\Omega^* = \frac{1}{8}$, $\mathcal{G} = 0$ **F)** $\Omega^* = \frac{1}{8}$, $\mathcal{G} = -0.7$

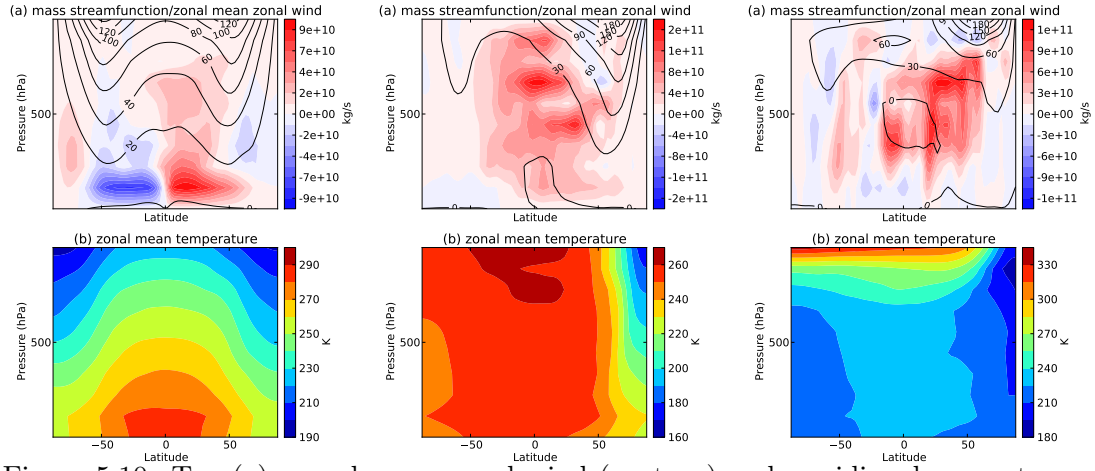

Figure 5.10: Top (a): zonal mean zonal wind (contour) and meridional mass stream function (colour); Bottom (b): zonal mean temperature (colour) for simulations with **atmospheric relaxation parameter** $\mathcal{A} = 16, 80, 400, 2000$, i.e. $p_s = 0.04, 0.2, 1, 5$ bar. Plots A, B, C show annual mean fields, while plots D, E, F show a snapshot at northern winter solstice. (Constants: $\Omega^* = \frac{1}{8}$, $\mathcal{G} = 1$, $\alpha = 0.16$, $\tau_f = 1$ day)

Annual mean

A) $\Omega^* = \frac{1}{8}$, $\mathcal{G} = 0$, $\mathcal{A} = 80$ **B)** $\Omega^* = \frac{1}{8}$, $\mathcal{G} = 0$, $\mathcal{A} = 400$ **C)** $\Omega^* = \frac{1}{8}$, $\mathcal{G} = 0$, $\mathcal{A} = 2000$

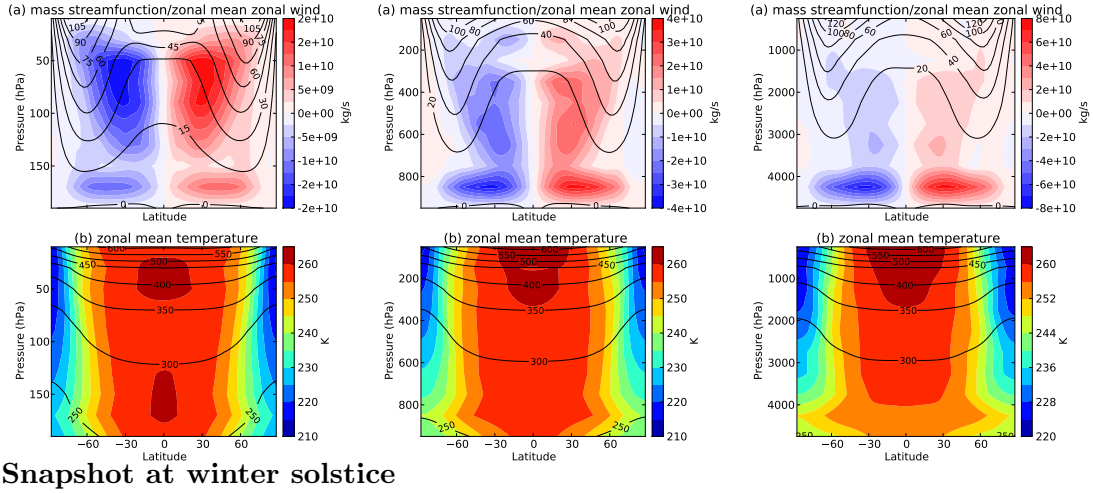

Snapshot at winter solstice

D) $\Omega^* = \frac{1}{8}$, $\mathcal{G} = 0$, $\mathcal{A} = 80$ **E)** $\Omega^* = \frac{1}{8}$, $\mathcal{G} = 0$, $\mathcal{A} = 400$ **F)** $\Omega^* = \frac{1}{8}$, $\mathcal{G} = 0$, $\mathcal{A} = 2000$

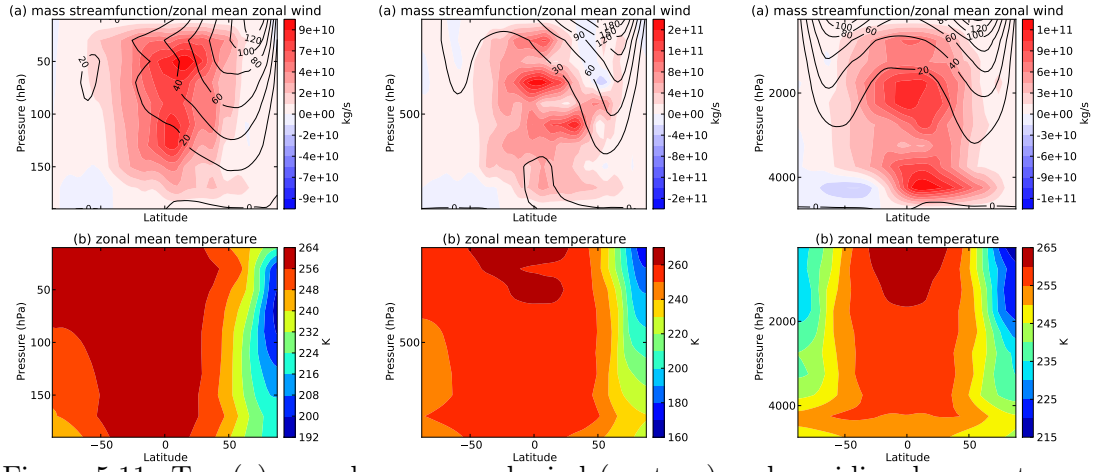

Figure 5.11: Top (a): zonal mean zonal wind (contour) and meridional mass stream function (colour); Bottom (b): zonal mean temperature (colour) for simulations with **atmospheric relaxation parameter** $\mathcal{A} = 80, 400, 2000$, i.e. $p_s = 0.2, 1, 5$ bar. Plots A, B, C show annual mean fields, while plots D, E, F show a snapshot at northern winter solstice. (Constants: $\Omega^* = \frac{1}{8}$, $\mathcal{G} = 0$, $\alpha = 0.16$, $\tau_f = 1$ day)

As a response to the weakening meridional temperature gradient with decreasing $\mathcal{G}$, the extratropical jets weaken in the annual mean plots (Fig. 5.10A-C). We also see a weakening of the equatorial super-rotating flow. This is a consequence of both weaker extratropical jets (from which eddy momentum flux converges at the equator) and from stronger seasons, which influence the effectiveness of both meridional eddy momentum flux convergence as well as vertical momentum flux at the equator.

Atmospheric thermal relaxation number $\mathcal{A}(p_0)$

In this section, we vary the atmospheric relaxation number $\mathcal{A}$ at constant $\mathcal{G} = 0$, $\alpha = 0.16$ and $\Omega^* = \frac{1}{8}$. The previous section has already shown that at $\mathcal{G} = 0$, the

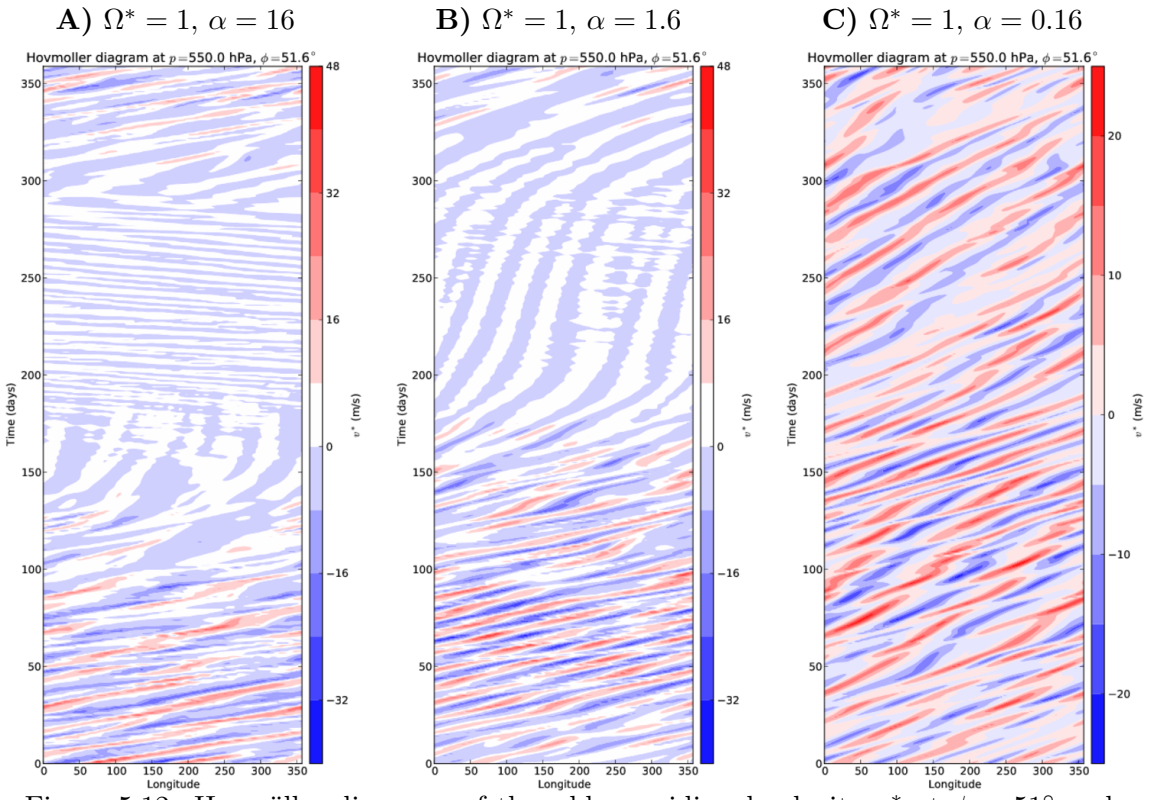

Figure 5.12: Hovmöller diagrams of the eddy meridional velocity v^* at $\phi = 51°$ and $p = 550$ hPa. Run with $\Omega^* = 1$, $\alpha = 0.16$, $\mathcal{G} = 1$, and $\mathcal{A} = 400$ ($\tau_{atm} = 40$ days)

atmosphere behaves strongly seasonal due to direct absorption of solar flux. In the annual mean (Fig. 5.11A-C) the simulated atmospheres do not strongly differ from each other. The snapshots at seasonal extremes (Fig. 5.11D-F), however, show that the extratropical jet on the summer hemisphere becomes weaker with decreasing $\mathcal{A}$. At $\mathcal{A} = 80$, this summer jet is nearly vanished. Super-rotating flow at the equator is still present in all cases, and slightly weakened at low $\mathcal{A}$. The temperature fields at winter solstice show how strongly the seasonal forcing affects the atmospheres in their extremes. As before, decreased $\mathcal{A}$ (i.e. increased α_{atm}) increases the seasonal variability.

5.4 Wave activity

In this section, we briefly show the wave activity of extratropical jets for simulations with varying surface seasonality parameter α using Hovmöller diagrams. This will provide further phenomenological understanding of the seasonal response within our parameter space. As an example for the geostrophic and cyclostrophic regimes, we again present only simulations with $\Omega^* = 1$ and $\Omega^* = \frac{1}{8}$, respectively.

Figure 5.12 shows three Hovmöller diagrams of the eddy meridional velocity $v^* =$

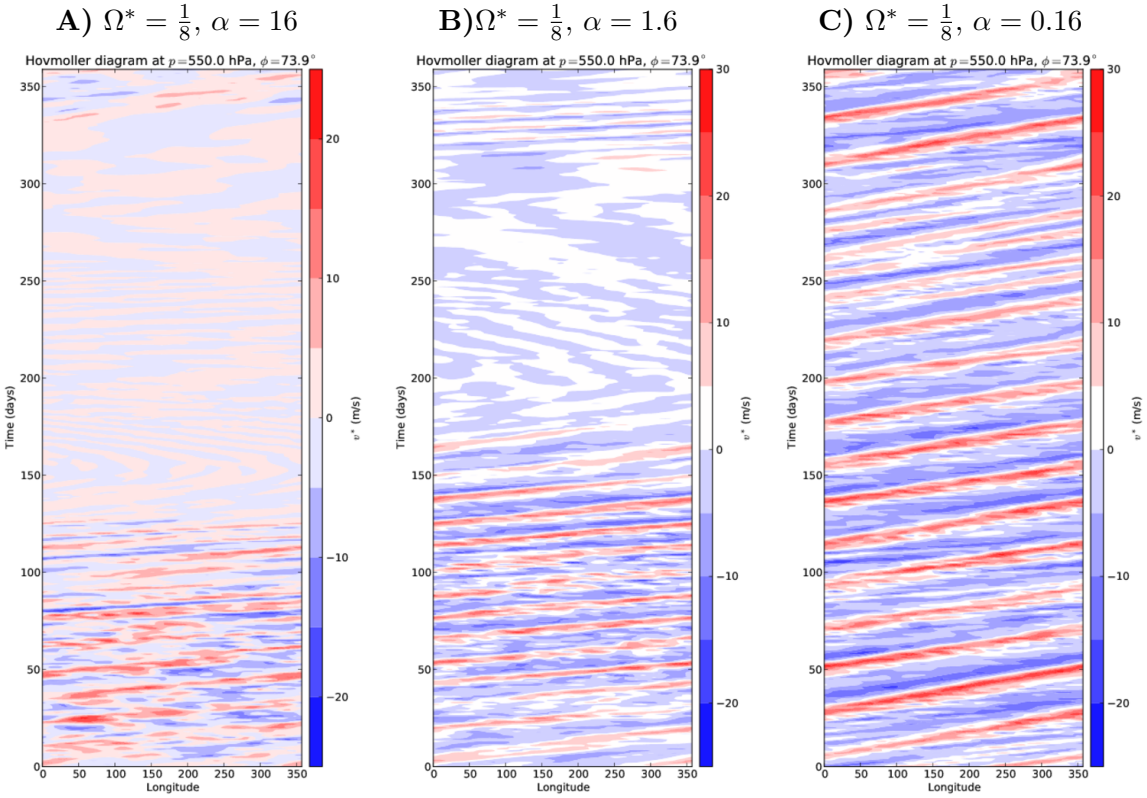

Figure 5.13: Hovmöller diagrams of the eddy meridional velocity v^* at $\phi = 51°$ and $p = 550$ hPa. Run with $\Omega^* = \frac{1}{8}$, $\alpha = 0.16$, $\mathcal{G} = 1$, and $\mathcal{A} = 50(\tau_{atm} = 40$ days)

$v - [v]$ at $\Omega^* = 1$ and varying α (c.f. Fig. 5.3 for zonal mean diagnostics). The plots show the northern hemisphere, extratropics at latitude $\phi = 51°$ and at pressure level $p = 550$ hPa. At $\alpha = 0.16$ (Figure 5.12C), we see a mixture of both wavenumber-3 and wavenumber-4 waves throughout the whole year. Around the spring equinox[5], the jet is slightly strengthened (from day 70 to day 160). In this range, wavenumber-3 and wavenumber-2 signals seem to be superposed.

With increasing α (Figure 5.12A, B), the speed of the jet during winter (and spring) increases. Additionally, the onset of the strengthening of the winter-hemisphere jet occurs earlier. This phenomenon is called seasonal lag, which is given by the time difference between maximum solar input at the solstices and when the maximum temperature of the surface is reached. This seasonal lag occurs on e.g. Earth and Titan. On Mars, however, both surface and atmospheric heating timescales are short enough, so that the seasonal lag is negligible. The same is true for the surface in our $\alpha > 1$ cases. In addition, we can see in Fig. 5.12A, B that, the jet ceases completely and the wave intensity becomes very small, between spring equinox (day 80) and summer solstice (day 170). This decrease in duration of the winter jet is also an effect of the rapid seasonal change of surface temperatures for $\alpha > 1$.

[5]which occurs roughly at day 80. Note that day 0 is January 1st

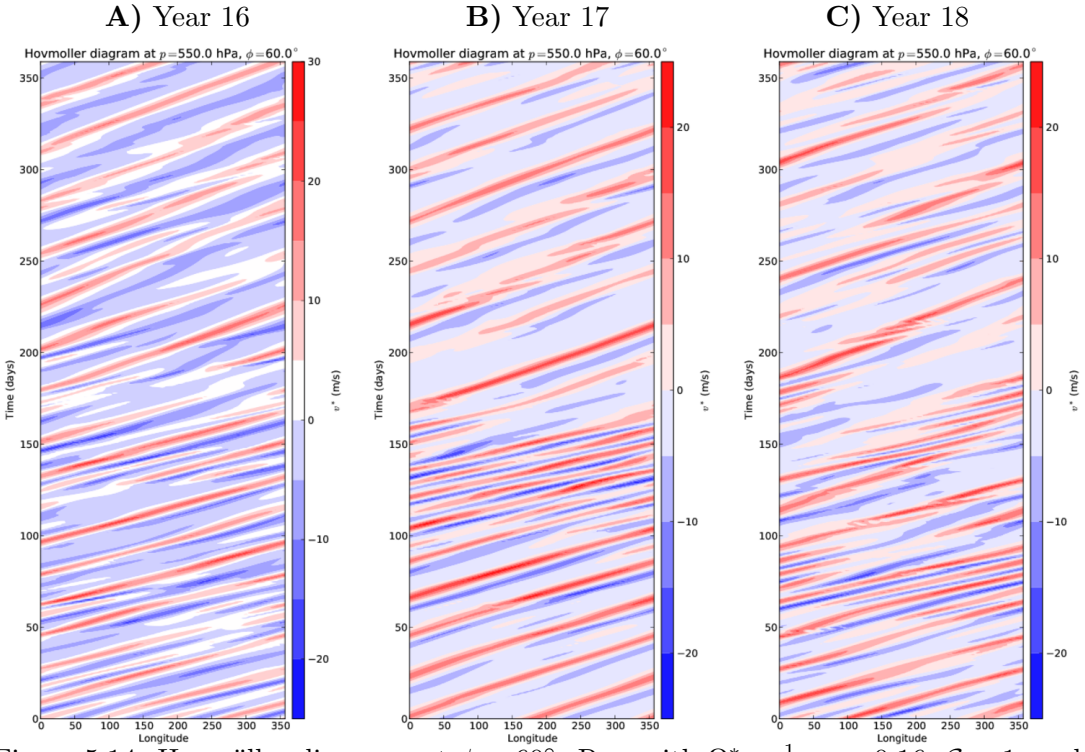

Figure 5.14: Hovmöller diagrams at $\phi = 60°$. Run with $\Omega^* = \frac{1}{2}$, $\alpha = 0.16$, $\mathcal{G} = 1$, and $\mathcal{A} = 200$ ($\tau_{atm} = 40$ days)

At slower rotation rates, increasing α will hinder the development of equatorial superrotation (c.f. Fig. 5.7, Mitchell et al., 2014). In Fig. 5.13 we show Hovmöller diagrams of eddy meridional velocity at $\phi = 51°$ and $p = 550$ hPa. As before we can see that with increasing α, the jet becomes stronger during the winter and early spring, but diminishes significantly at all other times. In the cyclostrophic regime these jets are usually dominated by wavenumber-1 waves (Mitchell and Vallis, 2010, Wang, 2014). This is the case in our simulations as well.

5.4.1 Interannual variability

Simulations without temporally-variable forcing (Wang, 2014, Kaspi and Showman, 2015, i.e. without seasonal forcing, e.g.) converge to an equilibrium state within a few model years. While our seaonally-forced simulations also converge, there is nevertheless a interannual variability present.

In Figure 5.14, we show Hovmöller diagrams in the extratropics of the final 3 years of the simulation with $\Omega^* = \frac{1}{2}$, $\alpha = 0.16$, $\mathcal{G} = 1$, and $\mathcal{A} = 200$ ($\tau_{atm} = 40$ days). From days 0 to 100, the first two years (Fig. 5.14A, B) show fairly stable wavenumber-2 signals. In the final year (Fig. 5.14C), however, a wave-3 pattern occurs between days 60 and 90. During the middle year (Fig. 5.14B), a similar wave-3 signal occurs between days 100 and 150. In this time frame, the first year exhibits wavenumber-4 jets

from days 130 to 160, whereas the third year exhibits a wavenumber-1 jet modulated by a wavenumber-3 pattern. In the other half of the years (days 180 to 360), the extratropical jet is mostly dominated by wavenumber 1 and 2 waves. One abberation from this behaviour is the development of a wavenumber 3 pattern at around day 250, which occurs in both the first and third year.

Overall, this behaviour is a strong argument for the occurrence of interannual variability in our seasonally-forced simulations when the atmosphere is only weakly susceptible to seasons (in this case due to $\alpha = 0.16$). For more strongly seasonal simulations the inherent signal of seasonal variability (see Fig. 5.12A, B) of intensifying and diminishing extratropical jets dominates over interannual variability. Generally, we expect weak seasonality cases to favour interannual variability, as the modulation in heating and cooling is then weaker. We find that the threshold for an onset of noticeable interannual variability occurs somewhere between $\alpha = 0.16$ and $\alpha = 1.6$.

5.5 Lorenz energy cycle

As mentioned before, the Lorenz energy cycle is an effective way of characterising the global dynamics of an atmosphere which results in a small amount of scalar diagnostics. In this section, we present Lorenz terms for several cross-sections through the PUMA-GT parameter dataset to quantify the effect of the varied parameters towards the energy and conversion cycle of the modelled atmospheres in terms of barotropic, baroclinic or zonal energy exchanges in the atmosphere. In addition, this analysis is helpful to compare with the time-evolution of, as well as the effect of seasonal contributions to the Lorenz energy budget of reanalysis data of actual planets (i.e. Earth and Mars, Chapter 2).

5.5.1 Regime Diagram

We first present the mean conversion terms over the last three model years in Fig. 5.15 with dependence upon multiple non-dimensional parameters. The regime diagrams given in Fig. 5.15 require some explanation. The figure consists of four plots, one for each Lorenz conversion term. Each plot displays multiple coloured dots, each repre-

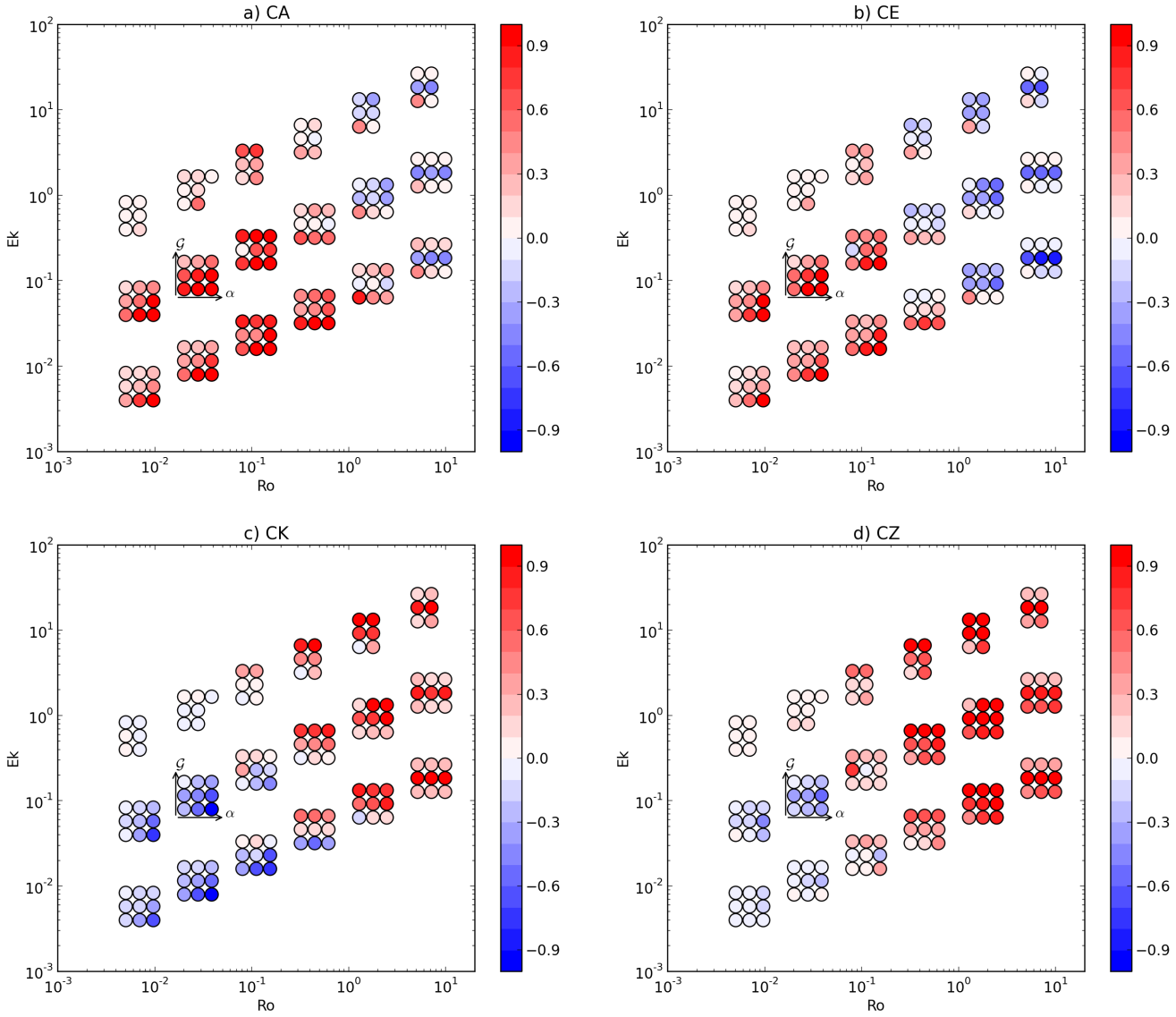

Figure 5.15: Regime diagrams of the Lorenz cycle conversion terms, averaged over 3 model years: a) C_A, b) C_E, c) C_K, d) C_Z, given in dependence upon $\mathcal{R}o$, Ek, $\mathcal{G}$ and α. Clusters of points are artificially moved to discern variations in greenhouse parameter $\mathcal{G} = 1, 0, -0.7$ (in y direction) and seasonality parameter $\alpha = 0.16, 1.6, 16$ (in x direction). Constants: $p_{surf} = p_0$, $n_\mu = 1$ (daily-averaged insolation). Conversion terms are given in Wm^{-2}.

senting a single value result for one model simulation (in this case the single value result is the three-year mean of a respective conversion term). These results are given by the colour of the dot (where blue is negative and red is positive) and in dependence upon 4 variables: the thermal Rossby number $\mathcal{R}o$ on the x-axis and the Ekman number Ek on the y-axis; and as offsets the greenhouse parameter $\mathcal{G} = 1, 0, -0.7$ (in y-direction) and the seasonality parameter $\alpha = 0.16, 1.6, 16$ (in x-direction). The Earth-like reference simulation with $\Omega^* = 1$, $\alpha = 0.16$, $\mathcal{G} = 1$, $\mathcal{A} = 400$ ($\tau_{atm} = 40$ days), $\tau_f = 1$ day is located at the point where the $\mathcal{G}$ and α arrows meet.

Interestingly, Fig. 5.15 shows that every conversion term experiences a change in sign somewhere in the four-dimensional parameter space. The key controlling parameter of this change seems to be $\mathcal{R}o$. However, $\mathcal{R}o$ does not act alone. Varying just Ω^* at otherwise Earth-like parameters (assuming constant $\alpha = 0.16$, $\mathcal{G} = 1$, $\mathcal{A} = 400$, $\tau_f = 1$ day), causes only C_K and C_Z to switch signs whereas C_E and C_A do not (see Fig. 5.17). Both $\mathcal{G}$, and to a smaller extent α, help in making that change in sign. While $\mathcal{G}$ has only a weak effect on C_A at Earth-like values ($\mathcal{R}o(\Omega^* = 1) = 0.02$), at larger $\mathcal{R}o$ (smaller Ω^*) a decrease of $\mathcal{G}$ can cause C_A (Fig. 5.15a) to become negative. This behaviour occurs due to (c.f. 5.10):

1. the expansion of the Hadley cell with rising $\mathcal{R}o$ and the consequent narrowing of the region where meridional temperature gradients occur,

2. the inversion of the vertical temperature profile with decreasing $\mathcal{G}$ (c.f. Eqn. 4.7)

C_E (Fig. 5.15b) also becomes negative for larger $\mathcal{R}o$ and smaller $\mathcal{G}$, which shows that the entire baroclinic conversion pathway (C_A, C_E) is significantly weakened. In this regime C_K (Fig. 5.15c) becomes positive and it rises significantly in magnitude at points where C_A and C_E are below -0.5 Wm^{-2}. This shows that barotropic instability (with which positive C_K is associated) overtakes baroclinic instability as the primary eddy generating mechanism in the region with larger $\mathcal{R}o$ and smaller $\mathcal{G}$ (roughly the right hand side of the regime diagram). C_Z also assumes positive values above 0.6 Wm^{-2} in this regime, which can be attributed to the expanding Hadley cell's enhanced thermally direct circulation.

Only comparatively minor changes can be observed with varying Ek by the values

chosen for this parameter study. Due to this reason we focus on the variation of $\mathcal{A}$ in Figure 5.16. Unlike Fig. 5.16, where variation in Ek changes mostly the intensity of the conversion terms, in Figure 5.16 we see that the atmosphere becomes less baroclinic with rising $\mathcal{A}$, causing the conversion rates of the Lorenz energy cycle in Fig. 5.16 to change signs in the bottom right-hand side of the regime. Also of note are the $\mathcal{G} = 0$ cases for larger Rossby numbers (Fig. 5.16, right hand side of each plot), which become dominated by barotropic conversion, as $C_K \geq 1$ and the baroclinic pathway is reversed ($C_A < 0$, $C_E < 0$).

Figure 5.16 also features the locations of terrestrial solar system bodies. In this figure, the labelled arrow points at the point in the $\mathcal{R}o$-$\mathcal{A}$ plane, where the respective planet is located. Venus is located beyond the right-hand edge of the plot at $\mathcal{R}o = 300$. For Earth and Mars, we display the values of the conversion terms from reanalysis data (Fig. 2.3). The Mars data is normalised to Earth-pressure so that the colour can be seen more clearly. For the Lorenz data for Titan we use modelling output (Del Genio and Zhou, 1996). The Earth data was already compared in previous sections as it lies at the point in parameter space of the reference simulation. Within our parameter space, Mars lies near a region where baroclinic conversion (C_A, C_E) gradually decreases so that C_E becomes negative at $\mathcal{R}o = 0.32$. The Lorenz energy cycle calculated from reanalysis data in Chapter 2 shows a stronger baroclinic conversion rate. Our analysis of purely seasonally-forced simulations at Mars-like values of $\mathcal{R}o = 0.08$, $\alpha = 16$ with dust-free conditions ($\mathcal{G} = 1$) and a thin atmosphere with $\mathcal{A}$ between 40 and 8 (i.e. $\tau_{atm} = 8, 1.6$ days, respectively) shows significantly weaker baroclinic conversion rates (especially for C_E). Even when the atmosphere is dusty (i.e. $\mathcal{G} < 1$), e.g. $\mathcal{G} = 0$, the simulations in the current Chapter do not meet values for C_E expected from our reanalysis data results. In Section 6.3.5, we will come back to this issue, when computing the Lorenz energy budget for simulations with both seasonal and diurnal effects. Overall, as the atmosphere becomes less baroclinic with declining $\mathcal{R}o$ in our seasonal simulations, barotropic instabilities rise ($C_K > 0$). C_Z also matches and both model and Mars data describe an atmosphere with thermally direct circulation. The behaviour of C_K, and C_Z matches well to the data from the Mars reanalysis featured in Chapter 2.

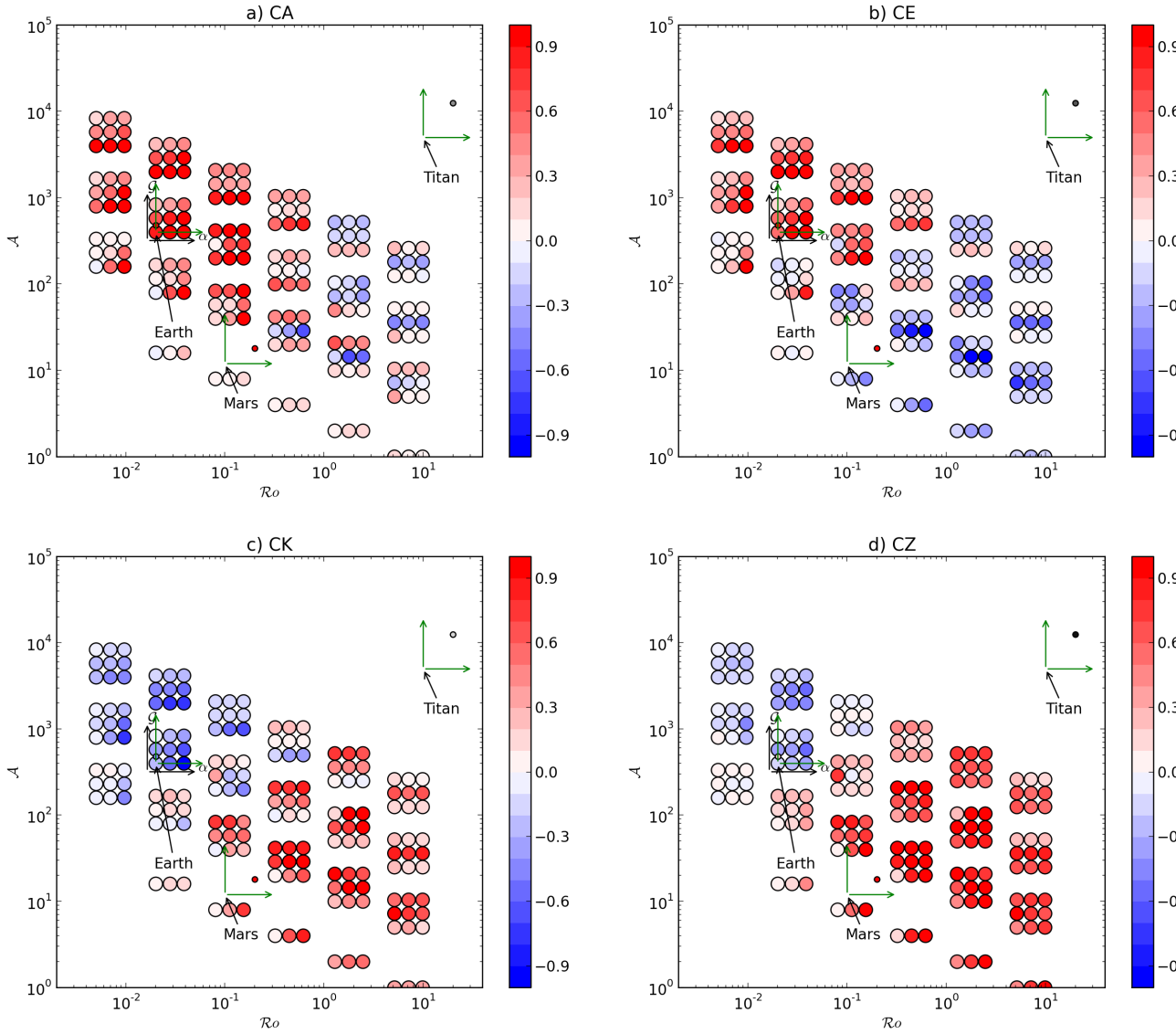

Figure 5.16: Regime diagrams of the Lorenz cycle conversion terms, averaged over 3 model years: a) C_A, b) C_E, c) C_K, d) C_Z, given in dependence upon $\mathcal{R}o$, $\mathcal{A}$, $\mathcal{G}$ and α. Clusters of points are artificially moved to discern variations in greenhouse parameter $\mathcal{G} = 1, 0, -0.7$ (in y direction) and seasonality parameter $\alpha = 0.16, 1.6, 16$ (in x direction). Constants: $\tau_f = 1$ day, $n_\mu = 1$ (daily-averaged insolation). Conversion terms are given in Wm^{-2}.

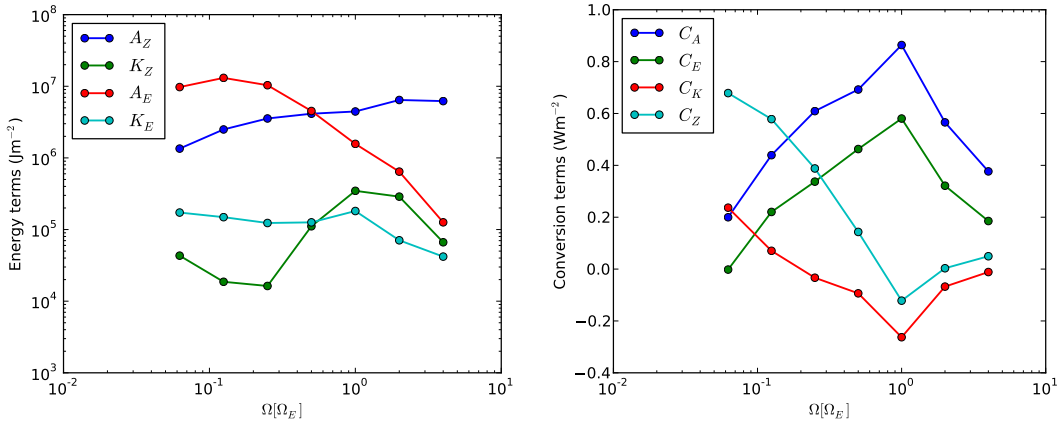

Figure 5.17: Energy (left) and conversion (right) terms of annual-mean, global-mean Lorenz energy cycle for different rotation rates Ω at constant $\alpha = 0.16$, $\mathcal{G} = 1$, $\mathcal{A} = 400$, $\tau_f = 1$ day.

5.5.2 Response to single parameters

Here we present a few detailed responses to variations of single parameters.

Response to thermal Rossby number $\mathcal{R}o(\Omega)$

This section shows the dependence of the Lorenz energy budget on varying $\mathcal{R}o$ via the planetary rotation rate Ω for the dataset computed using PUMA-GT with seasonally-varying solar forcing. The defined positive direction of the conversion terms is given in Fig. 2.1.

Figure 5.17 depicts the values for the Lorenz energy (left) and conversion (right) terms with varying Ω. Overall the behaviour of energy and conversion terms is in accord with the Lorenz budgets produced by Wang (2014) using PUMA-S (see Fig. 4.2). For the depicted parameter range, A_Z is small for small Ω and increases with increasing Ω. In contrast, an inverse dependence on Ω is observed for A_E and K_E. The zonal kinetic energy K_Z is less monotonic and features a peak value at Ω_E. Regarding conversion terms, there is a peak in the baroclinic conversion pathway (C_A, C_E) at Ω_E, which coincides with a corresponding minimum for C_K and C_Z. At lower Ω, C_Z and C_E become larger than the baroclinic pathway. This behaviour fits well to the values of Fig. 4.2. There are slight differences, however, since C_E becomes negative at $\Omega = \frac{1}{16}\Omega_E$ for the PUMA-GT simulations and the change of sign for C_K occurs at $\Omega = \frac{1}{8}\Omega_E$ instead of $\Omega = \frac{1}{4}\Omega_E$. The peak at $\Omega^* = 1$ occurs because at faster rotation

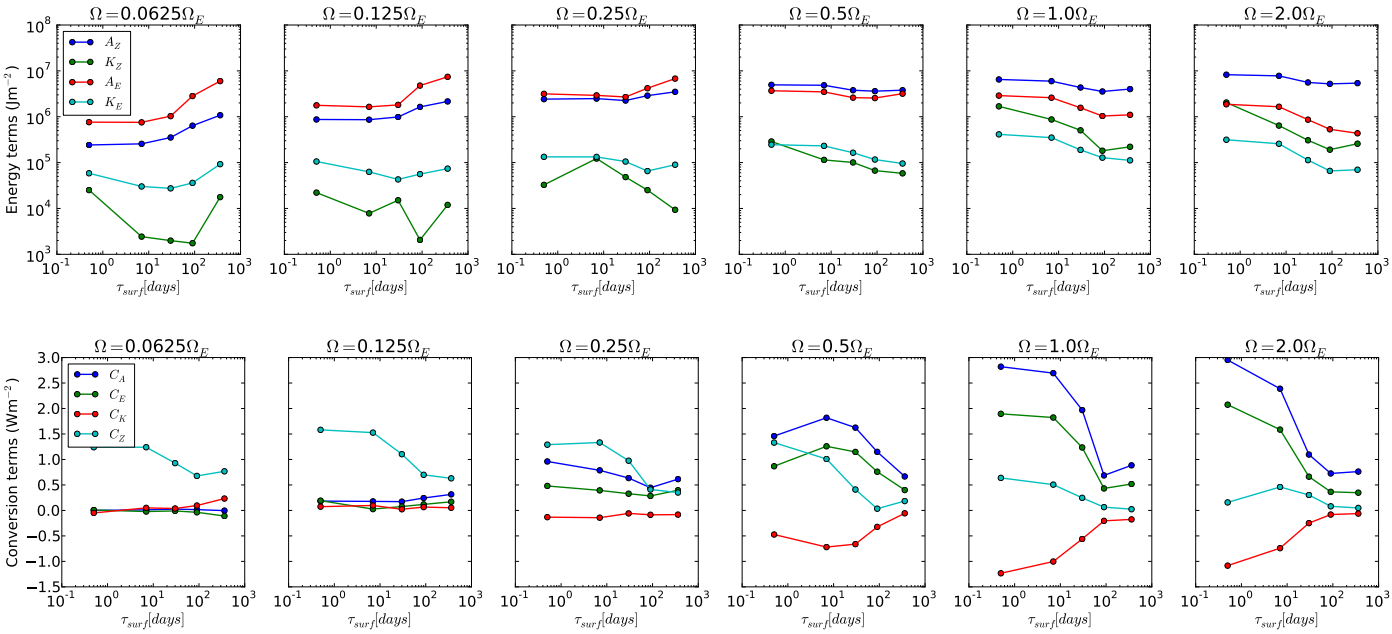

Figure 5.18: Energy (top) and conversion (bottom) terms of annual-mean, global-mean Lorenz energy cycle for each rotation rate Ω plotted against τ_{surf}.

rates, smaller eddy length scales and a smaller extent of the Hadley circulation cell both decrease the meridional transport of energy, which causes an overall decrease of wind velocities (see Fig. 4.2 and discussion). At larger Ω^*, the atmosphere is dominated by meridionally-extensive Hadley cells, and baroclinic wave activity weakens.

Response to seasonality parameter $\alpha(\tau_{surf})$

In this section, we present an alternative subset of simulations, which were used as a preliminary dataset to test PUMA-GT and to identify regions of interest for the final parameter space. The dataset is focussed on quantifying the effect of the surface's susceptibility to seasonality α by varying the surface thermal inertia time scale τ_{surf} in small steps (see Sect. 1.1.3).

In Fig. 5.18 Lorenz energy (top) and conversion (bottom) terms are displayed for simulations using PUMA-GT in the parameter space with $\Omega^* = \frac{1}{16} - 2$ (columns) and $\tau_{surf} = 0.5 - 360$ days (x-axis). As before, the defined positive direction of the conversion terms is given in Fig. 2.1.

Overall, K_Z strongly increases with increasing Ω whereas eddy kinetic energy rises more slowly. As above, A_Z rises and A_E falls with increasing Ω. The response of the

energy terms (Fig. 5.18, bottom) to varying τ_{surf} can be categorised into two distinct Ω-regions. For the first regime with $\Omega^* > 0.5$ most energy terms rise monotonically with decreasing τ_{surf} (increasing seasonality α). The second regime with lower $\Omega^* < 0.25$ features a decrease in available potential energies with increasing seasonality while kinetic energy terms act non-monotonically. There is an intermediate region with $\Omega^* = 0.25 - 0.5$, for which APE terms remain roughly constant for variations in τ_{surf} and kinetic energies begin to act non-monotonically.

Overall, the conversion terms (Fig. 5.18, bottom) show that simulations in the first regime ($\Omega^* \geq 1$) are more strongly affected by the surface thermal inertia timescale, as the conversion terms strongly diverge with decreasing τ_{surf}. Below $\Omega^* = 1$ this divergence is weakened. For $\Omega^* = 0.5$, C_A, C_E, and C_K increase their magnitude only up to a certain point, after which the increasing seasonality will weaken atmospheric energy conversion rates. An exception of this is the zonal conversion C_Z, which continues to increase with rising seasonality. In the second regime ($\Omega^* < 0.25$) the magnitude of the non-zonal conversions (C_A, C_E, and C_K) decreases strongly with decreasing τ_{surf}, so that the rising C_Z strongly outweighs other terms.

The surface seasonality α has a strengthening effect on the intra-annual variability of the circulation. In the first regime, larger variability seems to be mostly strengthening the flow of the underlying circulation, while the second regime is generally weakened by an increase in seasonality. The first regime is the quasi-geostrophic regime, and the second regime the superrotation regime. Mitchell et al. (2014) show that strong seasonal variation can have a weakening effect on the formation and maintenance of superrotation, due to limiting the equatorial convergence of angular momentum (see Section 5.3.2). The strong rise in C_Z with rising α for the superrotation regime is indicative of the expanded Hadley circulation cells, which cross further over the equator during the solstices with increasing seasonality α. This effect is also present in Mars, which, compared to its other conversion terms, has a large C_Z component. This increase in zonal conversion with larger seasonality is indicative of an enhanced thermally direct heating with increased seasonal variation.

For fast rotating planets seasonality seems to strengthen all atmospheric energies and conversion terms. Fig. 5.3 shows snapshots of the eastward wind, meridional mass

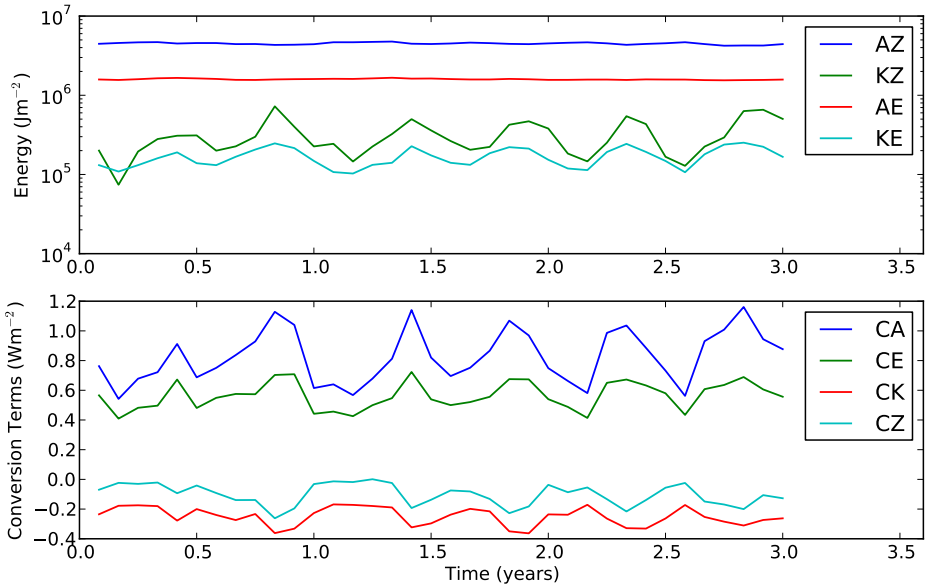

Figure 5.19: Time evolution of energy (top) and conersion (bottom) terms for the last 3 years of model data for the simulation with $\Omega = \Omega_E$, $\tau_{surf} =$ **360 days**, $\tau_f = 1$ day, $\mathcal{G} = 0$, $\tau_{atm} = 40$ days

streamfunction and temperature fields during winter solstice. For small α ($\alpha = 0.16$, $\tau_{surf} = 360$ days, see Fig. 5.3C, F), the temperature profile is fairly symmetrical and both hemispheres feature jets. With increasing α the seasonal extremes reach farther across hemispheres and the temperature maximum shifts towards the south pole. This shift results in a lower meridional temperature gradient in the southern hemisphere and a larger gradient in the northern hemisphere, which limits and strengthens the formation of thermal wind jets, in their respective hemispheres.

To shed more light on the impact of the seasonality parameter α on the seasonal evolution of the Lorenz cycle, we show time evolution plots, similar to Figure 2.6 in Chapter 2. Figure 5.19 depicts an Earth-like case with only weak seasonality ($\alpha = 0.16$). The time $t = 0$ is equivalent to January 1st. Our model simulations have an eccentricity of 0, and hence each season is exactly 0.25 years long.

Once again, the APE terms are larger than their kinetic counterparts. Both APE energy terms show next to no variation (when plotted logarithmically), whereas kinetic energies can be seen to vary periodically. The conversion terms show a strong baroclinic pathway, together with primarily negative C_K and C_Z. The conversion terms all vary noticeably over the years with C_A varying by ± 0.2 Wm^{-2} and the other conversions

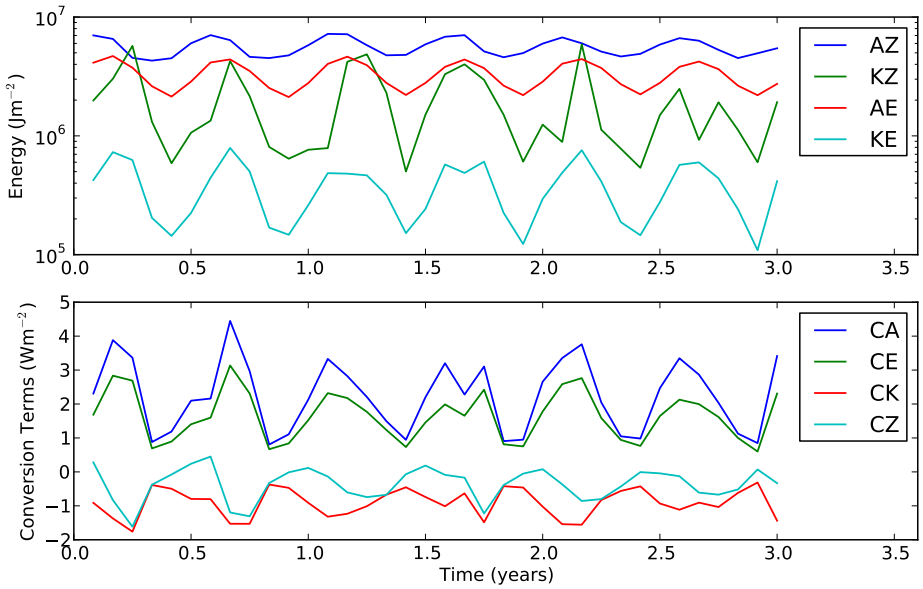

Figure 5.20: Time evolution of energy (top) and conersion (bottom) terms for the last 3 years of model data for the simulation with $\Omega = \Omega_E$, τ_{surf} =**3.6 days**, $\tau_f = 1$ day, $\mathcal{G} = 0$, $\tau_{atm} = 40$ days

by ± 0.1 Wm^{-2}. Spring and fall seasons ($t = 0.25 - 0.50$ and 0.75-1.00, respectively) show maxima in both the KE terms as well as the baroclinic pathway. Conversely, C_K and C_Z possess minima at those times and instead reach their respective maxima during the winter and summer months.

Figure 5.20 shows an example case for strong seasonality ($\alpha = 16$), but otherwise the same parameters as used for Figure 5.19. In this case large seasonal variations are clearly visible (even in the APE terms). The seasonal variation is more pronounced in this simulation. The kinetic energy terms vary by a factor of 10 during the year so that K_Z becomes as large as A_E during the time around the spring and autumn equinoxes at $t = 0.25$ and 0.75 years. The conversion terms also vary more strongly, with C_A varying by ± 1.5 Wm^{-2} and the other terms varying by ± 1.0 Wm^{-2}. C_Z even switches signs during the solstices, so that for a short time thermally direct heating dominates (positive C_Z) over thermally indirect heating in global mean. The baroclinic pathway (C_A, C_E) has a maximum in the winter and summer months ($t = 0.00 - 0.25$ and 0.50-0.75, respectively), which is exactly opposite to the case with weak seasonality in Fig. 5.19. This behaviour is characteristic of a change in seasonal phase lag, which can be discerned from e.g. the time at which the vertical mass flux in Fig. 5.8 reaches its

maximum latitude.

Both cases presented here feature a semiannual periodicity and hence do not match well with the corresponding Mars case in Chapter 2 (which varies annually). However, this is not surprising, as our simulations assume a flat surface, whereas the Mars topology features a strong dichotomy between northern and southern hemispheres.

5.6 Spectral energy budget

In this section we present the effect of seasonal variability on the spectral energy budget (see Section 4.2), by focussing on two parameters (namely, α, and $\mathcal{G}$), that increase the seasonal response of the atmosphere. The simulations shown in this chapter were performed at low resolutions of T42 to allow for a large total number of runs. This means that the spectra presented here will only include the very largest scales. However, slow-rotating atmospheres mostly feature zonal flow and nearly no significant forcing in the small scales, so the unresolved scales likely matter less than for fast-rotating planets. In summary, the results of this section are an important initial step in identifying the spectral behaviour of slowly-rotating planets with seasonal forcing under different atmospheric conditions.

5.6.1 Surface seasonality parameter α

In this section, spectral fluxes for simulations at Earth-like values ($\Omega^* = 1$, $\mathcal{G} = 1$, $\mathcal{A} = 400$ ($\tau_{atm} = 40$ days), $\tau_f = 1$ day and without diurnal cycle) with varying seasonality α are produced to identify its impact on the spectral behaviour of the simulated atmospheres. We show results in the annual mean.

In Figure 5.21 the spectral flux diagnostics for PUMA-GT simulations with varying α are displayed (c.f. Section 4.2). The Earth-like simulation (with weak surface seasonality $\alpha = 0.16$) in Figs. 5.21a,b is comparable to results obtained in the previous chapter with PUMA-S (Figs.4.10a, 4.11a). When considering that PUMA-S and PUMA-GT differ in their method of thermal forcing, the similarity between the spectral fluxes of both models is encouraging. In short, APE flux is downscale at

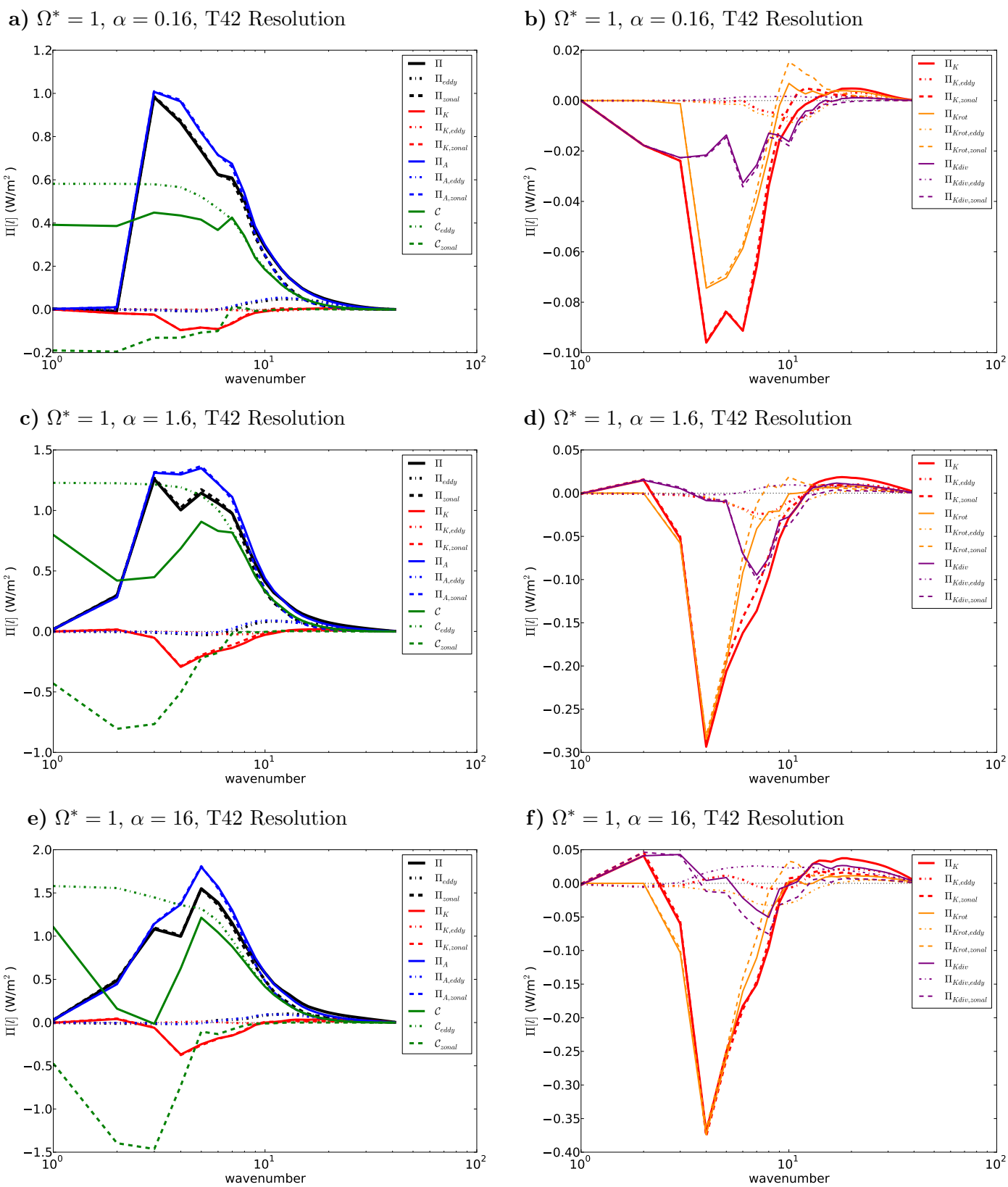

Figure 5.21: Spectral fluxes of KE Π_K, APE Π_A, total energy $\Pi = \Pi_A + \Pi_K$ as well as cumulative conversion $\mathcal{C}$ (left, a,c,e) and spectral fluxes of rotational and divergent KE Π_K (right, b,d,f) (each decomposed into eddy-eddy and residual zonal interaction components) for PUMA-GT runs with $\Omega = 1\Omega_E$ and $\alpha = 0.16, 1.6, 16$ at T42 resolution (annual mean).

all scales and is converted into KE at around wavenumber $k = 10$ (i.e. around the Rossby deformation radius), with a conversion rate of $C \approx 0.6$ W/m^2. The resulting KE is transported mostly upscale due to zonal interactions ($\Pi_{K,zonal}$), with a small fraction of KE going downscale due to mostly eddy-eddy interactions at the smaller scales. At large scales a zonal conversion rate transforms KE into APE. Note that the cumulative conversion terms at wavenumber 1 (i.e. the sum of C_{km}) $\mathcal{C}_{eddy}(k = 1)$ and $\mathcal{C}_{zonal}(k = 1)$ are comparable to the Lorenz energy cycle terms C_E and C_Z, respectively (c.f. Fig. 5.17 at $\Omega^* = 1$).

With increasing α all spectral fluxes become larger when averaged over a year. The total flux Π rises from 0.7 W/m^2 at $\alpha = 0.16$ (Fig. 5.21a) to 1.5 W/m^2 at $\alpha = 16$ (Fig. 5.21e). This occurs largely due to the increase in Π_A. This APE is then converted into KE by an increasing $\mathcal{C}$ in the eddy component, which signifies baroclinic activity. There also occurs an increase in intensity of the zonal component of $\mathcal{C}$. This transforms KE to APE at wavenumber 4, but then back again into KE at wavenumbers 1 and 2. This increase in zonal conversion is consistent with the increased strength of the thermally indirect Ferrel circulation in the winter hemisphere (see Fig. 5.7).

For $\alpha = 0.16$ the kinetic energy flux Π_K features an upscale transport from wavenumbers 13 to 1 and a downscale transport at wavenumbers > 13 with a generally dominating rotational component (Fig. 5.21b). With increasing seasonality, especially the downscale component becomes stronger, peaking at -0.4 W/m^2 for $\alpha = 16$ (Fig. 5.21b). This increase occurs predominantly in the rotational component of Π_K. The divergent component features a stronger downscale flux at very small ($k = 1 - 4$) and large ($k > 13$) wavenumbers. The total increase of the Π_K flux ocurs in association with a generation of stronger jets in the respective winter hemispheres caused by a stronger meridional temperature slope (see Fig. 5.7).

5.6.2 $\mathcal{G}$

The greenhouse parameter $\mathcal{G}$ is varied by changing the short-wave optical depth χ_{sw} of the simulated atmosphere (at a constant long-wave optical depth $\chi_{lw} = 2$). Hence, with smaller $\mathcal{G}$ the atmosphere gets heated from the top more strongly (as opposed to from the long-wave radiation emitted from the planet's surface).

a) $\Omega^* = 1$, $\mathcal{G} = 1$, T42 Resolution

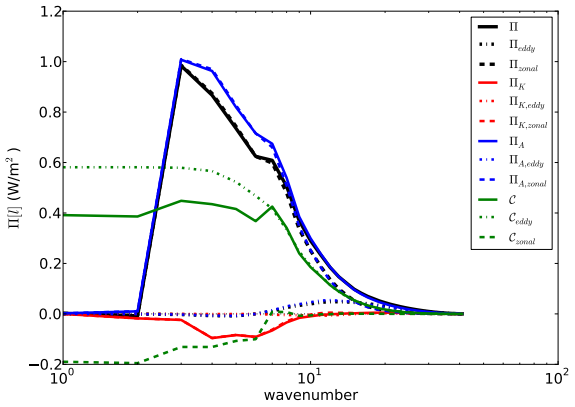

b) $\Omega^* = 1$, $\mathcal{G} = 1$, T42 Resolution

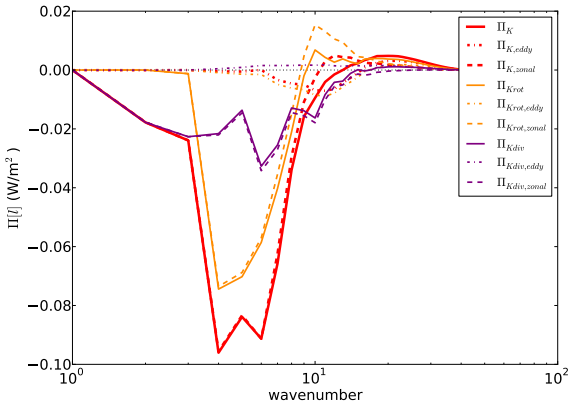

c) $\Omega^* = 1$, $\mathcal{G} = 0$, T42 Resolution

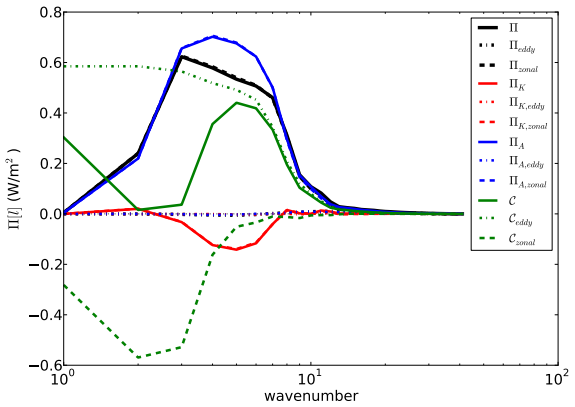

d) $\Omega^* = 1$, $\mathcal{G} = 0$, T42 Resolution

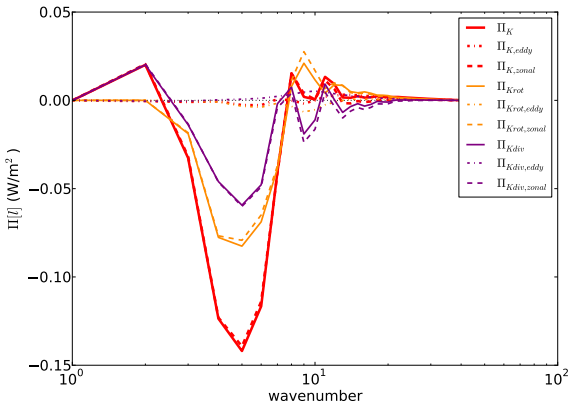

e) $\Omega^* = 1$, $\mathcal{G} = -0.7$, T42 Resolution

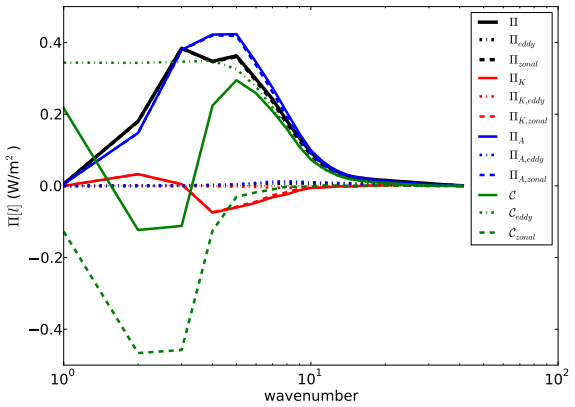

f) $\Omega^* = -1$, $\mathcal{G} = -0.7$, T42 Resolution

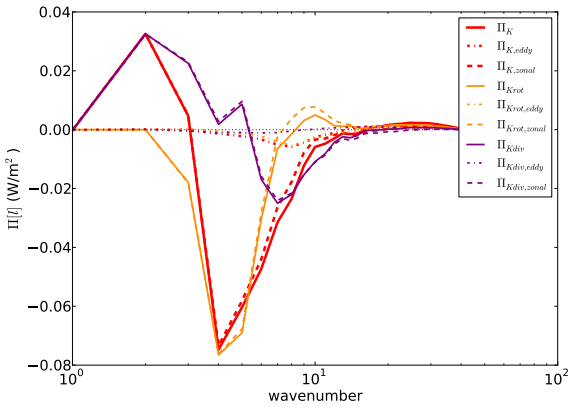

Figure 5.22: Spectral fluxes of KE Π_K, APE Π_A, total energy $\Pi = \Pi_A + \Pi_K$ as well as cumulative conversion $\mathcal{C}$ (left, a,c,e) and spectral fluxes of rotational and divergent KE Π_K (right, b,d,f) (each decomposed into eddy-eddy and residual zonal interaction components) for PUMA-GT runs with $\Omega = 1\Omega_E$ and $\mathcal{G} = 1, 0, -0.7$ at T42 resolution (annual mean).

Figure 5.22 shows the spectral flux diagnostics for varying $\mathcal{G}$. All simulations remain dominated by the APE flux Π_A, which decreases with rising $\mathcal{G}$. This APE flux also remains being baroclinically converted to KE via $\mathcal{C}_{eddy}$, albeit less strongly so with rising $\mathcal{G}$. Similar to the above case with varying α (Section 5.6.1), the zonal conversion $\mathcal{C}_{zonal}$ becomes more negative with decreasing $\mathcal{G}$.

The rotational component of Π_K (in Figs. 5.22b,d,f) remains mostly constant over varying $\mathcal{G}$, whereas the divergent component varies more strongly. Π_{Krot} is mostly upscale (negative) for runs with $\mathcal{G} > 0$, however, at $\mathcal{G} = 0$ and -0.7, Π_{Krot} becomes positive at the smallest wavenumbers, which causes an inflection point in wavenumber space for the Π_K at e.g. $k = 3$ for $\mathcal{G} = -0.7$. This indicates that the kinetic energy flux converges at this wavenumber so that for $\mathcal{G} = -0.7$ wavenumber 3 jets form. Such a behaviour can be observed in the upper atmosphere winter hemisphere.

The overall shape of the spectral fluxes for increasing $\mathcal{G}$ is reminiscent of that of the previous section, where α was increased. This suggests that similar mechanisms may be at play here. In the $\mathcal{G}$ case, stronger seasonality arises from the sun's direct involvement in atmospheric heating and the seasonally-varying insolation due the Earth-like obliquity chosen for these simulations. When calculating the spectral flux for different times of the year (not shown), it becomes clear that the effects of the seasonal circulation discussed here arise primarily during the seasonal extremes (close to the solstices). At these times, a strong winter jet and the corresponding Ferrel-like circulation occur (see e.g. Fig. 5.6F).

5.6.3 $\mathcal{G}$ at $\Omega^* = 1/8$

This section shows flux results in the super-rotating regime ($\Omega^* = \frac{1}{8}$) for variations in $\mathcal{G}$. Figures 5.23a,b show the simulation with $\mathcal{G} = 0$ and $\Omega^* = \frac{1}{8}$. Overall, this run shows a good qualitative comparability with the $\Omega^* = \frac{1}{8}$ PUMA-S run from Sect. 4.3.2 (see Fig. 4.10d). The main differences are that fluxes for $\mathcal{G}_{zonal}$ and Π_K in the PUMA-GT simulation (Fig. 5.23a) are smaller by about a factor of three. Due to the decrease in Π_K the Π_A spectral flux dominates throughout wavenumber space.

An explanation for this is that PUMA-GT simulations feature seasonal variations in solar forcing. The simulations presented in this section have a weak seasonality with

a) $\Omega^* = \frac{1}{8}$, $\mathcal{G} = 1$, T42 Resolution

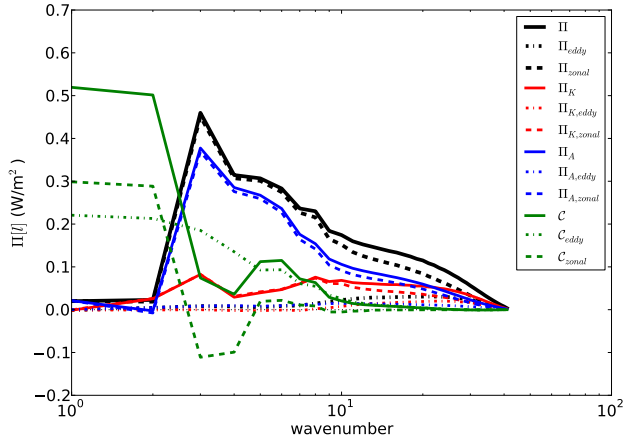

b) $\Omega^* = \frac{1}{8}$, $\mathcal{G} = 1$, T42 Resolution

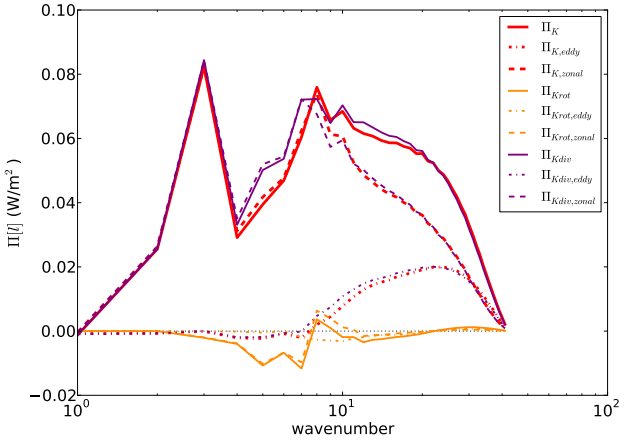

c) $\Omega^* = \frac{1}{8}$, $\mathcal{G} = 0$, T42 Resolution

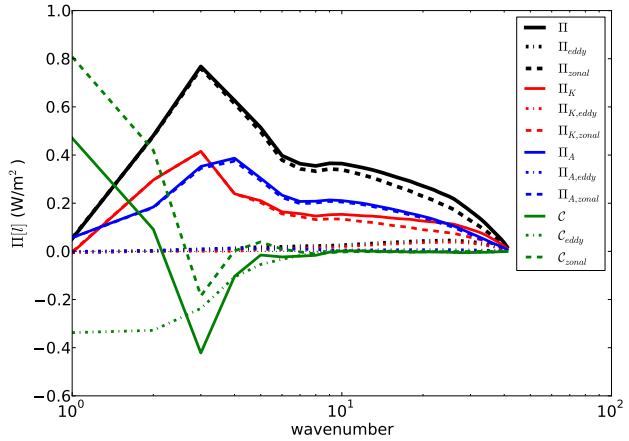

d) $\Omega^* = \frac{1}{8}$, $\mathcal{G} = 0$, T42 Resolution

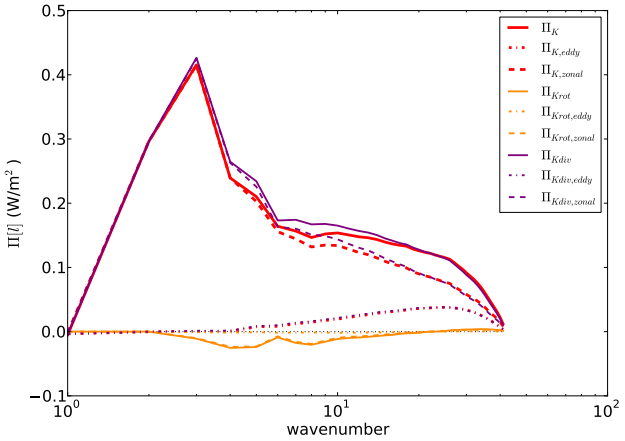

e) $\Omega^* = \frac{1}{8}$, $\mathcal{G} = -0.7$, T42 Resolution

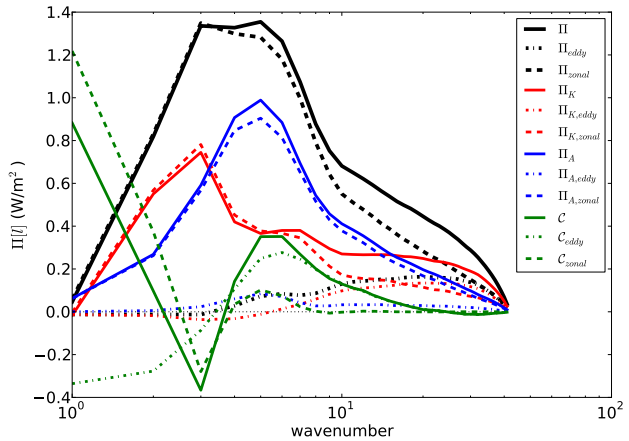

f) $\Omega^* = \frac{1}{8}$, $\mathcal{G} = -0.7$, T42 Resolution

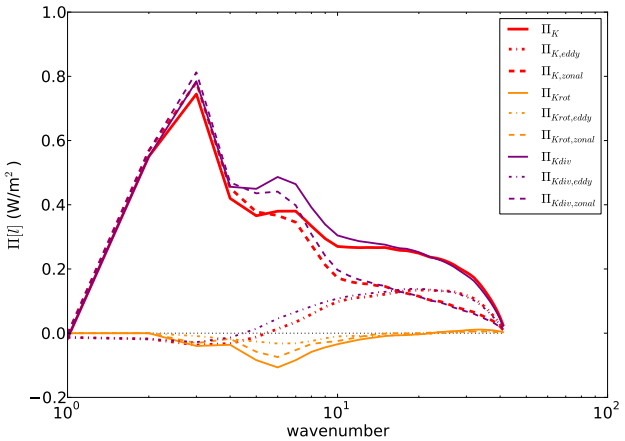

Figure 5.23: Spectral fluxes of KE Π_K, APE Π_A, total energy $\Pi = \Pi_A + \Pi_K$ as well as cumulative conversion $\mathcal{C}$ (left, a,c,e) and spectral fluxes of rotational and divergent KE Π_K (right, b,d,f) (each decomposed into eddy-eddy and residual zonal interaction components) for PUMA-GT runs with $\Omega = \frac{1}{8}\Omega_E$ and $\mathcal{G} = 0, 1, 5$ at T42 resolution (annual mean).

$\alpha = 0.16$. However, according to Mitchell et al. (2014) even weak seasonal signals can influence the equatorial angular momentum flux convergence responsible for producing equatorial superrotation on planets with $\mathcal{R}o > 1$. As this is the case here, there is much less kinetic energy in the annual-mean in this simulation compared to the non-seasonal PUMA-S simulation. As a consequence the spectral fluxes that depend on zonal wind are weakened when comparing Fig. 5.23a and Fig. 4.10d.

When increasing $\mathcal{G}$, annual mean spectral fluxes increase. In the cases of $\mathcal{G} = 0, -0.7$, residual zonal interactions of $\mathcal{C}$ have the strongest impact on converting APE to KE at $k = 1, 2$. This KE is transported downscale, and being converted into APE at $k = 4$. Both KE and APE show downscale fluxes at all scales. The simulation with $\mathcal{G} = -0.7$ has an additional interesting region, where APE is converted back to KE at $k = 7 - 10$. For $\mathcal{G} = -0.7$ the downscale flux of both KE and APE have a significant contribution from eddy-eddy interactions, while for $\mathcal{G} = 0$ this component is negligible and interactions with he zonal-mean flow dominate the downscale flux.

5.6.4 α at $\Omega^* = 1/8$

In this section, we present the energy budget response to α in the cyclostrophic regime at $\Omega^* = \frac{1}{8}$. In this regime, varying α can hinder the development of superrotation at the equator. Despite this significant effect on the global circulation, the spectral fluxes with strong surface seasonality (Fig. 5.24c,e) are very similar in their qualitative characteristics to the fluxes at varying $\mathcal{G}$ in Section 5.6.3. (c.f. Fig. 5.24c,e).

- At $\alpha > 1$, $\mathcal{C}_{zonal}$ has a minimum at $k = 3$ and becomes positive at the smallest wavenumbers.
- Π_K gains in relative importance to Π_A.
- Π_K has a large peak at $k = 3$, which flattens off quickly as larger k.
- At $\alpha = 16$, $\mathcal{C}_{eddy}$ becomes negative.

There are two significant differences between these two sets of spectral fluxes. In the case with $\alpha = 16$, super-rotating equatorial jets are weakened, which causes an overall, lower value of the spectral flux Π, compared to the cases where $\mathcal{G}$ is varied.

a) $\Omega^* = \frac{1}{8}$, $\alpha = 0.16$, T42 Resolution

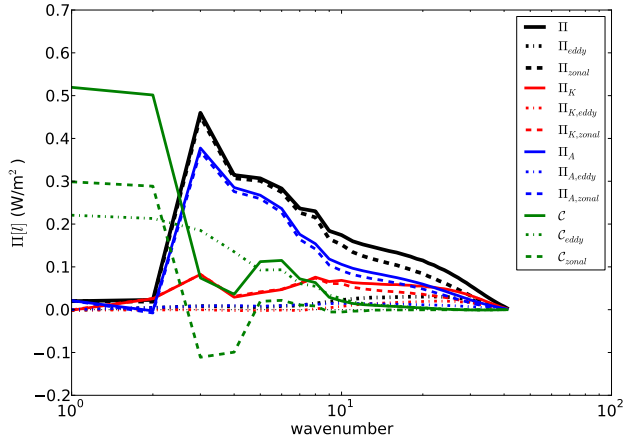

b) $\Omega^* = \frac{1}{8}$, $\alpha = 0.16$, T42 Resolution

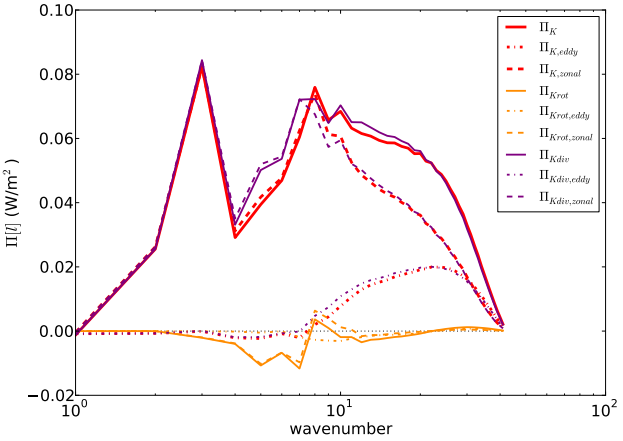

c) $\Omega^* = \frac{1}{8}$, $\alpha = 1.6$, T42 Resolution

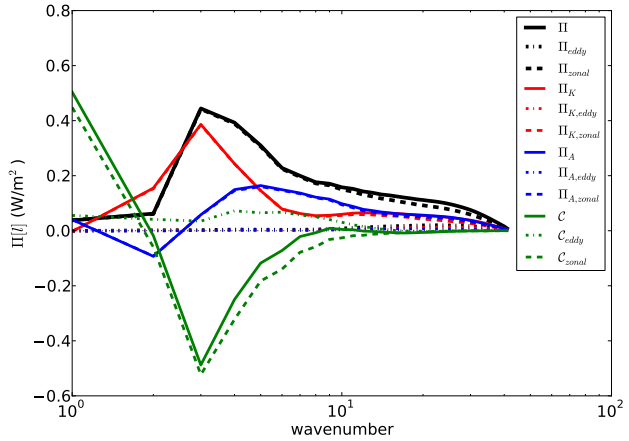

d) $\Omega^* = \frac{1}{8}$, $\alpha = 1.6$, T42 Resolution

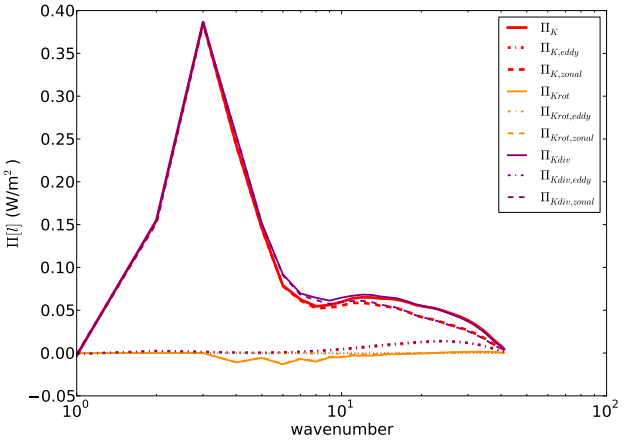

e) $\Omega^* = \frac{1}{8}$, $\alpha = 16$, T42 Resolution

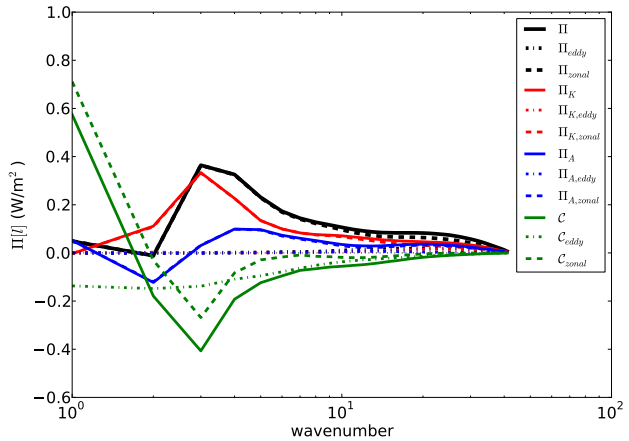

f) $\Omega^* = \frac{1}{8}$, $\alpha = 16$, T42 Resolution

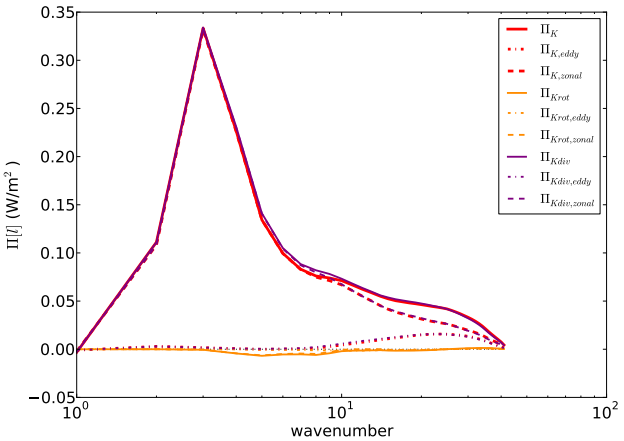

Figure 5.24: Spectral fluxes of KE Π_K, APE Π_A, total energy $\Pi = \Pi_A + \Pi_K$ as well as cumulative conversion $\mathcal{C}$ (left, a,c,e) and spectral fluxes of rotational and divergent KE Π_K (right, b,d,f) (each decomposed into eddy-eddy and residual zonal interaction components) for PUMA-GT runs with $\Omega = \frac{1}{8}\Omega_E$ and $\mathcal{G} = 0, 1, 5$ at T42 resolution (annual mean).

The other difference is that at $\alpha > 1$ the APE flux becomes slightly negative, signifying upscale transport of available potential energy.

5.6.5 Other parameters

We briefly discuss the spectral fluxes for simulations with other parameters in this section. In the investigated parameter space there seem to exist two conceptually different types of spectral fluxes that match with two circulation regimes. Firstly the baroclinic wave regime (see PUMA-S section, runs with $\Omega^* = \frac{1}{2} - 8$ where APE is converted into KE, injected at the Rossby deformation radius, with the resulting KE being transported upscale by an inverse barotropic cascade. Second, a super-rotating regime, where APE is converted into KE at the largest scales and then cascades downscale. Seasonal variations (even small ones) as seen in the case with $\alpha = 0.16$ can interfere with both the equatorial momentum flux convergence and with the annually-averaged spectral flux. The spectral flux of the strongly seasonal simulations presented above receives its dominating contribution during the seasonal extremes (i.e. during solstices).

5.7 Conclusion

In this chapter we have shown the response of the dynamical regimes within our parameter space to seasonally-varying forcing. We have described the effect of seasonal forcing phenomenologically in Section 5.3. We show that when varying single parameters, the simulated atmospheres behave strongly seasonal for $\mathcal{G} < 1$, $\alpha \gtrsim 1$, and $\mathcal{A} < 400$, respectively. For both the fast- and slow-rotating regimes, we find that this seasonality is characterised by a strong cross-equatorial Hadley circulation cell during seasonal extremes with a strong thermally-driven jet in the winter hemisphere. In the cyclostrophic circulation regime (i.e. at slow rotation rates), seasonality affects the development of equatorial superrotation. We identify that our simulations behave in accordance to findings of Mitchell et al. (2014); in simulations with $\mathcal{G} = 1$ and $\alpha \gtrsim 1$ equatorial superrotation no longer develops due to enhanced seasonal variation. This occurs because firstly because less angular momentum is transported from the

boundary layer into the free atmosphere and secondly eddy angular momentum no longer converges at the equator for most of the year (Mitchell et al., 2014). They show that for large radiative atmospheric timescales, equatorial super-rotation reemerges, because the atmosphere reacts too slowly to temperature changes to respond to the seasonal change in surface temperatures. They argue that this may be the mechanism that allows equatorial superrotation to persist in the atmosphere of Titan.

Apart from this, our study has shown that equatorial superrotation is generally not arrested for variation in $\mathcal{G}$, even though a strong seasonal reaction can be seen in cases with $\mathcal{G} < 1$. In addition, for $\mathcal{G} < 1$, as more short-wave radiation is directly absorbed by the atmosphere, the influence of the surface seasonality parameter α decreases. Hence, short-wave absorbing gases in the atmosphere may negate the surface-seasonality-induced arrest of superrotation discussed above. This may be an alternative explanation as to why Titan exhibits equatorial superrotation.

We have also studied the spatial and spectral energy budgets of the simulations in our parameter study. Within our parameter regime every conversion rate switches its sign, which occurs roughly at $\mathcal{R}o = O(10^{-1})$ and $\mathcal{A} = O(10^2)$. In terms of a variation of the surface seasonality-parameter α, the fast-rotating regime shows increasing annual-mean Lorenz conversion rates with increasing α. This behaviour occurs at the same time as an increase in extratropical jets in the winter hemisphere. Our PUMA-GT simulations with a weak seasonal response (i.e. small α, $\mathcal{G} = 1$) have annual mean spectral energy budgets that compare well to the PUMA-S simulations without seasonal variation (c.f. Section 4.2). Simulations with stronger seasonal responses (due to either α, $\mathcal{G}$, or $\mathcal{A}$) show similar trends in their spectra (e.g. conversion from KE to APE due to eddy-eddy interactions between wavenumbers 3 and 8) that occur during seasonal extremes.

Chapter 6

Effects of diurnal solar forcing in simplified atmosphere models

6.1 Introduction

In this chapter, we analyse the impact of diurnally-varying solar forcing on the circulation of planetary atmospheres with a large parameter space. Recent modelling efforts of the Venus atmosphere have found that the diurnal tide plays an important role in the equatorial super-rotating jet (e.g. Lebonnois et al., 2010, 2016). We also look at the effect of the combination of diurnally- and seasonally-varying solar forcing. This may be of interest for two real-world examples. Firstly, Saturn's moon Titan is subject to seasonal forcing, but the long atmospheric timescales (large $\mathcal{A}$) weaken the effects of seasonal forcing so that superrotation can be developed (Mitchell et al., 2014). Due to these long atmospheric timescales diurnal effects are even weaker on Titan, so we expect only a weak influence of diurnally-varying forcing. Secondly, in Chapter 5, our simplified model simulations with only seasonally-varying forcing in the Mars-like regime, with both low surface and atmospheric timescales, have shown weaker baroclinic conversion rates in the Lorenz energy cycle, than we have calculated from reanalysis data of the Mars atmosphere (see Chapter 2, Tabataba-Vakili et al., 2015). In Section 6.3.5 we will analyse how this changes when adding diurnally-varying solar forcing.

6.1.1 Chapter overview

In this chapter, we first present a subset of parameter runs with purely diurnally-varying forcing in Section 6.2. In Section 6.3, we describe the effect of the diurnal forcing on the equatorial jets for a large set of simulations with diurnally- and seasonally-varying forcing. In Section 6.4, we detail the atmospheric behaviour of a few example simulations and compare their reaction to diurnally-varying forcing. Finally, in Section 6.5, we compare the wind speeds of these simulations with theoretical findings on the acceleration of equatorial jets by diurnal thermal forcing and find a simple scaling law.

6.2 Simulations with diurnally-varying solar forcing

In this section, we focus on the impact of diurnal solar forcing on a subset of our parameter space. Here, we have turned off seasonal forcing by setting the planetary obliquity to zero. We focus only on the diurnally-varying solar forcing in order to characterise the effect of diurnally accelerated zonal winds, without the added confusion of seasonal variability. This data will be used in Section 6.5 to analyse if the enhancement of zonal winds is caused by interactions with thermally excited gravity waves (Fels and Lindzen, 1974).

An alternative method of removing seasonal variability would be to use an annually-averaged solar forcing (with nonzero obliquity) and superpose a diurnal cycle. However, since the theory of Fels and Lindzen (1974) focusses on explaining superrotation on Venus, the Venus-like configuration with zero obliquity presents itself as the more suitable option.

6.2.1 Varying the greenhouse parameter

In Figure 6.1, we show three simulations with varying greenhouse parameter $\mathcal{G}$ in the cyclostrophic regime at constant $\Omega^* = \frac{1}{8}$, $\alpha = 0.16$, $\mathcal{A} = 50$ ($\tau_{atm} = 40$days). In Chapter 5, we have shown that this regime features equatorial super-rotating jets. In the present case, we do not show the $\mathcal{G} = 1$ case, as the diurnally-varying forcing has a negligible effect if solar flux is only absorbed at the surface and both surface and

I) No diurnal forcing

A) $\Omega^* = \frac{1}{8}$, $\mathcal{G} = 0.8$ **B)** $\Omega^* = \frac{1}{8}$, $\mathcal{G} = 0$ **C)** $\Omega^* = \frac{1}{8}$, $\mathcal{G} = -0.7$

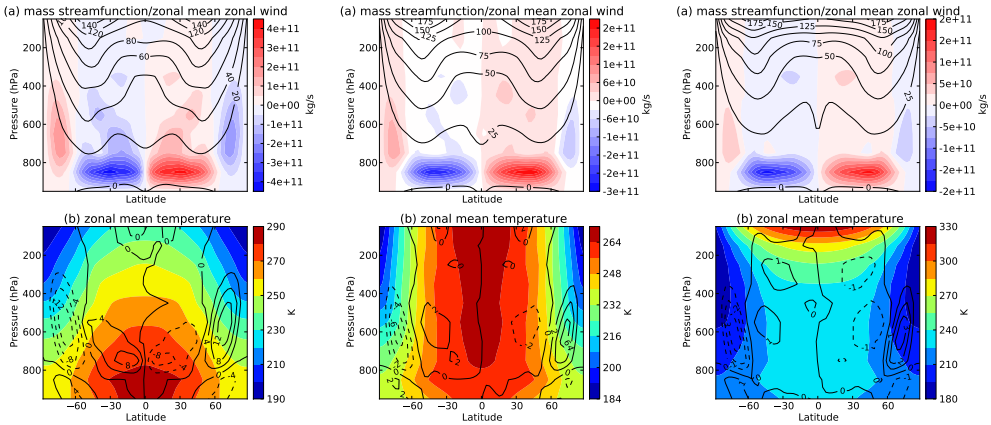

II) Diurnally-varying forcing

D) $\Omega^* = \frac{1}{8}$, $\mathcal{G} = 0.8$ **E)** $\Omega^* = \frac{1}{8}$, $\mathcal{G} = 0$ **F)** $\Omega^* = \frac{1}{8}$, $\mathcal{G} = -0.7$

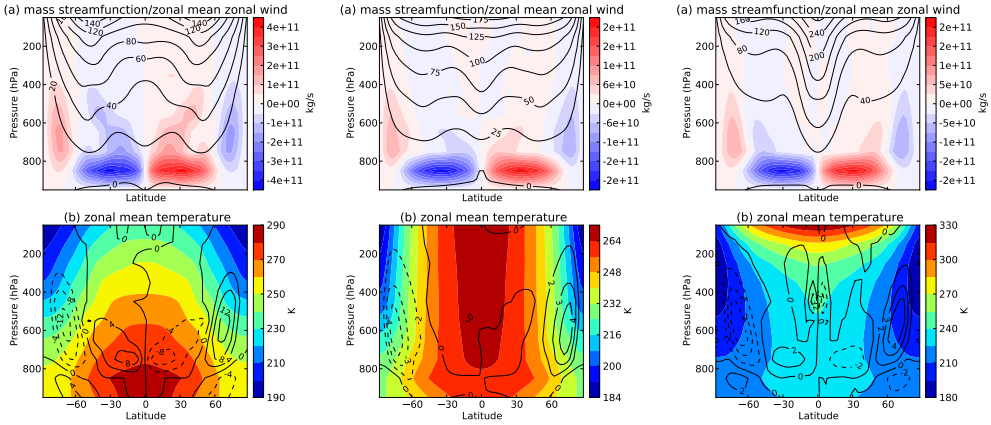

Figure 6.1: (a) meridional mass stream function (colour) and zonal mean zonal wind (contour), (b) zonal mean temperature (colour) and meridional eddy momentum flux (contour) for simulations with and without diurnal cycle. The plotted fields are averaged over one model year. (Constants: $\Omega^* = \frac{1}{8}$, $\alpha = 0.16$, $\mathcal{G} = 1$, $\mathcal{A} = 50$ ($\tau_{atm} = 40$days), $\tau_f = 1$ day

atmospheric timescales are large (i.e. small α, large $\mathcal{A}$). This is why we show the $\mathcal{G}(\chi_{lw} = 0.1) = 0.8$ case in Figure 6.1 instead.

As mentioned before, in these cases the seasonal variation is switched off by setting the obliquity to zero. Hence, the solar irradiance profile has changed to a constant equinox forcing (see Fig. 3.2) and as a result the temperature profile changes. Comparing Fig. 6.1A with the equivalent seasonal case in Fig. 5.7C, we see that the non-seasonal case has a steeper meridional temperature gradient. This occurs because in this case the equator receives more energy and the poles receive less energy in comparison to the seasonally-forced case (Fig. 3.2). When comparing Fig. 6.1A and Fig. 5.7C further, we see that the non-seasonal case features zonal winds that are roughly 20 ms^{-1} faster in the upper atmosphere than in the seasonally forced case. This is likely due to the weaker contrast between polar and equatorial heating rates with nonzero obliquity in the annual mean. A secondary effect is that the weak seasonality of the atmosphere in Fig. 5.7C weakens the super-rotating jet (Mitchell et al., 2014), which the case with zero obliquity does not exhibit (i.e. no seasonal variation).

In these plots, we show the meridional eddy momentum flux $\overline{u'v'\cos\phi}$, where u is the zonal velocity, v is the meridional velocity, ϕ is the latitude, $'$ is the deviation from the annual mean, denoted by $\overline{\ }$. When comparing the non-diurnally-varying (Fig. 6.1A) with the diurnally-varying (Fig. 6.1D) forcing case, we see that there are hardly any differences. This means that in the $\mathcal{G} = 0.8$ case the effect of diurnal forcing is negligible.

With declining values of $\mathcal{G}$, the atmosphere begins to absorb more and more direct solar energy. Once $\mathcal{G}$ becomes negative, the atmosphere is in an Anti-greenhouse state, as more energy is being directly absorbed in the atmosphere than reaches the surface. Without diurnally-varying forcing (Fig. 6.1A-C), this progression will intensify the zonal wind profiles by 20 ms^{-1} (at $\mathcal{G} = 0$, Fig. 6.1B) to 40 ms^{-1} (at $\mathcal{G} = -0.7$, Fig. 6.1C). In these last two cases, the diurnal cycle has a significant impact. In the $\mathcal{G} = 0$ case, the equatorial super-rotating jet is enhanced by 25 ms^{-1} to 60 ms^{-1} in the upper atmosphere. The speed-up in the $\mathcal{G} = -0.7$ case is even higher, with enhancements of over 100 ms^{-1} at the equator.

Normally, the meridional eddy momentum flux is a good diagnostic for under-

standing the speed-up of of the super-rotating jet, because this flux causes equatorial momentum flux convergence (Mitchell and Vallis, 2010, Wang, 2014). In our cases, however, this flux is mostly small. To understand this issue fully, we will look at the momentum flux more comprehensively.

Momentum fluxes

In this section, we examine the transport of relative specific angular momentum $M = au\cos\phi$ of the most strongly accelerated case with $\Omega^* = \frac{1}{8}$, $\alpha = 0.16$, $\mathcal{A} = 50$ ($\tau_{atm} =$ 40 days) and $\mathcal{G} = -0.7$. Figure 6.2 shows the total meridional momentum flux $[\overline{vM}]$ (Fig. 6.2a) with

$$[\overline{vM}] = [\overline{v}][\overline{M}] + [\overline{v}^*\overline{M}^*] + [\overline{v'M'}] \tag{6.1}$$

where $[\overline{v}][\overline{M}]$ is the mean meridional component (Fig. 6.2b), $[\overline{v}^*\overline{M}^*]$ is the stationary wave component [6] (Fig. 6.2c) and $[\overline{v'M'}]$ is the transient wave component (Fig. 6.2d) of the meridional momentum flux (see e.g. Lebonnois et al., 2016). Note that the transient wave component is the proportional to the meridional eddy momentum flux presented in the previous section. Note that in these plots, positive values signify northward and negative values signify southward momentum flux. The zonal wind is shown in contours.

Figure 6.2 shows that the stationary wave component (Fig. 6.2c) is negligible and that the dominant contributions to the meridional momentum flux are given by the mean (Fig. 6.2b) and the transient wave component (Fig. 6.2d). We see that the transient wave component of the diurnal mean case is slightly larger than that of the diurnal cycle case. However, it is the mean meridional component (Fig. 6.2b) that provides the dominant component in both non-diurnally and diurnally-forced cases.

In the non-diurnally-varying case (Fig. 6.2I), the mean meridional component (Fig. 6.2Ib) features a poleward momentum flux on both hemispheres at p=300 hPa and 900 hPa. The transient wave component provides a momentum flux convergence between 200 hPa and 700 hPa. The meridional flux of the diurnally-varying

[6] With a temporal sampling of once per model day, this component is stationary in reference both to the planetary surface and to the subsolar point.

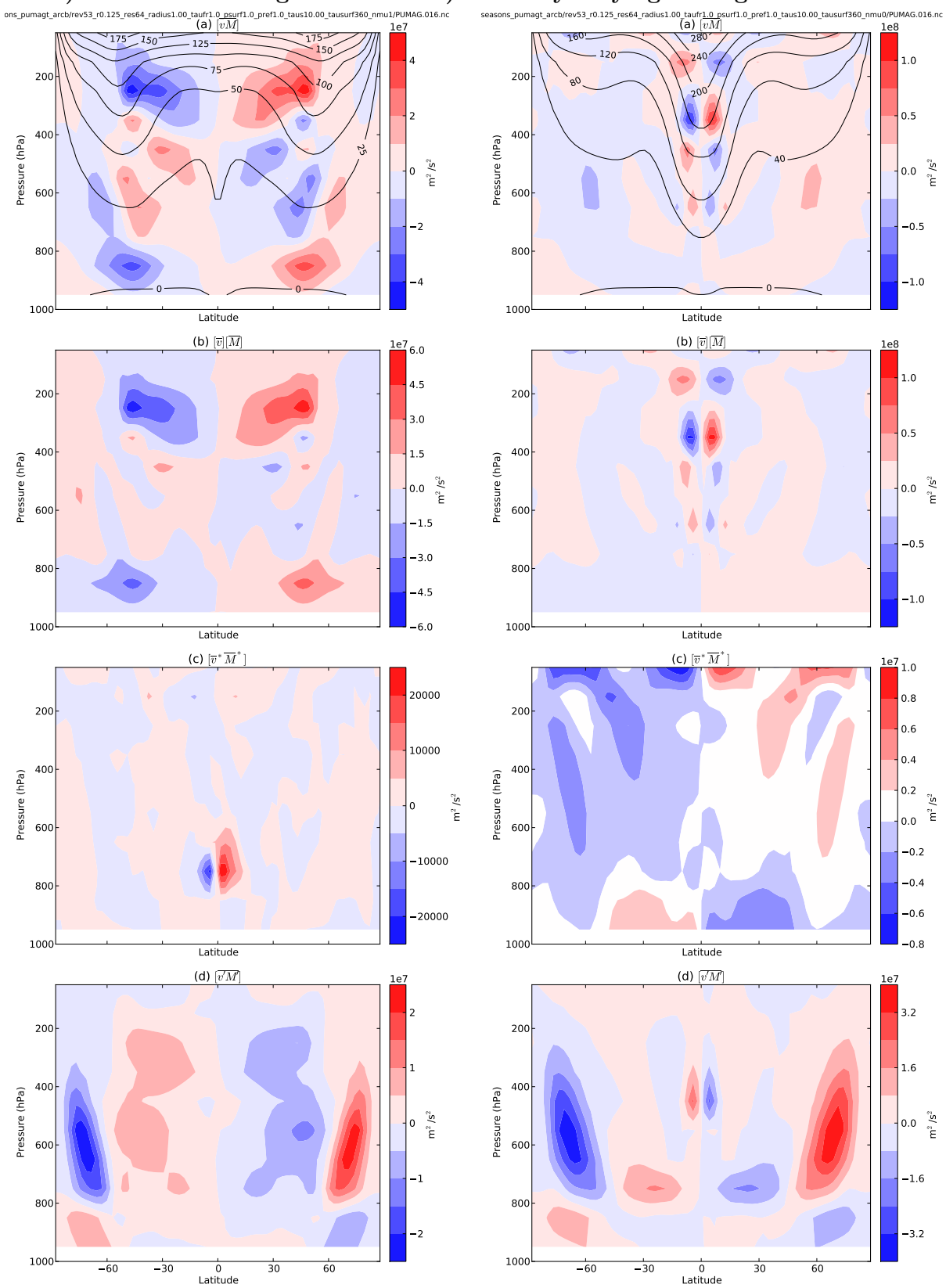

Figure 6.2: Annual mean zonal mean meridional momentum fluxes $[\overline{vM}]$ (a), decomposed into mean meridional $[\overline{v}][\overline{M}]$ (b), stationary wave $[\overline{v}^*\overline{M}^*]$ (c), and transient wave $[\overline{v'M'}]$ (d) components. Fluxes are show for (I) the case with diurnal mean solar forcing (left) and (II) the case with diurnal cycle solar forcing. Contours show mean zonal wind. (Parameters: $\Omega = \frac{1}{16}\Omega_E$, $\tau_{surf} = 360$ days, $\mathcal{G} = -0.7$, $\tau_f atm = 40$ days, $\tau_f = 1$ day)

case (Fig. 6.2II) is more strongly dominated by the mean meridional component (Fig. 6.2IIb). This features a divergent flux from the middle of the equatorial jet at 300 hPa. In this case, the meridional momentum flux converges at 100 hPa and again at 500 and 600hPa. However, in both cases the converging regions of the meridional momentum fluxes do not seem large enough to offset the diverging fluxes with regard to the strong equatorial winds present in both cases.

Due to this reason, we also analyse the vertical momentum fluxes for both cases. Figure 6.3 shows the vertical momentum flux $[\overline{\omega M}]$ and its equally decomposed components. Both forcing cases show a downward (red) momentum flux at the poleward edges of the extratropical jet stream in the mean wave component. In both cases there is an upward (blue) momentum flux at the equator. This looks to be the missing flux responsible for maintaining the equatorial jet in the diurnally forced case. In this case (Fig. 6.3II) the upward flux is larger by a factor of 20 (when compared to the non-diurnal case).

It is unclear in which way the solar forcing at the top of the atmosphere triggers upward momentum fluxes from the surface in the diurnal cycle case. The initial phase of the GRW-mechanism relies on an injection of momentum from the surface (via friction) into the equatorial upper atmosphere via the equatorward and upward arms of the Hadley circulation. The GRW-mechanism just requires this surface momentum flux during the spin-up phase and further convergence of momentum at the equator is generated by barotropic instability. In the diurnally-forced case, however, the equatorial super-rotating jet is rather directly energised by vertical momentum fluxes at the equator as opposed to meridional momentum flux convergence from other latitudes.

6.2.2 Varying the atmospheric relaxation parameter

Variation of the atmospheric relaxation parameter $\mathcal{A}$ is controlled by the radiative timescale τ_{atm} in the atmosphere. The model variable that is varied in these cases is the surface pressure. Note that to keep these simulations comparable the optical depths used to control $\mathcal{G}$ are normalised towards the respective surface pressure. Figure 6.4 shows the cases for varying $\mathcal{A}$ at constant $\Omega^* = \frac{1}{8}$ and $\mathcal{G} = -0.7$. The case with $\mathcal{A} = 50$ (Fig. 6.4B,F) was already shown in the previous section. When going to

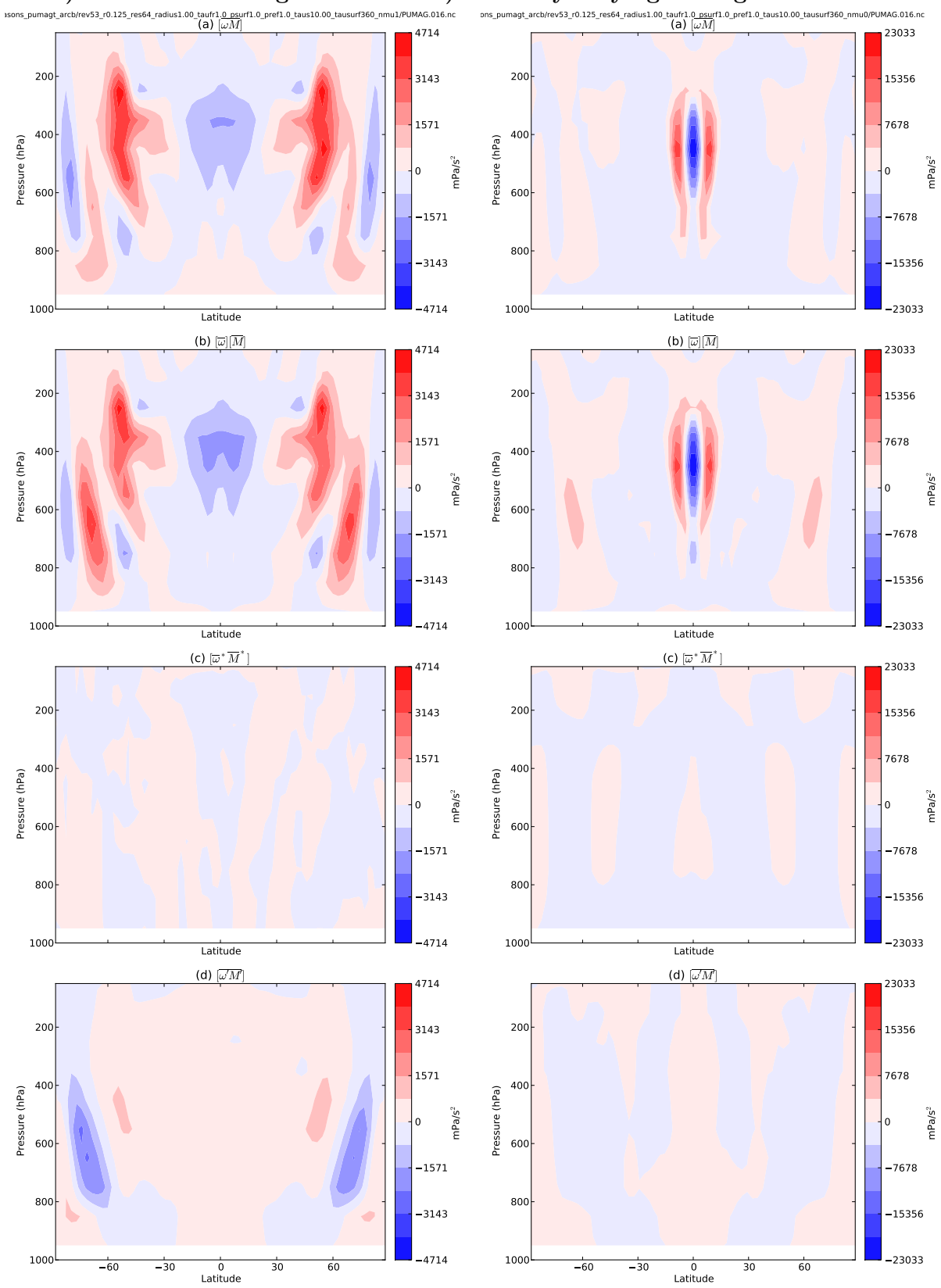

Figure 6.3: Annual mean zonal mean vertical momentum fluxes $[\overline{\omega M}]$ (a), decomposed into mean meridional $[\overline{\omega}][\overline{M}]$ (b), stationary wave $[\overline{\omega}^*\overline{M}^*]$ (c), and transient wave $[\overline{\omega' M'}]$ (d) components. Fluxes are show for (I) the case with diurnal mean solar forcing (left) and (II) the case with diurnal cycle solar forcing. (Parameters: $\Omega = \frac{1}{16}\Omega_E$, $\tau_{surf} = 360$ days, $\mathcal{G} = -0.7$, $\tau_{atm} = 40$ days, $\tau_f = 1$ day)

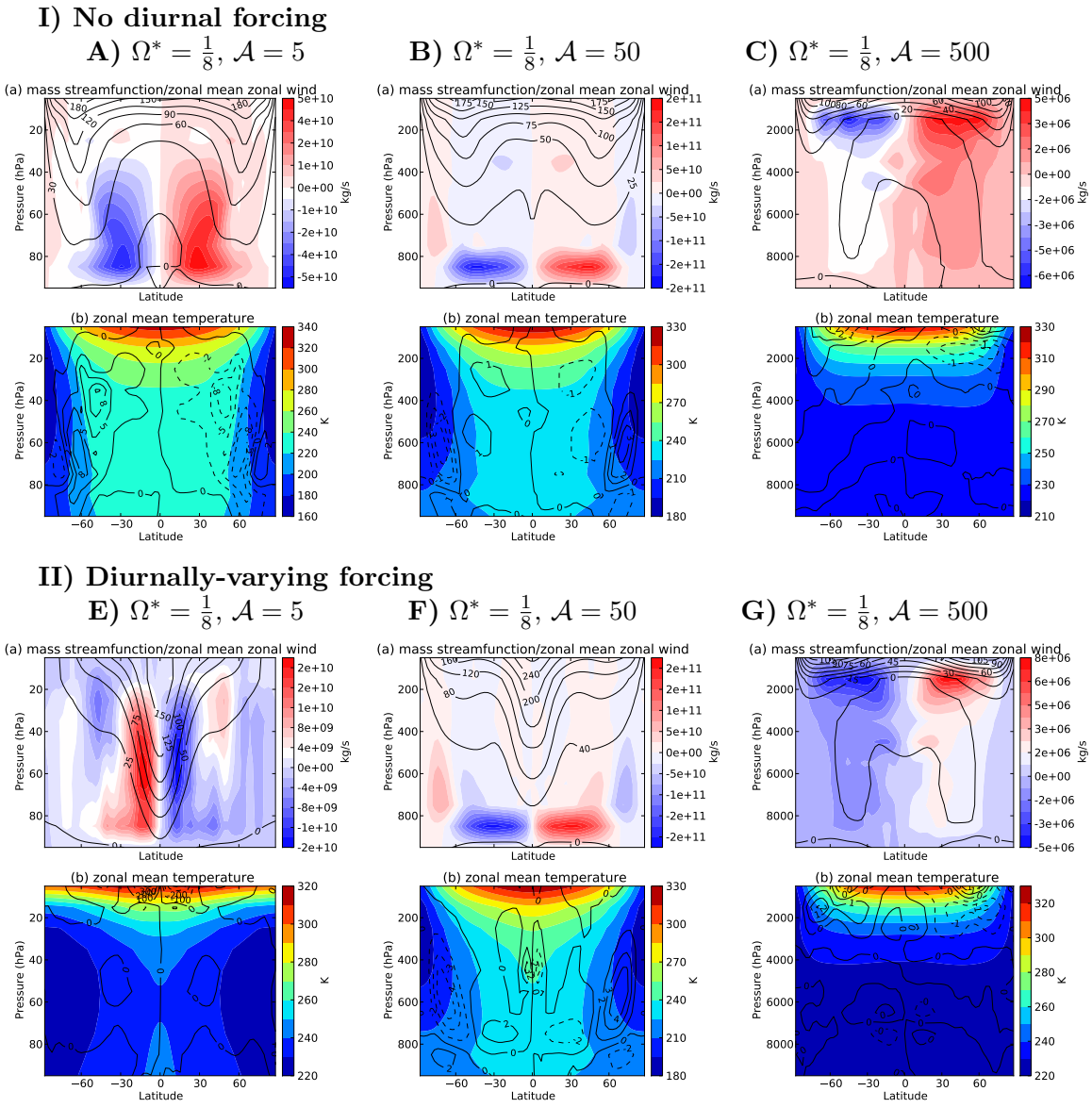

Figure 6.4: (a) meridional mass stream function (colour) and zonal mean zonal wind (contour), (b) zonal mean temperature (colour) and meridional eddy momentum flux (contour) for simulations with and without diurnal cycle and with varying $\mathcal{A} = 5, 50, 500$ i.e. $\tau_{atm} = 4, 40, 400$ days. The plotted fields are averaged over one model year. (Constants: $\Omega^* = \frac{1}{8}$, $\tau_{surf} = 360$ days, $\mathcal{G} = -0.7$, $\tau_f = 1$ day

lower $\mathcal{A}$ the difference between the non-diurnal and diurnal cases are very large. In the non-diurnal case (Fig. 6.4A) there are strong extratropical jets with wind speeds of up to 180 ms^{-1}. The equatorial wind reaches speeds of up to 150 ms^{-1} in the upper atmosphere. The meridional eddy momentum flux converges on the equator so that momentum is transported from the extratropical jets towards the equator. In the diurnally-varying case, the super-rotating jet is located strongly at the equator with wind speeds of 150 ms^{-1}, with almost no extratropical wind jets present. In this case there is both a very strong equatorial convergence of momentum located at 10 hPa very close to the equator. We also note that in this case a strong vertical transport of momentum occurs (not shown). The case with larger $\mathcal{A}$ has a wind profile that is mostly focussed on the upper 2000hPa of the atmosphere with wind speeds of 100 ms^{-1} at the extratropics and 40 ms^{-1} at the equator. Addition of a diurnal cycle adds only 5 ms^{-1} to this wind. Overall, this shows that the diurnal cycle has an important accelerating effect that scales with the radiative timescale τ_{atm}.

6.2.3 Varying the rotation rate

For completeness, we show variations of the rotation rate with and without diurnally-varying forcing, to make future comparisons with the seasonally and diurnally forced cases in Section 6.3.

Figure 6.5 shows zonal diagnostic plots with varying Ω^* at constant $\mathcal{G} = -0.7$ and $\mathcal{A} = 400 \cdot \Omega^*$. We see that in the non-diurnally forced cases, fast-rotating ($\Omega = 1, \frac{1}{2}$) planets do not have an equatorial super-rotating jet due to eddy momentum flux divergence. At slower rotation rates, eddy (and mean) momentum converges towards the equator and equatorial superrotation can be observed. When the solar forcing has an additional diurnal cycle, however, all rotation rate cases feature significantly accelerated equatorial super-rotating jets, each with wind speeds of over 150 ms^{-1}.

6.2.4 Discussion

Looking at these simulations without seasonal variations, the question arises how applicable these simulations are for real planetary bodies. Both Titan and Venus show significant equatorial super-rotating winds. Titan would not be reproduced well by the

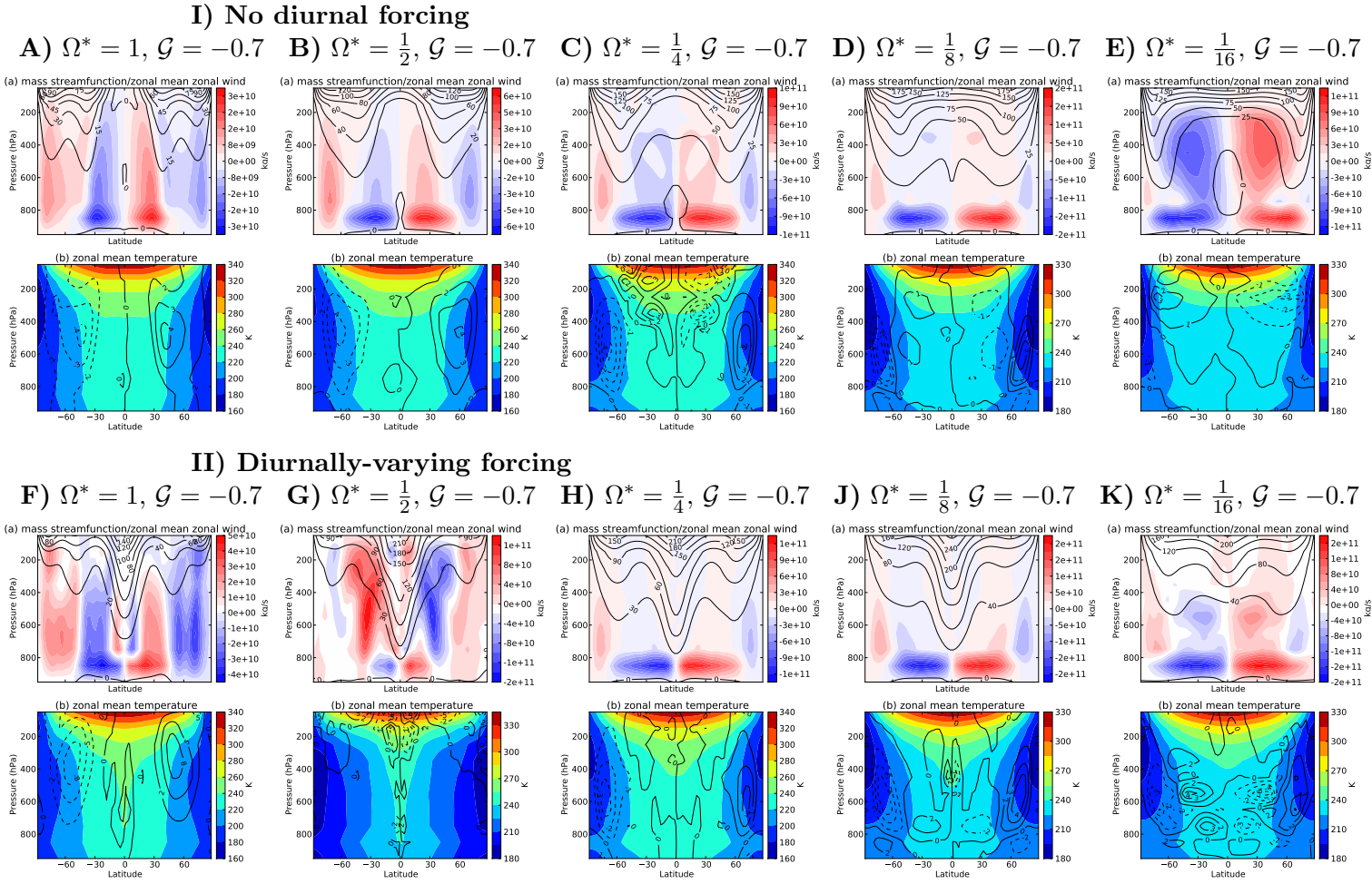

Figure 6.5: (a) meridional mass stream function; (b) zonal mean temperature (colour) and potential temperature fields (contour), (c) zonal mean zonal wind (contour), and (d) meridional eddy momentum flux for simulations with and without diurnal cycle. The plotted fields are averaged over one model year. (Constants: $\Omega = \frac{1}{8}\Omega_E$, $\tau_{surf} = 360$ days, $\tau_{atm} = 40$ days, $\tau_f = 1$ day

simulations featured in this section. Firstly, Titan's year is controlled by Saturn's orbit around the sun which is 29 years at an obliquity angle of 27°, and is therefore strongly influenced by seasons. Secondly, Titan has a very cold atmosphere, which, according to Eqn. (1.10) controls the radiative timescale in the atmosphere (τ_{atm}(Titan) = 20 years, Table 1.1). We come somewhat close to this value in Fig. 6.4 and show that the diurnal cycle has only a minor effect on the atmosphere in this regime.

While these simulations may not describe Titan very well, they may be important to understanding the atmosphere of Venus. Venus has an axial tilt of -2.6°, which is nearly zero, so seasonal effects would not be very large. The radiative timescale of the atmosphere is very large at the surface ($p_0(Venus) = 90$ bar). However, at the upper cloud deck where the super-rotating winds occur, the pressure is low enough so that the diurnal cycle of radiative processes may have a significant effect. In this regime, our simulations show that the thermal tide has a significant impact by enhancing the superrotating flow at the equator.

6.3 Simulations with diurnally and seasonally-varying solar forcing

6.3.1 Regime diagrams

Here, we attempt to display the influence of all non-dimensional parameters on the existence and strength of equatorial superrotation. This influence is depicted in the form of regime diagrams similar to the ones shown in Section 5.5 (see e.g Fig. 5.16). In the following sections (6.3.2, 6.3.3, 6.3.4) a number of scalar diagnostics are shown that characterise the winds in each simulated atmosphere. These diagnostics are used to identify regions in parameter space, where interesting effects occur. Our main focus lies on identifying the strengthening of super-rotating winds due to a diurnally forced solar heating profile. However, as these simulations have both seasonal and diurnal forcing, it may prove difficult to understand the exact processes involved. Thus the following sections will deal with this issue in different ways. The current section will characterise integer global diagnostics, like zonal wind and Lorenz energy budgets. In Section 6.4, we will show detailed diagnostics of a few selected simulations. And in Section 6.5

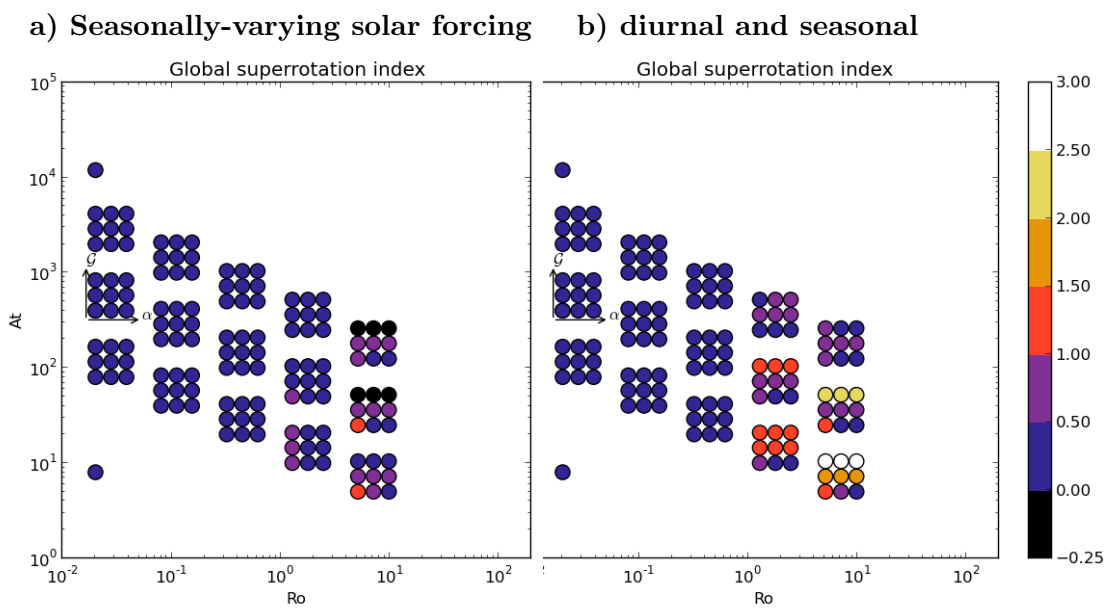

Figure 6.6: Regime diagram of annual-mean **global superrotation index** S over Rossby number $\mathcal{R}o$ and $\mathcal{A}$ (at constant Ek with $\tau_f = 1\,\text{day}$). Clusters of points are artificially moved to discern variations in greenhouse parameter $\mathcal{G} = 1, 0, -0.7$ (in y direction) and seasonality parameter $\alpha = 0.16, 1.6, 16$ (in x direction). The values of the global superrotation index are given by the colour of the data points.

we will compare the enhancement of superrotation to a theory of thermally-excited gravity waves.

In addition, in Section 6.3.5 we compare the Lorenz energy cycle conversion terms from simulations with both diurnally and seasonally-varying solar forcing to the simulations with only seasonally-varying forcing from Chapter 5. This will provide information on the globally dominating form of energy conversion, which can help identify predominantly barotropic or baroclinic flow. We do this not only to identify global trends in super-rotating atmospheres, but also to identify other effects of both seasonal and diurnal forcing on the atmospheric circulation within our parameter space.

6.3.2 Global superrotation

To better quantify super-rotating winds, we calculate the global superrotation index S (see Eqn. 5.1). Global values of $S > 0$ describe a super-rotating and $S < 0$ a sub-rotating atmosphere. As a global value this kind of analysis cannot specifically inform about the intensity of superrotation at the equator, but instead shows global trends of superrotation behaviour.

Figure 6.6 shows the annual-mean global superrotation index S in dependence upon $\mathcal{R}o$, $\mathcal{A}$, $\mathcal{G}$, and α. Figure 6.6a shows S in the seasonally-varying solar forcing case. It is apparent that S is largely dependent on $\mathcal{R}o$. This is the case because S compares the total angular momentum of the atmosphere $\int mdV$ with that of the planet, M_0, which depends strongly on Ω. Consequently, significantly large values of the superrotation index only occur when the planetary rotation rate is small. Apart from this trend, two further trends are discernible in Figure 6.6a: with rising seasonality α (at constant $\mathcal{G} = 0$) global superrotation is weakened (Mitchell et al., 2014), and with declining $\mathcal{A}$ (i.e. rising thermal equilibrium timescale), S increases weakly. For varying $\mathcal{G}$, a change in S is discernible for $\mathcal{R}o \geq 1$ (i.e. $\Omega^* = \frac{1}{8}, \frac{1}{16}$) where S decreases with increasing $\mathcal{G}$. At $\mathcal{G} \leq 0$ global superrotation becomes largely independent of α. In addition, at $\mathcal{G} = -0.7$ and $\mathcal{R}o = 5$ a majority of simulations feature subrotation.

When introducing a diurnal cycle to the solar forcing (Figure 6.6b), the superrotation index increases to values up to $S = 3$. To give a comparison, it is approximated that this value is $S \approx 10$ for the Venus atmosphere (Read, 1986). It is apparent that only simulations with $\mathcal{G} \leq 0$ and $\mathcal{R}o > 1$ are affected by this acceleration effect. Superrotation values for simulations with $\mathcal{G} = 1$ remain unchanged. As before, S increases with decreasing $\mathcal{A}$. Additionally, a clear dependence on the seasonality α is not found in the $\mathcal{G} \leq 0$ regime.

It is interesting to note that the global superrotation values for simulations with large $\mathcal{R}o$ and $\mathcal{G} = -0.7$ show the highest superrotation index at $S \approx 3$ with diurnal cycle turned on, but show only weak prograde winds, or even globally subrotating winds when the diurnal cycle is turned off. This specific case is mentioned in further detail in Section 6.4.5.

6.3.3 Equatorial superrotation

In this section, we focus on the local superrotation index $S_{up,eq}$ in the upper equatorial atmosphere. The local superrotation index s is defined as (Read, 1986)

$$s = [m]/(\Omega a^2) - 1. \tag{6.2}$$

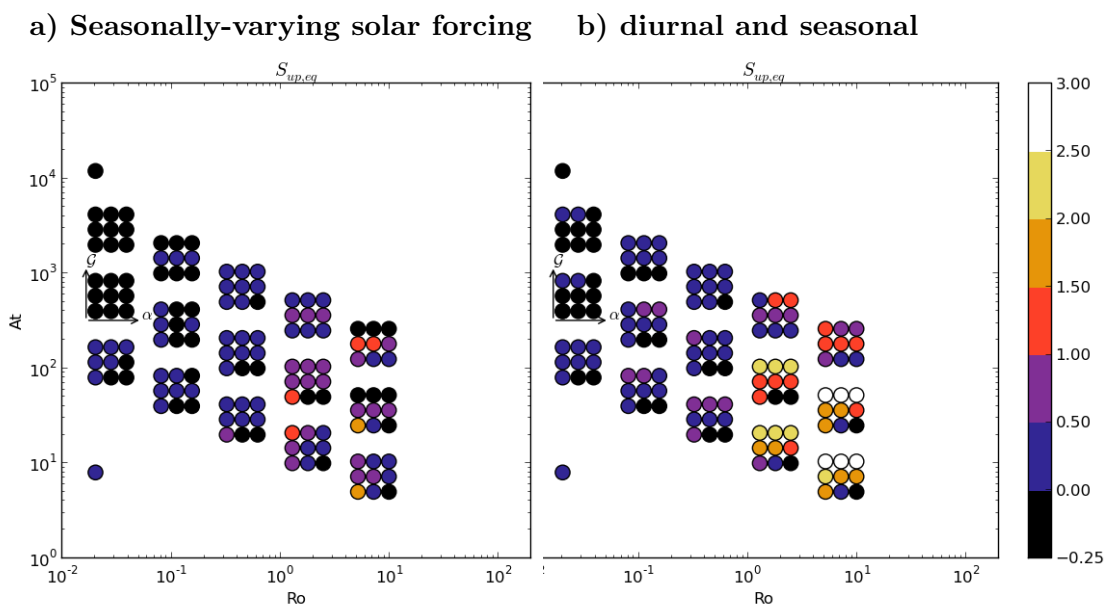

Figure 6.7: Regime diagram of annual-mean **upper atmosphere equatorial superrotation index** $S_{up,eq}$ over Rossby number $\mathcal{R}o$ and $\mathcal{A}$. Clusters of points are artificially moved to discern variations in greenhouse parameter $\mathcal{G} = 1, 0, -0.7$ (in y direction) and seasonality parameter $\alpha = 0.16, 1.6, 16$ (in x direction). The values of $S_{up,eq}$ are given by the colour of the data points.

where $[m]$ is the zonal-mean total specific angular momentum (see Eqn. 5.2). The upper equatorial superrotation index $S_{up,eq}$ is then defined as

$$S_{up,eq} = \frac{1}{\phi_2 - \phi_1} \int_{\phi_2=-10^\circ}^{\phi_1=10^\circ} d\phi \frac{1}{\sigma_2 - \sigma_1} \int_{\sigma_2=0.3}^{\sigma_1=0} d\sigma \, s \tag{6.3}$$

as the latitudinal mean over the equatorial region $-10^\circ < \phi < 10^\circ$ and the vertical mean in the upper atmosphere $\sigma \leq 0.3$ of the local superrotation index s. This index removes the influence of the tropical jets as well as the winds at lower altitudes. The differences between Fig. 6.7 and Figure 6.6 can be seen mostly in simulations with $\alpha > 1$ and $\mathcal{R}o < 1$, showing that the equatorial zonal flow in many of these runs subrotate (see e.g. Fig. 5.1).

For the diurnal cycle case (Fig. 6.7b) this subrotation persists for runs with either $\mathcal{R}o < 0.1$ or $\alpha > 1$. However, for cases with $\mathcal{G} \leq 0$, solar forcing causes prograde winds in the upper equatorial atmosphere. The largest superrotation cases are still found at $\mathcal{R}o > 1$. Most of these have a larger equatorial superrotation index $S_{up,eq}$ (Fig. 6.7b) compared to the globally integrated value S (Fig. 6.6b).

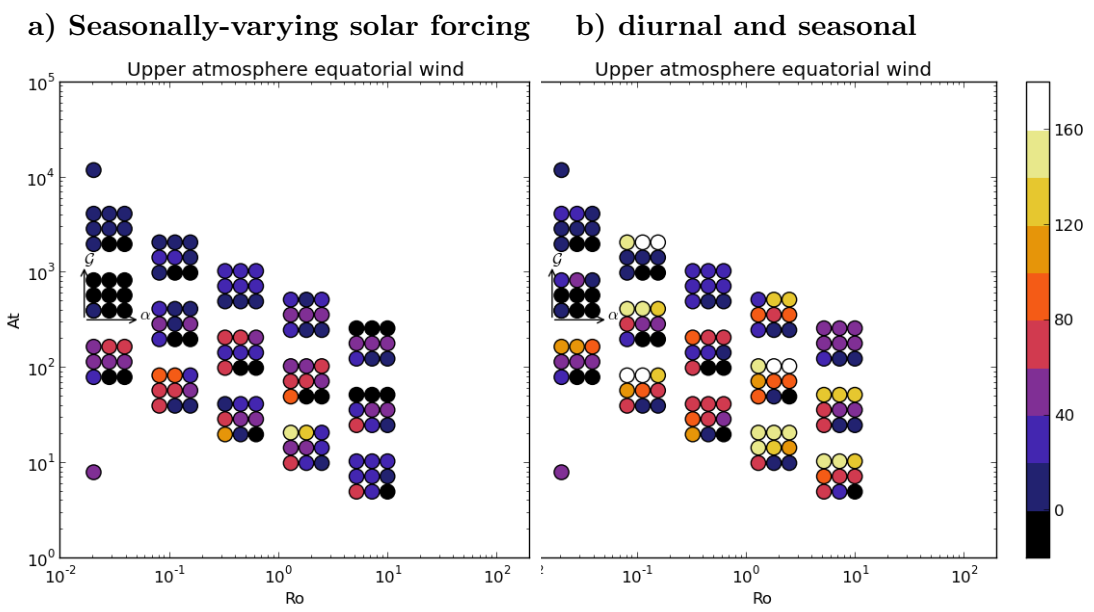

Figure 6.8: Regime diagram of annual-mean **maximum equatorial zonal wind** $\overline{u}_{eq,max}$ over Rossby number $\mathcal{R}o$ and $\mathcal{A}$. Clusters of points are artificially moved to discern variations in greenhouse parameter $\mathcal{G} = 1, 0, -0.7$ (in y direction) and seasonality parameter $\alpha = 0.16, 1.6, 16$ (in x direction). The values of equatorial wind strength are given by the colour of the data points.

6.3.4 Maximum equatorial zonal velocity

Another quantity that can be compared to identify the effect of diurnally-varying forcing on equatorial superrotation is the maximum value of the annual-mean zonal velocity $\overline{u}_{eq,max}$. $\overline{u}_{eq,max}$ is the maximum zonal wind velocity value in the equatorial upper atmosphere region (see Eqn. 6.3). Compared to the two quantities above (S, $S_{up,eq}$), $\overline{u}_{eq,max}$ is not scaled by the solid-body rotation $M_0 \propto \Omega$ of the planetary surface.

Fig. 6.8a shows $\overline{u}_{eq,max}$ for the seasonally-varying forcing case. Here, different wind speeds can be discerned for simulations with $\mathcal{R}o < 1$. At $\mathcal{G} = 1$ and $\alpha = 0$, equatorial wind speeds are higher with decreasing $\mathcal{A}$ and larger $\mathcal{R}o$. When varying by $\mathcal{R}o$ there is a maximum of u_{max} at $\mathcal{R}o \approx 1$ ($\Omega^* = 0.125$, see Fig. 6.14). When taking into account the other parameters an interesting region emerges at $\mathcal{G} = -0.7$, small $\mathcal{A}$ ($p_s = 0.2p_0$) and $\mathcal{R}o \approx 0.1$ and 1, where zonal winds reach a maximum of 160 ms^{-1} (at $\mathcal{R}o \approx 1$) and 80 ms^{-1} (at $\mathcal{R}o \approx 0.1$), respectively.

In the simulations with diurnal cycle, maximum winds exceeding 140 ms^{-1} are reached, especially for the $\mathcal{G} = -0.7$ series of runs. The two regions with the strongest

winds are again given by $\mathcal{R}o \approx 1$ and $\mathcal{R}o \approx 0.1$.

In conclusion the regime plots presented in this section have shown that super-rotating winds that exceed 100 ms^{-1} can be easily produced by introducing a diurnal cycle to the solar forcing as long as the atmosphere strongly absorbs short-wave radiation. Purely axisymmetrically forced simple GCMs (e.g. Williams, 2003, Mitchell and Vallis, 2010, Mitchell et al., 2014, Wang, 2014) in the slow-rotation regime usually only reach equatorial wind speeds between 40 and 90 ms^{-1}.

6.3.5 Lorenz energy cycle

The Lorenz energy cycle provides information about global energy transport within the atmosphere (see Section 2.1). With the help of the conversion terms of the Lorenz cycle, we can identify how the simulated atmosphere converts available potential energy (APE) into kinetic energy (KE), and how strongly they are affected by baroclinic or barotropic processes.

In Figures 6.9 and 6.10 we show the Lorenz energy cycle conversion terms for a large set of simulations with varying parameters ($\mathcal{R}o$, $\mathcal{A}$, α, $\mathcal{G}$). Figure 6.9 displays the Lorenz data of the previous chapter, with seasonally-varying forcing. In Figure 6.10 we show the same data for the simulations with both diurnally- and seasonally-varying forcing. The setup of this kind of plot is explained in detail in Section 5.3 on page 117.

In the purely seasonal case (Fig. 6.9), the plot can be split into two regions, according to the atmospheric behaviour. On the left side of each plot (with around $\mathcal{R}o < 0.2$), the atmospheres are mostly dominated by baroclinic conversion (positive C_A, C_E). In these cases C_K is mostly negative, which points towards the existence of barotropically enhanced jets. According to Held and Andrews (1983), a baroclinically unstable flow with a barotropic zonal jet will result in enhancement of the zonal jet if the meridional scale of the jet is larger than the deformation radius. This is consistent with our findings insofar as the deformation radius becomes smaller at faster planetary rotation rates. Even more important than the relationship between deformation radius and meridional scale of the jets seems to be the baroclinicity (as determined by the strength of the baroclinic energy conversion rate) of the atmosphere. This is apparent from the agreement between baroclinic and barotropic conversion terms (c.f.

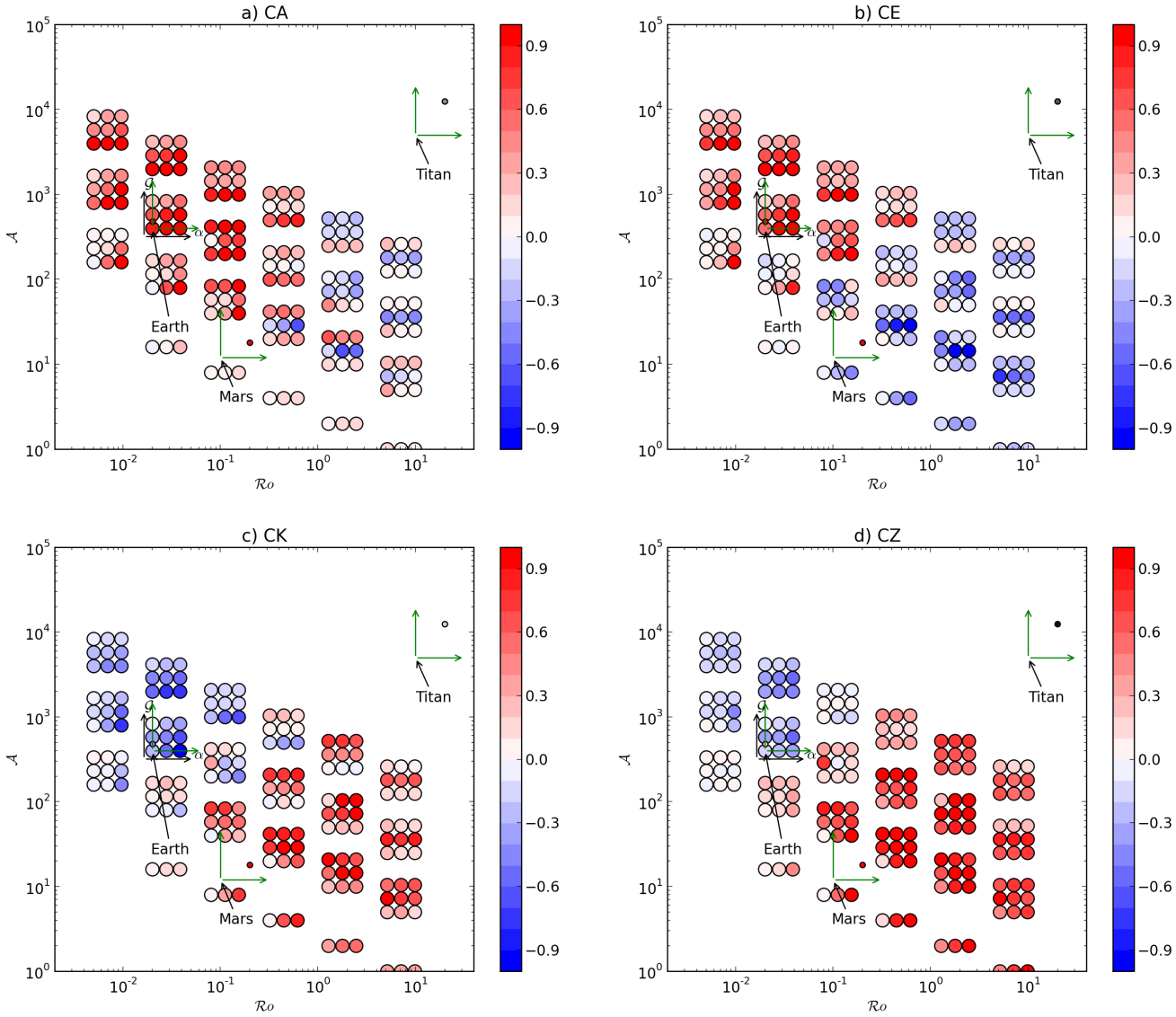

Figure 6.9: Regime diagrams of the Lorenz cycle conversion terms, averaged over 3 model years: a) C_A, b) C_E, c) C_K, d) C_Z, given in dependence upon $\mathcal{R}o$, $\mathcal{A}$, $\mathcal{G}$ and α. Constants: $\tau_f = 1$ day, $n_\mu = 1$ **(seasonally-varying insolation)**. Conversion terms are given in Wm^{-2}.

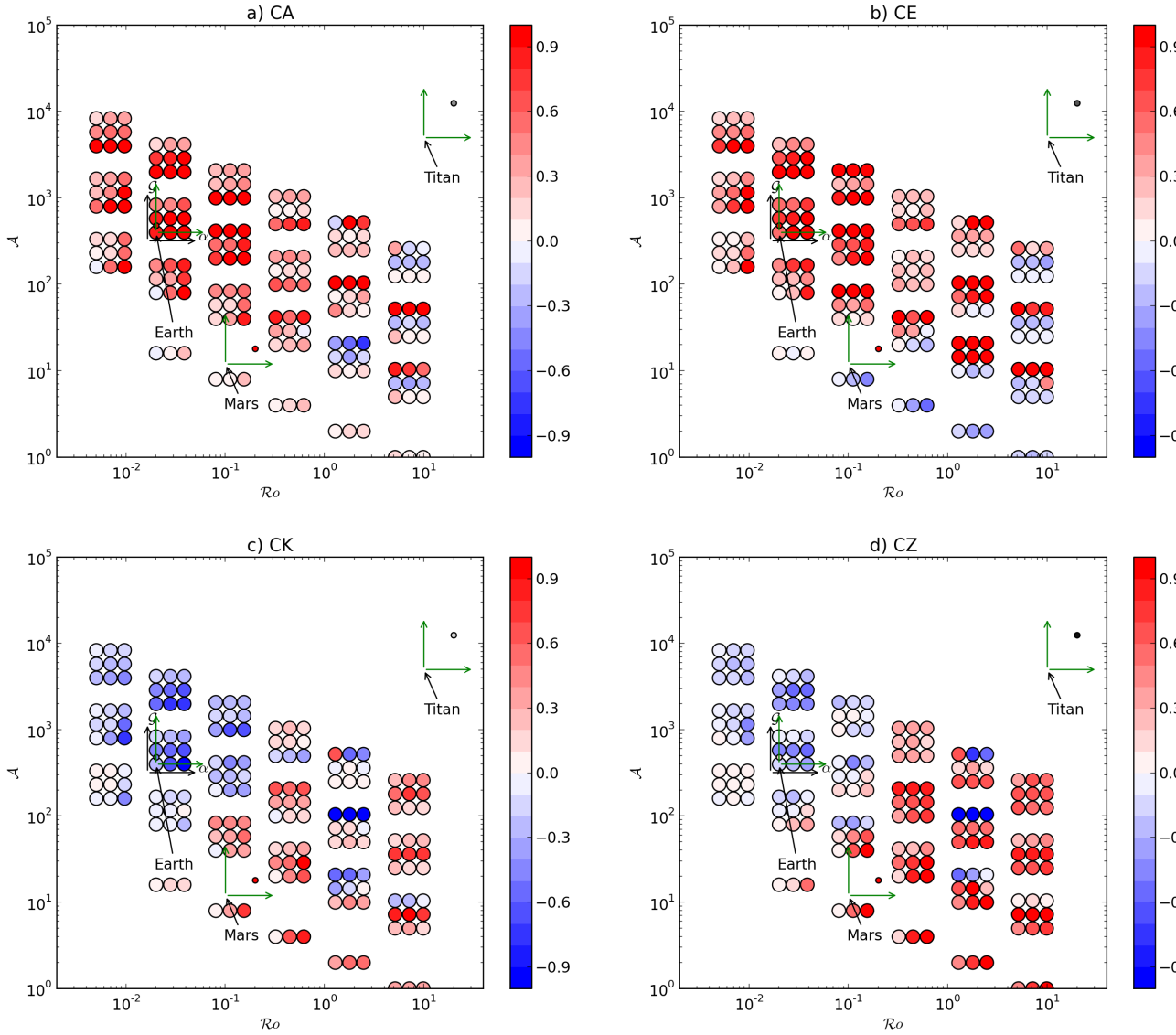

Figure 6.10: Regime diagrams of the Lorenz cycle conversion terms, averaged over 3 model years: a) C_A, b) C_E, c) C_K, d) C_Z, given in dependence upon $\mathcal{R}o$, $\mathcal{A}$, $\mathcal{G}$ and α. Constants: $\tau_f = 1$ day, $n_\mu = 0$ **(diurnally- and seasonally-varying insolation)**. Conversion terms are given in Wm^{-2}.

Fig. 6.9, positive C_E and negative C_K for $\mathcal{R}o < 0.2$). In this region, C_Z mostly has values either close to zero or negative. This paints the picture of an atmosphere with baroclinic jets, in which eddies strengthen the mean flow (negative C_K) and the net circulation in the atmosphere is equally influenced by thermally direct and thermally indirect processes.

The second region lies at around $\mathcal{R}o > 0.2$ (right side of each plot). Here, the thermally-direct mean meridional circulation (positive C_Z) and barotropic eddy processes (positive C_K) appear as a large term in the budget. The baroclinic conversion terms in this region are mostly negative, so that eddy energy is converted back into zonal mean APE. As noted before, while Earth values of the Lorenz cycle from reanalysis data fit well to our simplified atmospheres, the Mars case does not. For the Mars like regime (with low surface pressure), both baroclinic terms are underestimated in our simulations.

When comparing the purely seasonal case (Fig. 6.9) with the diurnally and seasonally forced case (Fig. 6.10), we see that the simulations with an accelerated superrotating jet from the previous sections differ strongly in their Lorenz conversion terms. Simulations with accelerated equatorial jets show a much stronger baroclinic conversion, especially at $\mathcal{R}o > 1$ and $\mathcal{G} \leq 0$. At $\mathcal{R}o \approx 1$, we find some simulations with strongly negative C_K and C_Z, so that energy is effectively converted in the cycle from AZ to AE to KE with up to 4 W/m^2 of which half is then converted to KZ and again to AZ.

Another difference between the two forcing cases occurs in the region with small $\mathcal{A}$. Here the atmosphere will react more strongly to both variations in surface and atmospheric heating. As in the superrotation regime, the change that occurs due to the diurnally-varying forcing is a tendency to result in larger baroclinic conversion rates (when $\mathcal{G} \geq 0$). This may provide an explanation for the issue we had with the Mars-like simulations, where the baroclinic conversion pathway was underestimated by our purely seasonal simulations.

In the Mars-like regime (low $\mathcal{A}$, $\mathcal{G} \geq 0$ and strong surface seasonality α), we find that stronger baroclinic conversion occurs due to diurnal thermal forcing. On Mars the diurnal tide plays and important role for the atmospheric dynamics (see e.g. Wilson

and Hamilton, 1996, Lewis and Barker, 2005) We show in Chapter 2, that conversion in the baroclinic pathway on Mars occurs to a large part on timescales shorter than one day and hence is connected to the thermal tide.

6.4 The effect of diurnal heating in seasonally-forced atmospheres for specific cases

In this section, we focus on a few selected simulations in detail to identify the effect of diurnal heating on the simulated atmospheric dynamics as well as possible superrotation generation mechanisms. All of the following simulations feature seasonally-varying forcing.

6.4.1 Varying greenhouse parameter $\mathcal{G}$

Figure 6.11 compares the effect of diurnally and seasonally-varying forcing (Fig. 6.11D,E,F) with that of only seasonally-varying forcing (Fig. 6.11A,B,C) for different values of the greenhouse parameter $\mathcal{G}$. The subplots show annual mean values of the (a) the meridional mass streamfunction (Eqn. 4.1) and the mean zonal wind $\overline{u}$ and (b) the zonal mean temperature and the meridional eddy momentum flux $\overline{u'v'}\cos\phi$.

The case presented in Fig. 6.11A,D is our Earth reference case, which assumes no short-wave absorption ($\mathcal{G} = 1$). Both the seasonally-varying case (Fig. 6.11A) and the diurnal cycle case (Fig. 6.11D) are very similar with strong eastward extratropical jets. As shown from previous results (see e.g. 5.22a), these jets are baroclinic. The eddy momentum flux transports momentum polewards and has its maximum at the latitude where the maximum wind speeds of the baroclinic jets occur ($\phi \approx 40°$). Similar to Section 3.4.4 (c.f Fig. 3.4), we find that in this case the diurnally-varying forcing has a negligible effect on the annually-averaged atmosphere. Even in snapshots, there is only a minor difference between the two cases.

This occurs for two reasons. Firstly, due to $\mathcal{G} = 1$, short-wave flux is only absorbed at the surface. Here various effects dampen the diurnal signal, such as the thermal inertia of the surface and the convective adjustment timescale $\tau_{conv,adj}$ (see Eqn. 3.62) which controls the convective interaction between surface and atmosphere. Secondly,

I) Only seasonally-varying forcing

A) $\Omega^* = 1, \mathcal{G} = 1$ **B)** $\Omega^* = 1, \mathcal{G} = 0$ **C)** $\Omega^* = 1, \mathcal{G} = -0.7$

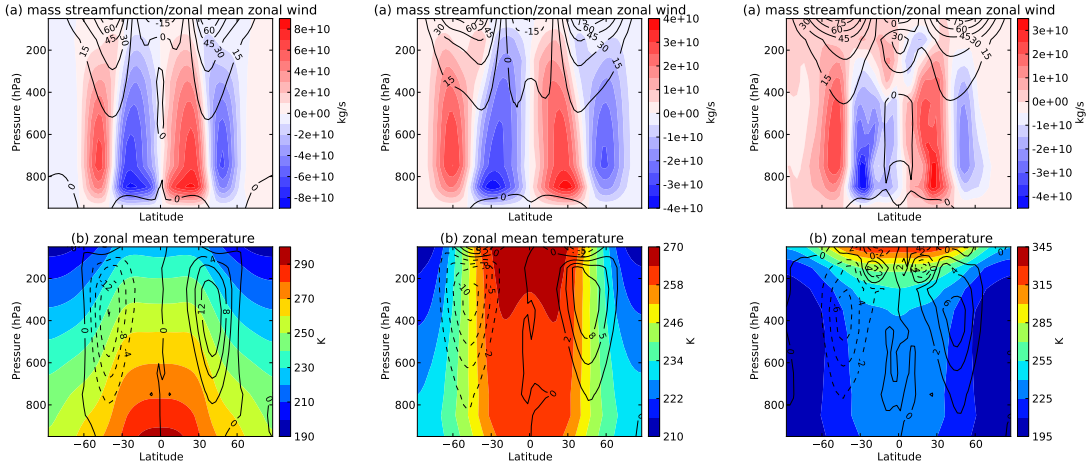

II) Seasonally- and Diurnally-varying forcing

D) $\Omega^* = 1, \mathcal{G} = 1$ **E)** $\Omega^* = 1, \mathcal{G} = 0$ **F)** $\Omega^* = 1, \mathcal{G} = -0.7$

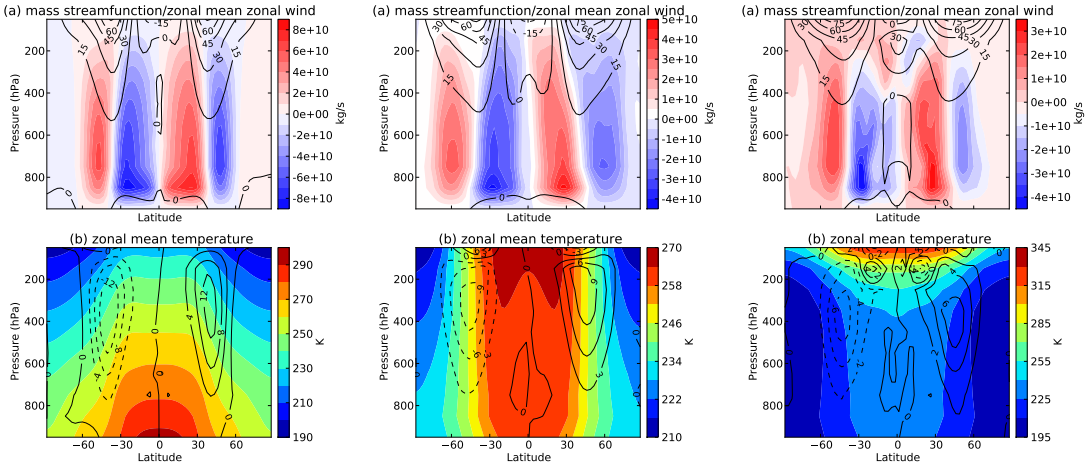

Figure 6.11: Annual mean atmospheric fields. Top (a): zonal mean zonal wind (contour) and meridional mass stream function (colour); Bottom (b): zonal mean temperature (colour) for simulations with **greenhouse parameter** $\mathcal{G} = 1, 0, -0.7$. Simulations A, B, C have only seasonally-varying forcing, while simulations D, E, F have both seasonally- and diurnally-varying forcing. (Constants: $\Omega^* = 1$, $\mathcal{G} = 1$, $\alpha = 0.16$, $\tau_f = 1$ day)

in this case the thermal relaxation timescale in the Earth's atmosphere is so long that the response to diurnally varying forcing is too weak to have much dynamical impact. In following subsections we will illuminate the interplay between atmospheric thermal inertia (i.e. via varying $\mathcal{A}$) and surface thermal inertia (via α). In Section 6.4.2 we vary both α and $\mathcal{A}$ to study the effect of the diurnal cycle in an environment with low thermal inertia in both atmosphere and surface (i.e. a thin atmosphere and a rocky surface, like Mars).

With decreasing $\mathcal{G}$, we can observe an increasing number of differences due to the diurnal forcing. Especially in the $\mathcal{G} = -0.7$ case, we can see that there is an enhancement of the upper equatorial wind by about 30 ms^{-1}. However, when comparing this to the cases without seasonal forcing in Section 6.2 (c.f. Fig. 6.5A,F with an enhancement of 120 ms^{-1} of the equatorial flow), we find that the cases in the present section show a much weaker enhancement of the equatorial flow due to the diurnal cycle. This is very likely an effect of the interseasonal variability causing a divergence of equatorial momentum. We show in Section 6.2 that in the purely diurnally-forced case the enhancement of equatorial wind coincides with a strong vertical momentum flux. When adding a seasonal cycle the solar forcing that initiates this vertical flux moves periodically along the meridional direction. As a result the vertical momentum flux at the equator is significantly weakened.

In Figure 6.12, we show the impact of varying $\mathcal{G}$ in the cyclostrophic regime (at $\Omega = \frac{1}{8}$). Here we see that the diurnally-varying forcing has a very significant effect on the cases with $\mathcal{G} = 0, -0.7$, with equatorial velocity enhancements of 50 and 100 ms^{-1}, respectively. The dependence of the diurnal equatorial enhancement due to planetary rotation rate is covered further in sections 6.4.3, 6.4.5.

6.4.2 Mars-like atmosphere

In this section, we present simulations with low atmospheric and surface thermal inertia, which should reproduce conditions analogous to the thin atmosphere and rocky surface of Mars. In Figure 6.13 we show a case in the Mars-like regime with $\mathcal{R}o = 0.08$ ($\Omega^* = \frac{1}{2}$), $\alpha = 16$ ($\tau_{surf} = 3.6$ days), $\mathcal{A} = 40$ ($\tau_{atm} = 8$ days), $\mathcal{G} = 0.8$ ($\chi_{sw} = 0.2$, $\chi_{lw} = 2.0$) with only seasonally-varying forcing (Fig. 6.13I) and with both diurnally-

I) Only seasonally-varying forcing

A) $\Omega^* = \frac{1}{8}$, $\mathcal{G} = 1$ **B)** $\Omega^* = \frac{1}{8}$, $\mathcal{G} = 0$ **C)** $\Omega^* = \frac{1}{8}$, $\mathcal{G} = -0.7$

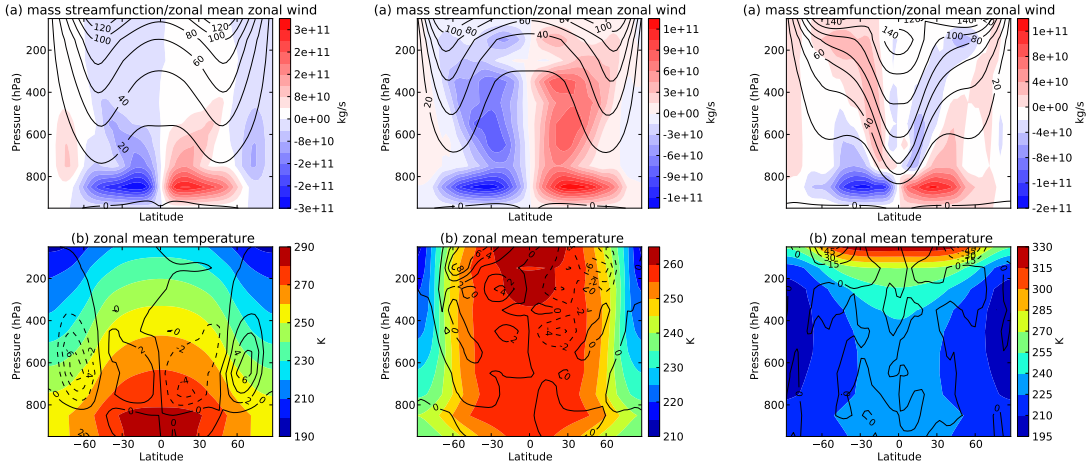

II) Seasonally- and Diurnally-varying forcing

D) $\Omega^* = \frac{1}{8}$, $\mathcal{G} = 1$ **E)** $\Omega^* = \frac{1}{8}$, $\mathcal{G} = 0$ **F)** $\Omega^* = \frac{1}{8}$, $\mathcal{G} = -0.7$

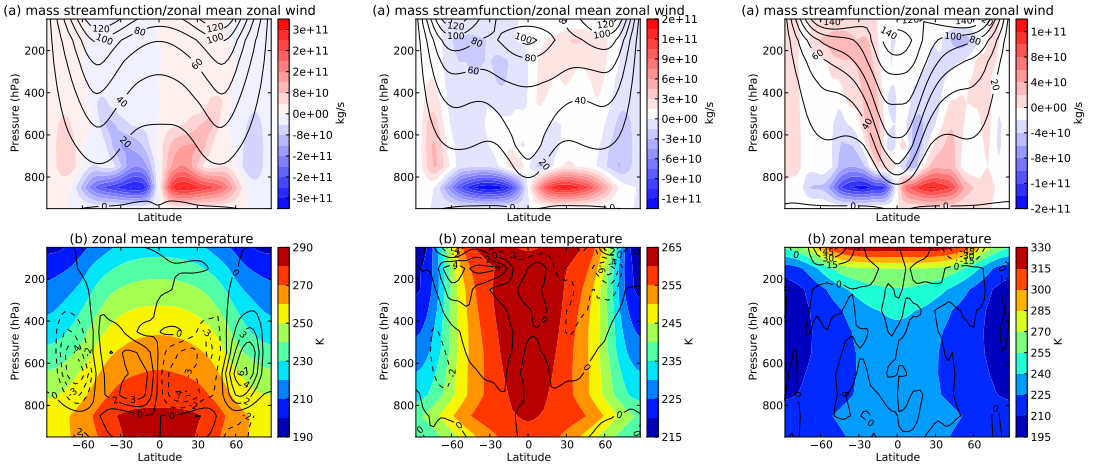

Figure 6.12: Annual mean atmospheric fields. Top (a): zonal mean zonal wind (contour) and meridional mass stream function (colour); Bottom (b): zonal mean temperature (colour) for simulations with **greenhouse parameter** $\mathcal{G} = 1, 0, -0.7$. Simulations A, B, C have only seasonally-varying forcing, while simulations D, E, F have both seasonally- and diurnally-varying forcing. (Constants: $\Omega^* = \frac{1}{8}$, $\mathcal{G} = 1$, $\alpha = 0.16$, $\tau_f = 1$ day)

I) Only seasonally-varying forcing

A) $\Omega^* = \frac{1}{2}$, $\mathcal{G} = 1$ **B)** $\Omega^* = \frac{1}{2}$, $\mathcal{G} = 0$ **C)** $\Omega^* = \frac{1}{2}$, $\mathcal{G} = -0.7$

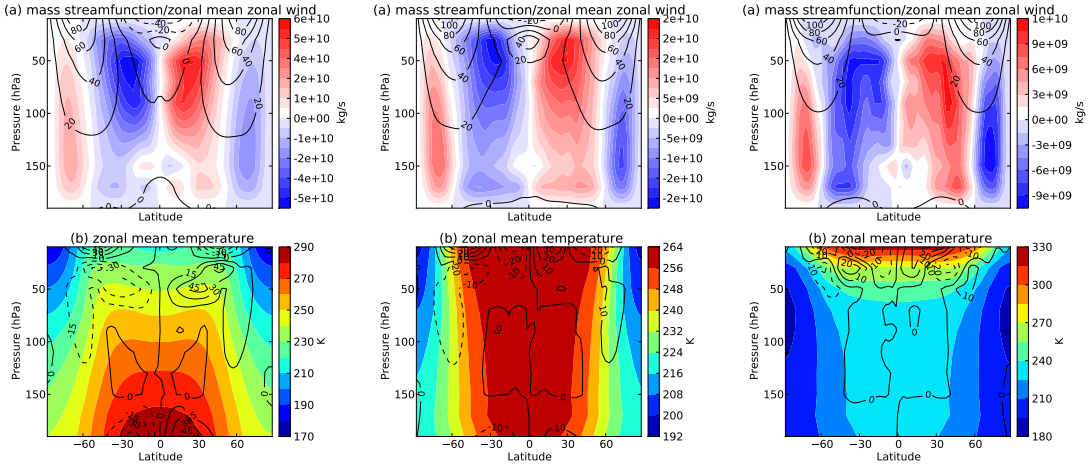

II) Seasonally- and Diurnally-varying forcing

D) $\Omega^* = \frac{1}{2}$, $\mathcal{G} = 1$ **E)** $\Omega^* = \frac{1}{2}$, $\mathcal{G} = 0$ **F)** $\Omega^* = \frac{1}{2}$, $\mathcal{G} = -0.7$

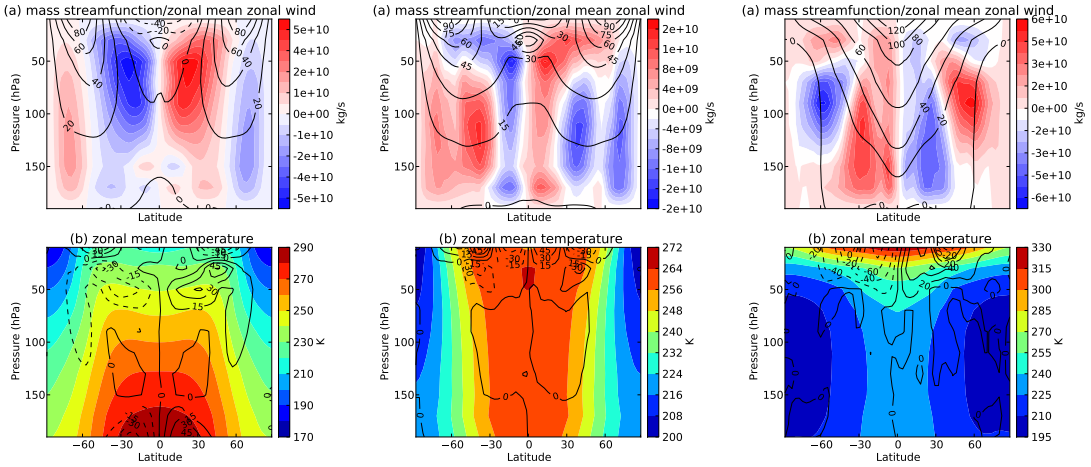

Figure 6.13: Annual mean atmospheric fields. Top (a): zonal mean zonal wind (contour) and meridional mass stream function (colour); Bottom (b): zonal mean temperature (colour) for simulations with **greenhouse parameter** $\mathcal{G} = 1, 0, -0.7$. Simulations A, B, C have only seasonally-varying forcing, while simulations D, E, F have both seasonally- and diurnally-varying forcing. (Constants: $\Omega^* = \frac{1}{2}$, $\alpha = 16$ ($\tau_{surf} = 3.6$ days), $\mathcal{A} = 40$ ($\tau_{atm} = 8$ days), $\tau_f = 1$ day)

and seasonally-varying forcing (Fig. 6.13II).

At $\mathcal{G} = 0$, the two atmospheres (Fig. 6.13I.A, II.D) exhibit only minute differences. This shows that when the solar irradiance is mostly absorbed at the surface, the diurnal signal will not strongly affect the zonal-mean atmosphere. This observation can be compared to Mars. In Figure 2.7c, the zonal energy terms are hardly affected by the thermal tide, whereas eddy-activity is. Another important point is that the thermal tide shows its most notable effects through changes in wave activity and zonal flow in the dust season or during a global dust storm event, i.e. when dust particles in the atmosphere enhance the shortwave optical depth (Read and Lewis, 2004). This is equivalent to having a greenhouse parameter $\mathcal{G}$ smaller than one. Our simulations with $\mathcal{G} = 0, -0.7$ show what would happen if significant short-wave absorption occurred throughout the year. As with simulations presented in previous sections, the effect of varying $\mathcal{G}$ can produce strong equatorial jets due to diurnally-varying forcing, even in the Mars-like, low thermal inertia case. This again compares well with the Martian atmosphere, as a prograde equatorial jet can be discerned in dusty conditions in Mars atmosphere reanalysis data and Mars GCM simulations (see e.g. Lewis et al., 2012, Lewis and Read, 2003).

6.4.3 Varying rotation rate at $\mathcal{G} = 0$

In this section, we focus on simulations with $\mathcal{G} = 0$ and varying Ω^* and try to explain the mechanism by which equatorial flow is enhanced by the diurnal cycle in these cases. Figure 6.14 shows the annual mean field diagnostics detailed in earlier sections. We find that, while all simulations with $\Omega^* \leq \frac{1}{2}$ receive some sort of enhancement of the equatorial superrotation due to the diurnal cycle, the case with $\Omega^* = \frac{1}{8}$ experiences the largest enhancement by wind speeds of up to 50 ms^{-1}. Additionally, in this case, a large region of the atmosphere (between $\pm 50^\circ$ latitude and above $p = 800\text{hPa}$) is affected by this enhancement. In the following subsection, we use this case, to provide a detailed view of the simulated atmosphere and the effect of the diurnal cycle.

I) Only seasonally-varying forcing

A) $\Omega^* = 1, \mathcal{G} = 0$ **B)** $\Omega^* = \frac{1}{2}, \mathcal{G} = 0$ **C)** $\Omega^* = \frac{1}{4}, \mathcal{G} = 0$ **D)** $\Omega^* = \frac{1}{8}, \mathcal{G} = 0$ **E)** $\Omega^* = \frac{1}{16}, \mathcal{G} = 0$

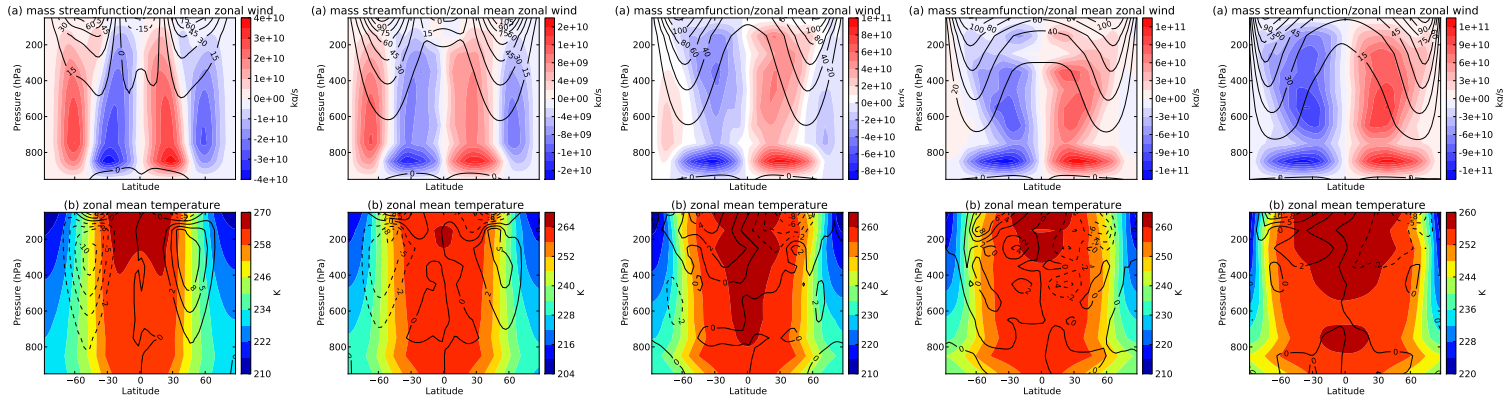

II) Seasonally- and Diurnally-varying forcing

F) $\Omega^* = 1, \mathcal{G} = 0$ **G)** $\Omega^* = \frac{1}{2}, \mathcal{G} = 0$ **H)** $\Omega^* = \frac{1}{4}, \mathcal{G} = 0$ **J)** $\Omega^* = \frac{1}{8}, \mathcal{G} = 0$ **K)** $\Omega^* = \frac{1}{16}, \mathcal{G} = 0$

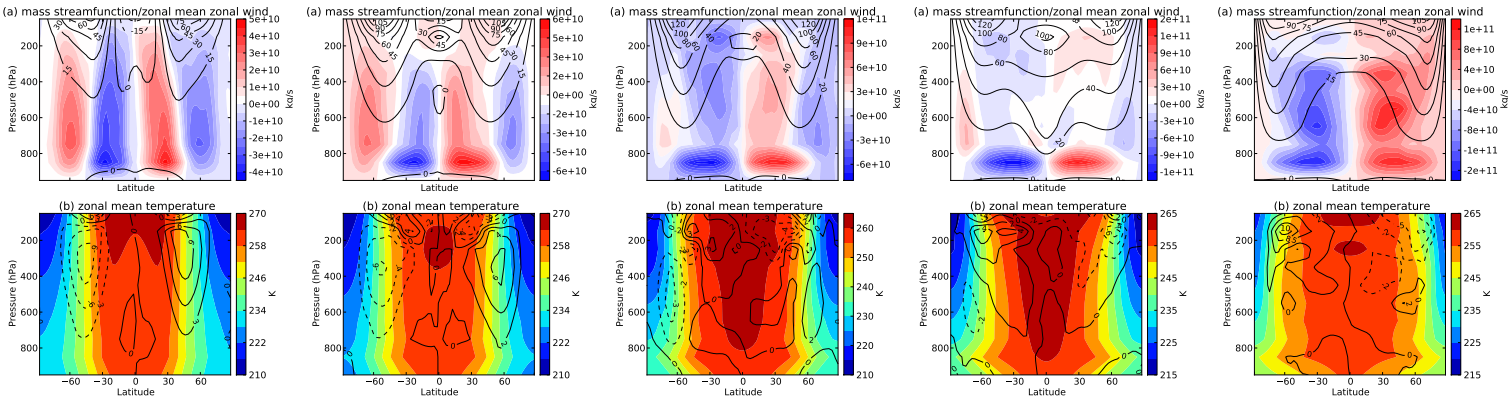

Figure 6.14: Annual mean atmospheric fields. Top (a): zonal mean zonal wind (contour) and meridional mass stream function (colour); Bottom (b): zonal mean temperature (colour) for simulations with constant greenhouse parameter $\mathcal{G} = 0$ and varying rotation rate Ω^*. Simulations A, B, C, D ,E have only seasonally-varying forcing, while simulations F, G, H, J, K have both seasonally- and diurnally-varying forcing. (Constants: $\tau_{surf} = 360$ days, $\tau_{atm} = 40$ days, $\tau_f = 1$ day

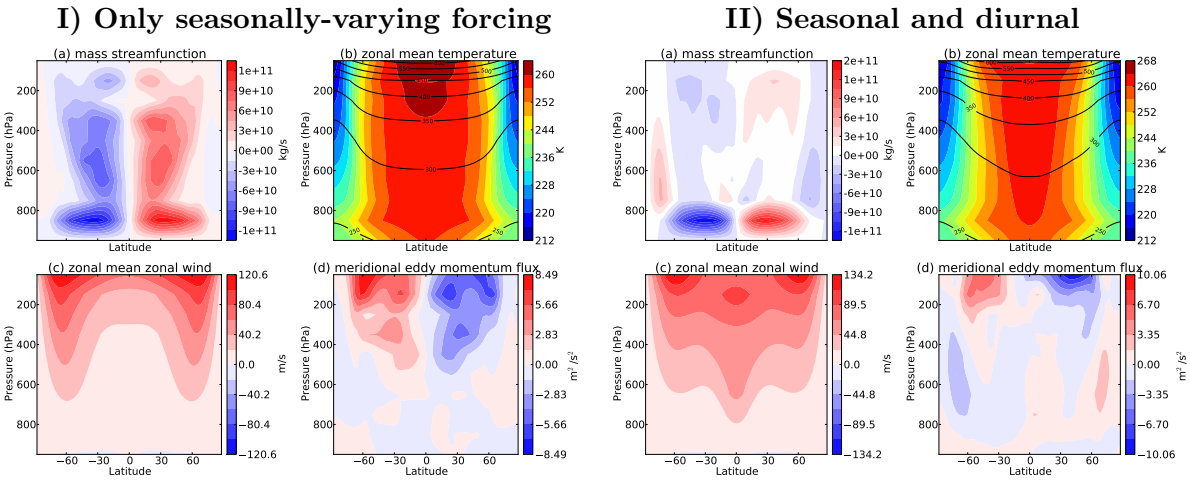

Figure 6.15: (a) meridional mass stream function; (b) zonal mean temperature (colour) and potential temperature fields (contour), (c) zonal mean zonal wind (contour), and (d) meridional eddy momentum flux for simulations with and without diurnal cycle. The plotted fields are averaged over one model year. (Constants: $\Omega = \frac{1}{8}\Omega_E$, $\tau_{surf} = 360$ days, $\mathcal{G} = 0$, $\tau_{atm} = 40$ days, $\tau_f = 1$ day

6.4.4 Simulation with $\Omega = \frac{1}{8}\Omega_E$, $\tau_{surf} = 360$ days, $\mathcal{G} = 0$, $\tau_{atm} = 40$ days, $\tau_f = 1$ day

This subsection aims to show a detailed view of one of the simulations performed with both seasonally- and diurnally-varying forcing. Here, we first present zonal diagnostics and momentum fluxes to understand the mechanism of equatorial momentum convergence. After that, further diagnostics (e.g. Lorenz energy budget, spectral energy budget) of this simulation are shown to depict the effect of diurnally-varying forcing in an example case.

Figure 6.15 shows the comparison of the cases with and without diurnal cycle with the zonal-mean diagnostics shown above. The case with seasonally-varying forcing (Fig. 6.15I) has a nearly constant vertical temperature profile, except at the lowest model layer and the polar regions. The atmosphere features two strong barotropic (see Fig. 6.18) zonal jets polewards of 60° latitude with eastwards winds up to 120 ms^{-1}. At the equator, super-rotating winds with speeds up to 60 ms^{-1} are observed. The meridional eddy momentum flux shows that momentum is transported equatorwards from the equatorwards flank of the zonal jets. In the standard GRW-mechanism this eddy momentum flux is produced by horizontal shear instabilities due to the poleward branch of the Hadley circulation cell (see e.g. Read, 2013). The kind of waves being

generated in this case are discussed in Section 6.5.5.

The diurnal cycle case (Fig. 6.15II) has a slightly narrower horizontal temperature distribution, i.e. the temperature gradient is steeper in the tropical region. The vertical temperature gradients of both cases match well. The meridional circulation cells mostly reach the two bottom layers of the model. The meridional eddy momentum flux is roughly equal in magnitude at pressure levels above 200 hPa. At lower altitudes, the meridional eddy momentum flux of the seasonally- and diurnally-forced case is significantly smaller than for the purely seasonally-forced case. Even though total meridional eddy momentum flux decreases in the diurnal cycle case, we find a significant enhancement of zonal wind speeds, with a local maximum at the equator at around 100 ms^{-1} and extra-tropical jets with winds speeds of up to 130 ms^{-1}. As the meridional eddy momentum flux is decreased in the diurnal case, the question arises what the source of the additional momentum is that enhances the equatorial winds. To answer this question we analyse the horizontal and vertical momentum fluxes in detail, in the following subsection.

Momentum fluxes

In this subsection, the transport of specific relative angular momentum $M = au\cos\phi$ is examined. Figure 6.16 shows the total meridional momentum flux $[\overline{vM}]$ (Fig. 6.16a) with

$$[\overline{vM}] = [\overline{v}][\overline{M}] + [\overline{v}^*\overline{M}^*] + [\overline{v'M'}] \tag{6.4}$$

where $[\overline{v}][\overline{M}]$ is the mean meridional component (Fig. 6.16b), $[\overline{v}^*\overline{M}^*]$ is the stationary wave component (Fig. 6.16c) and $[\overline{v'M'}]$ is the transient wave component (Fig. 6.16d) of the meridional momentum flux (see e.g. Lebonnois et al., 2016). Note that the transient wave component is proportional to the meridional eddy momentum flux presented in the previous section. Figure 6.16 shows that the stationary wave component (Fig. 6.16c) is negligible and that the dominant contributions to the meridional momentum flux are given by the mean (Fig. 6.16b) and the transient wave component (Fig. 6.16d). As shown before, the transient wave component of the seasonally-forced

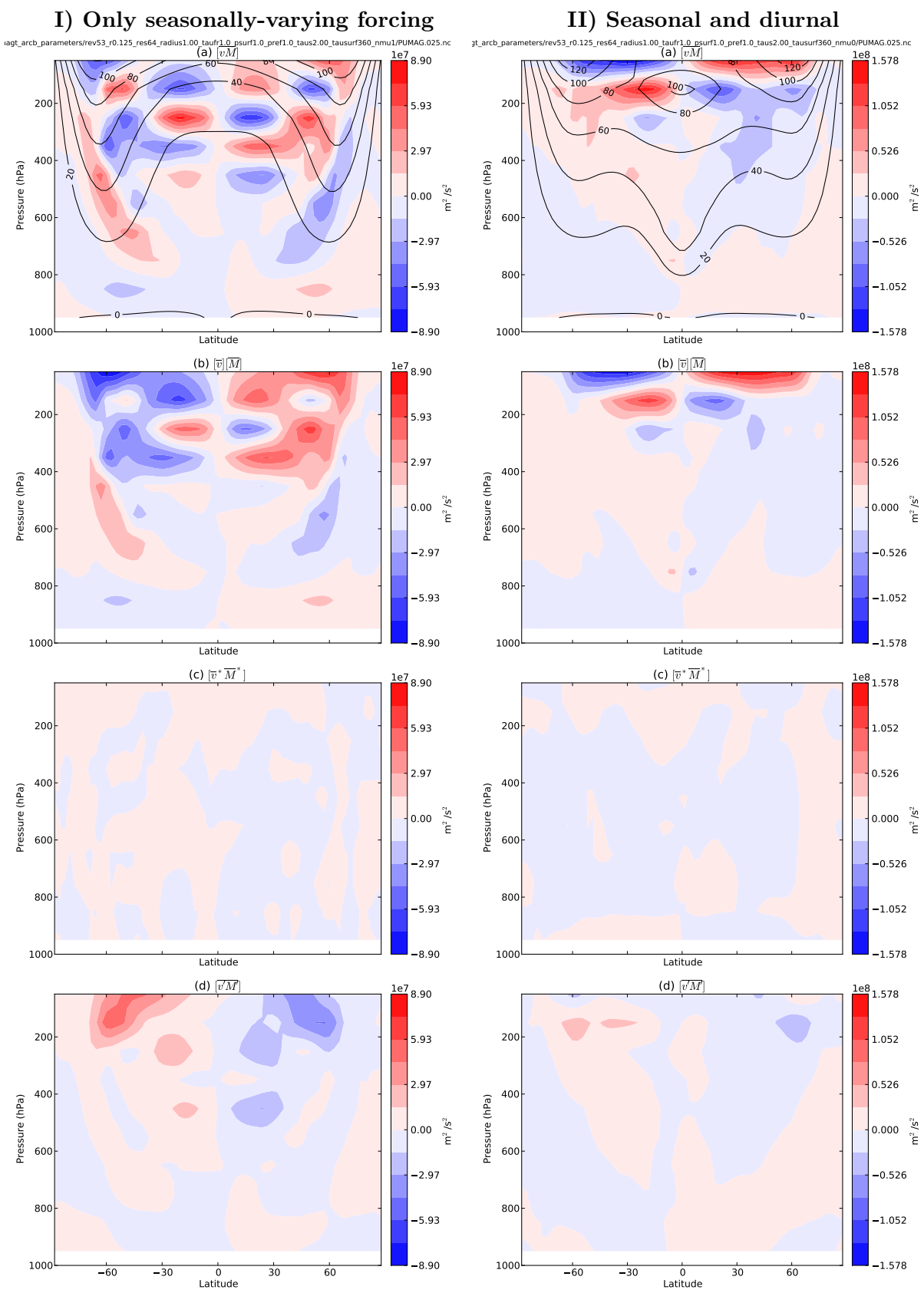

Figure 6.16: Annual mean zonal mean meridional momentum fluxes $[\overline{vM}]$ (a), decomposed into (b) mean meridional $[\overline{v}][\overline{M}]$, (c) stationary wave $[\overline{v}^*\overline{M}^*]$, and (d) transient wave $[\overline{v'M'}]$ components. Fluxes are show for (I) the case with seasonally-varying solar forcing (left) and (II) the case with diurnal cycle solar forcing. Contours show mean zonal wind. (Parameters: $\Omega = \frac{1}{8}\Omega_E$, τ_{surf} = 360 days, $\mathcal{G} = 0$, $\tau_{atm} = 40$ days, $\tau_f = 1$ day)

case is roughly double that of the diurnal cycle case. The mean meridional component (Fig. 6.16b) shows a more complicated structure. For the seasonally-forced case, a large part of $[\overline{v}][\overline{M}]$ transports momentum polewards with just a small region at 250 hPa showing significant equatorwards momentum fluxes. In total $[\overline{vM}]$ receives an intricate pattern of poleward and equatorward momentum fluxes in the seasonally-forced case. In the diurnal cycle case, however, the mean momentum transport is less convoluted and transports momentum polewards at the top-most layer, but equatorwards in a deep altitude region from 100 to 700 hPa. This shows that in total the mean meridional momentum flux of the diurnal cycle case is more effective in transporting momentum towards the equator, which is consistent with faster equatorial super-rotating winds.

Figure 6.17 shows the vertical momentum flux $[\overline{\omega M}]$ and its decomposed components. Both forcing cases show a downward (red) momentum flux at the poleward edges of the extratropical jet stream that stems largely from the zonal mean and transient wave component. However, the difference between the two cases is that the diurnal cycle case exhibits a significant upward (blue) flux, both at the ground and at the equator. The upward flux at the ground results from the stationary wave component $[\overline{\omega}^*\overline{M}^*]$ (Fig. 6.17c) and the equatorial upward flux from the mean component (Fig. 6.17b).

It is unclear in which way the solar forcing at the top of the atmosphere triggers upward momentum fluxes from the surface in the solar cycle case. The initial phase of the GRW-mechanism relies on an injection of momentum from the surface (via friction) into the equatorial upper atmosphere via the equatorward and upward arms of the Hadley circulation. Such an upward momentum flux is, however, absent from the seasonally-varying case, which also shows superrotation, albeit with weaker wind speeds. Additionally, the GRW-mechanism just requires this surface momentum flux during the spin-up phase and further convergence of momentum at the equator is generated by shear instability.

Diurnal component Lorenz budget

In this subsection we compare the strength of the diurnal components of the Lorenz terms to their daily-averaged counterparts using the Lorenz energy budget calculated

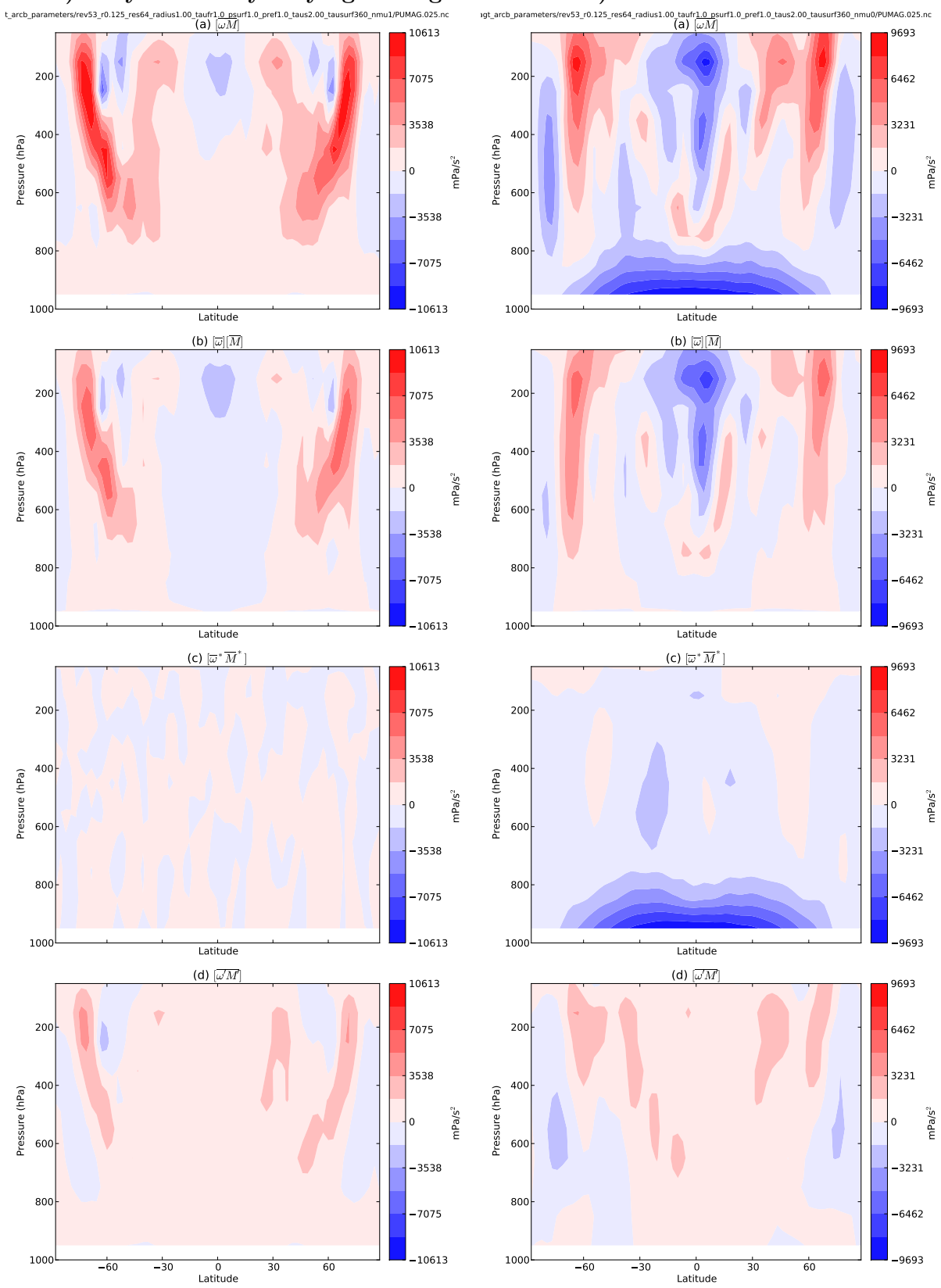

Figure 6.17: Annual mean zonal mean vertical momentum fluxes $[\overline{\omega M}]$ (a), decomposed into mean meridional $[\overline{\omega}][\overline{M}]$ (b), stationary wave $[\overline{\omega}^*\overline{M}^*]$ (c), and transient wave $[\overline{\omega' M'}]$ (d) components. Fluxes are show for (I) the case with seasonally-varying solar forcing (left) and (II) the case with seasonally- and diurnally-varying solar forcing. (Parameters: $\Omega = \frac{1}{8}\Omega_E$, $\tau_{surf} = 360$ days, $\mathcal{C} = 0$, $\tau_{atm} = 40$ days, $\tau_f = 1$ day)

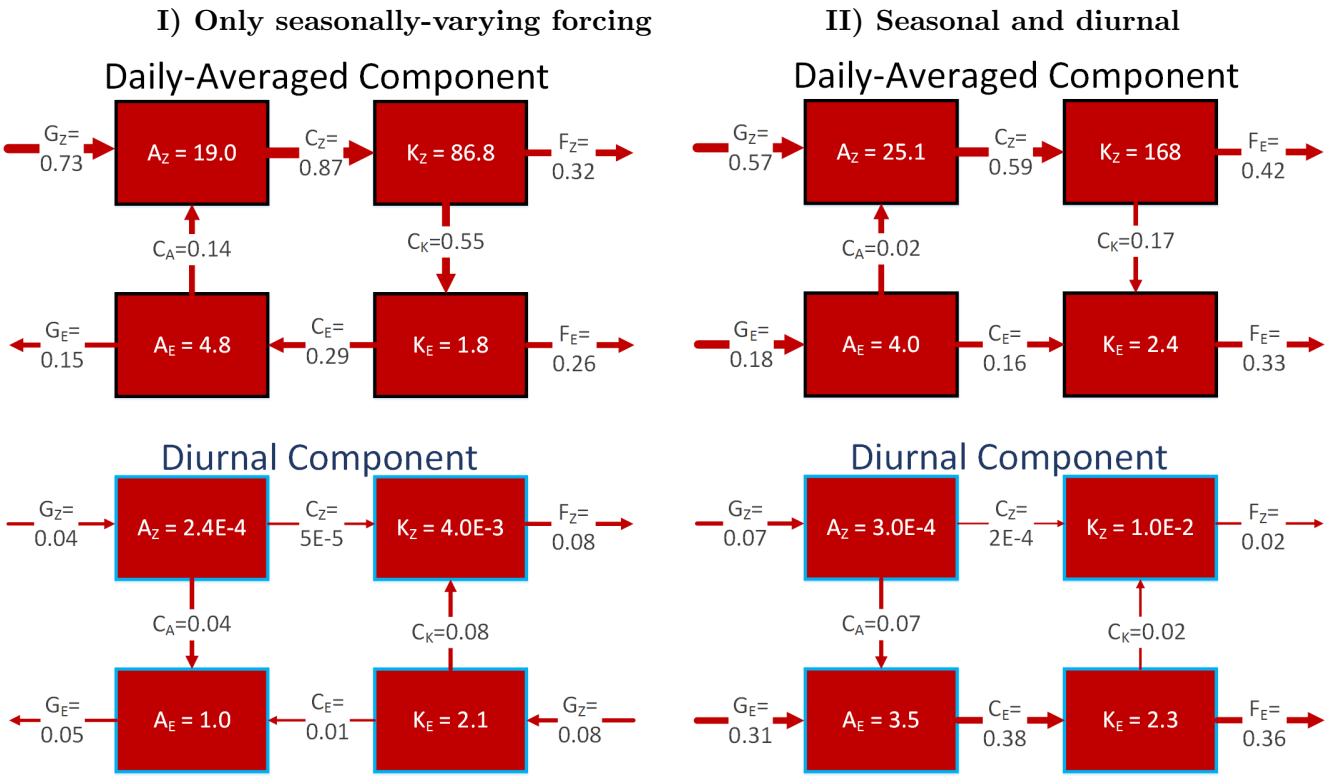

Figure 6.18: Lorenz energy cycle for PUMA-GT simulation at $\Omega = \frac{1}{8}\Omega_E$, $\tau_f = 1$ day, $\mathcal{G} = 0$, $\tau_{surf} = 360$ days, with seasonally-varying solar forcing (left) and diurnal solar forcing (right).

for Mars in Chapter 2.

Figure 6.18 shows Lorenz box diagrams for the daily-averaged (top) and the diurnal (bottom) component of the example simulation with seasonally-varying solar forcing (left) and seasonally- and diurnally-varying solar forcing (right). Overall, both simulations are dominated by their daily-averaged components. The purely seasonally-forced case shows a strong conversion of A_Z into K_Z, which is in line with the spectral energy budget (see Fig. 6.19a, C_{zonal}) showing that kinetic energy is injected at the largest scales. This K_Z is then converted into eddy kinetic energy K_E via barotropic instabilities. The baroclinic conversion (C_A, C_E) is reversed in this case. The diurnal component of the purely seasonally-forced case (Fig. 6.18), bottom) has only minor contributions to the energy cycle.

In the seasonally- and diurnally-varying forcing case (Fig. 6.18II) the daily-averaged component also shows strong zonal conversion C_Z. This is, however, where similarities with the seasonally-varying case end. In total there are only minor conversions from zonal to eddy terms with both C_A and C_K being relatively small. The eddy conversion

C_E is significant in both daily-averaged and diurnal component and is the main source of eddy kinetic energy. In this case, the diurnal component of C_E dominates. This conversion is only slightly baroclinic (as C_A is small) and mostly originates from direct generation of eddy APE. Because total C_A and C_E are small, the analysis of the global-mean annual-mean Lorenz cycle suggests that APE is equally generated in both zonal and eddy component via G_E and G_Z is converted directly from A_Z to K_Z and from A_E to K_E and is then lost via friction via $F_{E,Z}$, respectively. So apart from a small interaction in the daily-averaged component to the barotropic conversion, zonal and eddy terms do not strongly interact with one another. However, as this diagnostic occurs in the annual mean there is still the possibility that seasonal variations occur in the conversions between these terms.

Spectral energy budgets

This subsection presents the spectral energy budget of of the example simulation with $\Omega = \frac{1}{8}\Omega_E$, $\tau_{surf} = 360$ days, $\mathcal{G} = 1$, $\tau_{atm} = 40$ days, $\tau_f = 1$ day. The case with purely seasonal forcing (Fig. a,b) was shown before in Section 5.6.3.For this case APE and KE are generated at the largest scales and cascade downscale (via Π_A and Π_K) throughout the region of resolved scales. Both Π_A and Π_K are dominated by residual zonal interactions. KE is mostly generated at small wavenumbers ($k \leq 3$) via the zonal-zonal interaction component of $\mathcal{C}$ (c.f. C_Z in Fig. 6.18I). The reverse baroclinic conversion (KE to APE) seen in Fig. 6.18I (C_A, C_E) occurs at wavenumbers $k = 2-8$.

For the diurnal cycle case (Fig. 6.19c,d) the total downscale energy flux is smaller than for the seasonally-varying case. This decrease originates from a decrease of Π_A at $k > 8$ and a decrease of Π_K for wavenumbers larger than 6. In addition, APE at small wavenumbers is transported upscale (Π_A negative). The conversion term $\mathcal{C}$ features positive slopes (APE to KE) at wavenumbers $k \geq 3$ in both the residual zonal interaction term as well as the eddy-eddy interaction term. This occurence, together with a large C_E value in the diurnal component of Lorenz energy cycle (Fig. 6.18II) confirms that kinetic energy is directly produced at the largest scales due to eddy-eddy interactions. As energy is directly injected by the tidal eddy forcing, Figs. 6.19c,d show a small eddy-eddy related downscale flux for both Π_A and Π_K at $k < 10$, which

I) Only seasonally-varying forcing

a) $\Omega^* = \frac{1}{8}$, $\mathcal{G} = 1$, $n_{\overline{\mu}=1}$, T42 Resolution

b) $\Omega^* = \frac{1}{8}$, $\mathcal{G} = 1$, $n_{\overline{\mu}=1}$, T42

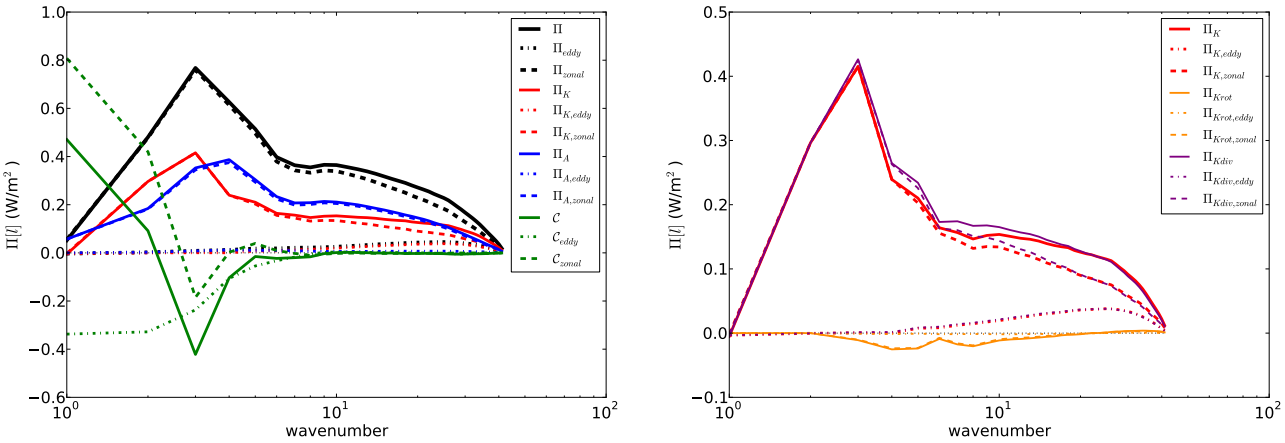

II) Seasonally- and diurnally-varying forcing

c) $\Omega^* = \frac{1}{8}$, $\mathcal{G} = 1$, $n_{\overline{\mu}=0}$, T42 Resolution

d) $\Omega^* = \frac{1}{8}$, $\mathcal{G} = 1$, $n_{\overline{\mu}=0}$, T42

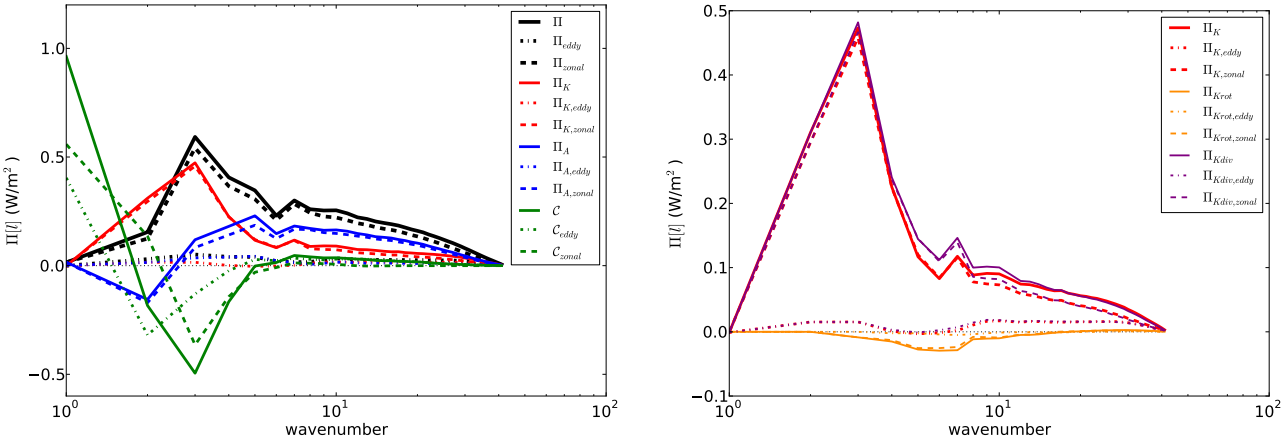

Figure 6.19: Spectral fluxes of KE Π_K, APE Π_A, total energy $\Pi = \Pi_A + \Pi_K$ as well as cumulative conversion $\mathcal{C}$ (left, a,c,e) and spectral fluxes of rotational and divergent KE Π_K (right, b,d,f) (each decomposed into eddy-eddy and residual zonal interaction components) for PUMA-GT run with $\Omega = 0.125\Omega_E$ and $\mathcal{G} = 0$ with seasonally-varying (a,b, $n_{\overline{\mu}=1}$) and both seasonally- and diurnally-varying (c,d, $n_{\overline{\mu}=0}$) forcing at T42 resolution (annual mean).

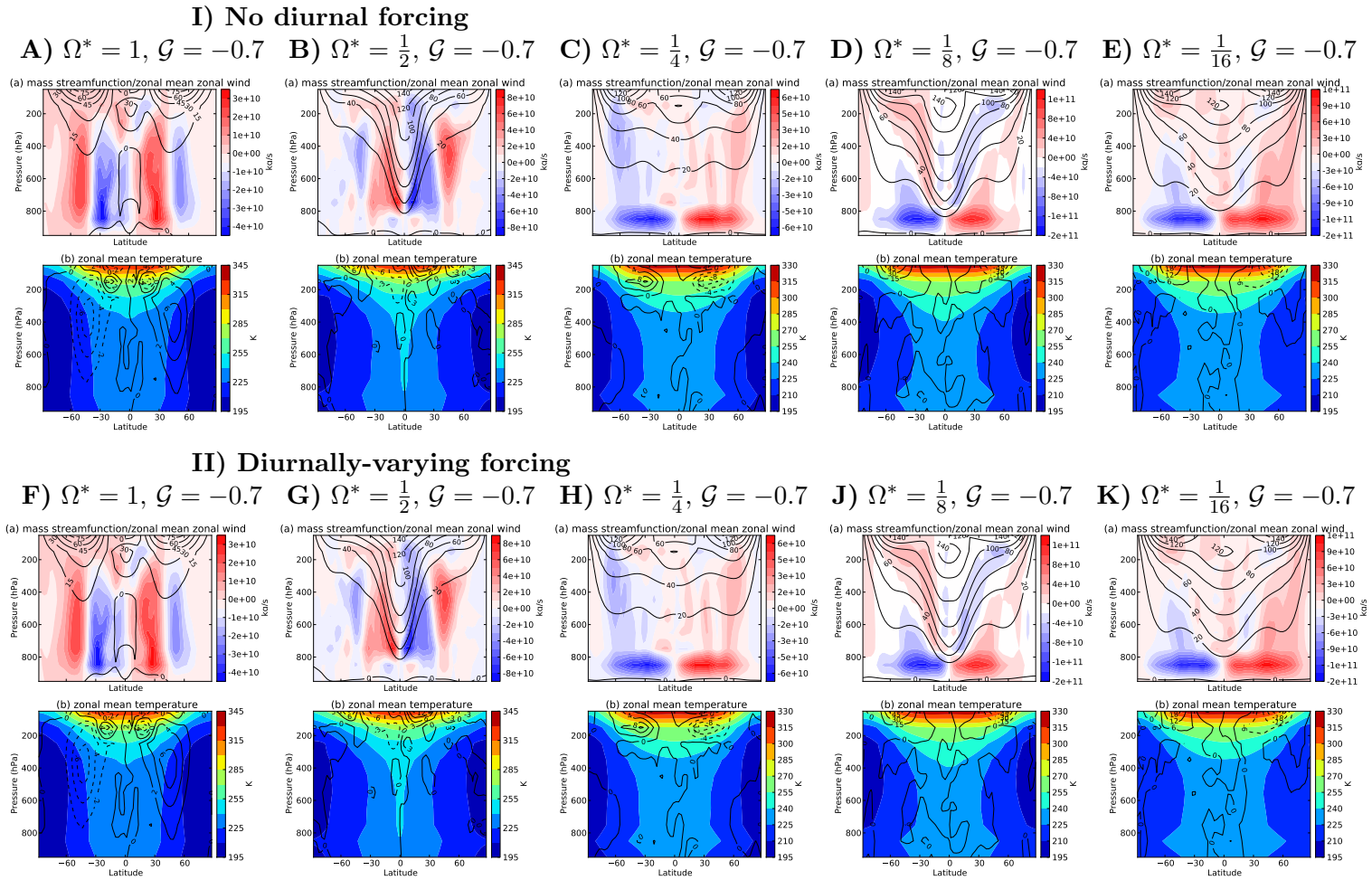

Figure 6.20: (a) meridional mass stream function; (b) zonal mean temperature (colour) and potential temperature fields (contour), (c) zonal mean zonal wind (contour), and (d) meridional eddy momentum flux for simulations with and without diurnal cycle. The plotted fields are averaged over one model year. (Constants: $\Omega = \frac{1}{8}\Omega_E$, $\tau_{surf} = 360$ days, $\tau_{atm} = 40$ days, $\tau_f = 1$ day

is absent for the seasonally-varying case (Fig. 6.19a,b).

6.4.5 Varying rotation rate at $\mathcal{G} = -0.7$

Here, we briefly describe the effect of varying Ω^* in the $\mathcal{G} = -0.7$ regime. For the sake of comparison, the other variables are chosen to be equal to the previous section. We find that cases with $\Omega^* = \frac{1}{2}, \frac{1}{8}, \frac{1}{16}$ are subject to a significant enhancement of the equatorial jet by over wind speeds of over 100 ms^{-1}. The cases with $\Omega^* = 1, \frac{1}{4}$, however, only experience an enhancement of up to 20 ms^{-1}. Another interesting distinction can be seen in the $\Omega^* = \frac{1}{16}$ case, where the simulation with purely seasonally-varying forcing exhibits sub-rotating winds.

The cases with a significant enhancement of equatorial superrotation due to the diurnal forcing all feature upward vertical momentum fluxes at the equator. It may be that these cases experience a resonance between their rotation rate, the seasonal and diurnal variation of the solar forcing and resulting atmospheric waves. A comparison with seasonally-constant forcing (see Fig. 6.5) suggests, that seasonal variation introduces a non-linear response in Ω to the enhancement of equatorial superrotation due to diurnally-varying forcing.

Instead of showing further in-depth analysis of specific simulations, which may prove to cumbersome to accomplish, we will attempt to compare the data of our large set of simulations to an existing theory. This theory is tested in Section 6.5 and may explain the mechanism by which the super-rotating jet is enhanced via upward vertical momentum fluxes.

6.5 Theoretical relationships and scaling laws

There are theoretical calculations that predict the effect of diurnal heating on a slowly-rotating planet with super-rotating winds. The so called "moving flame effect" (Schubert and Whitehead, 1969) is capable of accelerating zonal wind speeds to up to 100 ms^{-1} in Venus-like conditions via gravity waves (Fels and Lindzen, 1974, Plumb, 1975). Eliassen and Palm (1961) show that internal gravity waves do not exchange momentum with the mean flow in the absence of forcing, dissipation or transience. In the presence of thermal forcing, gravity waves with both vertically propagating and trapped modes will lead to a vertical redistribution of momentum (Fels and Lindzen, 1974). In recent years, comprehensive models of the Venus atmosphere have found that thermal tides have a significant effect on the general circulation (Takagi and Matsuda, 2007, Lebonnois et al., 2010, 2016).

In this section, we will first provide a crude comparison between purely diurnally-forced simulations (from Section 6.2) and an estimate of Venus-like winds due to thermally driven gravity waves (Fels and Lindzen, 1974) in Section 6.5.1. Section 6.5.2 will ascertain the effect of the solar irradiance. Finally, in Section 6.5.3, we provide an initial scaling relationship between enhancement of zonal wind and the atmospheric

heating rate.

6.5.1 Approximate Venus-like wind speeds due to thermal forcing

Fels and Lindzen (1974) analytically derive initial accelerations $\dot{U}$ due to thermally excited gravity waves. They find that e.g. for a thin heating region $\dot{U}$ is a function of the absorbed power $\mathcal{P}$ with

$$\dot{U} \propto \mathcal{P}^2. \tag{6.5}$$

The acceleration for a thick heating region is provided as

$$\dot{U} \propto \left(\frac{\mathcal{P}\lambda_{gw}}{2 \cdot h_{th}} \right)^2 \tag{6.6}$$

where λ_{gw} is the vertical wavelength of the internal gravity wave and h_{th} is the height of the thermally excited region. Apart from showing via numerical computation that their theory produces realistic thermally induced winds in the Earth's mesosphere, Fels and Lindzen (1974) provide a rough analytical approximation of the resulting wind speeds in the case of the super-rotating stratosphere of Venus. According to them, under the assumption that a developing zonal jet in a thin vertical layer will quickly develop critical levels of wind shear. Under Venus conditions, equilibrium flow should be reached when the Richardson number is $Ri = \frac{N^2}{(d\overline{u}/dz)^2} = 1/4$ in the jet (Fels and Lindzen, 1974). Here N is the Brunt-Väisälä frequency, and $\overline{u} = c + U$, where c is the phase speed of the thermal forcing and U is the resulting speed of the super-rotating jet. Under the assumption that $c << U$ they arrive at a surprisingly simple relation between the two velocities:

$$U \approx -\pi \cdot c. \tag{6.7}$$

where for Venus $c = 4$ ms^{-1} so that $U \approx 13$ ms^{-1}. However, when a underlying mean flow U_{mean} is considered, Eqn. 6.7 becomes

$$U \approx \pi(U_{mean} - c). \tag{6.8}$$

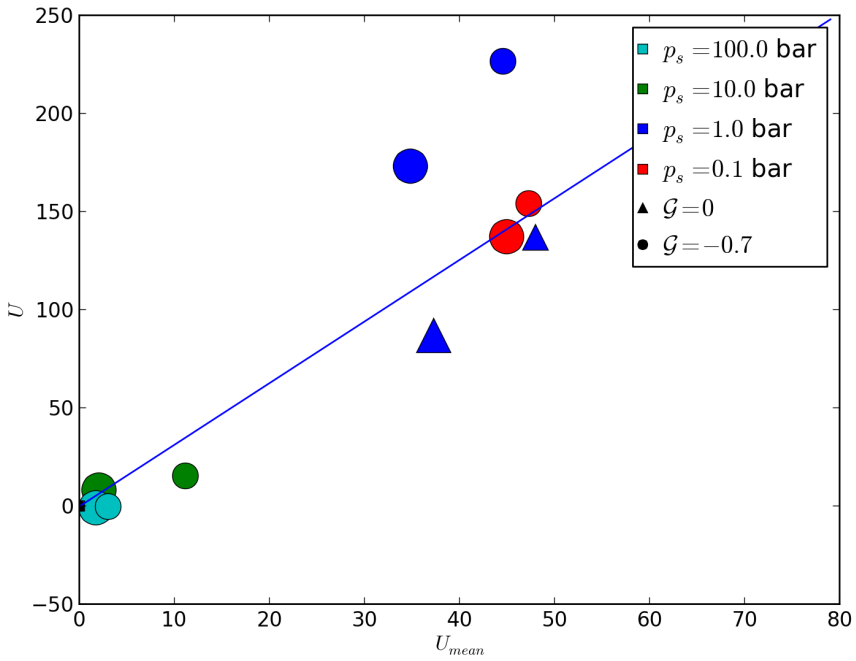

Figure 6.21: Comparison of theoretical wind velocity of equatorial jets according to Fels and Lindzen (1974, blue line) and model output for simulations with $\mathcal{G} = -0.7$ and $\mathcal{R}o > 1$ ($\Omega^* = \frac{1}{8}, \frac{1}{16}$), where smaller symbols represent simulations with $\Omega^* = \frac{1}{8}$ and larger symbols simulations with $\Omega^* = \frac{1}{16}$ and with varying $p_s = 0.1, 1, 10, 100$ bar (red, blue, green symbols respectively) and $\tau_f = 0.1, 1, 10$ days (dots, stars, and triangles, respectively). In this case U is the annual mean, equatorial mean ($-10° < \phi < 10°$), upper atmosphere mean $\sigma = p/p_s \leq 0.3$, zonal mean zonal velocity of the case with diurnal cycle and U_{mean} is the global mean zonal velocity of the case with seasonally-varying forcing.

and U can realistically reach Venus-like wind speeds of 100 ms^{-1} (Fels and Lindzen, 1974).

While this last result is extremely approximate, a tentative comparison can be easily made with runs in our parameter space that fit the assumptions above. For instance the thin source assumption may apply to simulations with $\mathcal{G} = -0.7$, and the $c << U$ approximation should be met for our slow rotating planets (i.e. $\Omega^* = \frac{1}{8}, \frac{1}{16}$ with $c \approx 29, 58$ ms^{-1}) that experience strong accelerations due to the diurnal cycle. Since the above derivation requires a very small, Venus-like value of $c \approx 4$ ms^{-1}, we will perform another approximation to allow for a crude comparison with our simulations:

$$U \approx \pi U_{mean}. \tag{6.9}$$

We can now directly compare the global mean zonal wind U_{mean} of the case without diurnally-varying forcing with the equatorial ($-10^\circ < \phi < 10^\circ$) zonal wind U in the upper atmosphere ($\sigma = p/p_s \leq 0.3$) of the case with diurnally-varying forcing. Figure 6.21 shows this comparison of U and U_{mean}. The blue line in Fig. 6.21 represents the equation in Eqn. 6.9. This comparison may be a bit unsatisfactory, but the two simulations with $p_s = 0.1$ bar, which is roughly where the upper cloud deck of Venus is located, fit quite well to this very approximate comparison. That means that for these specific simulations the approximations of Fels and Lindzen (1974) may hold true and superrotation in these cases may be primarily caused by thermally-excited gravity waves.

6.5.2 Acceleration and absorbed solar power

For this section we have performed ten runs with varying insolation $S = \frac{1}{4}, \frac{1}{2}, 1, 2, 4 \cdot S_0$, where S_0 is the solar irradiance on Earth, and with and without diurnal forcing at $\Omega^* = \frac{1}{8}$ and $\mathcal{G} = 1$. These runs are then used to compare the initial acceleration caused by the diurnal tide with Eqn. (6.5) under the assumption that in our $\mathcal{G} = 0, -0.7$ cases the absorbed power $\mathcal{P}$ is directly proportional to S.

In Figure 6.22 we compare the acceleration of the maximum zonal wind speed in the upper atmosphere $\sigma = p/p_s \leq 0.3$, equatorial region ($-10^\circ < \phi < 10^\circ$) with the amount of insolation incident on the planet. The plotted data scales fairly well for $S \geq 1$, as indicated by the purple curve that is proportional to S^2. This may be another clue towards validating the theory of Fels and Lindzen (1974).

6.5.3 Scaling relations of diurnal superrotation acceleration

In this subsection we will motivate a simple scaling law to quantify the parameter dependence of the speed up that occurs in the meridional wind due to the diurnally-varying forcing. This comparison is better than those of the two previous subsections, yet it is still only meant as a rough approach to a scaling law. Hence, the following motivation requires only a heuristic derivation.

According to Fels and Lindzen (1974), diurnally-varying solar forcing will excite gravity-waves that are able to interact with the mean flow. This interaction can lead

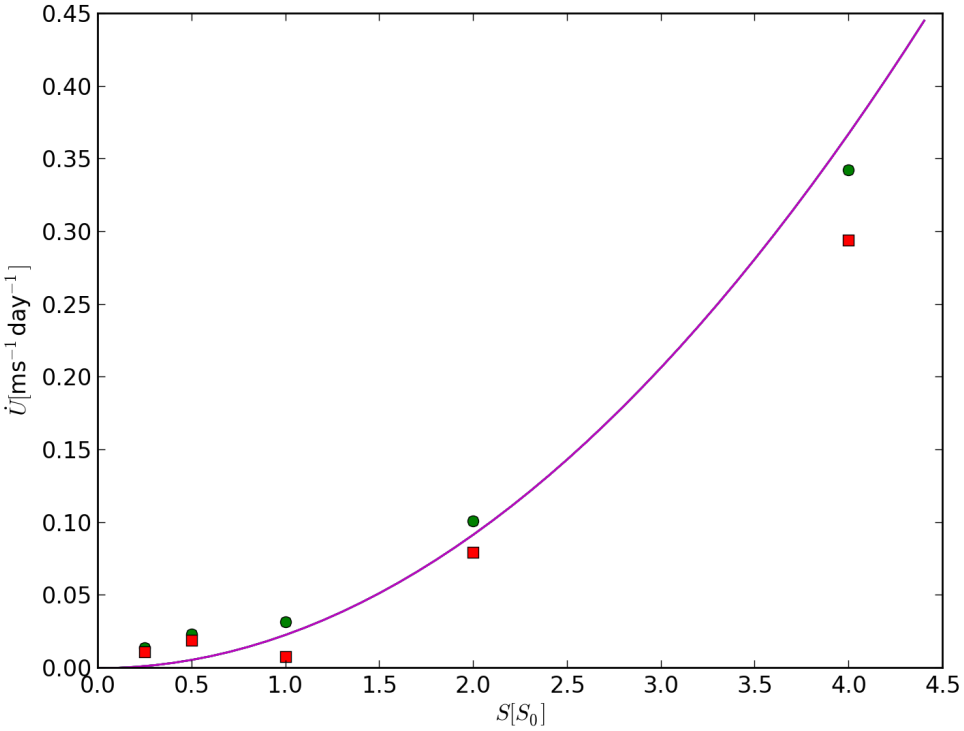

Figure 6.22: Acceleration of the maximum upper atmosphere equatorial zonal wind $u_{eq,st}$ of the diurnally forced run (dots), difference between the accelerations of $u_{eq,st}$ of the diurnally forced and the non-diurnally forced run (squares), plotted against the solar irradiance S. The data was averaged over the first 6 months of model data. The plotted curve is a fit so that $\dot{U} \propto S^2$.

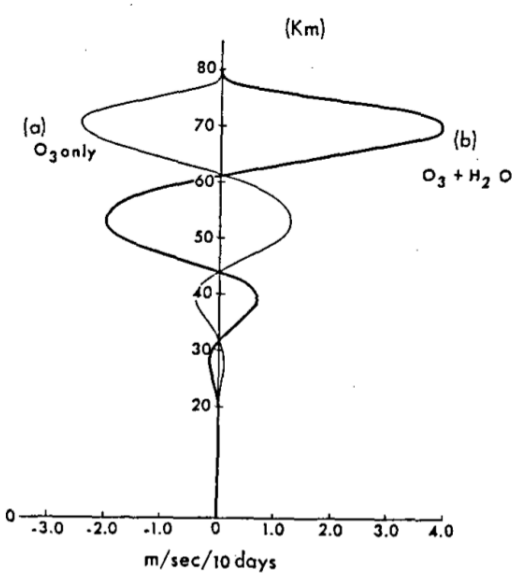

Figure 6.23: Velocities resulting from diurnal thermal forcing in the Earth atmosphere. The velocity profile can change dramatically depending on whether thin or wide vertical regions in the atmosphere absorb incident solar flux. Reproduced with permission from (Fels and Lindzen, 1974, their Fig. 1)

to a vertical redistribution of angular momentum, which (depending on the size of the absorbing atmospheric layer) will accelerate and decelerate the zonal wind in different levels of the atmosphere. Fig. 6.23 displays a possible solution for the zonal wind velocities for an Earth-like case that includes only absorption of O_3 and of both O_3 and H_2O.

The solar forcing is controlled by a heating rate Q, which controls the resulting vertical momentum flux $\rho_0\overline{uw}$ via

$$\frac{\partial}{\partial z}(\rho_0\overline{uw}) \propto -\frac{\kappa\rho_0}{U_0 - c}\overline{Q} \tag{6.10}$$

where z is the vertical direction, u and w are periodic motions of the gravity waves in zonal and vertical direction, respectively, $\kappa = R/c_p$, ρ_0 is the mass density, U_0 is a mean flow in the zonal direction, and c is the phase speed of the diurnal forcing (see Fels and Lindzen, 1974, their Eqn. 13). The initial acceleration of U due to the angular momentum redistribution is approximated by

$$\rho_0 T\dot{U} = \rho_0\overline{uw} \tag{6.11}$$

where T is the temperature (see Fels and Lindzen, 1974, their Eqn. 19).

Due to the above equations we will attempt to show the relationship between the speed-up of zonal wind due to diurnal forcing and the heating rate Q as a function of our non-dimensional parameters (see Section 1.1). The heating rate can be written as.

$$Q(z) = \frac{1}{\rho(z)c_p}\frac{\partial}{\partial z}F^{net}(z) = \frac{g}{c_p}\frac{\partial}{\partial p}F^{net}(p) \tag{6.12}$$

where c_p is the specific heat capacity of the atmosphere and F^{net} is the net radiative flux. Here F^{net} is similar to the fluxes calculated in Section 3.3.1 and is a function both the incident top-of atmosphere solar flux S_0 as well as the optical depths in short-wave χ_{sw} and long-wave χ_{lw},

$$F^{net} \propto S_0 e^{-\chi z}. \tag{6.13}$$

In our case we will take the Greenhouse parameter $\mathcal{G} = \frac{\chi_{lw}-\chi_{sw}}{\chi_{lw}+\chi_{sw}}$ and add one so that it does not produce negative values:

$$Q \propto \frac{\partial}{\partial z}F^{net} \approx (1-\mathcal{G})e^{1-\mathcal{G}} \tag{6.14}$$

The heat capacity of the atmosphere c_p scales linearly with the radiative time scale $c_p \propto \tau_{atm}$, which features prominently in the atmospheric relaxation parameter $\mathcal{A} = 2\Omega\tau_{atm}$ (see Section 1.1.4). Hence,

$$Q \propto \frac{1}{c_p} \propto \frac{1}{\tau_{atm}} \propto \frac{1}{\mathcal{A}}. \tag{6.15}$$

so that in total we will use

$$Q \propto \frac{(1-\mathcal{G})e^{1-\mathcal{G}}}{\mathcal{A}}. \tag{6.16}$$

this scaling parameter will be called $P = (1-\mathcal{G})e^{1-\mathcal{G}}/\mathcal{A}$.

Next is the choice of the atmospheric quantity that we can use to quantify the speed up of the equatorial super-rotating jet. Two such quantities are the mean zonal wind $[\overline{U}]$ and the superrotation index S. Another important choice is the extent of

the region in the atmosphere that we average over in this comparison. In their scaling law approach, Laraia and Schneider (2015) used the zonal wind in the equatorial upper atmosphere region, which they compared to their propensity for superrotation S_r. In the current work, we want to compare the difference between simulations with and without diurnally-varying forcing with a quantify that is a function of our non-dimensional parameters. When including only diurnal variation (i.e. without seasonal variation, see Section 6.2), we have seen that the speed up of the super-rotating jet occurs at the equator and can extend from the stratosphere down to $p = 800$ hPa.

In Figures 6.24a-c, we compare three such quantities for simulations with no seasonal forcing (obliquity $\epsilon = 0°$). The values on the y-axis are the difference between simulations with diurnally-varying and with diurnally-averaged forcing. The quantities depicted are the equatorial mean zonal wind (Fig. 6.24a), the global superrotation index (Fig. 6.24b) and the equatorial mean local superrotation index (Fig. 6.24c). The local superrotation index s is the ratio between the total specific angular momentum m (Eqn. 5.2) and the angular momentum of the atmosphere at rest:

$$s = m/\Omega a^2 - 1. \tag{6.17}$$

The "equatorial" superrotation index s_{eq} plotted in Fig. 6.24 is calculated by averaging over the year, longitude, pressure as well as the equatorial region in latitude $-10° < \phi < 10°$. From Figs. 6.1-6.4 we can see that most changes due to diurnal forcing occur in the equatorial region.

These three plots in Fig. 6.24 show a rising slope with rising scaling parameter P. Fig. 6.24a shows the difference in zonal wind due to diurnal forcing. While wind speeds are generally rising with rising P, there is a large spread in wind speeds because simulations with faster rotation rate are also affected by the diurnal forcing when there is no seasonal variation (see Fig. 6.5). When looking at the superrotation index Figs. 6.24b,c these fast rotating cases become less important, i.e. the relative speed-up is still pretty minor compared to the inherent planetary rotation rate. In Fig. 6.24b we see that the global superrotation index becomes larger than 0.2 at around $P = 0.05$. Overall, in the case with seasonal variation, s_{eq} scales best with P (Fig. 6.24c as the

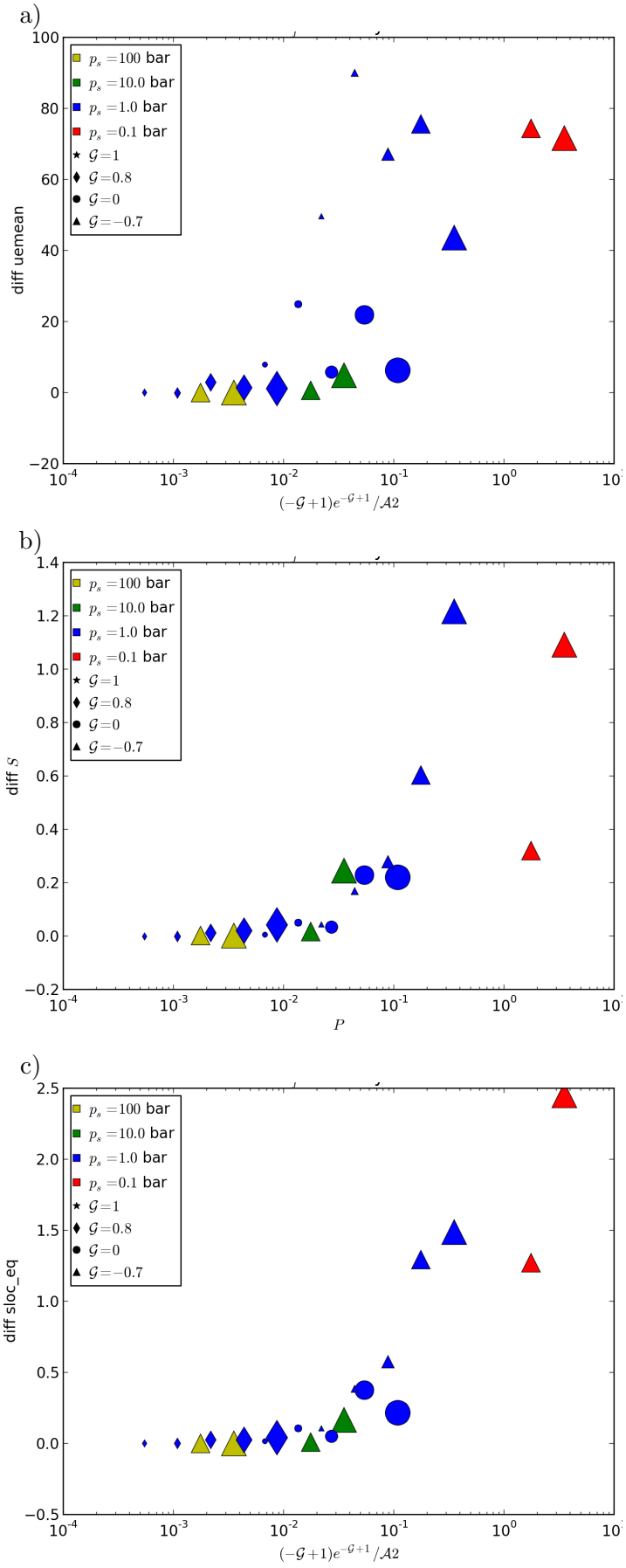

Figure 6.24: Difference in (a) zonal wind u_{eq} (mean over year, longitude, pressure, and equatorial region $\pm 10°$), (b) global superrotation index, (c) local superrotation index (mean over year, longitude, pressure, and equatorial region $\pm 10°$) due to diurnally-varying solar forcing. Colours denote different surface pressures, shapes denote different values of $\mathcal{G}$, symbol sizes are determined by the planetary rotation Ω, with $\Omega^* = 1$ is the smallest and $\Omega^* = \frac{1}{16}$ is the largest size.

plot has minimal spread and the curve depicted in Fig. 6.24c is generally monotonic. This shows that s_{eq} scales linearly with P and therby proportional to the heating rate Q. This proportionality as well as the previous comparisons in this section show that the speed-up of superrotation observed in our simulations may occur due to interaction with thermally-excited gravity waves (i.e. the induced thermal tide) (Fels and Lindzen, 1974).

However, there is a small caveat. The dataset we have regarded in the current section up to now is very limited with only 21 data points. A proper comparison with the full dataset with diurnally and seasonally-varying forcing (with over 800 simulations) is featured below.

6.5.4 Scaling law for simulations with both seasonally and diurnally varying forcing

With additional seasonal variation, the evaluation of the effect of diurnally-varying solar forcing becomes more difficult. This is because the diurnal cycle is superposed on top of seasonal variations, which introduces a further non-linearity into the problem, which may influence even the mechanism by which momentum is transported.

In his section we will again compare how well certain quantities of the superrotation scale with P. Due to the seasonal variability in these simulations, taking the equatorial value is not ideal, because the strongest point of solar irradiance is outside of our equatorial region for a large part of the year. As we cannot individually map the atmospheric region that experiences the most speed-up, the best choice of variable to compare in this case should be the difference in the global superrotation index S due to diurnally-varying forcing. Our dataset in this case is comprised of over 800 simulations with and without diurnally-varying forcing (but always with seasonally-varying forcing) within a wide range of parameters.

In Fig. 6.25, we compare how well S and P scale with each other. In this case we show comparisons for different values of boundary layer Rayleigh friction with $\tau_f = 0.1, 1, 10$ days (corresponding to Figs. 6.25a, b, c). From these plots, it is apparent that with smaller τ_f (stronger friction), S and P scale better with one another (Fig. 6.25a). If the mechanism by which momentum is redistributed is in fact governed by a vertical

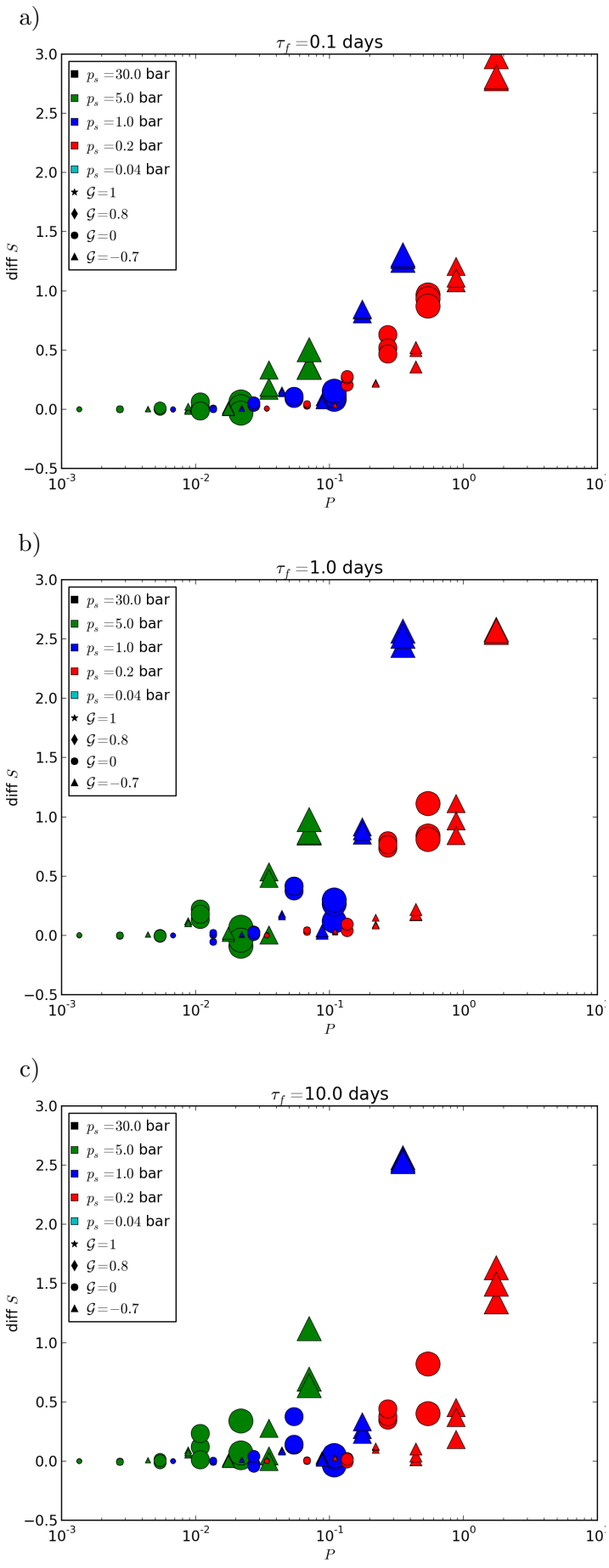

Figure 6.25: Difference in global superrotation index due to diurnally-varying solar forcing with frictional timescale a) $\tau_f = 0.1$ days, b) $\tau_f = 1$ days, c) $\tau_f = 10$ days . Colours denote different surface pressures, shapes denote different values of $\mathcal{G}$, symbol sizes are determined by the planetary rotation Ω, with $\Omega^* = 1$ is the smallest and $\Omega^* = \frac{1}{16}$ is the largest size.

momentum flux due to thermally excited gravity waves (Fels and Lindzen, 1974) then it would make sense, that the mechanism works better with stronger friction. For superrotation to develop, angular momentum that is generated at the surface due to friction is transported upwards (see section 6.1). In conclusion, the diurnally-induced vertical momentum redistribution may work more efficiently with stronger boundary layer friction.

To better depict the dependencies between P and the enhancement of S due to diurnally-varying forcing, we show the scaling data as a log-log-plot in Fig. 6.26. We can note that our choice of P with $P = \frac{(1-\mathcal{G})e^{1-\mathcal{G}}}{\mathcal{A}}$, works very well for strong surface friction ($\tau_f = 0.1$), but less well for larger τ_f. However, if our enhancement of super-rotating winds results from thermally-excited gravity waves that vertically redistribute angular momentum, as the work in sections 6.4 and 6.5 suggests, then an improved momentum exchange between surface and atmosphere (via increase in strength of the frictional layer) would facilitate the equatorial convergence of vertical momentum flux. Hence, the $\tau_f = 0.1$ case should be the most effective at enhancing the super-rotating flow via the atmospheric heating rate $Q \propto P$.

While this result does not explain all cases, it shows that with strong friction, the angular momentum redistribution responsible for enhancing the super-rotating wind is controlled by the diurnally-varying heating rate. In the cases with weaker friction, there seems to exist an additional effect that may be related to the seasonal-variation in our simulations.

6.5.5 Discussion

The scaling relationships found in this chapter showed that the increase of superrotation due to diurnally-varying forcing is strongly correlated to a heating rate. This may lead us to the conclusion that thermally excited gravity waves may be at play here (Fels and Lindzen, 1974). Another clue for this is that the momentum fluxes shown in Section 6.4 have a similarly alternating pattern in altitude as the velocity profiles produced by Fels and Lindzen (1974). While this may be the case, however, the wind velocities resulting in our model simulations do not show this alternating pattern. This may be explained by the fact that Fels and Lindzen (1974) have worked mostly in two

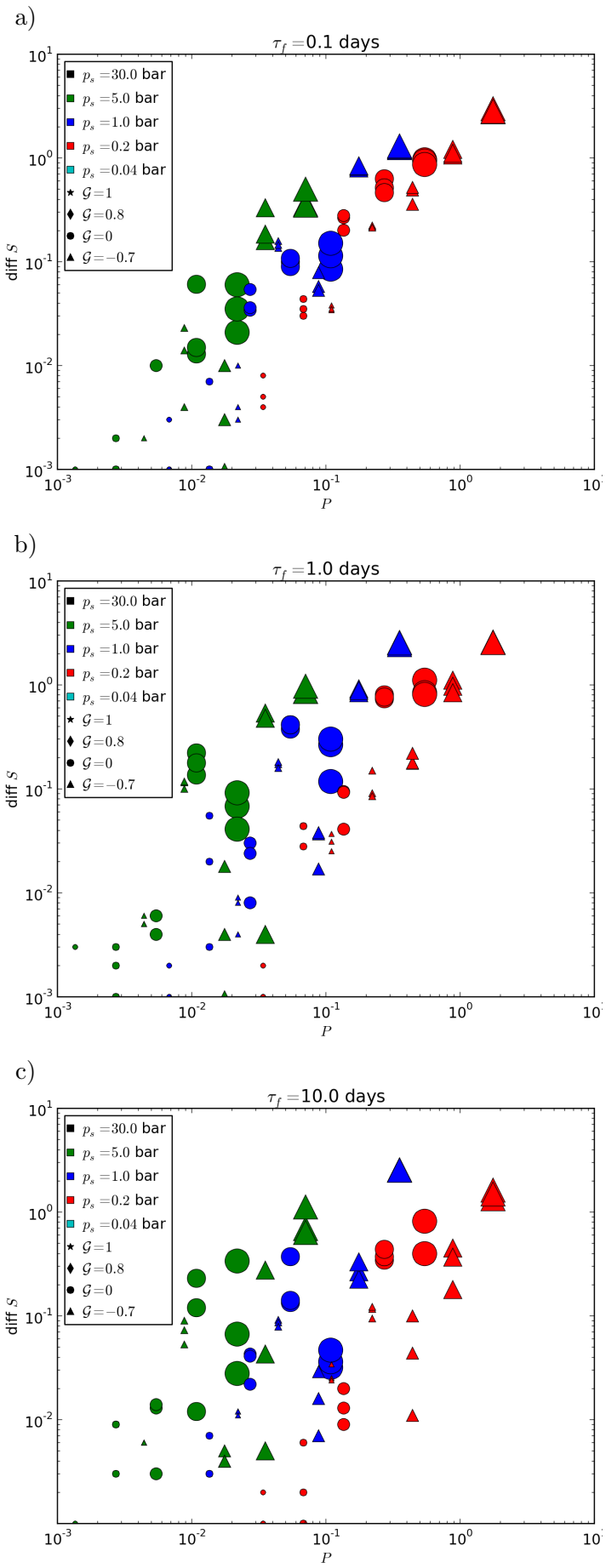

Figure 6.26: Difference in global superrotation index due to diurnally-varying solar forcing with frictional timescale a) $\tau_f = 0.1$ days, b) $\tau_f = 1$ days, c) $\tau_f = 10$ days . Colours denote different surface pressures, shapes denote different values of $\mathcal{G}$, symbol sizes are determined by the planetary rotation Ω, with $\Omega^* = 1$ is the smallest and $\Omega^* = \frac{1}{16}$ is the largest size.

dimensions (zonal and vertical) and did not account for the background flow. In our simulations the thermal tide is superposed upon a zonal flow driven by a Hadley-like circulation, with input from mid-latitude eddy fluxes, which is more complicated than what Fels and Lindzen (1974) considered. It is possible that meridional momentum fluxes provide a further non-linear effect, which may change the expected outcome in the velocity profile. This may very well be the case, as meridional eddy momentum flux convergence is one of the essential mechanisms required for maintaining superrotation that is not forced by diurnally-varying heating (Read, 1986, Mitchell and Vallis, 2010).

This spectral data is divided by a smoothed version of this data, so that the resulting spectra can be used to identify wave activity. This method is used by Potter et al. (2014), where they identify equatorial Kelvin waves as essential in aiding with the horizontal convergence of angular momentum, which maintains the super-rotating jets in their simulations.

To get a better understanding of the waves involved in maintaining the super-rotating jet, we have computed Wheeler-Kiladis diagrams (Wheeler and Kiladis, 1999) of the example case presented in Section 6.4.3. Wheeler-Kiladis diagrams are wavenumber-frequency diagrams of outgoing longwave radiation (Wheeler and Kiladis, 1999) or other atmospheric diagnostics such as zonal wind (e.g. Ferguson et al., 2009), precipitation (e.g. Slawinska et al., 2014), or geopotential height (Potter et al., 2014). They can be utilised to identify the atmospheric waves about the equator.

Similar to Potter et al. (2014), we obtain a Wheeler-Kiladis diagram by performing a Fourier transform in zonal direction and time of the geopotential height in the equatorial region (e.g. $\phi = \pm 15^{\circ}$). This spectral data is divided by a smoothed version of this data, so that the resulting spectra can be used to identify wave activity. This method is used by Potter et al. (2014), where they identify equatorial Kelvin waves as essential in aiding with the horizontal convergence of angular momentum, which maintains the super-rotating jets in their simulations.

Figure 6.27 shows Wheeler-Kiladis diagrams decomposed into symmetric and antisymmetric component for all four cases presented in Section 6.4.3. These four cases are

I Purely seasonally-varying forcing

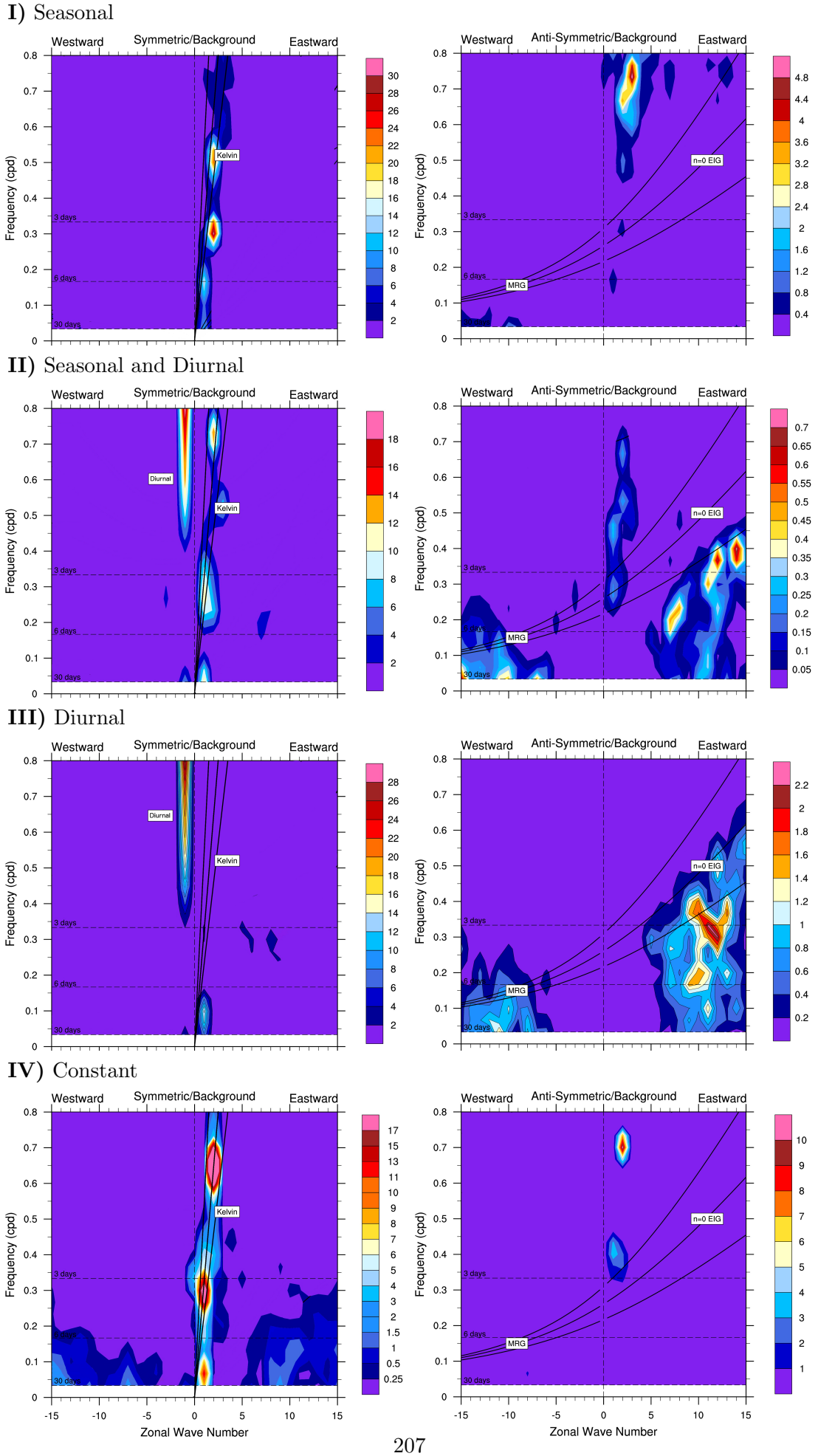

Figure 6.27: Symmetric (left) and Antisymmetric (right) component of the Wheeler-Kiladis diagram. (Parameters: $\Omega = \frac{1}{8}\Omega_E$, $\tau_{surf} = 360$ days, $\mathcal{G} = 0$, $\tau_{atm} = 40$ days, $\tau_f = 1$ day)

II Seasonally- and diurnally-varying forcing

III Purely diurnally-varying forcing

IV Annually-averaged, constant forcing

These plots are calculated using data of a 30-day period with time-steps of 2 hours. The geopotential height field used is located at 250hPa. For the seasonally-forced cases we study a 30-day period during which the flow is roughly centred about the equator (i.e. after the spring equinox). The Dispersion relations of relevant atmospheric waves are plotted into the Figures as labelled curves.

In Figures 6.27(left) we show the symmetric component of the Wheeler-Kiladis spectra. We see that all cases, except the purely diurnally forced case (case III), exhibit a Kelvin-wave signal with a steep slope. This Kelvin wave is located between zonal wavenumbers 1 and 3. It is likely that this Kelvin wave plays an important role in the horizontal angular momentum convergence, in concordance with Potter et al. (2014). The cases with diurnally varying forcing (cases II and III) feature another signal in the symmetric spectrum. This signal is localised at zonal wavenumber -1 and at timescales ≤ 1 day and is indicative of the diurnal tide.

Figures 6.27(right) show the antisymmetric component of the Wheeler-Kiladis spectra. A Comparison with Figures 6.27(left) shows that cases II and III feature a signal between zonal wavenumbers 5 and 15 that is indicative of equatorial inertial gravity waves. The existence of gravity waves in the diurnally-forced cases is another indication that thermally induced gravity waves are involved in the diurnal enhancement of the equatorial super-rotating jet via vertical angular momentum convergence.

Overall, these plots provide an indication that in cases I, II, and IV Kelvin waves are present and may play an important role in maintaining the equatorial super-rotation. In cases II and III, the diurnal tide is visible in the Wheeler-Kiladis plots as well as signals that indicate the involvement of gravity waves. To make sure that we have identified the diurnal tide correctly we show further plots of the symmetric components going up to larger frequencies on the y-axis in Fig, 6.28. The black lines in this Figure represent the dispersion relation of Kelvin waves with different speeds. Overall this Figure reaffirms our former conclusions cases I, II and IV have significant Kelvin wave

signals and cases II and III show a signal of the thermal tide. In this case, because the frequency in these plots goes up to 6 cycles per day, we see harmonics (diurnal, semi-diurnal etc.) of the thermal tide on the left side of the plot.

I) Seasonal

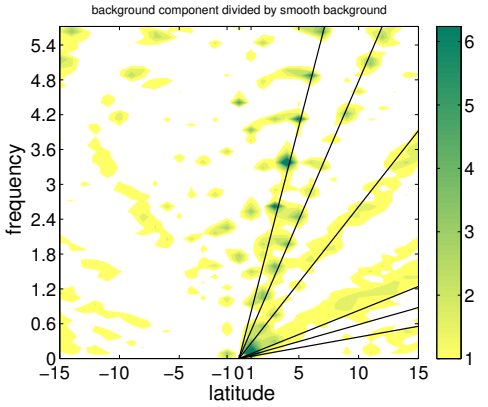

II) Seasonal and Diurnal

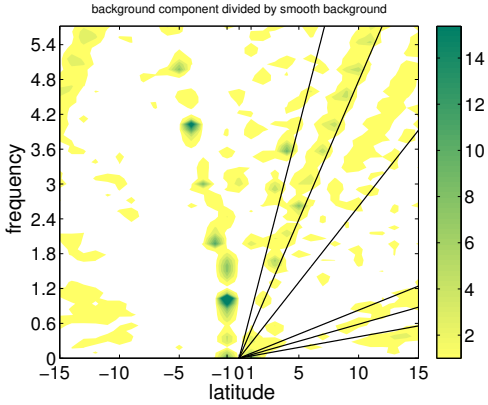

III) Diurnal

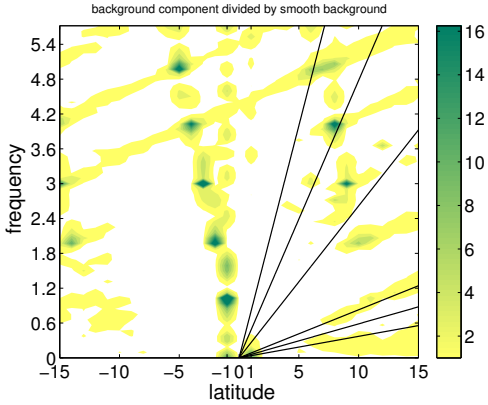

IV) Constant

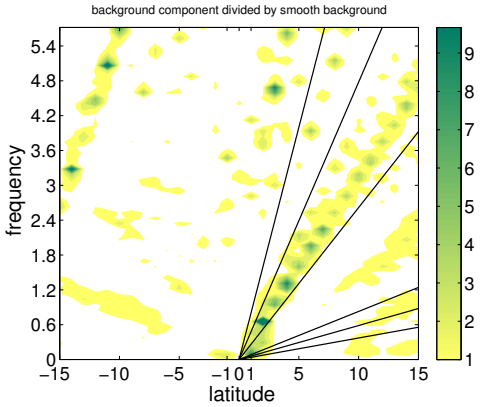

Figure 6.28: Symmetric component of the Wheeler-Kiladis diagram. (Parameters: $\Omega = \frac{1}{8}\Omega_E$, $\tau_{surf} = 360$ days, $\mathcal{G} = 0$, $\tau_{atm} = 40$ days, $\tau_f = 1$ day)

Chapter 7

Conclusion and outlook

The goal of this thesis is to improve our understanding of the general circulation of atmospheres for a wide range of planetary and atmospheric parameters with specific regard to the effects of seasonally- and diurnally-varying forcing. This work focusses on answering the following questions.

- How is mechanical energy transferred through planetary atmospheres? How does the Martian atmosphere compare to that of Earth? How does the transfer of atmospheric energy depend on planetary and atmospheric parameters?

- How is atmospheric macro-turbulence controlled by planetary parameters?

- What are the effects of seasonal variation within our parameter space?

- How is the angular momentum transfer affected by the presence of diurnally-varying forcing?

To this end, we have performed a large parameter study that concurrently varies the rotation rate, the surface thermal inertia, the atmospheric thermal inertia, the short-wave optical thickness, and the friction in the boundary layer. For this study we used and developed PUMA-GT (see Chapter 3), a simplified GCM with a semi-grey two-band radiation scheme (Wang, 2014) and time-dependent solar forcing.

7.1 Lorenz energy cycle

We have analysed the atmospheric transport of energy by using the Lorenz energy cycle. In Chapter 2, we present the first Lorenz energy budget computed from reanalysis data of a non-Earth planet. This shows that in the global mean, the Martian atmosphere behaves differently to Earth in terms of how energy is converted between zonal kinetic energy and eddy kinetic energy. On Earth, the annual mean Lorenz energy budget shows a stengthening of the zonal flow due to eddies, whereas for Mars the opposite is the case. This suggests a barotropically unstable contribution to eddy generation in the Martian atmosphere. By explicitly including topography (see Boer, 1989), we find that additional surface components provide a significant contribution to the conversion between kinetic energy (C_K) reservoir as well as the eddy and zonal available potential energy.

Another important difference to Earth is that the Martian atmosphere is strongly influenced by both seasonal and diurnal effects. A hemispheric decomposition of the Lorenz cycle revealed that there is a strong seasonal variation between direct and indirect heating mechanisms. A decomposition between diurnal and longer timescales showed that all conversion terms have diurnal contributions and that the generation of eddies occurs on diurnal timescales. This can be related to the thermal tide in the Martian atmosphere. In addition, during global dust storm events, the eddy kinetic energy increases considerably, so that 90% of eddy kinetic energy can be attributed to processes that operate on diurnal or smaller timescales.

7.2 Spectral energy transfer

We compute the spectral energy budget to understand the turbulence which occurs in our parameter simulations. For this we use a very recent scheme by Augier and Lindborg (2013), which includes the spectral fluxes of the available potential energy and the kinetic energy as well as the spectral conversion rate between these energy reservoirs. We first compute the spectral energy budget for simulations with constant forcing (see Chapter 4) for different rotation rates, performed by Wang (2014).

We find that simulations with rotation rates of $\frac{1}{2}$ the Earth's rotation rate or larger

adhere to the geostrophic turbulence theory; available potential energy is converted into kinetic energy at a scale close to the Rossby deformation radius. This kinetic energy is then mostly transported upscale in an inverse energy cascade. A smaller fraction of kinetic energy is transported downscale, which e.g. Wang (2014) has identified as an enstrophy flux. Below $\frac{1}{4}$ of Earth's rotation rate, the Rossby deformation radius becomes larger than the planetary radius and most available potential energy is directly converted into kinetic energy at the largest planetary scales. We generally find that the overwhelming spectral transfer in the respective available potential and kinetic energy reservoirs occurs due to zonal-eddy or zonal-zonal interactions. This means that within our simulations, the overwhelming component of the spectral flux does not occur in form of a cascade, from one consecutive wavenumber to the next, but rather like a waterfall, where each total wavenumber interacts directly with the zonal flow.

7.3 Response to seasonally-varying forcing

Within our parameter space we find that, for surface seasonality parameter $\alpha \gtrsim 1$ and Greenhouse parameter $\mathcal{G} \neq 1$, seasonal variation of the total atmospheric energy exceeds 1% of the annual mean. Below rotation rates of $\frac{1}{2}$ of the Earth rotation rate, the atmospheric relaxation parameter $\mathcal{A}$ also has an effect, so that for decreasing $\mathcal{A}$ (i.e. decreasing thermal inertia) the amplitude of seasonal variation increases.

At $\mathcal{G} = 1$ equatorial super-rotation is arrested when $\alpha \gtrsim 1$. This occurs because the seasonal variation results in less angular momentum to converge at the equator. This effect is also reported by Mitchell et al. (2014) and we show that their mechanism of the arrested angular momentum convergence is similar to ours. Mitchell et al. (2014) show that for large radiative atmospheric timescales, equatorial super-rotation reemerges, because the atmosphere reacts too slowly to temperature changes to respond to the seasonal change in surface temperatures. They argue that this may be the mechanism that allows equatorial superrotation to persist in the atmosphere of Titan.

In this thesis, we show that for decreasing $\mathcal{G}$ more solar energy is absorbed directly by the atmosphere and the effect surface seasonality becomes less important. Hence, superrotation may be unaffected by seasonal changes if enough atmospheric short-

wave absorption is present. This is an alternative explanation of why the atmosphere of Titan can maintain equatorial super-rotation despite strong seasonal responses. Because Titan has both a strong atmospheric short-wave absorption (with a short-wave optical thickness of $\chi_{sw} = 2.2$) and a large radiative timescale of about 20 years (due to temperatures of around 100 K), it is very likely that both effects are involved in allowing equatorial superrotation to persist.

We have also examined the spatial and spectral energy budgets of the simulations in our parameter study. Within our parameter regime every conversion rate switches its sign, which occurs roughly at $\mathcal{R}o = O(10^{-1})$ and $\mathcal{A} = O(10^2)$. In terms of a variation of the surface seasonality-parameter α, the fast-rotating regime shows increasing annual-mean Lorenz conversion rates with increasing α. This behaviour occurs at the same time as an increase in extratropical jets in the winter hemisphere. Our PUMA-GT simulations with a weak seasonal response (i.e. small α, $\mathcal{G} = 1$) have annual mean spectral energy budgets that compare well to the simulations without seasonal variation (c.f. Section 4.2). Simulations with stronger seasonal responses (due to either α, $\mathcal{G}$, or $\mathcal{A}$) show similar trends in their spectra (e.g. conversion from KE to APE due to eddy-eddy interactions between wavenumbers 3 and 8) that occur during seasonal extremes.

7.4 Diurnally-induced enhancement of equatorial super-rotation

We find that in simulations with non-zero short-wave absorption, the equatorial super-rotating jet is significantly enhanced by diurnally-varying forcing. For simulations without seasonally-varying forcing we find that the diurnal forcing enhances the equatorial jet across the whole range of rotation rates (from 1 to $\frac{1}{16}$ of the Earth rotation rate) with maximum wind speeds exceeding 100 ms^{-1}. Super-rotation at Earth-equivalent rotation speeds has been modelled by e.g. Saravanan (1993), Caballero and Huber (2010). With added seasonal forcing, only a fraction of the simulations in our parameter study show a significant contribution from diurnal forcing. These mostly lie in the slow-rotating regime (e.g. $\frac{1}{8}$, $\frac{1}{16}$ of the Earth rotation rate) for runs with a non-zero

greenhouse parameter. In this regime the equatorial jet is enhanced by velocities of up to 130 ms^{-1}.

In both solely diurnally-forced as well as seasonally- and diurnally forced cases, we find an increase in vertical angular momentum transfer from the surface due to diurnal forcing, whereas eddy momentum flux does not dramatically change. We try to explain this enhancement of vertical transfer with a theory on thermally excited gravity waves interacting with the mean flow (Fels and Lindzen, 1974), which states that zonal flow can be enhanced due to diurnally-varying forcing as a function of the atmospheric heating rate. We produce an initial scaling law that connects the heating rate with the enhancement of superrotation. Our scaling parameter scales very well with the global superrotation for strong friction in the boundary layer. Intermediate and weaker friction cases scale less well. However, if vertical angular momentum transport is indeed responsible for the enhancement of super-rotation, it would make sense that the cases with strong surface friction can more effectively convert the angular momentum of the surface into atmospheric angular momentum. We conclude that there is a strong case for simulations with strong surface friction to be influenced by thermally excited gravity waves.

We use a spectral diagnostic in both time and zonal-direction, usually referred to as a Wheeler-Kiladis diagram (Wheeler and Kiladis, 1999), for one example simulation, to identify the waves present in the different forcing cases. We find that constant and seasonal forcing cases show a Kelvin-wave-like signal which would support work by e.g. Mitchell and Vallis (2010), Potter et al. (2014) that the super-rotating jet is maintained by interaction with Kelvin waves. Our cases with diurnal forcing show the signal of the thermal tide. These cases have signals in the anti-symmetric component of the Wheeler-Kiladis diagram that are reminiscent of gravity waves. This further supports the case that the diurnal enhancement of equatorial superrotation is maintained by vertical angular momentum flux, which is transported by thermally-excited gravity waves.

7.5 Seasonal and diurnal effects in Mars-like simulations

We define the Mars-like regime as the parameter region with small surface and atmospheric thermal inertia (large α, small $\mathcal{A}$). In this region, the Lorenz energy cycle of our simulations with only seasonally-varying forcing compares quite well with the values calculated from Mars reanalysis data. The exception is that the C_E term, which represents a part of the baroclinic conversion, is underestimated by our simulations.

Within our parameter regime, we can only observe a non-negligible effect of diurnally-varying forcing if $\mathcal{G} \neq 1$ (i.e. $\chi_{sw} > 0$). Even in the Mars-like regime with small surface and atmosphere thermal inertia, our simulations with $\mathcal{G} = 1$ only show a minimal reaction from adding diurnally-varying forcing. Hence, underestimation of the C_E term still occurs. However, in cases with $\mathcal{G} \leq 0$, which is the case on Mars during dusty seasons, C_E increases and becomes comparable to the data from reanalysis data. This suggest that on Mars (at least in the annual and global mean) processes associated with baroclinic conversion are connected to the thermal tide.

7.6 Outlook and future work

7.6.1 Further diagnostics with existing data

For this thesis a large set of simulations was performed that can be further diagnosed in multiple ways. One possible way is to study the heat transfer efficiency of these simulations. This would help in understanding the temperature distribution of the simulated atmospheres which may provide important insights for planetary habitability studies. A similar study was already performed by Kaspi and Showman (2015), however, our dataset concurrently varies multiple parameters, which may provide further insights.

Another approach to analysing the existing data is to focus more on identifying the atmospheric waves present in the atmosphere. This should result in further insights to the mechanism of diurnally-induced enhancement of equatorial superrotation. Doing this on a large scale for the over 800 simulations was outside the scope of this work. We have used an approximate scaling law and found the global super-rotation index scales very well with our scaling parameter $\mathcal{P}$ for strong friction in the boundary layer. This approach can be improved in future studies by finding a scaling parameter that

scales better to the cases with weak friction.

7.6.2 New simulations with PUMA-GT

Our simplified model is very flexible and may easily be expanded by a hydrological scheme. This will enable the study of the effect of seasonally- and possibly diurnally-varying forcing on the hydrological cycle within a large parameter space.

Another possible study would include the variation of obliquity in combination with seasonally-varying forcing. This case may be interesting to compare with the atmosphere of Uranus, which has an obliquity of 98°. However, as Uranus is a giant planet, and terrestrial solar system analogues do not have large variations in obliquity, it may be better to use a model optimised for giant planets, so that an observable control case exists.

7.6.3 Further comparisons with Mars

Mars is the only planet, apart from Earth, for which reanalysis data exists. This reanalysis data can be used to calculate the spectral energy budget of the Martian atmosphere. Valeanu et al. (2017) have calculated a preliminary version of the spectral energy budget for the current version of the MACDA reanalysis dataset (Montabone et al., 2014b), which has a resolution of T31 (i.e. 96 by 48 horizontal grid cells). They are working on a T170 version of this dataset, which is expected to result in interesting spectral energy and flux diagnostics.

Fig. 7.1 shows the preliminary T31 version of the spectral energy budget of Mars from the MACDA reanalysis data set (Montabone et al., 2014b). This plot, however, does not yet accurately account for the Martian surface elevation, which may be an explanation as to why the APE flux does not add up to zero. The plot shows that both APE and KE are transported downscale, apart from a small rotational component of the KE flux, which is negative from wavenumbers $k = 2$ to 11. The conversion term features an interesting region between $k = 3$ and $k = 5$ where KE is converted into APE. It would be interesting to see the results of a zonal-eddy decomposition for these fluxes. We see a similar behaviour of the $\mathcal{C}$ term in cases where we changed the α and $\mathcal{G}$ parameters away from Earth-like values, thereby making the atmosphere react

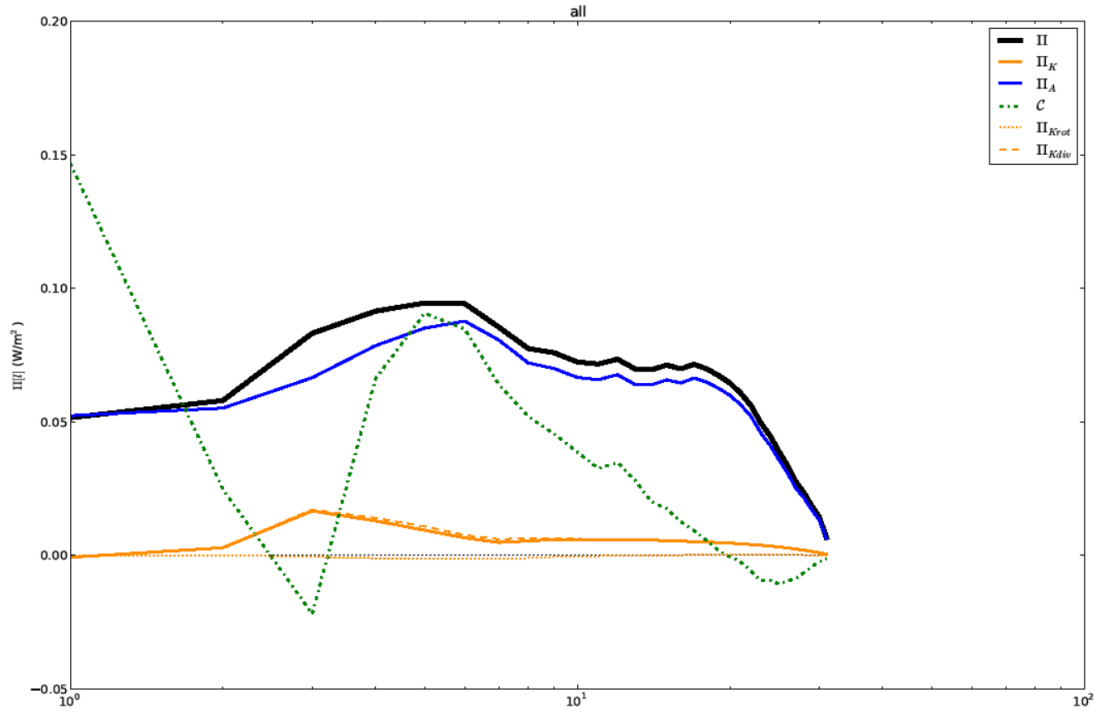

Figure 7.1: Spectral fluxes of KE Π_K, APE Π_A, total energy $\Pi = \Pi_A + \Pi_K$ as well as cumulative conversion $\mathcal{C}$ plotted against the total wavenumber k of the Martian atmosphere from reanalysis data. Figure reproduced from Valeanu et al. (2017).

stronger to the seasonally-varying forcing (see Figs. 5.21 and 5.22).

We show a comparison from our model with $\mathcal{G} = 0$ and $\alpha = 16$ (and otherwise reference values) in Fig. 7.2 to show that the phenomenological behaviour of our Mars-like simulations compares quite well to the preliminary values from Martian reanalysis data. Both cases show mostly downscale KE and APE fluxes, and the conversion of APE to KE in wavenumbers 3 to 5. The spectral fluxes from Martian data are only in a preliminary stage, further comparisons (for instance of the APE flux at large wavenumbers) would go too far. The role of eddy and zonal components of the conversion terms would be interesting to compare in the future.

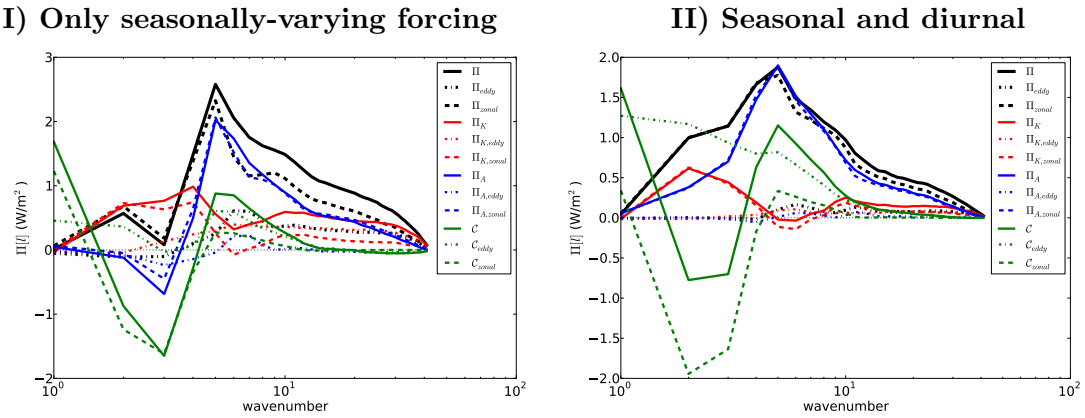

Figure 7.2: Spectral fluxes of KE Π_K, APE Π_A, total energy $\Pi = \Pi_A + \Pi_K$ as well as cumulative conversion $\mathcal{C}$ plotted against the total wavenumber k of the PUMA-GT simulation with $\Omega = \frac{1}{2}\Omega_E$, $\tau_{surf} = 3.6$ days, $\tau_{atm} = 40$ days, $\tau_f = 1$ day, $\mathcal{G} = 0$ with (I) only seasonal solar forcing and (II) both seasonally- and diurnally-varying forcing.

References

D. G. Andrews. *An introduction to atmospheric physics*. Cambridge University Press, 2010.

N. P. Arnold, E. Tziperman, and B. Farrell. Abrupt transition to strong superrotation driven by equatorial wave resonance in an idealized GCM. *Journal of the Atmospheric Sciences*, 69(2):626–640, 2012.

P. Augier and E. Lindborg. A new formulation of the spectral energy budget of the atmosphere, with application to two high-resolution general circulation models. *Journal of the Atmospheric Sciences*, 70(7):2293–2308, 2013.

D. Banfield, B. Conrath, J. C. Pearl, M. D. Smith, and P. Christensen. Thermal tides and stationary waves on Mars as revealed by Mars global surveyor thermal emission spectrometer. *Journal of Geophysical Research: Planets*, 105(E4):9521–9537, 2000.

M. Battalio, I. Szunyogh, and M. Lemmon. Energetics of the martian atmosphere using the Mars analysis correction data assimilation (MACDA) dataset. *Icarus*, 276:1–20, 2016.

A. Belu, F. Selsis, J.-C. Morales, I. Ribas, C. Cossou, and H. Rauer. Primary and secondary eclipse spectroscopy with JWST: exploring the exoplanet parameter space. *Astronomy & Astrophysics*, 525:A83, 2011.

G. J. Berry and C. D. Thorncroft. African easterly wave dynamics in a mesoscale numerical model: The upscale role of convection. *Journal of the Atmospheric Sciences*, 69(4):1267–1283, 2012.

A. K. Betts. A new convective adjustment scheme. part i: Observational and theoret-

ical basis. *Quarterly Journal of the Royal Meteorological Society*, 112(473):677–691, 1986.

G. J. Boer. Zonal and eddy forms of the available potential energy equations in pressure coordinates. *Tellus*, 27(5):433–442, 1975.

G. J. Boer. Diagnostic equations in isobaric coordinates. *Monthly Weather Review*, 110(12):1801–1820, 1982.

G. J. Boer. On exact and approximate energy equations in pressure coordinates. *Tellus A*, 41(2):97–108, 1989.

G. J. Boer and S. Lambert. The energy cycle in atmospheric models. *Climate dynamics*, 30(4):371–390, 2008.

C. Broeg, A. Fortier, D. Ehrenreich, Y. Alibert, W. Baumjohann, W. Benz, M. Deleuil, M. Gillon, A. Ivanov, R. Liseau, et al. Cheops: A transit photometry mission for ESA's small mission programme. In *EPJ Web of Conferences*, volume 47, page 03005. EDP Sciences, 2013.

B. H. Burgess, A. R. Erler, and T. G. Shepherd. The troposphere-to-stratosphere transition in kinetic energy spectra and nonlinear spectral fluxes as seen in ecmwf analyses. *Journal of the Atmospheric Sciences*, 70(2):669–687, 2013.

R. Caballero and M. Huber. Spontaneous transition to superrotation in warm climates simulated by CAM3. *Geophysical Research Letters*, 37(11), 2010.

J. A. Carter and J. N. Winn. The detectability of transit depth variations due to exoplanetary oblateness and spin precession. *The Astrophysical Journal*, 716(1):850, 2010.

J. G. Charney. Geostrophic turbulence. *Journal of the Atmospheric Sciences*, 28(6): 1087–1095, 1971.

J. Y. Cho and E. Lindborg. Horizontal velocity structure functions in the upper troposphere and lower stratosphere. 1. observations. *J. Geophys. Res*, 106(10):223–10, 2001.

D. S. Choi and A. P. Showman. Power spectral analysis of Jupiter's clouds and kinetic energy from Cassini. *Icarus*, 216(2):597–609, 2011.

A. D. Del Genio and W. Zhou. Simulations of superrotation on slowly rotating planets: Sensitivity to rotation and initial condition. *Icarus*, 120(2):332–343, 1996.

A. D. Del Genio, W. Zhou, and T. P. Eichler. Equatorial superrotation in a slowly rotating GCM: Implications for titan and venus. *Icarus*, 101(1):1–17, 1993.

E. Dewan. Saturated-cascade similitude theory of gravity wave spectra. *Journal of Geophysical Research: Atmospheres*, 102(D25):29799–29817, 1997.

J. R. Dias Pinto and R. P. da Rocha. The energy cycle and structural evolution of cyclones over southeastern South America in three case studies. *Journal of Geophysical Research: Atmospheres*, 116(D14112), 2011.

J. R. Dias Pinto and J. L. Mitchell. Atmospheric superrotation in an idealized GCM: Parameter dependence of the eddy response. *Icarus*, 2014.

C. D. Dressing, D. S. Spiegel, C. A. Scharf, K. Menou, and S. N. Raymond. Habitable climates: the influence of eccentricity. *The Astrophysical Journal*, 721(2):1295, 2010.

P. Driscoll and P. Olson. Optimal dynamos in the cores of terrestrial exoplanets: Magnetic field generation and detectability. *Icarus*, 213(1):12–23, 2011.

J. A. Dutton and D. R. Johnson. The theory of available potential energy and a variational approach to atmospheric energetics. *Advances in geophysics*, 12(333):t5, 1967.

A. Eliassen and E. Palm. On the transfer of energy in stationary mountain waves. *Geofysiske Publikasjoner*, 22:1–23, 1961.

S. B. Fels and R. S. Lindzen. The interaction of thermally excited gravity waves with mean flows. *Geophysical and Astrophysical Fluid Dynamics*, 6(2):149–191, 1974.

J. Ferguson, B. Khouider, and M. Namazi. Two-way interactions between equatorially-trapped waves and the barotropic flow. *Chinese Annals of Mathematics, Series B*, 30(5):539–568, 2009.

F. Forget, F. Hourdin, R. Fournier, C. Hourdin, O. Talagrand, M. Collins, S. R. Lewis, P. L. Read, and J.-P. Huot. Improved general circulation models of the Martian atmosphere from the surface to above 80 km. *Journal of Geophysical Research: Planets*, 104(E10):24155–24175, 1999.

K. Fraedrich, E. Kirk, and F. Lunkeit. Portable university model of the atmosphere. *DKRZ Rep*, 16, 1998.

K. Fraedrich, E. Kirk, U. Luksch, and F. Lunkeit. The portable university model of the atmosphere (puma): Storm track dynamics and low-frequency variability. *Meteorologische Zeitschrift*, 14(6):735–745, 2005.

B. Galperin, S. Sukoriansky, and N. Dikovskaya. Zonostrophic turbulence. *Physica Scripta*, 2008(T132):014034, 2008.

B. Galperin, R. M. Young, S. Sukoriansky, N. Dikovskaya, P. L. Read, A. J. Lancaster, and D. Armstrong. Cassini observations reveal a regime of zonostrophic macroturbulence on Jupiter. *Icarus*, 229:295–320, 2014.

P. J. Gierasch. Meridional circulation and the maintenance of the Venus atmospheric rotation. *Journal of the Atmospheric Sciences*, 32(6):1038–1044, 1975.

R. M. Haberle, J. B. Pollack, J. R. Barnes, R. W. Zurek, C. B. Leovy, J. R. Murphy, H. Lee, and J. Schaeffer. Mars atmospheric dynamics as simulated by the NASA Ames general circulation model: 1. the zonal-mean circulation. *Journal of Geophysical Research: Planets*, 98(E2):3093–3123, 1993.

H. Hammel, I. De Pater, S. Gibbard, G. Lockwood, and K. Rages. Uranus in 2003: Zonal winds, banded structure, and discrete features. *Icarus*, 175(2):534–545, 2005.

P. Hedelt, P. von Paris, M. Godolt, S. Gebauer, J. L. Grenfell, H. Rauer, F. Schreier, F. Selsis, and T. Trautmann. Spectral features of earth-like planets and their detectability at different orbital distances around F, G, and K-type stars. *Astronomy & Astrophysics*, 553:A9, 2013.

I. M. Held and D. G. Andrews. On the direction of the eddy momentum flux in baroclinic instability. *Journal of the Atmospheric Sciences*, 40(9):2220–2231, 1983.

R. Hide. Dynamics of the atmospheres of the major planets with an appendix on the viscous boundary layer at the rigid bounding surface of an electrically-conducting rotating fluid in the presence of a magnetic field. *Journal of the Atmospheric Sciences*, 26(5):841–853, 1969.

J. R. Holton and G. J. Hakim. *An introduction to dynamic meteorology*. Academic press, 2013.

B. J. Hoskins and A. J. Simmons. A multi-layer spectral model and the semi-implicit method. *Quarterly Journal of the Royal Meteorological Society*, 101(429):637–655, 1975.

H.-P. Huang, B. Galperin, and S. Sukoriansky. Anisotropic spectra in two-dimensional turbulence on the surface of a rotating sphere. *Physics of Fluids (1994-present)*, 13 (1):225–240, 2001.

I. N. James. *Introduction to circulating atmospheres*. Cambridge University Press, 1995.

T. Jiang, Y. Deng, and W. Li. Local kinetic energy budget of high-frequency and intermediate-frequency eddies: winter climatology and interannual variability. *Climate dynamics*, 41(3-4):961–976, 2013.

Y. Kaspi and G. R. Flierl. Formation of jets by baroclinic instability on gas planet atmospheres. *Journal of the Atmospheric Sciences*, 64(9):3177–3194, 2007.

Y. Kaspi and A. P. Showman. Atmospheric dynamics of terrestrial exoplanets over a wide range of orbital and atmospheric parameters. *The Astrophysical Journal*, 804 (1):60, 2015.

M. J. Kavulich, I. Szunyogh, G. Gyarmati, and R. J. Wilson. Local dynamics of baroclinic waves in the martian atmosphere. *Journal of the Atmospheric Sciences*, 70(11):3415–3447, 2013.

T. L. Koehler. A terrain-dependent reference atmosphere determination method for available potential energy calculations. *Tellus A*, 38(1):42–48, 1986.

D. D. Koll and D. S. Abbot. Temperature structure and atmospheric circulation of dry tidally locked rocky exoplanets. *The Astrophysical Journal*, 825(2):99, 2016.

I. Kraucunas and D. L. Hartmann. Equatorial superrotation and the factors controlling the zonal-mean zonal winds in the tropical upper troposphere. *Journal of the atmospheric sciences*, 62(2):371–389, 2005.

L. Kreidberg, J. L. Bean, J.-M. Désert, B. Benneke, D. Deming, K. B. Stevenson, S. Seager, Z. Berta-Thompson, A. Seifahrt, and D. Homeier. Clouds in the atmosphere of the super-earth exoplanet gj [thinsp] 1214b. *Nature*, 505(7481):69–72, 2014.

A. A. Lacis and V. Oinas. A description of the correlated k distribution method for modeling nongray gaseous absorption, thermal emission, and multiple scattering in vertically inhomogeneous atmospheres. *Journal of Geophysical Research: Atmospheres*, 96(D5):9027–9063, 1991.

A. L. Laraia and T. Schneider. Superrotation in terrestrial atmospheres. *Journal of the Atmospheric Sciences*, 72(11):4281–4296, 2015.

S. Lebonnois, F. Hourdin, V. Eymet, A. Crespin, R. Fournier, and F. Forget. Superrotation of Venus' atmosphere analyzed with a full general circulation model. *Journal of Geophysical Research: Planets*, 115(E6), 2010.

S. Lebonnois, J. Burgalat, P. Rannou, and B. Charnay. Titan global climate model: A new 3-dimensional version of the ipsl titan GCM. *Icarus*, 218(1):707–722, 2012.

S. Lebonnois, N. Sugimoto, and G. Gilli. Wave analysis in the atmosphere of Venus below 100-km altitude, simulated by the lmd Venus GCM. *Icarus*, 278:38–51, 2016.

C. Lee and M. Richardson. A general circulation model ensemble study of the atmospheric circulation of Venus. *Journal of Geophysical Research: Planets*, 115, 2010.

C. Lee, S. R. Lewis, and P. L. Read. Superrotation in a Venus general circulation model. *Journal of Geophysical Research: Planets (1991–2012)*, 112(E4), 2007.

C. Leovy. Weather and climate on mars. *Nature*, 412(6843):245–249, 2001.

C. B. Leovy and R. W. Zurek. Thermal tides and martian dust storms: Direct evidence for coupling. *Journal of Geophysical Research: Solid Earth*, 84(B6):2956–2968, 1979.

S. Lewis, P. Read, T. Ruan, and L. Montabone. Super-rotating jets in a re-analysis of the martian atmosphere. 2012.

S. R. Lewis and P. R. Barker. Atmospheric tides in a Mars general circulation model with data assimilation. *Advances in Space Research*, 36(11):2162–2168, 2005.

S. R. Lewis and P. L. Read. Equatorial jets in the dusty martian atmosphere. *Journal of Geophysical Research: Planets*, 108(E4), 2003.

S. R. Lewis, D. P. Mulholland, P. L. Read, L. Montabone, R. J. Wilson, and M. D. Smith. The solsticial pause on mars: 1 a planetary wave reanalysis. *Icarus*, 2015.

L. Li, A. P. Ingersoll, X. Jiang, D. Feldman, and Y. L. Yung. Lorenz energy cycle of the global atmosphere based on reanalysis datasets. *Geophysical Research Letters*, 34(16), 2007.

J. Liakka. Validation of the dynamical core of the Portable University Model of the Atmosphere (PUMA). Master's thesis, Upsalla University, 2006.

D. K. Lilly. Stratified turbulence and the mesoscale variability of the atmosphere. *Journal of the Atmospheric Sciences*, 40(3):749–761, 1983.

E. Lindborg. The energy cascade in a strongly stratified fluid. *Journal of Fluid Mechanics*, 550:207–242, 2006.

E. Lindborg. A helmholtz decomposition of structure functions and spectra calculated from aircraft data. *Journal of Fluid Mechanics*, 762:R4, 2015.

M. Linsenmeier, S. Pascale, and V. Lucarini. Habitability of Earth-like planets with high obliquity and eccentric orbits: results from a general circulation model. In *EGU General Assembly Conference Abstracts*, volume 16 of *EGU General Assembly Conference Abstracts*, page 15068, May 2014.

E. N. Lorenz. Available potential energy and the maintenance of the general circulation. *Tellus*, 7(2):157–167, 1955.

E. N. Lorenz. *The nature and theory of the general circulation of the atmosphere*. World Meteorological Organization Geneva, 1967.

S. Lovejoy, J.-P. Muller, and J. Boisvert. On Mars too expect macroweather. *Geophysical Research Letters*, 41(21):7694–7700, 2014.

N. Madhusudhan, J. Harrington, K. B. Stevenson, S. Nymeyer, C. J. Campo, P. J. Wheatley, D. Deming, J. Blecic, R. A. Hardy, N. B. Lust, et al. A high c/o ratio and weak thermal inversion in the atmosphere of exoplanet wasp-12b. *Nature*, 469 (7328):64–67, 2011.

S. Manabe and R. F. Strickler. Thermal equilibrium of the atmosphere with a convective adjustment. *Journal of the Atmospheric Sciences*, 21(4):361–385, 1964.

S. Manabe and R. T. Wetherald. Thermal equilibrium of the atmosphere with a given distribution of relative humidity. *Journal of the Atmospheric Sciences*, 1967.

M. Margules. *Über die Energie der Stürme*. KK Hof-und Staatsdruckerei, 1905.

M. M. Marinova, O. Aharonson, and E. Asphaug. Mega-impact formation of the Mars hemispheric dichotomy. *Nature*, 453(7199):1216–1219, 2008.

C. A. F. Marques, A. Rocha, and J. Corte-Real. Global diagnostic energetics of five state-of-the-art climate models. *Climate dynamics*, 36(9-10):1767–1794, 2011.

C. P. McKay, J. B. Pollack, and R. Courtin. The greenhouse and antigreenhouse effects on titan. *Science*, 253(5024):1118–1121, 1991.

J. M. Mendonça and P. L. Read. Exploring the Venus global super-rotation using a comprehensive General Circulation Model. *Planetary and Space Science*, 134:1–18, 2016.

S. M. Mills and D. S. Abbot. Utility of the weak temperature gradient approximation for earth-like tidally locked exoplanets. *The Astrophysical Journal Letters*, 774(2): L17, 2013.

J. L. Mitchell and G. K. Vallis. The transition to superrotation in terrestrial atmospheres. *Journal of Geophysical Research: Planets*, 115(E12), 2010.

J. L. Mitchell, G. K. Vallis, and S. F. Potter. Effects of the seasonal cycle on superrotation in planetary atmospheres. *The Astrophysical Journal*, 787(1):23, 2014.

L. Montabone, K. Marsh, S. Lewis, P. Read, M. Smith, J. Holmes, A. Spiga, D. Lowe, and A. Pamment. The Mars analysis correction data assimilation (MACDA) dataset v1. 0. *Geoscience Data Journal*, 2014a.

L. Montabone, K. Marsh, S. R. Lewis, P. L. Read, M. D. Smith, J. Holmes, A. Spiga, D. Lowe, and A. Pamment. The Mars Analysis Correction Data Assimilation (MACDA) dataset v1. 0. *Geoscience Data Journal*, 1(2):129–139, 2014b.

D. P. Mulholland, S. R. Lewis, P. L. Read, J.-B. Madeleine, and F. Forget. The solsticial pause on mars: 2 modelling and investigation of causes. *Icarus*, 2015.

G. Nastrom and K. S. Gage. A climatology of atmospheric wavenumber spectra of wind and temperature observed by commercial aircraft. *Journal of the atmospheric sciences*, 42(9):950–960, 1985.

C. E. Newman, C. Lee, Y. Lian, M. I. Richardson, and A. D. Toigo. Stratospheric superrotation in the titanwrf model. *Icarus*, 213(2):636–654, 2011.

A. H. Oort. Global atmospheric circulation statistics, 1958-1973. *NOAA Prof. Pap.*, (14), 1983.

E. Pallé, E. B. Ford, S. Seager, P. Montañés-Rodríguez, and M. Vazquez. Identifying the rotation rate and the presence of dynamic weather on extrasolar earth-like planets from photometric observations. *The Astrophysical Journal*, 676(2):1319, 2008.

J. P. Peixóto and A. H. Oort. The annual distribution of atmospheric energy on a planetary scale. *Journal of Geophysical Research*, 79(15):2149–2159, 1974.

R. Plumb. Momentum transport by the thermal tide in the stratosphere of venus. *Quarterly Journal of the Royal Meteorological Society*, 101(430):763–776, 1975.

S. F. Potter, G. K. Vallis, and J. L. Mitchell. Spontaneous superrotation and the role of kelvin waves in an idealized dry GCM. *Journal of the Atmospheric Sciences*, 71 (2):596–614, 2014.

V. Ramanathan, R. J. Cicerone, H. B. Singh, and J. T. Kiehl. Trace gas trends and their potential role in climate change. *Journal of Geophysical Research: Atmospheres (1984–2012)*, 90(D3):5547–5566, 1985.

H. Rauer, S. v. Gebauer, P. v. Paris, J. Cabrera, M. Godolt, J. Grenfell, A. Belu, F. Selsis, P. Hedelt, and F. Schreier. Potential biosignatures in super-earth atmospheres-i. spectral appearance of super-earths around m dwarfs. *Astronomy & Astrophysics*, 529:A8, 2011.

E. Rauscher and K. Menou. The role of drag in the energetics of strongly forced exoplanet atmospheres. *The Astrophysical Journal*, 745(1):78, 2012.

P. Read. Super-rotation and diffusion of axial angular momentum: Ii. a review of quasi-axisymmetric models of planetary atmospheres. *Quarterly Journal of the Royal Meteorological Society*, 112(471):253–272, 1986.

P. Read, L. Montabone, D. Mulholland, S. Lewis, B. Cantor, and R. Wilson. Midwinter suppression of baroclinic storm activity on mars: observations and models. 2011.

P. Read, J. Barstow, B. Charnay, S. Chelvaniththilan, P. Irwin, S. Knight, S. Lebonnois, S. Lewis, J. Mendonça, and L. Montabone. Global energy budgets and trenberth diagrams for the climates of terrestrial and gas giant planets. *Quarterly Journal of the Royal Meteorological Society*, 2015.

P. L. Read. Dynamics and circulation regimes of terrestrial planets. *Planetary and Space Science*, 59(10):900–914, 2011.

P. L. Read. The dynamics and circulation of Venus atmosphere. In *Towards Understanding the Climate of Venus*, pages 73–110. Springer, 2013.

P. L. Read and S. R. Lewis. *The martian climate revisited: Atmosphere and environment of a desert planet*. Springer Science & Business Media, 2004.

P. B. Rhines. Waves and turbulence on a beta-plane. *Journal of Fluid Mechanics*, 69 (03):417–443, 1975.

M. I. Richardson and R. J. Wilson. A topographically forced asymmetry in the Martian circulation and climate. *Nature*, 416(6878):298–301, 2002.

E. Roeckner, R. Brokopf, M. Esch, M. Giorgetta, S. Hagemann, L. Kornblueh, E. Manzini, U. Schlese, and U. Schulzweida. Sensitivity of simulated climate to horizontal and vertical resolution in the echam5 atmosphere model. *Journal of Climate*, 19(16):3771–3791, 2006.

W. B. Rossow and G. P. Williams. Large-scale motion in the Venus stratosphere. *Journal of the Atmospheric Sciences*, 36(3):377–389, 1979.

W. B. Rossow, A. D. Del Genio, and T. Eichler. Cloud-tracked winds from pioneer Venus ocpp images. *Journal of the Atmospheric Sciences*, 47(17):2053–2084, 1990.

C. Russell. *Venus aeronomy*. Springer, 2012.

R. Salmon. Baroclinic instability and geostrophic turbulence. *Geophysical & Astrophysical Fluid Dynamics*, 15(1):167–211, 1980.

A. Sanchez-Lavega. *An introduction to planetary atmospheres*. CRC Press, 2011.

A. Sánchez-Lavega, R. Hueso, G. Piccioni, P. Drossart, J. Peralta, S. Pérez-Hoyos, C. F. Wilson, F. W. Taylor, K. H. Baines, D. Luz, et al. Variable winds on Venus mapped in three dimensions. *Geophysical Research Letters*, 35(13), 2008.

R. Saravanan. Equatorial superrotation and maintenance of the general circulation in two-level models. *Journal of the atmospheric sciences*, 50(9):1211–1227, 1993.

T. Schneider and J. Liu. Formation of jets and equatorial superrotation on Jupiter. *arXiv preprint arXiv:0809.4302*, 2008.

T. Schneider and C. C. Walker. Self-organization of atmospheric macroturbulence into critical states of weak nonlinear eddy-eddy interactions. *Journal of the atmospheric sciences*, 63(6):1569–1586, 2006.

G. Schubert and J. Whitehead. Moving flame experiment with liquid mercury: Possible implications for the Venus atmosphere. *Science*, 163(3862):71–72, 1969.

R. B. Scott and B. K. Arbic. Spectral energy fluxes in geostrophic turbulence: Implications for ocean energetics. *Journal of physical oceanography*, 37(3):673–688, 2007.

S. Seager and L. Hui. Constraining the rotation rate of transiting extrasolar planets by oblateness measurements. *The Astrophysical Journal*, 574(2):1004, 2002.

S. Seager, D. Deming, and J. Valenti. Transiting exoplanets with JWST. In *Astrophysics in the Next Decade*, pages 123–145. Springer, 2009.

A. P. Showman. Numerical simulations of forced shallow-water turbulence: Effects of moist convection on the large-scale circulation of Jupiter and saturn. *Journal of the Atmospheric Sciences*, 64(9):3132–3157, 2007.

A. P. Showman and L. M. Polvani. Equatorial superrotation on tidally locked exoplanets. *The Astrophysical Journal*, 738(1):71, 2011.

P. Siegmund. The generation of available potential energy, according to lorenz' exact and approximate equations. *Tellus A*, 46(5):566–582, 1994.

J. Slawinska, O. Pauluis, A. J. Majda, and W. W. Grabowski. Multiscale interactions in an idealized walker circulation: Mean circulation and intraseasonal variability. *Journal of the Atmospheric Sciences*, 71(3):953–971, 2014.

D. E. Smith, M. T. Zuber, H. V. Frey, J. B. Garvin, J. W. Head, D. O. Muhleman, G. H. Pettengill, R. J. Phillips, S. C. Solomon, H. J. Zwally, et al. Mars orbiter laser altimeter: Experiment summary after the first year of global mapping of mars. *Journal of Geophysical Research: Planets*, 106(E10):23689–23722, 2001.

I. A. Snellen, B. R. Brandl, R. J. de Kok, M. Brogi, J. Birkby, and H. Schwarz. Fast spin of the young extrasolar planet β Pictoris b. *Nature*, 509(7498):63–65, 2014.

A. H. Sobel, J. Nilsson, and L. M. Polvani. The weak temperature gradient approximation and balanced tropical moisture waves. *Journal of the atmospheric sciences*, 58(23):3650–3665, 2001.

D. S. Spiegel, Z. Haiman, and B. S. Gaudi. On constraining a transiting exoplanet's rotation rate with its transit spectrum. *The Astrophysical Journal*, 669(2):1324, 2007.

D. S. Spiegel, K. Menou, and C. A. Scharf. Habitable climates: the influence of obliquity. *The Astrophysical Journal*, 691(1):596, 2009.

K. Srinivasan and W. Young. Zonostrophic instability. *Journal of the atmospheric sciences*, 69(5):1633–1656, 2012.

K. B. Stevenson, J.-M. Désert, M. R. Line, J. L. Bean, J. J. Fortney, A. P. Showman, T. Kataria, L. Kreidberg, P. R. McCullough, G. W. Henry, et al. Thermal structure of an exoplanet atmosphere from phase-resolved emission spectroscopy. *Science*, 346 (6211):838–841, 2014.

M. J. Suarez and D. G. Duffy. Terrestrial superrotation: A bifurcation of the general circulation. *Journal of the atmospheric sciences*, 49(16):1541–1554, 1992.

S. Sukoriansky, N. Dikovskaya, and B. Galperin. On the arrest of inverse energy cascade and the rhines scale. *Journal of the Atmospheric Sciences*, 64(9):3312–3327, 2007.

F. Tabataba-Vakili, P. L. Read, S. R. Lewis, L. Montabone, T. Ruan, Y. Wang, A. Valeanu, and R. Young. A lorenz/boer energy budget for the atmosphere of Mars from a "reanalysis" of spacecraft observations. *Geophysical Research Letters*, 42(20):8320–8327, 2015.

M. Takagi and Y. Matsuda. Effects of thermal tides on the Venus atmospheric superrotation. *Journal of Geophysical Research: Atmospheres*, 112(D9), 2007.

M. Tessenyi, G. Tinetti, G. Savini, and E. Pascale. Molecular detectability in exoplanetary emission spectra. *Icarus*, 226(2):1654–1672, 2013.

A. F. Thompson and W. R. Young. Two-layer baroclinic eddy heat fluxes: Zonal flows and energy balance. *Journal of the Atmospheric Sciences*, 64(9):3214–3231, 2007.

R. Tulloch and K. S. Smith. Quasigeostrophic turbulence with explicit surface dynamics: Application to the atmospheric energy spectrum. *Journal of the Atmospheric Sciences*, 66(2):450–467, 2009.

K. K. Tung and W. W. Orlando. The k-3 and k-5/3 energy spectrum of atmospheric turbulence: Quasigeostrophic two-level model simulation. *Journal of the atmospheric sciences*, 60(6):824–835, 2003.

D. Tyler, Jr. and J. R. Barnes. Mesoscale modeling of the circulation in the gale crater region: An investigation into the complex forcing of convective boundary layer depths. *Mars*, 8:58–77, 2013.

A. M. Valeanu, P. L. Read, F. Tabataba-Vakili, S. R. Lewis, and L. Montabone. Spectrally resolved energetics of the martian atmosphere. In *Mars Atmosphere: Modelling and Observation, 6th International Workshop*, 2017.

A. Vallgren, E. Deusebio, and E. Lindborg. Possible explanation of the atmospheric kinetic and potential energy spectra. *Physical review letters*, 107(26):268501, 2011.

G. K. Vallis. *Atmospheric and oceanic fluid dynamics: fundamentals and large-scale circulation*. Cambridge University Press, 2006.

G. K. Vallis and M. E. Maltrud. Generation of mean flows and jets on a beta plane and over topography. *Journal of physical oceanography*, 23(7):1346–1362, 1993.

I. M. Vardavas and F. Taylor. *Radiation and Climate: Atmospheric energy budget from satellite remote sensing*, volume 138. Oxford University Press, 2011.

H. Wang, M. I. Richardson, A. D. Toigo, and C. E. Newman. Zonal wavenumber three traveling waves in the northern hemisphere of Mars simulated with a general circulation model. *Icarus*, 223(2):654–676, 2013.

P. Wang and J. L. Mitchell. Planetary ageostrophic instability leads to superrotation. *Geophysical Research Letters*, 41(12):4118–4126, 2014.

Y. Wang. *Comparative planetary circulation regimes in simple general circulation models*. PhD thesis, University of Oxford, 2014.

Y. Wang, P. L. Read, F. Tabataba-Vakili, and R. M. B. Young. Comparative terrestrial atmospheric circulation regimes in simplified global circulation models: I. from cyclostrophic super-rotation to geostrophic turbulence. *Quarterly Journal of the Royal Meteorological Society*, in prep.a.

Y. Wang, P. L. Read, F. Tabataba-Vakili, and R. M. B. Young. Comparative terrestrial atmospheric circulation regimes in simplified global circulation models: II. *Quarterly Journal of the Royal Meteorological Society*, in prep.b.

N. C. Wells. *The atmosphere and ocean: a physical introduction*, volume 5. John Wiley & Sons, 2011.

M. Wheeler and G. N. Kiladis. Convectively coupled equatorial waves: Analysis of clouds and temperature in the wavenumber-frequency domain. *Journal of the Atmospheric Sciences*, 56(3):374–399, 1999.

G. P. Williams. The dynamical range of global circulations I. *Climate dynamics*, 2(4): 205–260, 1988a.

G. P. Williams. The dynamical range of global circulations II. *Climate Dynamics*, 3 (2):45–84, 1988b.

G. P. Williams. Barotropic instability and equatorial superrotation. *Journal of the atmospheric sciences*, 60(17):2136–2152, 2003.

G. P. Williams. Equatorial superrotation and barotropic instability: Static stability variants. *Journal of the atmospheric sciences*, 63(5):1548–1557, 2006.

J. R. Wilson and K. Hamilton. Comprehensive model simulation of thermal tides in the martian atmosphere. *Journal of the Atmospheric Sciences*, 53(9):1290–1326, 1996.

M. Yamamoto and M. Takahashi. The fully developed superrotation simulated by a general circulation model of a venus-like atmosphere. *Journal of the atmospheric sciences*, 60(3):561–574, 2003.

M. Yamamoto and M. Takahashi. Superrotation maintained by meridional circulation and waves in a venus-like AGCM. *Journal of the atmospheric sciences*, 63(12): 3296–3314, 2006.

M. Yamamoto and M. Takahashi. General circulation driven by baroclinic forcing due to cloud layer heating: Significance of planetary rotation and polar eddy heat transport. *Journal of Geophysical Research: Planets*, 121(4):558–573, 2016.

R. M. B. Young and P. L. Read. Forward and inverse kinetic energy cascades in Jupiter's weather layer. submitted.

L. Zasova, N. Ignatiev, I. Khatuntsev, and V. Linkin. Structure of the Venus atmosphere. *Planetary and Space Science*, 55(12):1712–1728, 2007.